

**Trace gas measurements from different spectral regions  
using FTIR spectroscopy**

Zur Erlangung des akademischen Grades eines  
DOKTORS DER NATURWISSENSCHAFTEN

von der Fakultät für Physik des  
Karlsruher Instituts für Technologie

genehmigte

DISSERTATION

von

Matthäus Kiel  
aus Tichau/Pleß

Tag der mündlichen Prüfung: 08.07.2016

Referent: Prof. Dr. Johannes Orphal

Korreferent: Priv. Doz. Dr. Michael Höpfner



# Abstract

In this thesis, atmospheric trace gas measurements from different spectral regions using Fourier Transform Infrared (FTIR) spectroscopy are analyzed and compared. Currently, there are two established global ground-based FTIR networks which provide long-term atmospheric trace gas records for climate studies, namely the Total Carbon Column Observing Network (TCCON) and the Network for the Detection of Atmospheric Composition Change (NDACC). Both networks measure total columns of trace gases from different spectral regions. The Karlsruhe FTIR spectrometer, however, is a prototype of a merged TCCON and NDACC instrument, which makes Karlsruhe a favorable site to compare measurements from different spectral regions, aiming at harmonizing NDACC and TCCON data records. If a precise relationship between data sets provided by both global networks can be established, a combined data record will improve the spatial and temporal coverage over each individual network. This is highly desirable for future satellite validations and model studies as well as long-term trend studies.

The unique Karlsruhe optical setup induces broad variations in the background continuum of measured spectra. These variations account for differences in column averaged dry-air mole fractions which exceed the TCCON's precision (e.g. 1 ppm for CO<sub>2</sub>). In the first part of this thesis, a new analysis approach for TCCON measurements is presented, allowing for an appropriate treatment of the background continuum variations. A higher order Legendre polynomial fit has been enabled to properly fit the background continuum. The new retrieval strategy significantly improves the root mean square for residuals of the most important TCCON target gases CO<sub>2</sub>, CO, CH<sub>4</sub>, and N<sub>2</sub>O. Moreover, airmass dependent artefacts are minimized. The new modified retrieval strategy improves Karlsruhe TCCON data in context of other TCCON stations and reduces a site-specific bias at Karlsruhe. Column averaged dry-air mole fractions of CO<sub>2</sub> changed by 0.2 %, CH<sub>4</sub> by 0.1 %, CO by 2.0 %, and N<sub>2</sub>O by 0.7 % compared to the obsolete analysis strategy.

The second part of the thesis describes a comparison between column averaged dry-air mole fractions of CO retrieved from the fundamental band at 4.7  $\mu\text{m}$  and from the first overtone band at 2.3  $\mu\text{m}$ . A constant bias of about 4.5 ppb is identified with a seasonal variation of about 2.1 ppb. In this work, contributions to the constant bias are identified

and quantified. Several factors contribute to the observed bias, including the airmass independent and airmass dependent correction factor for TCCON data, a different treatment of isotopic identities, and differing a priori information used for TCCON and NDACC analyses. The remaining bias of about 0.4 ppb might be caused by imperfect knowledge of the spectroscopic parameters in the different spectral regions. The seasonal variation in the comparison between NDACC and TCCON total columns of CO is estimated by the smoothing effect using simulated vertical concentration profiles of CO from a global chemistry model. It is shown that the seasonal variation is caused by different vertical resolutions for measurements in the different spectral regions.

The findings in this thesis show that the identification and quantification of differences between trace gas measurements from different spectral regions are essential for a joint use of both data records. One harmonized primary data set is highly desirable for satellite validations and model studies, aiming at better understanding the Earth's climate system.





## List of Author's Publications

**Kiel, M.**, Hase, F., Blumenstock, T., and Kirner, O.: *Comparison of XCO abundances from the Total Carbon Column Observing Network and the Network for the Detection of Atmospheric Composition Change measured in Karlsruhe*, Atmos. Meas. Tech., 9, 2223-2239, doi:10.5194/amt-9-2223-2016, 2016

**Kiel, M.**, Wunch, D., Wennberg, P. O., Toon, G. C., Hase, F., and Blumenstock, T.: *Improved retrieval of gas abundances from near-infrared solar FTIR spectra measured at the Karlsruhe TCCON station*, Atmos. Meas. Tech., 9, 669-682, doi:10.5194/amt-9-669-2016, 2016

Hase, F., Frey, M., **Kiel, M.**, M., Blumenstock, T., Harig, R., Keens, A., and Orphal, J.: *Addition of a channel for XCO observations to a portable FTIR spectrometer for greenhouse gas measurements*, Atmos. Meas. Tech., 9, 2303-2313, doi:10.5194/amt-9-2303-2016, 2016

Barthlott, S., Schneider, M., Hase, F., Blumenstock, T., **Kiel, M.**, Dubravica, D., García, O. E., Sepúlveda, E., Mengistu Tsidu, G., Takele Kenea, S., Grutter, M., Plaza, E. F., Stremme, W., Strong, K., Weaver, D., Palm, M., Warneke, T., Notholt, J., Mahieu, E., Servais, C., Jones, N., Griffith, D. W. T., Smale, D., and Robinson, J.: *Tropospheric water vapour isotopologue data ( $H_2^{16}O$ ,  $H_2^{18}O$  and  $HD^{16}O$ ) as obtained from NDACC/FTIR solar absorption spectra*, Earth Syst. Sci. Data Discuss., 8, 3047-3057, doi:10.5194/essd-2016-9, in review, 2016

Hase, F., Frey, M., Blumenstock, T., Groß, J., **Kiel, M.**, Kohlhepp, R., Mengistu Tsidu, G., Schäfer, K., Sha, M. K., and Orphal, J.: *Application of portable FTIR spectrometers for detecting greenhouse gas emissions of the major city Berlin*, Atmos. Meas. Tech., 8, 3059-3068, doi:10.5194/amt-8-3059-2015, 2015

Frey, M., Hase, F., Blumenstock, T., Groß, J., **Kiel, M.**, Mengistu Tsidu, G., Schäfer, K., Sha, M. K., and Orphal, J.: *Calibration and instrumental line shape characterization of a set of portable FTIR spectrometers for detecting greenhouse gas emissions*, Atmos. Meas. Tech., 8, 3047-3057, doi:10.5194/amt-8-3047-2015, 2015



# Contents

**Abstract**

**List of Author's Publications**

<b>1</b>	<b>Introduction</b>	<b>1</b>
<b>2</b>	<b>Theoretical Background</b>	<b>5</b>
2.1	The Earth's atmosphere . . . . .	5
2.1.1	Composition and vertical structure of the Earth's atmosphere . . .	5
2.1.2	The Earth's radiation budget . . . . .	8
2.1.3	The greenhouse effect . . . . .	9
2.2	Molecular Spectroscopy . . . . .	12
2.2.1	The Born-Oppenheimer approximation . . . . .	12
2.2.2	Absorption and emission of radiation . . . . .	13
2.2.3	The harmonic oscillator . . . . .	16
2.2.4	The anharmonic oscillator . . . . .	17
2.2.5	The rigid rotor . . . . .	19
2.2.6	The non-rigid rotor . . . . .	20
2.2.7	Vibrating rotor . . . . .	21
2.2.8	Spectral line shapes . . . . .	24
2.3	Fourier Transform Infrared spectroscopy . . . . .	27
2.3.1	The Michelson interferometer . . . . .	28
2.3.2	The Fourier Transformation . . . . .	30
2.3.3	Phase correction . . . . .	31
2.3.4	Apodization and instrumental line shape . . . . .	32
2.3.5	Global FTIR networks for atmospheric observations . . . . .	33
2.4	Basics of the radiative transfer in the Earth's atmosphere . . . . .	35
2.5	Inversion theory . . . . .	37
<b>3</b>	<b>Ground-based solar absorption FTIR measurements in Karlsruhe</b>	<b>41</b>
3.1	The Karlsruhe FTS site . . . . .	41
3.1.1	Basic setup of the Karlsruhe FTIR instrumentation . . . . .	42

3.1.2	Differences between the Karlsruhe instrumental setup and standard TCCON and NDACC FTIR instruments . . . . .	45
3.2	Analysis of solar absorption FTIR spectra . . . . .	49
3.2.1	Analysis of TCCON data . . . . .	49
3.2.2	Analysis of NDACC data . . . . .	52
3.3	Discussion of error sources . . . . .	56
3.3.1	Spectral noise . . . . .	56
3.3.2	Detector nonlinearity . . . . .	56
3.3.3	Pointing offset . . . . .	57
3.3.4	A priori temperature . . . . .	57
3.3.5	A priori pressure . . . . .	58
3.3.6	Spectroscopic parameters . . . . .	58
3.3.7	Calculation of column averaged dry-air mole fractions . . . . .	59
3.3.8	Background continuum variations . . . . .	60
3.4	Impact of the Karlsruhe instrumental setup on background continuum variations . . . . .	61
3.5	Impact of the background continuum variations on spectral fits in the NIR and MIR . . . . .	65
<b>4</b>	<b>Improvement of retrievals of gas abundances from TCCON measurements</b>	<b>71</b>
4.1	Fitting the background continuum . . . . .	71
4.2	Impact of background continuum fitting on airmass dependence of DMFs . . . . .	77
4.3	Impact of background continuum fitting on column averaged DMFs . . . . .	80
4.4	Karlsruhe data in context of other TCCON stations . . . . .	81
4.5	Airmass dependence of O <sub>2</sub> retrievals in the MIR . . . . .	86
4.6	Conclusions . . . . .	88
<b>5</b>	<b>Harmonization of XCO abundances from Karlsruhe NDACC and TCCON measurements</b>	<b>91</b>
5.1	Atmospheric carbon monoxide . . . . .	92
5.2	XCO retrieved from NDACC and TCCON measurements in Karlsruhe . . . . .	94
5.2.1	NDACC CO retrievals in the MIR spectral region . . . . .	94
5.2.2	TCCON CO retrievals in the NIR spectral range . . . . .	97
5.3	Theoretical error estimation for CO retrievals from MIR and NIR spectral regions . . . . .	98
5.3.1	Vertical profile and total column error estimation . . . . .	98
5.4	Calculation of column averaged DMFs . . . . .	102
5.5	Impact of a priori information on retrieved XCO . . . . .	103
5.5.1	Impact of a priori VMR profiles on retrieved XCO . . . . .	105

5.5.2	Impact of spectroscopic parameters on retrieved XCO . . . . .	107
5.6	Identification of differences between NDACC and TCCON XCO . . . . .	108
5.7	Analysis of bias . . . . .	110
5.7.1	Impact of the airmass independent calibration factor . . . . .	110
5.7.2	Impact of the airmass dependent correction factor . . . . .	112
5.7.3	Impact of different isotopic identities . . . . .	113
5.7.4	Impact of differing a priori VMR profiles . . . . .	114
5.7.5	Remaining bias . . . . .	114
5.8	Analysis of seasonal variations between NDACC and TCCON XCO . . . . .	115
5.8.1	Applying averaging kernels to model data . . . . .	116
5.8.2	ECHAM/MESSy Atmospheric Chemistry model data . . . . .	116
5.8.3	Estimation of the smoothing effect . . . . .	117
5.9	Conclusions . . . . .	120

**6 Summary and Outlook** **123**

**7 Bibliography** **127**

**List of Figures**

**List of Tables**

**List of Acronyms**

**Acknowledgements**



# 1 Introduction

Trace gases account for less than 1 % of the Earth's atmospheric chemical composition but strongly influence the climate system. The increase of trace gas concentrations has a large impact on the Earth's radiative budget and substantially enhances the greenhouse effect. The radiative forcing of well mixed greenhouse gases (GHG) increased by  $2.83 \text{ W m}^{-2}$  from the start of the industrial era in the year 1750 to 2011 (IPCC, 2013). This change is largely due to the increase of carbon dioxide ( $\text{CO}_2$ ) concentrations in the atmosphere. Over the last decade, the radiative forcing of  $\text{CO}_2$  has a growth rate of  $0.27 \text{ W m}^{-2}$  per decade. The net radiative forcing of GHGs other than  $\text{CO}_2$  accounted for about  $1.00 \text{ W m}^{-2}$  between 1750 and 2011 (IPCC, 2013). The growth in concentrations of GHGs and other trace gases can be largely attributed to anthropogenic emissions, mainly driven by energy related industries burning fossil fuels and land use change (Le Quéré et al., 2015). This leads to a continuous increase of the radiative forcing affecting the global climate.

In the recent years, great effort was undertaken to improve the understanding of the changing climate. Several measurement programs were initiated to monitor trace gas concentrations and long-term trends in the Earth's atmosphere. These programs include observations of the atmosphere and surface, aiming at providing long-term regional and global climate quality data records to support scientific studies and future climate projections (e.g. Meul et al., 2016). The assimilation of different measurement methods, including in situ measurements, satellite observations and ground-based remote sensing measurements provide a unique data set which yields results that could not have been uncovered by one single measurement method. Ground-based remote sensing measurements provide a transfer standard between the highly precise but locally limited in situ measurements and global observations by satellite-borne instruments which are limited in precision and temporal resolution. An established ground-based remote sensing technique is provided by the Fourier Transform Infrared (FTIR) Spectroscopy using direct Sun light as source to measure gas abundances in the Earth's atmosphere. FTIR instruments measure quantities comparable to satellite data but are more precise than space-borne observations.

Currently, two established ground-based FTIR networks, the Total Carbon Column Observing Network (TCCON, Wunch et al., 2011) and the Network for the Detection of

---

Atmospheric Composition Change - Infrared Working Group (NDACC - IRWG, Kurylo, 1991) provide total column measurements of gas abundances in the Earth's atmosphere. These are independent of vertical transport processes and are highly suitable for inverse modelling studies. The TCCON measures solar absorption spectra in the near infrared (NIR) spectral region. The network aims at providing accurate total column measurements of atmospheric constituents, including CO<sub>2</sub>, CH<sub>4</sub>, CO, N<sub>2</sub>O, HF, H<sub>2</sub>O, and HDO. The NDACC primarily provided total column measurements of O<sub>3</sub> and ozone related gases to study their response to anthropogenic chlorofluorocarbons (CFCs). In the recent years, these measurements were extended to gases which affect the air quality, including total column measurements of CO, N<sub>2</sub>O, CH<sub>4</sub>, NO, C<sub>2</sub>H<sub>6</sub>, and various other atmospheric gaseous constituents of interest for climate studies. The NDACC measures spectra in the mid infrared (MIR) spectral region, also using the Sun as source. Both networks provide primary data records for the validation of satellite measurements and model studies (e.g. Frankenberg et al., 2006, 2015; Morino et al., 2011; de Laat et al., 2010; Sussmann et al., 2005).

Measurements of several gases are provided by both networks. For example, CH<sub>4</sub>, CO, and N<sub>2</sub>O are accessible in different molecular absorption bands in the MIR and NIR spectral regions. If a precise relationship between measurements of gas abundances from both spectral regions can be established, a combined data set consisting of measurements from both global FTIR networks will improve the spatial and temporal coverage over each individual network. This is highly desirable for future satellite validations and model studies as well as long-term trend studies. However, comparisons of trace gas measurements from both spectral regions reveal discrepancies of the order that exceed each network's precision for several gases. Therefore, great effort is required to identify and characterize potential factors which contribute to the observed differences.

The Institute of Meteorology and Climate Research (IMK) at the Karlsruhe Institute of Technology (KIT) - Campus North operates a prototype FTIR spectrometer which allows for measurements in the MIR and NIR spectral range simultaneously. The instrumental setup is a prototype of a merged TCCON and NDACC instrument, which makes Karlsruhe a favorable site to compare measurements from both spectral regions.

This thesis focuses on the identification and quantification of differences between trace gas measurements from different spectral regions using FTIR spectroscopy. In the first part of this work, instrumental influences of the Karlsruhe FTIR prototype setup on atmospheric measurements of gas abundances are identified, which require special attention in the analysis of solar absorption spectra. A modified analysis strategy is developed to account for these effects which is necessary when a direct comparison between measurements from

both spectral regions is performed. The second part of the thesis focuses on the identification and quantification of differences between long-term measurements of trace gas abundances in Karlsruhe analyzed from the MIR and NIR spectral region. Here, the focus lies on the analysis of the trace gas carbon monoxide (CO). CO is an air pollutant which directly affects human health due to its toxicity. It has a significant impact on the formation of O<sub>3</sub> and also affects concentrations of other GHGs due to its reaction with the hydroxyl radical OH and therefore implicitly affects the Earth's climate. This comparison aims at harmonizing CO data records from the two ground-based FTIR networks NDACC and TCCON which is highly desirable in support of future satellite validations and model studies.



# 2 Theoretical Background

## 2.1 The Earth's atmosphere

The Earth's atmosphere is essential for life on Earth and is the origin of various chemical and physical processes which are of utmost interest in many scientific fields. In the next sections, an excerpt of relevant aspects and processes in the Earth's atmosphere is given. This summary includes a brief overview of the composition and vertical structure of the Earth's atmosphere including its major and minor constituents. The latter includes trace gases which have a crucial impact on the Earth's radiative budget. This includes the greenhouse effect which is strongly correlated with natural and anthropogenic emissions of greenhouse gases and near-term climate forcers. The contents of the following sections are mainly based on Schlager et al. (2012), Meerkötter and Vázquez-Navarro (2012), Ponater et al. (2012) and the latest Intergovernmental Panel on Climate Change report from 2013 (IPCC, 2013).

### 2.1.1 Composition and vertical structure of the Earth's atmosphere

The Earth's atmosphere is comprised of a mixture of gases. The most abundant constituents, assuming dry-air, are molecular nitrogen ( $\text{N}_2$ ), molecular oxygen ( $\text{O}_2$ ), and the noble gas argon (Ar). The fractional concentration by volume of  $\text{N}_2$  is about 78 %, about 21 % for  $\text{O}_2$  and about 0.9 % for Ar. The relative concentrations of these gaseous constituents vary little with time and are considered as fairly constant in the Earth's atmosphere. Together,  $\text{N}_2$ ,  $\text{O}_2$ , and Ar account for almost 99.9 % of the chemical proportion of the atmosphere. In addition, the terrestrial atmosphere contains a variety of minor compounds, including the so called trace gases. Prominent examples are carbon dioxide ( $\text{CO}_2$ ), methane ( $\text{CH}_4$ ), ozone ( $\text{O}_3$ ), nitrous oxide ( $\text{N}_2\text{O}$ ), carbon monoxide (CO), and the man-made halocarbons. The relative concentrations of these gases are small, ranging from  $10^{-6}$  to  $10^{-15}$  mol mol<sup>-1</sup> (IPCC, 2013). Although these trace gases account for less than 1 % by volume as well as mass of the Earth's atmosphere, they are of great importance for many atmospheric processes. For example, the long-lived trace gases  $\text{CO}_2$ ,  $\text{CH}_4$ ,  $\text{N}_2\text{O}$ , and  $\text{O}_3$  have impact on thermodynamic and radiative processes leading to large effects on the total radiation budget of the atmosphere

and collectively contribute to the greenhouse effect (see Sects. 2.1.2 and 2.1.3).

Water vapor ( $\text{H}_2\text{O}$ ) is of particular importance for the energy exchange in the atmosphere (Bengtsson, 2010; Held and Soden, 2006).  $\text{H}_2\text{O}$  appears in three different phases, namely vapor, liquid, and solid. Transitions between these phases affect the thermodynamic state of an air parcel as large quantities of heat might be absorbed or freed.  $\text{H}_2\text{O}$  is highly variable in the atmosphere with fractional concentrations by volume which vary between 0 % and 5 % for regions with either dry or humid airmasses. Abundances of  $\text{H}_2\text{O}$  are mainly concentrated in the lower atmosphere (troposphere) and are controlled by the Earth's hydrological cycle.

Many trace gases are emitted due to biogenic processes at the Earth's surface or produced by chemical and photochemical processes in the atmosphere. In addition, a large proportion of trace gas concentrations is directly emitted into the atmosphere by anthropogenic activities like fossil fuel combustion ( $\text{CO}_2$ ,  $\text{NO}_x$ ,  $\text{SO}_2$ ), traffic ( $\text{CO}$ ,  $\text{CO}_2$ ,  $\text{NO}_x$ ), and agriculture ( $\text{CH}_4$ ,  $\text{N}_2\text{O}$ ,  $\text{NH}_3$ ). Among the trace gases, the so called short-lived species have the highest chemical reactivity and have the ability to affect the oxidation capacity of the atmosphere. Prominent short-lived oxidizing compounds in the atmosphere are free radicals like hydroxyl ( $\text{OH}$ ), nitric oxide ( $\text{NO}$ ), and atoms of chlorine ( $\text{Cl}$ ) and bromine ( $\text{Br}$ ) which, for example, cause a depletion of the ozone layer in the stratosphere. The origin of this layer is the photolysis of molecular oxygen by solar ultraviolet (UV) radiation. Thereafter, the oxygen atoms bond with  $\text{O}_2$  and form  $\text{O}_3$ . The formed  $\text{O}_3$  molecules absorb UV radiation and break up into molecular and atomic oxygen. The oxygen atom instantaneously reacts with molecular oxygen, producing  $\text{O}_3$ . The excess energy of this process leads to a warming of the stratosphere. The ozone layer functions as a protective shield for the biosphere against UV radiation. Moreover,  $\text{O}_3$  is infrared active and absorbs and re-emits infrared radiation emitted by the Earth's surface contributing to the greenhouse effect (see Sect. 2.1.3).

Several trace gases, either directly emitted or photochemically produced, are toxic and therefore directly affect human health. In contrast to the major components of the atmosphere, trace gases are variable in space and time as their distributions depend on the strength of their sources and sinks, large-scale transport, mixing processes, and their interactions with clouds and radiation propagating through the Earth's atmosphere.

In general, the Earth's atmosphere can be distinguished by two major layers, the homosphere and heterosphere. The homosphere reaches up to approximately 100 km and its major gaseous constituents are well-mixed. Above the homosphere lies the heterosphere, where the various constituents are separated by molecular mass. The chemical composition varies with altitude, with the heavier molecules being concentrated at the lower layer of the

heterosphere. In addition to the homosphere and heterosphere, distinct layers are classified according to the atmosphere's vertical temperature profile. A schematic depiction of the vertical terrestrial temperature profile is given in Fig. 2.1. The lower most vertical layer is called troposphere and its average height is about 8 km in the polar regions and up to 17 km near the equator in the tropics. This layer contains about 80 % of the atmosphere's mass, is well-mixed and is the key driver for most weather phenomena (Seinfeld and Pandis, 2006). In a standard atmosphere representing average conditions, the troposphere has a negative temperature gradient of  $-6.5 \text{ K km}^{-1}$  with increasing altitude. Atop the troposphere is the tropopause, the boundary between troposphere and stratosphere. The tropopause is an inversion layer where a change in the lapse rate occurs and the temperature gradient becomes positive with increasing altitude. In the stratosphere, which reaches up to approximately 50 km, the temperature increases with increasing height due to absorption of UV radiation by  $\text{O}_3$  molecules. The stratospheric temperature reaches maximum values up to 270 K ( $\sim -3^\circ\text{C}$ ) at its highest point. This region is called stratopause and splits the stratosphere from the mesosphere. In the mesosphere, the temperature decreases as altitude increases. The upper boundary of the mesosphere varies with latitude and season but reaches usually up to 85 km. In this layer, the temperature gradient changes and becomes negative. This is caused by the diminishing radiative heating of  $\text{O}_3$  due to lower  $\text{O}_3$  concentrations. In the thermosphere, which is separated from the mesosphere by the mesopause, the temperature gradient becomes positive due to absorption of UV radiation by  $\text{O}_2$  and  $\text{N}_2$ . With increasing altitude, the temperature may exceed 1000 K ( $\sim 726^\circ\text{C}$ ) and the processes in the thermosphere are mainly driven by solar activity. Above the

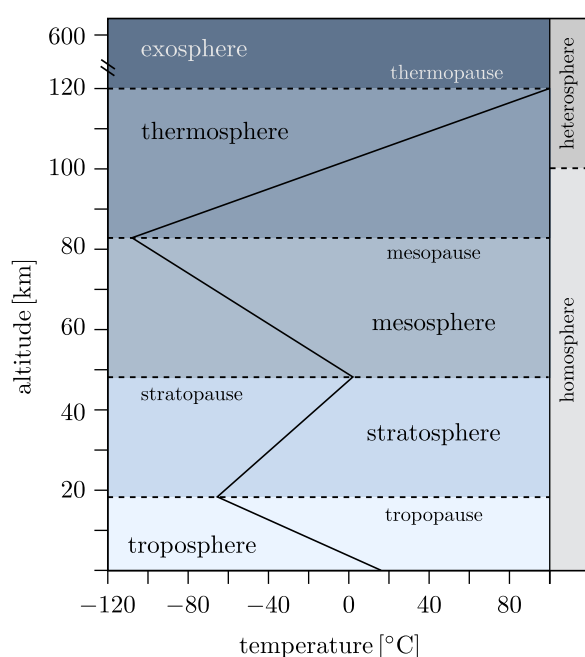


**Figure 2.1:** Schematic illustration of the vertical structure of the Earth's atmosphere which is defined by its vertical temperature profile. The exosphere merges the uppermost layer with interplanetary space. In the homosphere, which reaches up to 100 km, the major atmospheric constituents are well mixed, whereas in the heterosphere, the various constituents are separated by molecular mass. This figure is adapted from Dörnbrack (2012).

thermosphere, the exosphere is located. The exosphere, which starts at about 500 to 1000 km, merges the upper most layer of the atmosphere with interplanetary space.

### 2.1.2 The Earth's radiation budget

The radiation budget of the Earth's atmosphere describes the energy balance between the Sun's shortwave radiation (in the UV and visible spectral range) entering the Earth's atmosphere and emitted longwave radiation by the Earth's surface (in the IR spectral region). The energy balance is the key driver for the Earth's climate system and is essential for many physical and chemical processes in the atmosphere.

The total solar irradiance (TSI) at the top of the atmosphere (TOA) is about  $1372 \text{ W m}^{-2}$  which represents the solar constant  $S_0$ . Due to the Earth's cross section and rotation, the TSI globally distributed across the entire Earth's surface area  $4\pi R_E^2$ , with  $R_E$  the radius of the Earth, is one-fourth of the solar constant. This corresponds to an incoming annual averaged TSI of  $340 \text{ W m}^{-2}$  entering the Earth's atmosphere (Kopp and Lean, 2011). About  $100 \text{ W m}^{-2}$  of the incoming TSI escapes at the TOA due to backscattering at the atmosphere and at the Earth's surface. Parts of the remaining  $240 \text{ W m}^{-2}$  are absorbed by the atmosphere and a remaining estimated global mean value of  $161 \text{ W m}^{-2}$  is absorbed by the surface (IPCC, 2013) heating it to a global mean temperature of about  $288 \text{ K}$  ( $\sim 15^\circ\text{C}$ ).

The Earth's surface emits longwave radiation and can be described as a black body in thermal equilibrium. The emitted spectral irradiance is given by Planck's law:

$$B(T, \nu) = \frac{8\pi h\nu^3}{c^2} \frac{1}{\exp\left(\frac{h\nu}{k_B T}\right) - 1} \quad (2.1)$$

Here,  $k_B$  is the Boltzmann constant,  $h$  the Planck constant,  $\nu$  the frequency of the radiation,  $T$  the temperature and  $c$  the speed of light. The emitted radiation  $j$  from a black body is described by the Stefan Boltzmann law:

$$j = \epsilon_S \sigma T_S^4 \quad (2.2)$$

Here,  $\epsilon_S$  is the emissivity ( $\epsilon_S = 1$  for a black body),  $\sigma$  the Stefan Boltzmann constant, and  $T_S$  the black body's temperature. To bring the Earth's radiation budget into equilibrium, the absorbed and emitted energy needs to be balanced. Neglecting the existence of the Earth's atmosphere and therefore any radiative interaction between the Earth's surface and atmosphere, the radiation budget is in equilibrium when:

$$\epsilon_S \sigma T_S^4 = (1 - A) \frac{S_0}{4} \quad (2.3)$$

The right hand sided term represents the incoming solar radiation reduced by the reflected amount at the TOA and at the Earth’s surface, here represented by  $A$ , the albedo of the Earth. A schematic illustration of this simplified radiation balance is given in Fig. 2.2 (left panel). Assuming an albedo of  $A = 0.3$ ,  $S_0 = 1372 \text{ W m}^{-2}$  and an emissivity of  $\epsilon_S = 0.95$ , a surface temperature of  $T_S = 258 \text{ K}$  is obtained. This corresponds to a surface temperature of about  $-18^\circ\text{C}$  when no atmosphere is assumed. This theoretically estimated surface temperature differs by about  $30 \text{ K}$  from the measured mean surface temperature of  $288 \text{ K}$  ( $\sim 15^\circ\text{C}$ ) (Hansen et al., 2010). This discrepancy is caused by the interaction of longwave radiation with the Earth’s atmosphere. This interaction is sensitive to changes in abundances of a variety of atmospheric trace gases, the so called greenhouse gases. These gases absorb and re-emit longwave radiation (emitted by the Earth’s surface) in upward and downward direction where the latter leads to a heating of the Earth’s surface. This process is called greenhouse effect and is described in more detail in the next section. In general, the total radiative balance of the atmosphere is more complex and several absorption, emission, scattering, and heating processes contribute to the total energy at the TOA, the Earth’s surface and the atmospheric layers in between. This is described in more detail in IPCC (2013).

### 2.1.3 The greenhouse effect

The greenhouse effect describes the absorption and re-emission of longwave radiation, primarily emitted by the Earth’s surface, by gaseous constituents in the atmosphere. The re-emitted longwave radiation is partly downward directed and causes a warming of the Earth’s surface. As seen in the previous section, the disregard of the Earth’s atmosphere in the radiation balance leads to a discrepancy between measured and calculated surface temperatures of about  $30 \text{ K}$ , implying a theoretical surface temperature of  $258 \text{ K}$  ( $\sim -18^\circ\text{C}$ ). Hence, the existence of an atmosphere containing absorbing constituents is essential for the

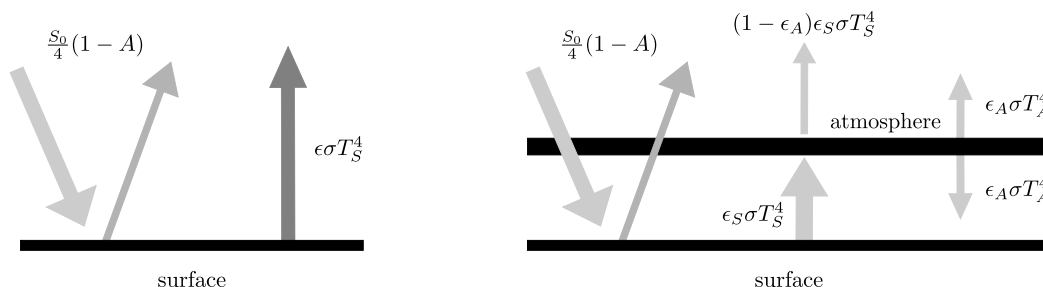


**Figure 2.2:** Simplified model of the Earth’s radiation budget. Left panel: one-layer model without taking into account the Earth’s atmosphere; right panel: two-layer model including the atmosphere as an absorbing and re-emitting medium to illustrate the greenhouse effect (see Sect. 2.1.3). This figure is adapted from Ponater et al. (2012).

Earth's radiation budget and the temperature at the surface. In the atmosphere, various atmospheric trace gases absorb and re-emit the thermal radiation emitted by the surface, the so called greenhouse gases (GHG), e.g.  $\text{CO}_2$ ,  $\text{CH}_4$  and  $\text{N}_2\text{O}$ . This process of absorption and re-emission is called greenhouse effect. The net radiative effect taking into account the greenhouse effect, appears to warm the Earth's surface.

In order to qualitatively and illustratively describe the radiation budget of the Earth's atmosphere including the greenhouse effect, the simple approach of the radiation balance as used in the previous section can be expanded. Here, the presence of an atmosphere is taken into account, leading to a simplified model of the Earth's climate system containing two layers, the surface and the atmosphere. A simplified depiction is given in Fig. 2.2 (right panel). Again, the TSI is given by  $\frac{S_0}{4}(1 - A)$  and the thermal emission by  $\epsilon_S \sigma T_S^4$ . Moreover, the absorption and re-emission of the atmosphere is taken into account. The radiative budget of this simple model is described by the following equations:

$$\epsilon_S \sigma T_S^4 = (1 - A) \frac{S_0}{4} + \epsilon_A \sigma T_A^4 \quad (2.4)$$

$$\epsilon_S \sigma T_S^4 = (1 - \epsilon_A) \epsilon_S \sigma T_S^4 + 2 \epsilon_A \sigma T_A^4 \quad (2.5)$$

Here,  $\epsilon_S$  and  $\epsilon_A$  stand for the emissivity of the Earth's surface and the atmospheric layer, respectively. In analogy,  $T_S$  and  $T_A$  represent the temperature of the surface and atmosphere. Assuming  $S_0 = 1372 \text{ W m}^{-2}$ ,  $\epsilon_S = 0.95$  and  $\epsilon_A = 0.75$ , a surface temperature  $T_S$  of 287 K is obtained which corresponds to about 14 °C and is in good agreement with measured temperatures based on observational data (Jones et al., 1999). The temperature of the atmosphere is determined to be  $T_A = 240 \text{ K}$  which corresponds to  $-33 \text{ °C}$ . This shows how important the greenhouse effect is for the surface temperature and life support on Earth. Hence, naturally occurring abundances of GHGs in the atmosphere are essential for the Earth's climate system.

Nevertheless, since the start of the industrial era in about 1760, concentrations of several GHGs increased in the Earth's atmosphere. This growth is due to the increased use of fossil fuels and causes the so called anthropogenic greenhouse effect, a man-made warming of the atmosphere and surface. The Intergovernmental Panel on Climate Change (IPCC) is a scientific body that provides reviews of research results on global climate change induced due to anthropogenic interference with the Earth's climate system. The IPCC uses the concept of radiative forcing (RF) as a metric to examine how various GHGs contribute to the natural and anthropogenic greenhouse effect. RF is defined as the change in the radiative balance induced by a concentration change of a certain factor, e.g. a GHG or aerosol. The change in concentration is relative to preindustrial conditions from 1750 and

might be due to direct or indirect anthropogenic activities. Typically, RF is expressed in units of  $\text{W m}^{-2}$ . The latest IPCC report from 2013 identifies the RF of well-mixed GHGs and other atmospheric constituents which contribute to the greenhouse effect. The total RF of well-mixed GHGs is  $(2.83 \pm 0.29) \text{ W m}^{-2}$  and increased by  $(0.20 \pm 0.02) \text{ W m}^{-2}$  from 2005 to 2011. This increase mainly results from the increase of RF for  $\text{CO}_2$  of nearly 10 % from 2005 to 2011 (IPCC, 2013).

The RF for  $\text{CO}_2$  is  $(1.82 \pm 0.19) \text{ W m}^{-2}$  and has the largest global average RF (IPCC, 2013).  $\text{CO}_2$  is naturally released into the Earth's atmosphere due to, e.g. the decay of organic materials, ocean release, volcanic outgassing, and respiration. Nevertheless, the rapid increase of  $\text{CO}_2$  concentrations in the Earth's atmosphere since the start of the industrial revolution is mainly due to burning carbon-based fuels (Tans, 2009) and deforestation that removes the natural sink of  $\text{CO}_2$  (Bala et al., 2007). The average growth rate of  $\text{CO}_2$  RF is  $(0.27 \pm 0.03) \text{ W m}^{-2}$  per decade since 1750 (IPCC, 2013). Additionally, there is an inter annual variability in the rate of increase in the RF. This variability is due to the  $\text{CO}_2$  uptake by the biosphere and the oceans. The positive trend is mainly driven by the increase of anthropogenic emissions. The global annual mean abundance of  $\text{CO}_2$  in the atmosphere is  $(390.44 \pm 0.13) \text{ ppm}$  and increased by  $(11.66 \pm 0.13) \text{ ppm}$  since 2005 (IPCC, 2013). Natural sinks of  $\text{CO}_2$  are the absorption by the oceans via physiochemical and biological processes and photosynthesis when atmospheric  $\text{CO}_2$  is absorbed in cells of plants.

Globally averaged  $\text{CH}_4$  concentrations increased by  $(28.6 \pm 0.9) \text{ ppb}$  to  $(1803.2 \pm 1.2) \text{ ppb}$  from 2005 to 2011 (IPCC, 2013). In general, since 1750, global  $\text{CH}_4$  concentrations increased by about 150 % (Meinshausen et al., 2011). Anthropogenic sources are landfills, agriculture, livestock farming and natural gas distributions and account for about 65 % of the total  $\text{CH}_4$  emissions in the Earth's atmosphere. The main natural sources include wetlands and the oceans. The RF of  $\text{CH}_4$  increased by 2 % to  $(0.48 \pm 0.05) \text{ W m}^{-2}$  from 2005 to 2011. The drivers of the inter annual variability of  $\text{CH}_4$  are emissions from natural wetlands and biomass burning during fire seasons.  $\text{CH}_4$  concentrations show a renewed increase since 2007 while from 1996 to 2005 the concentration was nearly constant (Rigby et al., 2008; Dlugokencky et al., 2009). The reason for this renewed growth is still under investigation. Several studies indicate that the renewed increase is due to growing oil and natural gas productions (e.g. Hausmann et al., 2016). The main loss process of  $\text{CH}_4$  is due to photochemical reduction with the OH radical.

$\text{N}_2\text{O}$  increased by about 20 % from 1750 to 2011 (Prather et al., 2012) and reached a globally averaged concentration of  $(324.2 \pm 0.1) \text{ ppb}$  in 2011 (IPCC, 2013). This is an increase of 5 ppb from 2005 (IPCC, 2007). The RF of  $\text{N}_2\text{O}$  is at  $(0.17 \pm 0.03) \text{ W m}^{-2}$  which

is an increase of 6 % since 2005. Therefore,  $\text{N}_2\text{O}$  is the third most GHG contributing to the total RF (Elkins and Dutton, 2009). About 30 to 45 % of the emission is man-made, mostly from agriculture, fertilizers, soil sources, and fossil-fuel activities (Fowler et al., 2009). The main natural source is microbial activity in the soil. Oxidation reactions and photodissociation are the major sinks of  $\text{N}_2\text{O}$  in the stratosphere.

There are several other near-term climate forcers in the Earth's atmosphere like stratospheric  $\text{H}_2\text{O}$ , stratospheric and tropospheric  $\text{O}_3$ ,  $\text{NO}_2$ ,  $\text{CO}$ , and other non methane volatile organic compounds (NMVOCs). These constituents are not defined as GHGs but implicitly contribute to the greenhouse effect. For example,  $\text{CO}$  indirectly affects RF due to its impact on OH concentrations and therefore on tropospheric  $\text{O}_3$ . A more detailed description on  $\text{CO}$ , its trends and involvement in chemical reactions in the atmosphere is given in Sect. 5.1 when analyzing  $\text{CO}$  abundances measured in Karlsruhe using spectroscopic methods.

## 2.2 Molecular Spectroscopy

Molecular spectroscopy is the discipline which investigates the interactions of molecules with electromagnetic radiation. Absorption, emission, or scattering of electromagnetic radiation by molecules or molecular ions can be used to study molecular structures or physical processes in which molecules are involved. Analyzing molecules using spectroscopic methods is widely used in many scientific fields including physics, chemistry, biology, astronomy and environmental sciences. In the latter, it is an established technique for detecting and measuring the concentrations of molecules in the Earth's atmosphere. In general, molecular spectral lines result from internal changes of energetic states of molecules, namely electronic, translational, vibrational and rotational transitions. The resulting spectral signatures are characteristic for each kind of molecule and provide an excellent scientific tool to detect and identify molecules. In the next sections, the formation of spectral lines is described for diatomic molecules. In analogy to atoms, the same quantum mechanical principles hold for molecules. However, molecular spectra are more complex due to additional internal degrees of freedom which results in additional quantum numbers. The contents of the next sections are mainly based on Demtröder (2010), Haken and Wolf (2006a), and Haken and Wolf (2006b).

### 2.2.1 The Born-Oppenheimer approximation

Molecules are a composition of two or more atoms hold together by chemical bonds resulting from, e.g. the electrostatic force of attraction or a covalent bond. The corresponding time-independent Schrödinger equation might contain a large number of variables. The

equation has to be solved to obtain the energy states and wavefunctions of a molecule. An exact solution is generally not possible. A simplification of the basic concepts underlying the quantum mechanical treatment of molecules is provided by the Born-Oppenheimer approximation (Born and Oppenheimer, 1927). The Born-Oppenheimer approximation assumes that the motions of atomic nuclei and electrons in a molecule can be separated. Typically, the mass of a nucleus is about three orders of magnitude larger than the mass of an electron. Therefore, the acceleration and motion of atomic nuclei is slow compared to those of electrons. Thus, in a dynamical sense, there is a separation of time scales between the motion of atomic nuclei and electrons. The electrons are instantaneously drawn along with the nuclei, following the nuclear motion adiabatically. This means that the total wavefunction of a molecule can be separated into individual wavefunctions of the particular motion of nuclei and electrons. As a consequence, the total energy of a molecule  $E_{\text{tot}}$  can be expressed as the sum of its electronic energy  $E_{\text{el}}$ , vibrational energy  $E_{\text{vib}}$ , and rotational energy  $E_{\text{rot}}$ :

$$E_{\text{tot}} = E_{\text{el}} + E_{\text{vib}} + E_{\text{rot}} \quad (2.6)$$

Here, the translational energy of a molecule is neglected since it has no influence on the internal structure of molecules. The corresponding transition energies for electrical, vibrational and rotational states are given by  $\Delta E_{\text{el}}$ ,  $\Delta E_{\text{vib}}$ , and  $\Delta E_{\text{rot}}$ , respectively. Moreover, combinations of these energies might occur as discussed in Sect. 2.2.7. In general, it holds that  $\Delta E_{\text{el}} > \Delta E_{\text{vib}} > \Delta E_{\text{rot}}$ . Transitions between electronic states usually generate spectral lines in the visible spectrum, vibrational transitions in the infrared region and rotational transitions in the microwave and far infrared spectral domain. The main focus of this work lies on the analysis of atmospheric solar absorption spectra recorded in the infrared spectral domain. Therefore, the origin of vibrational and rotational states for diatomic molecules is described in more detail in the next sections.

### 2.2.2 Absorption and emission of radiation

Energy levels of molecules are quantized and transitions between different energy states (either electrical, vibrational, or rotational) may occur when interacting with photons. A photon may be absorbed by a molecule if its energy is:

$$E_2 - E_1 = h\nu \quad (2.7)$$

Here,  $E_2$  represents a higher energy state of the molecule, the so called excited state,  $E_1$  a lower energy state and  $h\nu$  the energy of the photon. The same energy  $E_2 - E_1$  is required for emission of a photon. There are three major energy transition phenomena: spontaneous

emission, stimulated emission and absorption of radiation.

Spontaneous emission of a photon occurs when a molecule, which is in an excited state (e.g. due to thermal energy) undergoes a spontaneous transition to a lower energy state by emitting a photon (see Fig. 2.3, left). Typical lifetimes of excited state for transition energies in the visible spectrum are approximately  $10^{-8}$  sec. Then, the molecule spontaneously falls into a lower energy state by emitting a photon with the energy equivalent to the difference between both energy states. The direction and phase of the emitted photon is random. If an unit volume with the number of molecules  $N_1$  and  $N_2$  in the energy levels  $E_1$  and  $E_2$  is considered, the probability of spontaneous emission from the excited energy level  $E_2$  to the lower level  $E_1$  per unit time is given by:

$$P_{21, \text{spont.}} = A_{21} \quad (2.8)$$

Here,  $A_{21}$  represents the Einstein's  $A$  coefficient of spontaneous emission. Accordingly, the number of photons per second emitted by spontaneous emission is  $N_2 A_{21}$ .

Stimulated emission is induced when a photon with the energy  $E_2 - E_1 = h\nu$  incidents a molecule which is in the excited state  $E_2$ . This may cause the molecule to fall back into the lower energy state  $E_1$  by emitting a photon of the same energy, phase and direction as the incoming photon (see Fig. 2.3, center). The probability that a photon is emitted by stimulated emission is given by:

$$P_{21, \text{stim.}} = B_{21} u(\nu) \quad (2.9)$$

Here,  $B_{21}$  is the Einstein's  $B$  coefficient of induced emission and  $u(\nu)$  the energy density of the radiation with the frequency  $\nu$ . The number of emitted photons with the energy  $E_2 - E_1 = h\nu$  per unit time is  $N_2 B_{21} u(\nu)$ .

An incoming photon with the energy  $E_2 - E_1 = h\nu$  can also be absorbed by a molecule which is in the lower energy state  $E_1$ , inducing an energy transition to the excited state  $E_2$  (see Fig. 2.3, right). The probability for the absorption of a photon per unit time is:

$$P_{12, \text{abs.}} = B_{12} u(\nu) \quad (2.10)$$

Here,  $B_{12}$  is called Einstein's  $B$  coefficient of absorption. The number of photons with energy  $E_2 - E_1 = h\nu$ , which are absorbed per unit time, is  $N_1 B_{12} u(\nu)$ .

In thermal equilibrium, the total number of absorbed and emitted photons per second is equal:

$$N_1 B_{12} u(\nu) = N_2 B_{21} u(\nu) + N_2 A_{21} \quad (2.11)$$

This is equivalent to:

$$u(\nu) = \frac{A_{21}}{B_{21}} \frac{1}{\frac{N_1 B_{12}}{N_2 B_{21}} - 1} \quad (2.12)$$

In thermal equilibrium, the populations of molecules  $N_1$  and  $N_2$  in the states  $E_1$  and  $E_2$  at temperature  $T$  follow the Boltzmann distribution:

$$N_1 \propto g_1 \exp(-E_1/(k_B T)) \quad (2.13)$$

$$N_2 \propto g_2 \exp(-E_2/(k_B T)) \quad (2.14)$$

Here,  $k_B$  is the Boltzmann constant,  $g_1$  and  $g_2$  represent the degeneration of the corresponding energy states. It can be written:

$$\frac{N_2}{N_1} \propto \frac{g_2}{g_1} \exp\left(-\frac{E_2 - E_1}{k_B T}\right) = \frac{g_2}{g_1} \exp\left(-\frac{h\nu}{k_B T}\right) \quad (2.15)$$

Together with Eq. (2.12), the energy density of the radiation can be written as:

$$u(\nu) \propto \frac{A_{21}}{B_{21}} \frac{1}{\frac{B_{12}}{B_{21}} \exp\left(\frac{h\nu}{k_B T}\right) - 1} \quad (2.16)$$

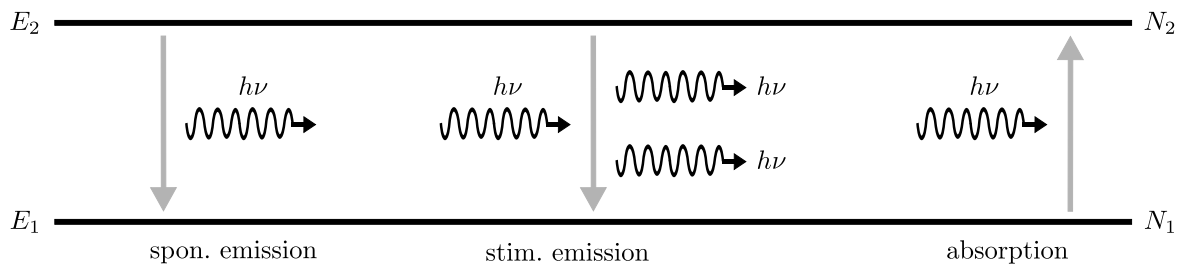


**Figure 2.3:** Illustration of the transition processes for spontaneous emission (left), stimulated emission (center), and absorption (right).  $E_1$  and  $E_2$  represent the energy levels of a lower and excited state with populations  $N_1$  and  $N_2$ .

Using the Planck function from Eq. (2.1), the Einstein coefficients are determined to be:

$$B_{12} = B_{21} \quad (2.17)$$

$$\frac{A_{21}}{B_{21}} = \frac{8\pi h\nu^3}{c^3} \quad (2.18)$$

The intensity of a observed spectral line depends on the transition probability between two energy levels and on the population ratio between the two states as seen in Eq. (2.15). For example, assuming a temperature of  $T = 300$  K and an energy difference  $E_2 - E_1 = 0.12$  eV, which corresponds to  $\sim 1000$   $\text{cm}^{-1}$  lying in the infrared spectral region, the population of the energy states is given by  $N_2/N_1 \approx 0.008$ . For  $E_2 - E_1 = 0.012$  eV, which corresponds to  $\sim 100$   $\text{cm}^{-1}$  lying in the microwave spectral region, the population ratio is  $N_2/N_1 \approx 1$ .

### 2.2.3 The harmonic oscillator

The vibration of a diatomic molecule can be approximated by a simple model describing the harmonic motion of two atoms with masses  $m_1$  and  $m_2$  connected by a massless spring in a potential  $V$  (see Fig. 2.4). For small energies,  $V$  can be approximated by a parabolic potential of the form:

$$V(x) = \frac{1}{2}k_f x^2 \quad (2.19)$$

Here,  $k_f$  is the force constant and  $x$  the distance between both atoms from the equilibrium position  $x_e$ . This motion can be considered as an harmonic oscillation of a single particle with an effective mass  $\mu$  in the given potential which can now be written in the form:

$$V(x) = \frac{1}{2}\mu\omega^2 x^2 \quad (2.20)$$

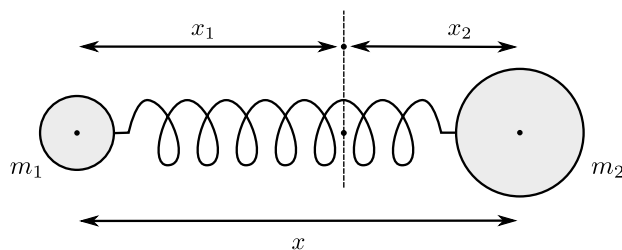


**Figure 2.4:** Simplified model of a vibrating diatomic molecule consisting of two atoms with masses  $m_1$  and  $m_2$  which are connected by a massless spring.

Here,  $\omega = (k_t/\mu)^{\frac{1}{2}}$  represents the angular frequency of the vibration and the effective mass is given by:

$$\mu = \frac{m_1 m_2}{m_1 + m_2} \quad (2.21)$$

The corresponding one-dimensional, time-independent Schrödinger equation for an oscillating particle in an harmonic potential is given by:

$$-\frac{\hbar^2}{2\mu} \frac{d^2}{dx^2} \Psi(x) + V(x) \Psi(x) = E \Psi(x) \quad (2.22)$$

$\Psi(x)$  is the wavefunction of a stationary state,  $E$  the energy of the state  $\Psi(x)$ , and  $\hbar = h/2\pi$  with  $h$  the Planck constant. The allowed energy levels of the harmonic oscillator are:

$$E_{\text{vib}} = \hbar\omega \left( v + \frac{1}{2} \right) \quad (2.23)$$

Here,  $v = 0, 1, 2, \dots$  represents the vibrational quantum number. The energy levels are quantized with equidistant energy differences  $\hbar\omega$  for energy transitions of the form  $\Delta E = E_{v+1} - E_v$  (see Fig. 2.5, left panel). In units of wavenumbers, the vibrational energy can be written as:

$$G_{\text{vib}} = \frac{E_v}{hc} = \tilde{\nu} \left( v + \frac{1}{2} \right) \quad (2.24)$$

Here,  $\tilde{\nu} = \omega/2\pi c$ . For  $v = 0$ , it remains a zero-point energy which follows from the Heisenberg's uncertainty principle.

Transitions between energy states of molecules caused by the absorption of a photon are only possible when the transition dipole matrix element is nonzero. This means that the vibrational transition must cause the dipole moment of the molecule to change. Therefore, following the quantum mechanical selection rules from the analysis of electric dipole transitions, only vibrational transitions with  $\Delta v = \pm 1$  are allowed for an harmonic oscillation of a molecule. Heteronuclear diatomic molecules like, e.g. CO, have a permanent dipole moment which changes when the molecule vibrates. Therefore, the CO molecule is a so called infrared active molecule and its vibrational modes are able to absorb radiation in the infrared spectral domain.

## 2.2.4 The anharmonic oscillator

The vibrations of diatomic molecules can only be in parts described by harmonic oscillators. For low energies and therefore for a distance  $x$  between both atoms close to the equilibrium position  $x_e$ , the potential of an diatomic molecule can be approximated by a parabolic function as seen above. For distances  $x \gg x_e$ , a real molecular potential deviates from a

parabolic shape. For example, assuming that  $x \rightarrow \infty$ , the energy seeks towards infinity for a parabolic potential instead of converging towards a particular dissociation energy  $E_D$  as expected for real molecules. Moreover, since the electric dipole transitions for an harmonic oscillator obey the selection rule  $\Delta v = \pm 1$  leading to equidistant transition energies, the spectrum of a molecule would consist only of one single spectroscopic line.

A more realistic potential has to be asymmetric with regard to the equilibrium distance  $x_e$  and can be approximated by the Morse potential (Morse, 1929):

$$V_M(x) = E_D [1 - \exp(-a(x - x_e))]^2 \quad (2.25)$$

Here,  $a$  is a constant which characterizes a specific molecule and is expressed by:

$$a = \left( \frac{\omega^2 \mu}{2E_D} \right)^{\frac{1}{2}} \quad (2.26)$$

A schematic depiction of the Morse potential is given in Fig. 2.5 (right panel). The Morse potential allows to solve the one-dimensional time-independent Schrödinger equation resulting in the following vibrational energy levels:

$$E_{\text{vib}} = \hbar\omega \left( v + \frac{1}{2} \right) - \hbar\omega k_a \left( v + \frac{1}{2} \right)^2 \quad (2.27)$$

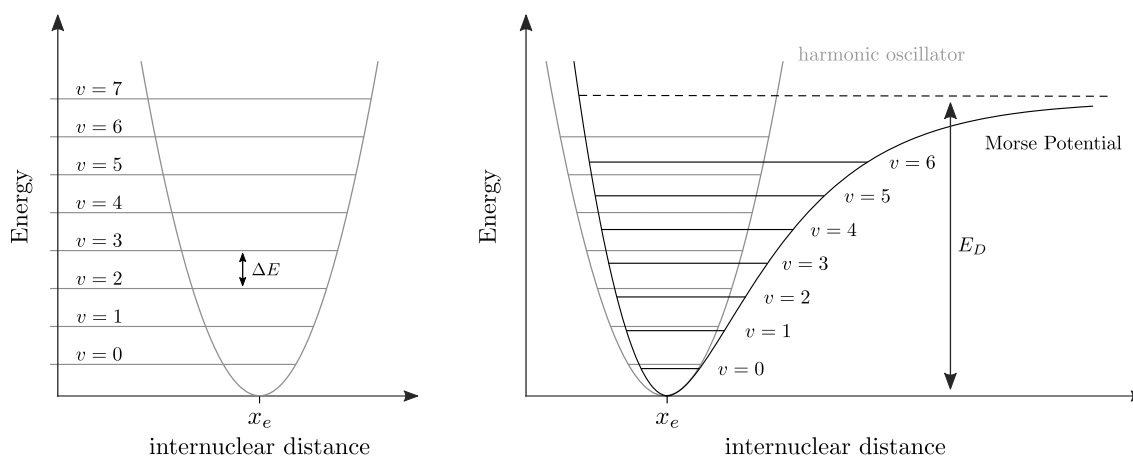


**Figure 2.5:** Schematic depiction of the potentials assumed for an harmonic and an anharmonic oscillator. Left panel: parabolic potential indicating the different quantized energy levels. The energy differences  $\Delta E$  are equidistant. Right panel: asymmetric Morse potential which converges towards the dissociation energy  $E_D$  for large internuclear distances. The energy differences are not equidistant. For reasons of comparison, the harmonic potential and its energy levels are depicted as shaded lines.

Here,  $k_a = (\hbar\omega)/(4E_D)$  is the anharmonicity constant. In terms of wavenumbers, Eq. (2.27) becomes:

$$G_{\text{vib}} = \frac{E_v}{hc} = \tilde{\nu} \left( v + \frac{1}{2} \right) - \tilde{\nu} k_a \left( v + \frac{1}{2} \right)^2 \quad (2.28)$$

The selection rule has to be modified for the anharmonic oscillator such that now  $\Delta v = \pm 1, \pm 2, \pm 3, \dots$  is allowed. In comparison to the harmonic oscillator, the energy differences for transition with  $\Delta v = \pm 1$  are not equidistant any more and decrease with increasing  $v$ . Furthermore, the relative intensities for transitions with  $\Delta v > 1$  decrease rapidly. The most likely transition is  $(v = 1) \leftarrow (v = 0)$  and is called the fundamental transition. Transitions with higher differences than  $\Delta v = \pm 1$  are called overtone transitions.

## 2.2.5 The rigid rotor

The rotational energy states of molecules can be described by the model of a rigid rotor. A simplified assumption of a rotating diatomic molecule is given by two atomic nuclei with masses  $m_1$  and  $m_2$  in a rigid distance  $x$ . The system rotates with an angular frequency  $\omega$  perpendicular to the internuclear axis. A simplified scheme is depicted in Fig. 2.6. The rotational kinetic energy of such a system is given by:

$$E_{\text{kin}} = \frac{L^2}{2\mu x^2} = \frac{L^2}{2I} \quad (2.29)$$

Here,  $I = m_1 x_1^2 + m_2 x_2^2 = \mu x^2$  is the moment of inertia with  $\mu$  the effective mass and  $x_1$  and  $x_2$  the distances to the masses  $m_1$  and  $m_2$  from the equilibrium position and  $x = x_1 + x_2$ . The angular momentum is represented by  $L = I\omega$ . Using polar coordinates, the Schrödinger equation can be written in the form:

$$-\frac{\hbar^2}{2I} \mathbf{L}^2 \Psi(\theta, \varphi) = E \Psi(\theta, \varphi) \quad (2.30)$$

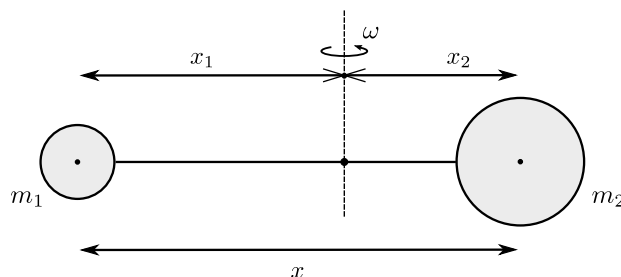


**Figure 2.6:** Schematic depiction of a rotating diatomic molecule consisting of two atoms with masses  $m_1$  and  $m_2$ . Simplified, the molecule can be assumed as a rigid rotor that rotates with the angular frequency  $\omega$ .

Here,  $\mathbf{L}^2$  is the angular momentum operator and  $\Psi(\theta, \varphi)$  is the wavefunction of a stationary state, both given in polar coordinates. The energy levels are given by the eigenvalues and are of the form:

$$E_{\text{rot}} = \frac{\hbar^2}{2I} J(J+1) \quad (2.31)$$

Here,  $J = 0, 1, 2, \dots$  is the rotational quantum number. In units of wavenumbers, Eq. (2.31) can be rewritten as:

$$F_{\text{rot}} = \frac{E_{\text{rot}}}{hc} = B_e J(J+1) \quad (2.32)$$

Here, the rotational constant  $B_e = \hbar^2/(2Ihc)$  is introduced. For transitions with  $\Delta J = \pm 1$ , the difference between the energy levels is given by:

$$\Delta F_{\text{rot}} = F_{\text{rot}}(J+1) - F_{\text{rot}}(J) = 2B_e(J+1) \quad (2.33)$$

The rotational spectrum of a diatomic molecule consists of a series of spectral lines evenly distributed within distances of  $2B_e$ . The selection rule  $\Delta J = \pm 1$  arises from the criterion, that the total angular momentum of a molecule has to be conserved for rotational transitions. Photons, emitted or absorbed by a molecule, do not have mass but carry one unit of quantized angular momentum. Therefore, the selection rule  $\Delta J = \pm 1$  has to be fulfilled for rotational transition processes of diatomic molecules. Transitions for  $\Delta J = 0$  are only allowed for a molecule with an electronic angular momentum which is parallel to the symmetry axis.

### 2.2.6 The non-rigid rotor

The rotation of a molecule cannot be fully described by the model of a rigid rotor. When a molecule rotates, the internuclear distance depends on the frequency with which the molecule rotates and increases with increasing rotational frequencies. This behaviour is described by the model of a non-rigid rotor and is schematically depicted in Fig. 2.7. The

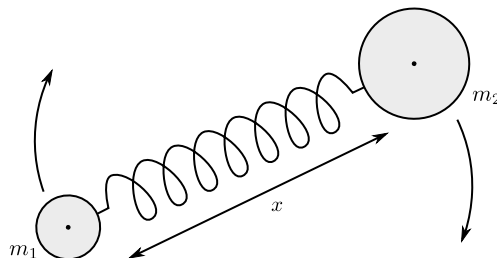


**Figure 2.7:** Schematic depiction of a non-rigid rotor. Similar to the model of a vibrating molecule, the model consists of two atoms with masses  $m_1$  and  $m_2$  connected by a massless spring. The system rotates which induces a stretching of the spring and therefore a change in the internuclear distance  $x$ .

internuclear distance is determined by the centrifugal force  $F_c$  and the restoring force  $F_r$  when both are balanced:

$$\begin{aligned} F_c &= F_r \\ \mu r \omega^2 &= k_f(x - x_e) \end{aligned} \quad (2.34)$$

Here,  $x$  is the internuclear distance,  $x_e$  the internuclear distance in equilibrium, and  $k_f$  the force constant. The angular frequency of the rotation is given by  $\omega$ . Using the relation  $L = I\omega$ , the difference from the internuclear distance in equilibrium can be written as:

$$x - x_e = \frac{L^2}{\mu x^3 k_f} \approx \frac{L^2}{\mu x_e^3 k_f} = \frac{J(J+1)\hbar^2}{\mu x_e^3 k_f} \quad (2.35)$$

Here, the quantum mechanical correspondence principle for the angular momentum  $L \rightarrow J(J+1)\hbar^2$  is used and  $x^3$  is replaced by  $x_e^3$ . The rotational energy is the sum of the kinetic and potential energies and can be written in the form:

$$E_{\text{rot}} = \frac{J(J+1)\hbar^2}{2\mu x_e^2} - \frac{J^2(J+1)^2\hbar^4}{2\mu^2 x_e^6 k_f} \quad (2.36)$$

In terms of wavenumbers, it follows:

$$F_{\text{rot}} = B_e J(J+1) - D_e J^2(J+1)^2 \quad (2.37)$$

The term  $B_e = \hbar^2/(2\mu x_e^2 hc)$  represents the rotational constant and  $D_e = \hbar^4/(2\mu x_e^6 k_f hc)$  the distortion constant. Applying the selection rule  $\Delta J = \pm 1$  leads to the energy difference between rotational transitions of the form:

$$\Delta F_{\text{rot}} = F_{\text{rot}}(J+1) - F_{\text{rot}}(J) = 2B_e(J+1) - 4D_e(J+1)^3 \quad (2.38)$$

Due to the change of the internuclear distance as a result of the rotation, the energy levels for a non-rigid rotor are lower than for the rigid rotor. A schematic depiction and comparison of the rotational energy states for both systems is given in Fig. 2.8.

## 2.2.7 Vibrating rotor

For molecular spectroscopy in the infrared spectral region, simultaneous changes in rotational and vibrational states, the so called rovibrational transitions, are of interest. Typically, in a diatomic molecule, the vibrational frequency is about two orders larger than the rotational frequency. Consequently, the internuclear distance changes permanently while the molecule is rotating. As seen in Sect. 2.2.4 for the anharmonic oscillator, the internuclear

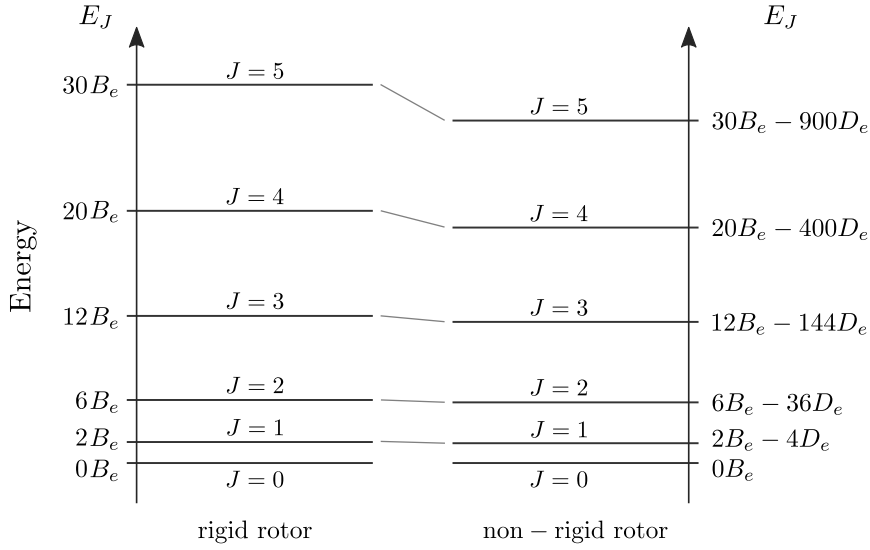


**Figure 2.8:** Schematic depiction of the energy levels for a rigid (left panel) and non-rigid rotor (right panel) for different rotational quantum numbers  $J$ . The difference between energy levels for both systems increases with increasing rotational quantum numbers due to the distortion term in Eq. (2.36).

distance increases with increasing vibrational quantum numbers  $v$ . Moreover, as described in Sect. 2.2.5, the moment of inertia  $I$  is directly dependent on the internuclear distance and therefore also increases. In total, the rotational constant  $B_e$  decreases. Consequently, the rotational constant depends on the vibrational state and therefore is a function of the vibrational quantum number  $v$  and can be written in the form:

$$B_v = B_e - \alpha \left( v + \frac{1}{2} \right) \quad (2.39)$$

Here,  $\alpha \ll B_e$  denotes a molecule specific constant. In analogy to Eq. (2.39), the distortion constant  $D_e$ , which is induced by the centrifugal force, also becomes dependent on the quantum number  $v$ :

$$D_v = D_e - \beta \left( v + \frac{1}{2} \right) \quad (2.40)$$

Here,  $\beta \ll D_e$  denotes a correction factor. Considering the interaction between rotational and vibrational motions of a molecule, the rovibrational energy levels in terms of wavenumbers are found in the Born-Oppenheimer approximation by the summation of Eq. (2.28) and Eq. (2.37):

$$\begin{aligned} T_{\text{rovib}} &= G_{\text{vib}} + F_{\text{rot}} \\ &= \tilde{\nu} \left( v + \frac{1}{2} \right) - \tilde{\nu} k_a \left( v + \frac{1}{2} \right)^2 + B_v J(J+1) - D_v J^2(J+1)^2 \end{aligned} \quad (2.41)$$

The eigenfunctions of the vibrational rotor consist of the eigenfunctions of the anharmonic oscillator and the non-rigid rotor. Therefore the same selection rules for transitions of the vibrational and rotational states are valid, namely  $\Delta v = \pm 1, 2, 3, \dots$  and  $\Delta J = \pm 1$ . Neglecting the last term on the right hand side of Eq. (2.41), the difference between rovibrational states become:

$$\Delta T_{\text{rovib}} = \Delta G_{\text{vib}} + B'_v J'(J' + 1) - B''_v J''(J'' + 1) \quad (2.42)$$

Here,  $\Delta G_{\text{vib}} = G'_{\text{vib}} - G''_{\text{vib}}$  is used. The higher energy levels are marked with prime and the lower level states with double prime. For  $\Delta J = J' - J'' = +1$  and  $\Delta J = J' - J'' = -1$ , two series of lines, the so called R-branch and P-branch, are obtained from Eq. (2.42):

$$\Delta T_{\text{rovib},R} = \Delta G_{\text{vib}} + 2B'_v + (3B'_v - B''_v) J + (B'_v - B''_v) J^2 \quad ; \quad J = 0, 1, 2, \dots \quad (2.43)$$

$$\Delta T_{\text{rovib},P} = \Delta G_{\text{vib}} - (B'_v + B''_v) J + (B'_v - B''_v) J^2 \quad ; \quad J = 1, 2, 3, \dots \quad (2.44)$$

Here,  $J''$  has been replaced by  $J$ . Lines of the R-branch,  $\Delta T_{\text{rovib},R}$ , extend to larger wavenumbers with regard to  $\Delta G_{\text{vib}}$  and lines of the P-branch,  $\Delta T_{\text{rovib},P}$ , extend to smaller wavenumbers. Due to the quadratic terms in Eq. (2.43) and Eq. (2.44), the difference between the lines in both branches are not equidistant. Lines in the R-branch group closer together while lines in the P-branch move farther apart.

For  $\Delta J = 0$ , the so called Q-branch appears. These lines are due to pure vibrational transitions and are much more closely spaced than the R- and P-branch. Often, these lines strongly overlap such that only one single intense line is observed in the spectrum. This special transition is allowed for molecules with a non-vanishing projection of the total electronic angular momentum to the internuclear axis. Again, neglecting the last term on the right hand side of Eq. (2.41), the differences between rovibrational transitions in terms of wavenumbers for the Q-branch are given by:

$$\Delta T_{\text{rovib},Q} = \Delta G_{\text{vib}} + (B'_v - B''_v) J + (B'_v - B''_v) J^2 \quad ; \quad J = 0, 1, 2, \dots \quad (2.45)$$

For most diatomic molecules including, e.g. CO, where the electronic angular momentum is zero in the electronic ground state, transitions with  $\Delta J = 0$  are not allowed. For polyatomic molecules like, e.g. CO<sub>2</sub>, the Q-branch is more common for some types of vibrational modes. A simulated transmission spectrum including the P- and R-branch of the fundamental band of the diatomic molecule CO, together with the schematic depiction of the energy transitions is shown in Fig. 2.9.

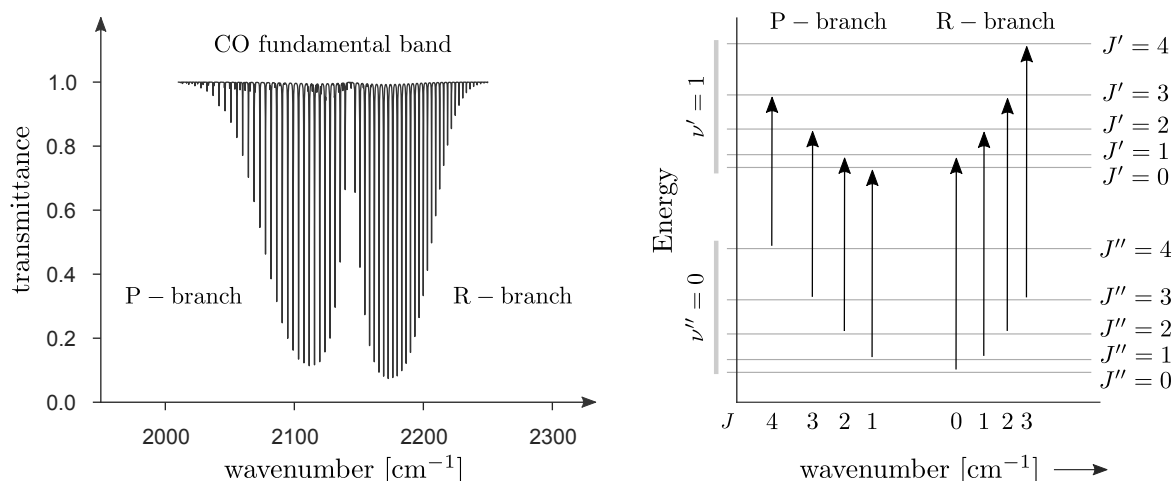


**Figure 2.9:** Simulated transmission spectrum of the fundamental band of carbon monoxide (CO) including the P- and R-branch (left panel). The right panel shows a schematic energy level diagram for the vibrating rotor for different vibrational and rotational quantum numbers.

The intensities of the individual lines in the R- and P-branch scale with different populations  $N_J$  in the rotational state and therefore vary for different rotational quantum numbers  $J$ . As seen in Sect. 2.2.2, the population  $N_J$  for a rotational state  $J$  follows the Boltzmann distribution:

$$N_J \propto (2J + 1) \exp\left(-\frac{B_v J(J + 1) hc}{k_B T}\right) \quad (2.46)$$

Here,  $k_B$  represents the Boltzmann constant and  $T$  the absolute temperature. For small  $J$ , the term  $(2J + 1)$  is dominating and the line intensities become stronger with increasing  $J$  until for large  $J$ , the thermal distribution in Eq. (2.46) becomes dominating and the line intensities decrease. The maximum can be approximated at:

$$J_{\max} = \sqrt{\frac{k_B T}{2B_v hc}} - \frac{1}{2} \quad (2.47)$$

The intensity change in the spectral lines for the CO fundamental band in the R- and P-branch for different temperatures is shown in Fig. 2.10.

## 2.2.8 Spectral line shapes

Observed spectral absorption lines are not infinitesimally narrow. Several physical mechanisms contribute to the broadening of these lines resulting in specific widths and shapes of the observed line profile. In general, the width of a spectral line is limited to the finite lifetime of excited states of a molecule which is a direct consequence of the uncertainty relation between energy and time. This effect is called lifetime or natural broadening and causes a Lorentzian shape of the spectral line profile with typically a full width at

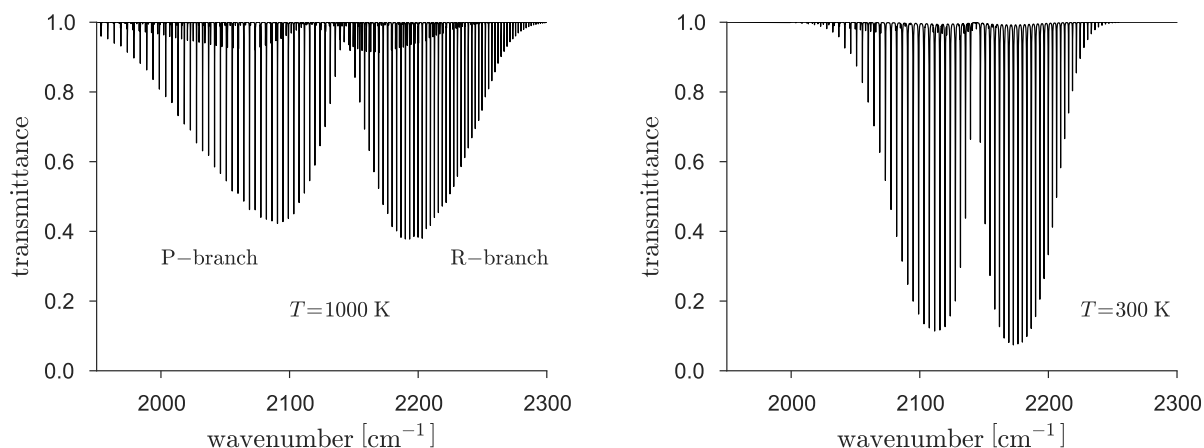


**Figure 2.10:** Simulated transmission spectra for the CO fundamental band for the temperatures 1000 K (left panel) and 300 K (right panel) to illustrate the change in line intensity and maximum shift. The weak superimposed spectrum for 1000 K is due to absorption of excited states.

half maximum (FWHM) in the order of  $\delta\bar{\nu} = 10^{-8} \text{ cm}^{-1}$  (Hase, 2000). This natural line width is a lower boundary for the width of any observed spectral line. However, for remote sensing of atmospheric spectra, more dominant physical mechanisms occur, namely the Doppler broadening and the collision broadening. These broadenings are typically several orders of magnitude larger than the natural broadening such that latter can be neglected when analyzing atmospheric spectra. Collision broadening is the dominating effect in the troposphere and also can be approximated by a Lorentzian line profile. The Doppler broadening is frequency dependent and dominates above 40 km in the upper stratosphere and results in a Gaussian line profile. The region in between is dominated by both broadening mechanisms leading to a Voigt profile of the observed spectral line profiles. In the following, the dominating broadening mechanisms are discussed in more detail.

### Doppler Broadening

The Doppler broadening of spectral line profiles is generated by the thermal motion of molecules in a gas. The emission or absorption of photons by molecules which move with different velocities lead to different Doppler shifts and in consequence to a broadening of observed spectral line shapes. The Doppler effect occurs when an emitting or absorbing source moves towards or away from an observer. Doppler broadened spectral lines have the shape of a Gaussian distribution:

$$P_D(\nu) = \frac{c}{\nu_0 v_w \sqrt{\pi}} \exp\left(-\frac{c(\nu - \nu_0)}{\nu_0 v_w}\right)^2 \quad (2.48)$$

The FWHM is:

$$\delta\nu_D = \frac{2v_w\nu_0}{c}\sqrt{\ln 2} = \nu_0\sqrt{\frac{8k_B T \ln 2}{mc^2}} \quad (2.49)$$

In units of wavenumbers, the FWHM becomes:

$$\delta\bar{\nu}_D = \frac{\nu_0}{c}\sqrt{\frac{8k_B T \ln 2}{mc^2}} \quad (2.50)$$

Typical values for  $\delta\bar{\nu}_D$  reach  $3 \times 10^{-3} \text{ cm}^{-1}$  for the CO fundamental band at  $2100 \text{ cm}^{-1}$  and 270 K (Hase, 2000).

### Collision Broadening

Collisions between molecules shorten the lifetime of excited states of molecules. This mechanism leads to a broadening of the observed spectral line, the so called collision or pressure broadening. The rate of collisions between molecules increases with increasing pressure, leading to a stronger collision broadening in the troposphere than in the higher layers of the atmosphere. Similar to the lifetime broadening, the collision induced broadening can be approximated by a Lorentzian spectral line shape of the form (see Fig. 2.11):

$$P_P(\nu) = \frac{1}{\sqrt{\pi}} \frac{\delta\nu_P}{(\nu - \nu_0)^2 + \Delta\nu_P^2} \quad (2.51)$$

The FWHM is proportional to the pressure of a gas:

$$\delta\nu_P = \frac{1}{2\pi\tau_c} \propto p \quad (2.52)$$

Here,  $\tau_c$  represents the mean time between two collisions with the relation:

$$\tau_c \propto \frac{T^{\frac{1}{2}}}{p} \quad (2.53)$$

Thus, in the troposphere, the collision broadening is the dominating factor which broadens spectral line profiles whereas the Doppler broadening dominates from the middle stratosphere upwards. For  $p = 1000 \text{ hPa}$ ,  $\delta\bar{\nu}_P$  reaches approximately  $0.01 \text{ cm}^{-1}$ .

### The Voigt Profile

In the case when  $\delta\bar{\nu}_D$  and  $\delta\bar{\nu}_P$  are of comparable magnitude, both, the Doppler broadening and the collision broadening contribute to the shape of a spectral line profile. For lines in the fundamental band of CO at  $2140 \text{ cm}^{-1}$  at 15 hPa and room temperature (296 K), both broadening mechanisms are equal with  $\delta\bar{\nu}_D = \delta\bar{\nu}_P \approx 5 \times 10^{-3} \text{ cm}^{-1}$ . The resulting shape

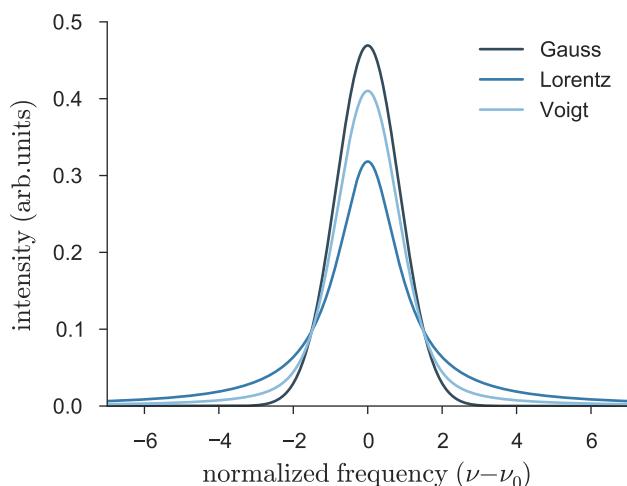


**Figure 2.11:** Schematic depiction of the different profile shapes for Doppler broadening (Gauss), for collision broadening (Lorentz) and the combination of Doppler and collision broadening (Voigt).

of the observed line profile can be described by the Voigt profile, the convolution of the Gaussian and Lorentzian profile:

$$\begin{aligned}
 P_V(\nu) &= (P_P \otimes P_D)(\nu) \\
 &= \int_{-\infty}^{\infty} P_P(\nu') P_D(\nu - \nu') d\nu'
 \end{aligned} \tag{2.54}$$

Equation (2.54) cannot be solved analytically. However, several approximations are used to numerically solve the convolution integral (e.g. Liu et al., 2001). At the line center, the Voigt profile follows the Gaussian profile from the Doppler behavior while in the line wings, the Voigt profile has a Lorentzian shape. An overview of the different spectral line profile shapes is shown in Fig. 2.11.

## 2.3 Fourier Transform Infrared spectroscopy

Fourier Transform Infrared (FTIR) spectroscopy can be used to obtain spectra from gaseous, liquid and solid constituents which are active in the infrared spectral region. It is a major technique for remote sensing of trace gases in the Earth's atmosphere. Fourier Transform Infrared spectrometers (FTS) are widely operated on different platforms, e.g. mounted on satellites, balloons, aircrafts or research vessels (e.g. Höpfner et al., 2016; Woiwode et al., 2016; Plieninger et al., 2016; Frankenberg et al., 2015; Toon, 1991; Klappenbach et al., 2015). The analyzed infrared radiation might originate directly from the Sun, from atmospheric emission or from radiation scattered back from the Earth's surface. Within the frame of this work, spectra are analyzed which originate from measurements by a direct solar viewing ground-based FTIR spectrometer. In the next sections, the basic principle of

an FTS is described followed by the mathematical background which is required to obtain a spectrum from the measured interferogram. The contents of the following sections are mainly based on Beer (1992).

### 2.3.1 The Michelson interferometer

Interferometric measurements require an optical setup based on a two (or more) beam interferometry. Usually, stationary ground-based FTS fulfil these requirements by featuring a cube corner Michelson interferometer containing a semi-transparent beam splitter (Michelson and Morley, 1887). For detecting and analyzing rovibrational transitions of molecules, common configurations of ground-based remote sensing FTS use the infrared portion of the Sun's radiation as source for observations of gases in the Earth's atmosphere.

Typically, an automated and camera-based astronomical pointer with active feedback directs the solar beam into the FTS by servo-controlled mirrors. The beam is focused on the input field stop ensuring that only radiation from the solar disc's center is guided into the interferometric optic. A beamsplitter (usually potassium bromide (KBr) or calcium fluoride ( $\text{CaF}_2$ ) as used in the Karlsruhe FTS) divides the incoming beam into two parts which are transmitted and reflected into the interferometer arms. Both beams are reflected by cube corner mirrors back towards the beamsplitter which also functions as a recombiner of the two beams. Typically, one reflecting mirror of the Michelson interferometer is linearly movable leading to different optical path differences and in consequence leading to constructive and destructive interference patterns in the recombined beam. The latter is directed to a photo diode which detects the intensity of the beam as a function of the optical path difference, the so called interferogram. A schematic representation of an FTIR spectrometer is depicted in Fig. 2.12. FTS have the advantage over dispersive spectrometers that the photodiode receives information about broad high resolution spectral regions simultaneously, the so called Fellgett advantage which also improves the signal-to-noise ratio compared to an scanning monochromator (Fellgett, 1949).

The intensity of the recombined beam results from the principle of superposition. Assuming two beams with same amplitudes  $A$ , then the most simple form of the wave equation is:

$$\begin{aligned} a_1 &= A \cos(2\pi x_1 \bar{\nu}) \\ a_2 &= A \cos(2\pi x_2 \bar{\nu}) \end{aligned} \tag{2.55}$$

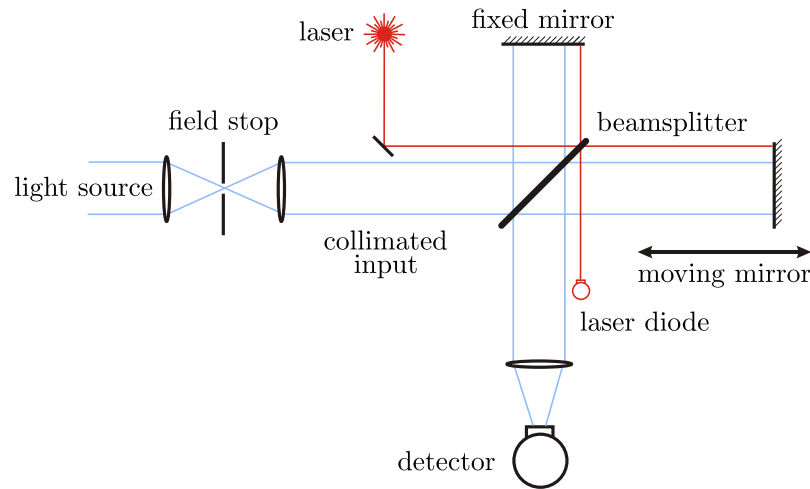


**Figure 2.12:** Schematic illustration of a Michelson interferometer. The laser beam passes the same path as the solar beam and is used to determine the position of the moving mirror (see Sect. 2.3.2). This figure is adapted from Gisi (2012).

Here,  $x_1$  and  $x_2$  denote the distance of propagation and  $\bar{\nu}$  a certain wavenumber. The superimposed wave results upon addition of both single wave equations:

$$\begin{aligned} a &= a_1 + a_2 = A [\cos(2\pi x_1 \bar{\nu}) + \cos(2\pi x_2 \bar{\nu})] \\ &= 2A \cos(\pi \bar{\nu} x) \cos(2\pi \bar{\nu} \{x_2 + x/2\}) \end{aligned} \quad (2.56)$$

Here,  $x$  represents the difference between  $x_1$  and  $x_2$ , namely the optical path distance. The measured intensity  $I$  by the photodiode can be approximated by the square of the superimposed amplitude:

$$\bar{I}(x) \approx a^2 = F [1 + \cos(2\pi \bar{\nu} x)] \quad (2.57)$$

Here, the relation  $F = 2A^2$  is used. For a constant  $\bar{\nu}$ ,  $\bar{I}$  alternates between 0 and  $2F$ . Constructive interference occurs when the optical path distance is  $x = n/\bar{\nu}$  with  $n = 0, 1, 2, 3, \dots$  while for  $n = 1/2, 3/2, 5/2, \dots$  destructive interference occurs. Assuming a polychromatic instead of a monochromatic radiation source, Eq. (2.57) has to be integrated over all frequencies:

$$\begin{aligned} \bar{I}(x) &= \int_0^{\infty} F(\bar{\nu}) [1 + \cos(2\pi \bar{\nu} x)] d\bar{\nu} \\ &= \int_0^{\infty} F(\bar{\nu}) d\bar{\nu} + \int_0^{\infty} F(\bar{\nu}) \cos(2\pi \bar{\nu} x) d\bar{\nu} \end{aligned} \quad (2.58)$$

In this case,  $F$  becomes dependent on  $\bar{\nu}$ . The first term on the right hand side of Eq. (2.58) represents the total energy incident whereas the second term is modulated and is identified as the interferogram:

$$I(x) = \int_0^{\infty} F(\bar{\nu}) \cos(2\pi\bar{\nu}x) d\bar{\nu} \quad (2.59)$$

The right hand side of Eq. (2.59) contains all spectral information of the measured interferogram and can be recovered by the Fourier transformation.

### 2.3.2 The Fourier Transformation

The integral Fourier transformation can be written in the form:

$$F(\bar{\nu}) = \int_{-\infty}^{\infty} I(x) \exp(-i2\pi\bar{\nu}x) dx \quad (2.60)$$

The corresponding inverse transformation is:

$$I(x) = \int_{-\infty}^{\infty} F(\bar{\nu}) \exp(i2\pi\bar{\nu}x) d\bar{\nu} \quad (2.61)$$

Expanding Eq. (2.59) to negative wavenumbers by assuming that  $F(-\bar{\nu}) = F^*(\bar{\nu})$ , shows that the desired spectrum can be recovered from the interferogram by applying a Fourier transformation. Moreover, from the physical point of view,  $I(x)$  is a measured quantity and therefore in a mathematical sense real. This holds for  $F(-\bar{\nu}) = F^*(\bar{\nu})$ . Therefore, the Fourier transformation allows to calculate a spectrum consisting of a real and imaginary part, an amplitude and a phase spectrum. Since now, it was assumed that the recorded interferogram is a continuous function of the optical path difference which, in practice, is not the case. Instead, a recorded interferogram consists of  $N$  discrete sampling points recorded at equidistant distances  $\delta x$ . A common formalism to transform discrete and equally spaced interferograms into a spectrum is provided by the discrete Fourier transformation. Accordingly, Eq. (2.60) and Eq. (2.61) are modified to:

$$F(n\delta\bar{\nu}) = \frac{1}{N} \sum_{j=0}^N I(j\delta x) \exp(-i2\pi n\delta\bar{\nu} j\delta x) \quad (2.62)$$

The corresponding inverse transformation is:

$$I(m\delta x) = \sum_{k=0}^N F(k\delta\bar{\nu}) \exp(i2\pi k\delta\bar{\nu} m\delta x) \quad (2.63)$$

Here, the continuous variables  $x$  and  $\bar{\nu}$  in equations (2.60) and (2.61) are replaced by  $j\delta x$  and  $k\delta\bar{\nu}$ , respectively, with  $j, k \in (0, \dots, N)$ . The result of the forward discrete Fourier transformation is a set of  $N$  spectral intensities. The spacing is equally in frequency with  $\delta\bar{\nu}$  the difference between two adjacent frequencies and the following relation between  $\delta\bar{\nu}$  and  $\delta x$  holds:

$$\delta\bar{\nu} = \frac{1}{N\delta x} \quad (2.64)$$

Hence the resolution of the spectrum is inverse proportional to the maximum optical path difference. Furthermore, the sampling of a continuous spectrum needs to satisfy the Nyquist theorem to reconstruct a continuous signal. The Nyquist frequency is defined as:

$$\nu_N = \frac{1}{2\delta x} \quad (2.65)$$

The Nyquist theorem states that the spectrum is not allowed to contain frequencies larger than  $\nu_N$  and therefore, the sampling interval  $\delta x$  has to be chosen appropriately when recording interferograms. If the Nyquist criterion is not satisfied, the discrete Fourier Transform formalism will fold spectral contributions from frequencies larger than the Nyquist frequency into the observed range, an effect also known as aliasing. In practice, to exactly determine equidistant distances  $\delta x$  for the sampling of the interferogram, the beam of a single-mode HeNe laser passes the same path in the interferometer as the solar beam which also results in interference patterns. Since the frequency of the laser is monochromatic and well known (632.988 nm), the interferogram can be sampled at exactly known constant intervals of the optical path difference defined by each zero crossings of the laser's interferogram (see Fig. 2.12).

To numerically calculate a discrete Fourier transformation, the fast Fourier transformation formalism by Cooley and Tukey is the favorable algorithm to use. The number of arithmetic operations is reduced from  $2N^2$  for the discrete Fourier transformation to  $3N \log_2 N$ . Thus, the number of sampling points requires to be a power of two.

### 2.3.3 Phase correction

In practice, optical components such as beamsplitters, mirrors and electronic devices might show a frequency dependent response leading to individual phase modulations for certain frequencies in the spectrum. Such undesirable dependencies can be taken into account

by correcting the phase with the correction term  $\phi(\bar{\nu})$ . Since  $\phi(\bar{\nu}) = -\phi(-\bar{\nu})$ , it can be written:

$$\begin{aligned} F'(\bar{\nu}) &= \int_{-\infty}^{\infty} I'(x) \exp(-i2\pi\bar{\nu}x + i\phi(\bar{\nu})) dx \\ &= F_{re}(\bar{\nu}) + iF_{im}(\bar{\nu}) \end{aligned} \quad (2.66)$$

Here,  $F_{re}(\bar{\nu})$  and  $F_{im}(\bar{\nu})$  are the real and imaginary part of  $F(\bar{\nu})$  from Eq. (2.60). The correction term  $\phi(\bar{\nu})$  can be calculated via:

$$\phi(\bar{\nu}) = \arctan\left(\frac{F_{im}(\bar{\nu})}{F_{re}(\bar{\nu})}\right) \quad (2.67)$$

Equation (2.67) is used to determine the phase corrected spectrum:

$$F'(\bar{\nu}) = F(\bar{\nu}) \exp(-i\phi(\bar{\nu})) \quad (2.68)$$

### 2.3.4 Apodization and instrumental line shape

In practice, FTS have only a limited range for the optical path difference. In the previous sections, interferograms of infinite length were assumed. An interferogram which is limited to a maximum optical path difference is mathematically equivalent to an infinite interferogram multiplied with a boxcar function  $B(x)$  with  $B(x) = 1$  for  $0 \leq x \leq D_{\max}$ , 0 otherwise. Here  $D_{\max}$  represents the maximum optical path difference. Modifying Eq. (2.60) leads to:

$$F_A(\bar{\nu}) = \int_{-\infty}^{\infty} I(x) B(x) \cos(2\pi\bar{\nu}x) dx \quad (2.69)$$

Following the convolution theorem which states that the point wise product in the space domain is equal to the convolution in the frequency domain leads to:

$$F_A(\bar{\nu}) = F(\bar{\nu}) \otimes J(\bar{\nu}) \quad (2.70)$$

Here,  $J(\bar{\nu})$  represents the Fourier transform of the boxcar function  $B(x)$ :

$$\begin{aligned} J(\bar{\nu}) &= \frac{\sin(2\pi\bar{\nu}D_{\max})}{2\pi\bar{\nu}D_{\max}} \\ &= \text{sinc}(2\pi\bar{\nu}D_{\max}) \end{aligned} \quad (2.71)$$

Equation (2.71) impacts the spectrum  $F_A(\bar{\nu})$  in a way that fine structures are lost since the sinc function is an ideal low-pass filter. The width of the sinc function sets the spectral

resolution with the full width at half maximum to  $(^{0.6035}/D_{\max})$ . Another impact of the sinc function is that non-physical negative side lobes can occur. To minimize such effects, the sinc function can be multiplied with other functions, e.g. a triangular or Gauss function. This approach is called apodization and leads to a reduction of negative side lobes but also reduces the spectral resolution of the observed spectral lines. Since different criteria are given in today's literature to define when two lines or peaks in a spectrum can be identified as fully separated, the spectral resolution of an FTS cannot explicitly be determined. Therefore, in this work, a widely used FTS spectral resolution of  $\delta\bar{\nu} = 0.9/D_{\max}$  is adopted. In practice, the spectral resolution is limited by the signal-to-noise ratio which declines with increasing optical path difference. Also, the scan time is a limiting factor since solar brightness fluctuation might occur during long scan times. Therefore, multiple recorded interferograms are coadded and averaged to improve the signal-to-noise ratio.

Equation (2.71) is also called the instrumental line shape (ILS). The ILS is a tool to diagnose misalignments of a spectrometer which leads to a deformation of spectral lines in the recorded spectrum. It characterizes the shape of a spectral line which the spectrometer would measure if the line is assumed as infinitesimally narrow. The maintenance of FTS includes the regular monitoring of the ILS. For that, a sequence of measurements using different gas cells (typically  $\text{N}_2\text{O}$ ,  $\text{C}_2\text{H}_2$ , and  $\text{HCl}$ ) are used to determine the ILS from the difference between the shape of the spectral lines retrieved from the gas cell and theoretical calculations (Hase, 2012). Furthermore, the knowledge of the monitored ILS can be integrated into the analysis of atmospheric spectra to correctly interpret the observed line shapes. A more detailed discussion about the ILS is given in Sect. 3.1.2.

### 2.3.5 Global FTIR networks for atmospheric observations

In the last years, ambitious efforts have been undertaken to map global abundances of trace gases in the Earth's atmosphere using satellite-borne instruments, e.g. the Greenhouse Gases Observing Satellite (GOSAT, Yokota et al., 2009), Envisat (Höpfner et al., 2013), and the Orbiting Carbon Observatory 2 (OCO-2, Frankenberg et al., 2015). Moreover, surface measurements from several in situ networks (e.g. GLOBALVIEW-CO<sub>2</sub>, 2010) allow to infer distributions and local strengths of sources and sinks of trace gases and analyze exchange processes between the surface and the atmosphere. Data sets obtained from FTS observations of trace gases in the Earth's atmosphere provide a link between satellite observations and in situ networks. In contrast to surface in situ measurements, the FTS data sets can be utilised directly for satellite validations since both techniques measure comparable quantities. Assimilations of ground-based FTS measurements, satellite observations and surface in situ measurements combine the advantages of all three methods and yield a better understanding of atmospheric processes than just using one single data set. Currently,

two global ground-based FTS networks operating FTIR spectrometers, namely the Total Carbon Column Observing Network (TCCON, Wunch et al., 2011) and the Network for the Detection of Atmospheric Composition Change (NDACC, Kurylo, 1991) provide primary validation data records of various gaseous atmospheric components.

The TCCON is a ground-based network of FTIR spectrometers initiated in 2004 by the California Institute of Technology, Pasadena, USA. The TCCON provides measurements of column averaged abundances of several atmospheric gases including  $\text{CO}_2$ ,  $\text{CO}$ ,  $\text{CH}_4$ ,  $\text{N}_2\text{O}$ ,  $\text{H}_2\text{O}$ ,  $\text{HF}$  and other atmospheric gases. Precise and accurate measurements are performed by operating stationary high-resolution FTIR spectrometers to measure near infrared (NIR) solar absorption spectra using direct sunlight. To this day, 23 globally distributed instruments are affiliated with the TCCON. The network aims to improve global carbon cycle studies and to provide a primary validation data record for retrievals from space-based instruments, e.g. OCO-2 (Frankenberg et al., 2015), the Scanning Imaging Absorption Spectrometer (SCIAMACHY, Frankenberg et al., 2006), and GOSAT (Morino et al., 2011).

The NDACC first started measuring in 1991 and is composed of more than 70 remote-sensing research stations using different remote sensing techniques. The network aims to observe and understand the chemical and physical conditions of the upper troposphere and stratosphere. Within the NDACC, the Infrared Working Group (IRWG) consists of 22 sites spread worldwide that measure absorption spectra in the mid infrared (MIR) spectral region using FTIR spectrometers and the Sun as source. The primary focus was on the change of stratospheric chemistry, especially on ozone and its response to anthropogenic chlorofluorocarbons (CFCs). The initial data products were total columns of  $\text{O}_3$ ,  $\text{HCl}$ ,  $\text{HNO}_3$ ,  $\text{ClONO}_2$  and  $\text{HF}$ . With increasing attention on air quality, measurements were

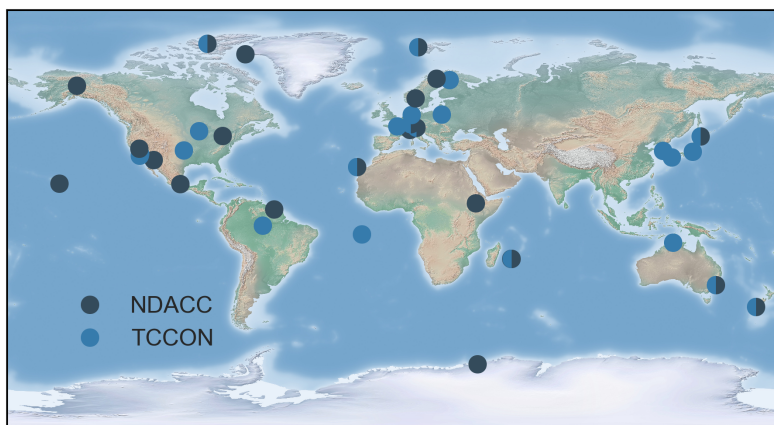


**Figure 2.13:** Locations of operating FTIR spectrometers which are affiliated either with the NDACC (dark blue markers) or TCCON (light blue markers). Several stations operate FTS which are affiliated with both networks.

extended to gases involved in the Earth's carbon cycle like CO, C<sub>2</sub>H<sub>6</sub>, HCN, N<sub>2</sub>O and CH<sub>4</sub>. Today, NDACC retrieves concentrations of even more gaseous components, including NO, C<sub>2</sub>H<sub>2</sub>, C<sub>2</sub>H<sub>4</sub>, OCS, H<sub>2</sub>O, and HDO. These data products have been widely used for satellite validations and model studies (e.g. de Laat et al., 2010; Sussmann et al., 2005). The network is highly adaptable and complements TCCON measurements by providing additional data products retrieved from the MIR spectral range. The locations of current TCCON and NDACC FTS sites are shown in Fig. 2.13.

## 2.4 Basics of the radiative transfer in the Earth's atmosphere

The radiative transfer equation (RTE) is the basis for the treatment of radiation processes in the field of remote sensing observations. The content of this section is mainly based on Rodgers (2000). The RTE describes the interaction between radiation and a medium. The propagation of radiation through such a medium, e.g. the Earth's atmosphere including clouds, molecules and aerosols, is affected by several effects including absorption, emission and scattering processes. On the one hand, variations of the radiance occur due to sources such as thermal emission and scattering of radiation into the direction of propagation and on the other hand due to extinction, meaning absorption and scattering of radiation out of the direction of propagation. In general, the RTE describes the variation of the radiance  $I(\bar{\nu}, s)$  propagating through an emitting, absorbing and scattering medium between two points  $ds = s_2 - s_1$  and propagating within an infinitesimal solid angle  $d\Omega$  (see Fig. 2.14). If the layers of the Earth's atmosphere are considered to be in local thermodynamic equilibrium (LTE) and assuming the atmosphere as a thin medium, the RTE for a given wavenumber  $\bar{\nu}$  can be written in the form:

$$I(\bar{\nu}, s) = I(\bar{\nu}, 0) \tau(\bar{\nu}, 0, s) + \int_0^s J(s', \Omega) \frac{d}{ds'} \tau(\bar{\nu}, s', s) ds' \quad (2.72)$$

Here,  $s$  is a distance coordinate along the propagation direction,  $I(\bar{\nu}, 0)$  the radiance at the beginning of the path,  $I(\bar{\nu}, s)$  the radiance at the end of the path and  $\tau(\bar{\nu}, s', s)$  represents the transmittance of the path from  $s'$  to  $s$ . The term  $J(s', \Omega)$  is called source function and depends on scattering and thermal emission. It is represented by:

$$J(s', \Omega) = (1 - \omega_0(\bar{\nu})) B(\bar{\nu}, T(s')) + \frac{\omega_0(\bar{\nu})}{4\pi} \int_{4\pi} I(\bar{\nu}, s, \Omega') P(\bar{\nu}, \Omega' \rightarrow \Omega) d\Omega' \quad (2.73)$$

The first term on the right hand side of Eq. (2.73) represents the thermal emission resulting from Kirchhoff's law of thermal radiation and the assumption of an LTE. Here,  $B(\bar{\nu}, T(s'))$

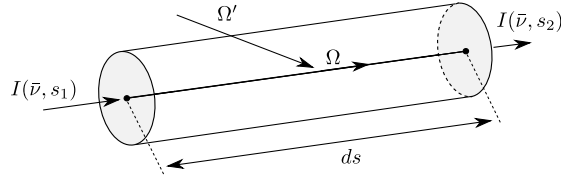


**Figure 2.14:** Illustration of the geometry of radiation propagation through a volume element.

is the Planck function as defined in Eq. (2.1) for a certain temperature  $T(s')$ . The single scattering albedo  $\omega_0$  is the ratio of scattering coefficient to total extinction coefficient, the sum of the scattering coefficient  $\sigma$  and absorption coefficient  $\kappa$ :

$$\omega_0(\bar{\nu}) = \frac{\sigma(\bar{\nu})}{\sigma(\bar{\nu}) + \kappa(\bar{\nu})} \quad (2.74)$$

The second term on the right hand side of Eq. (2.73) describes the scattering of radiation into the direction of propagation. It is characterized by the phase function  $P(\bar{\nu}, \Omega' \rightarrow \Omega)$  which describes the probability that radiation coming from  $\Omega'$  is scattered into  $\Omega$  where  $I(\bar{\nu}, s, \Omega')$  is the radiance incident at the position  $s$  from the direction  $\Omega'$ .

Remote sensing of solar atmospheric absorption spectra in the infrared spectral range can be described by the first term on the right hand side of Eq. (2.72). Thermal emission as a source of infrared radiation can be neglected for direct-sun viewing geometries. Moreover, since Rayleigh scattering is  $\propto \lambda^{-4}$ , with  $\lambda$  the wavelength of the radiation, scattering processes are negligible. Scattering processes involving aerosols are also negligible since the infrared spectral region covers wavelengths that are larger than the diameter of these particles. Therefore, if scattering and thermal emission is neglected, the transmittance is related to the absorption coefficient by:

$$\tau(\bar{\nu}, s', s) = \exp\left(-\int_{s'}^s \sum_i \kappa_i(\bar{\nu}, s'') \rho_i(s'') ds''\right) \quad (2.75)$$

The absorption may be due to molecular rovibrational transitions as seen in Sect. 2.2.7 where  $i$  refers to the  $i$ -th absorber along the path of propagation and  $\rho_i(s'')$  its density. The absorption coefficient can often be approximated by a superposition of spectral lines:

$$\kappa_i(\bar{\nu}, s'') = \sum_j k_{ij}(T(s'')) f_{ij}(\nu, p(s''), T(s'')) \quad (2.76)$$

Here,  $k_{ij}$  is the strength of the absorption of the  $j$ -th line of the  $i$ -th absorber and is in general temperature dependent. Its shape is normalized by the function  $f_{ij}(\nu, p(s''), T(s''))$

which also may depend on the pressure  $p(s'')$ . Line mixing effects caused by, e.g. rotationally inelastic collisions between molecules, cannot be described by a superposition of spectral lines and need a more complex treatment (Tonkov et al., 1996; Rosenkranz, 1975). For the retrieval of trace gas concentrations from atmospheric solar absorption spectra, the RTE is needed as part of the forward model in the inversion calculation. This is discussed in more detail in the next section.

## 2.5 Inversion theory

An established and widely used method to retrieve information about variables which cannot be directly observed by measurement techniques is provided by the inversion theory. Examples of such variables of interest might be aerosol properties in the Earth's atmosphere, meteorological measures like temperature, pressure and humidity, or concentrations of gases in several height layers in the Earth's atmosphere. The latter is usually the main variable of interest when performing ground-based remote sensing observations by FTS or space-borne observations using infrared radiation as source. However, for the retrieval of such vertical gas profiles from solar absorption spectra, the inversion problem might be ill-posed, meaning that the variable of interest cannot be determined unambiguously without adding side constraints. The content of this section gives a brief overview on inversion problems and is mainly based on the work of Rodgers (2000).

Typically, an inversion calculation starts with a so called forward model  $\vec{F}(\vec{x})$ , which approximates the physics of the measurement process:

$$\vec{y} = \vec{F}(\vec{x}) + \vec{\varepsilon}_y \quad (2.77)$$

Here,  $\vec{y}$  represents the measurement (for example a recorded solar absorption spectrum) with the corresponding measurement error  $\vec{\varepsilon}_y$ , and  $\vec{x}$  is called state vector which represents the *true* state and contains the target variables of interest. The forward model  $\vec{F}(\vec{x})$  includes the instrumental characteristics of the measurement device and the underlying physics which relates the measured quantities and the target variable.  $\vec{F}(\vec{x})$  is usually among other processes described by basics of the radiative transfer in the Earth's atmosphere. Generally, the underlying physical processes are complicated and not fully understood such that approximations are necessary. As seen in Sect. 2.3.2, measurements are typically a set of discrete sampling points while the quantities of interest usually are continuous functions. The discretization of an inverse problem is such a simplification and is necessary for solving it numerically.

The linearization of the forward model around a reference state  $\vec{x}_0$  is eligible when  $\vec{F}(\vec{x})$  is linear within the error bounds of the retrieval and is given by:

$$\begin{aligned}\vec{F}(\vec{x}) &\approx \vec{F}(\vec{x}_0) + \frac{\partial \vec{F}}{\partial \vec{x}} (\vec{x} - \vec{x}_0) + \vec{\varepsilon}_y \\ &= \vec{F}(\vec{x}_0) + \mathbf{K} (\vec{x} - \vec{x}_0) + \vec{\varepsilon}_y\end{aligned}\quad (2.78)$$

Here,  $\mathbf{K}$  is the Jacobian matrix with matrix elements  $K_{ij} = (\partial F_i(\vec{x})) / (\partial x_j)$  with  $i \in (0, \dots, N)$  and  $j \in (0, \dots, M)$ . Here,  $N$  represents the dimension of the measurement vector  $\vec{y}$  while  $M$  represents the dimension of the target variable  $\vec{x}$ . Typically  $N \neq M$  such that  $\mathbf{K}$  is a non-square matrix and therefore cannot be directly inverted. For example,  $N < M$  represents an underconstrained and  $M < N$  an overconstrained set of equations and might contain redundant information.

If the element  $y_i$  of the measurement  $\vec{y}$  occurs with a Gaussian probability with  $\bar{y}_i$  being the expectation value and  $\sigma_i^2$  its variance, the probability density function can be expressed in the form:

$$P_i = \frac{1}{\sqrt{2\pi}\sigma_i} \exp\left(-\frac{(y_i - \bar{y}_i)^2}{2\sigma_i^2}\right) \quad (2.79)$$

Equation (2.79) written as the product of the independent probability density functions of all elements of  $\vec{y}$  becomes:

$$P = \prod_{i=1}^N P_i = \exp\left(-\frac{1}{2} \sum_{i=1}^N \frac{(y_i - \bar{y}_i)^2}{\sigma_i^2}\right) \prod_{i=1}^N \frac{1}{\sqrt{2\pi}\sigma_i} \quad (2.80)$$

For the maximum likelihood, the sum in the exponent of Eq. (2.80) has to be minimized. If additionally assuming that  $F_i(\vec{x})$  is an appropriate forward model of  $\bar{y}_i$ , the following expression has to be minimized with regard to  $\vec{x}$ :

$$\chi^2 = \sum_{i=1}^N \frac{(y_i - F_i(\vec{x}))^2}{\sigma_i^2} \quad (2.81)$$

In matrix notation, Eq. (2.81) becomes:

$$\chi^2 = (\vec{y} - \vec{F}(\vec{x}))^\top \mathbf{S}_y^{-1} (\vec{y} - \vec{F}(\vec{x})) \quad (2.82)$$

Here,  $\mathbf{S}_y^{-1}$  is the covariance matrix with matrix elements  $S_{y,ii} = \sigma_i^2$ . Using Eq. (2.78) and for now neglecting the error term  $\vec{\varepsilon}_y$ , Eq. (2.82) becomes:

$$\chi^2 = (\vec{y} - \vec{F}(\vec{x}_0) - \mathbf{K}(\vec{x} - \vec{x}_0))^\top \mathbf{S}_y^{-1} (\vec{y} - \vec{F}(\vec{x}_0) - \mathbf{K}(\vec{x} - \vec{x}_0)) \quad (2.83)$$

The first derivative of  $\chi^2$  with respect to  $\vec{x}$  is zero for:

$$\vec{x} = \left( \mathbf{K}^\top \mathbf{S}_y^{-1} \mathbf{K} \right)^{-1} \mathbf{K}^\top \mathbf{S}_y^{-1} \left( \vec{y} - \vec{F}(\vec{x}) \right) + \vec{x}_0 \quad (2.84)$$

Here,  $\mathbf{K}^\top \mathbf{S}_y^{-1} \mathbf{K}$  is a square matrix. In a numerical sense, using for e.g. the Gauss-Newton algorithm, which accounts for the non-linearity of the RTE in the forward model, to solve this least squares problem, several iterations are necessary leading to:

$$\vec{x}_{n+1} = \vec{x}_n + \left( \mathbf{K}_n^\top \mathbf{S}_y^{-1} \mathbf{K}_n \right)^{-1} \mathbf{K}_n^\top \mathbf{S}_y^{-1} \left( \vec{y} - \vec{F}_n(\vec{x}_n) \right) \quad (2.85)$$

Here,  $n$  is the index of iterations. The iteration can be terminated if the difference  $\vec{x}_{n+1} - \vec{x}_n$  converges towards an arbitrary small value  $\delta$ . It should be noted that for inversion calculations it is favorable to choose small spectral windows (ranging from couple of tenths up to several wavenumber wide) rather than wide spectral ranges which might cover an entire measured FTIR spectrum, up to several thousand wavenumbers wide. This approach reduces the numerical effort.

If  $\mathbf{K}^\top \mathbf{S}_y^{-1} \mathbf{K}$  is singular, the retrieved quantity of interest, e.g. the vertical gas profiles, will show an oscillatory behavior. Due to the lack of information content in the measurement and due to the presence of measurement noise, the iteration will lead to non-realistic results. In order to retrieve realistic vertical gas profiles, side constraints are required, a so called regularization must be performed. Common regularization methods are the optimal estimation approach and the Tikhonov-Phillips regularization. The latter is applied in this work for the retrieval of vertical gas profiles from MIR solar absorption spectra. The optimal estimation method is not used within this work. Both methods are equivalent from the mathematical point of view. The optimal estimation method strives to determine the most likely solution including a priori knowledge of the target variable based on a covariance matrix derived from, for example a set of in situ measurements of vertical gas profiles providing an estimate for the most likely vertical profile. The Tikhonov-Phillips regularization instead uses ad-hoc side constraints and a priori information (e.g. to prescribe the slope of the vertical concentration) leading to the following term that has to be minimized:

$$\chi^2 = \left( \vec{y} - \vec{F}(\vec{x}) \right)^\top \mathbf{S}_y^{-1} \left( \vec{y} - \vec{F}(\vec{x}) \right) + \left( \vec{x} - \vec{x}_a \right)^\top \gamma \mathbf{W} \left( \vec{x} - \vec{x}_a \right) \quad (2.86)$$

The second term of the right hand side in Eq. (2.86) represents the regularization term where  $\vec{x}_a$  is the a priori knowledge, e.g. from numerical climate model calculations and  $\gamma$  is the regularization parameter which controls the strength of the regularization. In the simplest case, the matrix  $\mathbf{W} = \mathbf{L}^\top \mathbf{L}$  can be the unity matrix. However, in practice,

$\mathbf{L}$  is usually chosen as the discrete first order derivative operator. In analogy, for the optimal estimation method,  $\mathbf{W}$  is replaced by an a priori covariance matrix which contains statistical knowledge about the target variable of interest obtained from a set of additional measurements. Equation (2.86) is minimized when:

$$\vec{x} = \vec{x}_a + \underbrace{\left(\mathbf{K}^\top \mathbf{S}_y^{-1} \mathbf{K} + \gamma \mathbf{W}\right)^{-1} \mathbf{K}^\top \mathbf{S}_y^{-1}}_{\mathbf{G}} \left(\vec{y} - \vec{F}(\vec{x}_a)\right) \quad (2.87)$$

$\mathbf{G}$  is called the gain matrix. Using the Levenberg-Marquardt algorithm, the iterative solution becomes:

$$\vec{x}_{n+1} = \vec{x}_n + \left(\mathbf{K}_n^\top \mathbf{S}_y^{-1} \mathbf{K}_n + \gamma \mathbf{W}\right)^{-1} \left(\mathbf{K}_n^\top \mathbf{S}_y^{-1} \left(\vec{y} - \vec{F}_n(\vec{x}_n)\right) + \gamma \mathbf{W} (\vec{x}_a - \vec{x}_n)\right) \quad (2.88)$$

Again,  $n$  represents the number of iterations. The matrix  $\mathbf{A} = \mathbf{G}\mathbf{K}$  is called the averaging kernel matrix and describes the vertical resolution of the retrieval. It describes how the observing system (e.g. FTS) *smooths* the retrieved target variable. For an ideal instrument without noise and a measurement with complete information content about the target variable and a perfect retrieval without regularization constraints, the averaging kernel matrix  $\mathbf{A}$  becomes the identity matrix. For real instruments and measurements, the column vectors of  $\mathbf{A}$  are generally peaked functions which describe the vertical correlation between different elements of the state vector. The width of the peak describes the vertical resolution of the retrieval if  $\vec{x}$  describes a vertical gas profile.  $\mathbf{A}$  is an intrinsic part of the solution of the retrieval problem and needs to be taken into account when the retrieval data is used for validation purposes or intercomparison studies using model simulations. The number of the degrees of freedom of the retrieval procedure can be determined by the trace of  $\mathbf{A}$ .

# 3 Ground-based solar absorption FTIR measurements in Karlsruhe

Measurements of trace gas abundances in the Earth's atmosphere are the foundation for improving the understanding of the Earth's climate system. As part of the Total Carbon Column Observing Network (TCCON), the Karlsruhe Institute of Technology operates a high resolution ground-based FTIR spectrometer to measure concentrations of various trace gases in the atmosphere. These measurements aim at monitoring long-term trends and also represent a transfer standard between surface in situ measurements and satellite observations. This chapter describes measurements of ground-based solar absorption spectra at the Karlsruhe FTIR site in more detail. A brief summary of the basic instrumental setup of the Karlsruhe FTS is given. The optical prototype setup developed at the Karlsruhe Institute of Technology is an extension over other instruments usually operated within the two global FTIR networks TCCON and NDACC. It allows for TCCON- and NDACC-style measurements in the MIR and NIR spectral ranges at the same time. Therefore, resulting instrumental modifications are highlighted in this chapter. Potential error sources influencing the measurements are discussed. It is shown that the prototype instrumental setup of the Karlsruhe FTS induces variations in the background continuum which need an appropriate treatment in the TCCON retrieval strategy. Parts of the following chapter are adapted from Kiel et al. (2016b).

## 3.1 The Karlsruhe FTS site

The Karlsruhe FTIR spectrometer was initiated in 2009 at the Karlsruhe Institute of Technology (KIT) - Campus North (49.1° N, 8.4° E, 110 m above sea level). The instrument is operated by the Ground-Based FTIR Remote Sensing research group at the Institute of Meteorology and Climate Research - Atmospheric Trace Gases and Remote Sensing (IMK-ASF). Karlsruhe is an extensive, urban sprawled city in Central Europe. The city experiences an oceanic, mild climate similar to most cities in the mid-western part of Europe. The rather smooth orography ensures a model treatable airflow and the airmass in this region accurately reflects the greenhouse gas emissions in Central Europe. Moreover, the flat terrain is a favorable scene for nadir viewing satellite overpasses as well as model

studies. The surrounding boreal forest is the major carbon sink in this area. Several studies (e.g. Reuter et al., 2014) revealed that the European terrestrial carbon budget is still uncertain which makes this site interesting for ongoing and future carbon cycle studies. In addition, ground-based remote sensing measurements can be compared with in situ data from a nearby meteorological tall tower also operated by the KIT. The Karlsruhe FTIR site currently participates in measurements for the validation of the Orbiting Carbon Observatory 2 (OCO-2) satellite. OCO-2 was launched in 2014, a NASA mission designed to globally measure CO<sub>2</sub> abundances (Frankenberg et al., 2015). Moreover, the Karlsruhe FTS site participated in the Infrastructure for Measurement of the European Carbon Cycle campaign (IMECC) in 2009. IMECC was the first airborne campaign to calibrate the European TCCON FTS sites with respect to World Meteorological Organization (WMO) standards, e.g. Wunch et al. (2010), Messerschmidt et al. (2011) and Geibel et al. (2012). In addition, within the Multi-platform remote Sensing of Isotopologues for investigating the Cycle of Atmospheric water project (MUSICA, Schneider et al., 2012), long-term tropospheric water vapor isotopologues data records are provided from mid-infrared FTIR measurements which support the analysis of the European hydrological and carbon cycle.

#### 3.1.1 Basic setup of the Karlsruhe FTIR instrumentation

The stationary ground-based FTIR spectrometer operated at the Karlsruhe site is designed to measure concentrations of trace gases in the Earth's atmosphere using the Sun as natural source of radiation. Solar absorption spectra are acquired by operating a Bruker IFS 125HR spectrometer (Bruker Optics GmbH, Germany) which is currently the most robust and stable high-resolution FTS commercially available. The automated instrument is housed in an air-conditioned 20 ft sea transport certified shipping container (see Fig. 3.1). The container is equipped with a heating and an air conditioning unit to ensure a constant temperature surrounding the spectrometer's components over the year and seasons. The



**Figure 3.1:** Aerial photograph of the Karlsruhe FTS site at the Campus North of the KIT (left panel) and the certified shipping container wherein the spectrometer is hosted (right panel). Photograph courtesy of KIT (left panel) and F. Hase (right panel).

Bruker IFS 125HR features a cube-corner Michelson interferometer containing an exchangeable semi-transparent calcium fluoride ( $\text{CaF}_2$ ) beam splitter and a linearly moving scanner. Moreover, the instrument features a camera-based solar tracker developed at KIT (Gisi et al., 2011) which directs solar radiation into the interferometer. The azimuth-altitude dual axis tracker uses two optical mirrors which are movable around the elevation and the azimuth axis. The optical components provide good reflectivity in the infrared spectral region with a gold-coated flat surface to maximize signal levels. The tracker system automatically follows the position of the sun controlled by a tracking software exploiting astronomical calculations and camera data to control the motion of the tracker mirrors. The portion of the solar image on the spectrometer field stop is observed by a camera which ensures a high pointing accuracy of at least 11 arcs.

The optical setup has been optimized for measurements of atmospheric solar absorption spectra in the mid-infrared (MIR) and near-infrared (NIR) spectral regions covering the 1900 to 11 000  $\text{cm}^{-1}$  range where various infrared-active molecules in the atmosphere are detectable. Interferograms are sampled equidistantly in the time domain, digitized by a 24 bit analogue-to-digital converter and then resampled at constant intervals of optical delays as defined by the zero-crossings of a 633 nm HeNe laser (Sios GmbH, Germany). The full spectral range of recorded solar spectra from 1900 to 11 000  $\text{cm}^{-1}$  is covered by the simultaneous operation of two detectors. An indium antimonide (InSb) detector covers the spectral range from 1900 to 5250  $\text{cm}^{-1}$  and an indium gallium arsenide (InGaAs) detector covers the 5250 to 11 000  $\text{cm}^{-1}$  spectral range. The InSb diode is cryogenically cooled using a liquid nitrogen ( $\text{LN}_2$ ) microdosing autofill cooling system (Norhof, Netherlands) whereas the InGaAs detector is operated at room-temperature. A  $\text{CaF}_2$  dichroic beamsplitter (Optics Balzers Jena GmbH, Germany) is installed with a cut-off wavenumber of 5250  $\text{cm}^{-1}$ . The recombined beam is split into two partial beams by the dichroic mirror, one beam containing wavelength components in the MIR spectral region (reflected) and the second beam with components in the NIR range (transmitted). A schematic depiction of the Karlsruhe instrumental setup is given in Fig. 3.2. A photograph of the two detectors and the dichroic beamsplitter is seen in Fig. 3.3. This particular optical setup allows for simultaneous measurements using the MIR and NIR part of the solar spectrum, forming a bridge between instruments which are affiliated with the NDACC or the TCCON. Therefore, in the next section, the Karlsruhe instrumental prototype setup as well as differences to other FTS instruments which are usually operated within the NDACC and the TCCON are discussed in more detail.

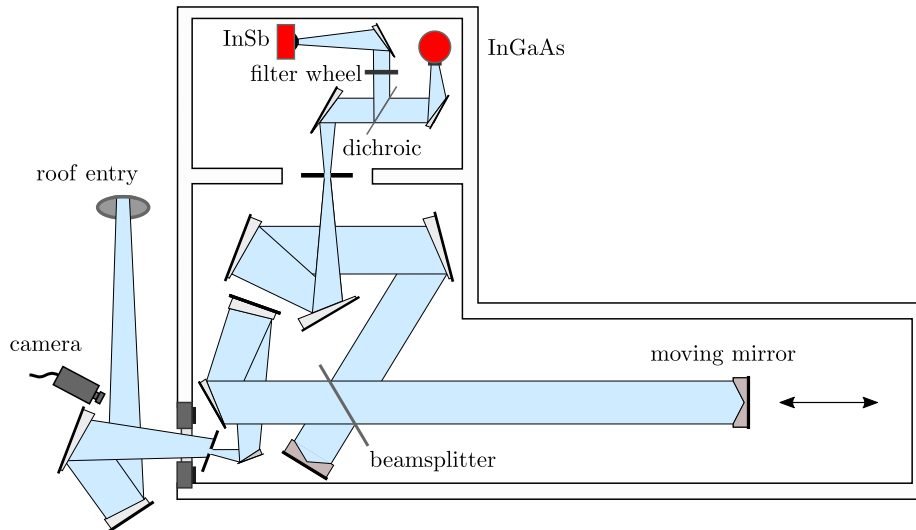


**Figure 3.2:** Simplified illustration of the Karlsruhe FTIR spectrometer. The incoming solar radiation is guided into the spectrometer using a camera based solar tracker (here indicated by a camera symbol) which observes the image of the sun on the input aperture. The recombined beam is split by the dichroic optic into two parts, each containing either MIR or NIR components of the solar radiation which are separately guided on the InSb and InGaAs diodes where the interferogram is recorded as a function of the optical path difference induced by the moving mirror. The InGaAs detector is equipped with a Si longpass filter. This figure is adapted from Gisi et al. (2011).

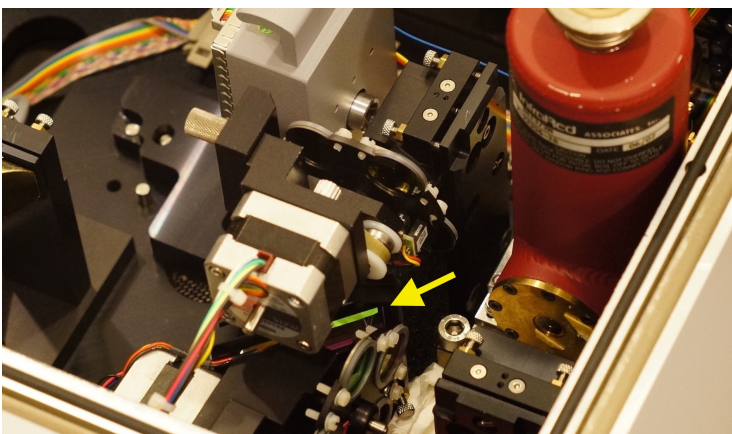


**Figure 3.3:** Photograph of the two detector elements used in the Karlsruhe setup. The red dewar contains the InSb diode which records spectra in the MIR whereas the gray block contains the InGaAs diode for measurements in the NIR. The dichroic optic is marked by the yellow arrow, next to it is the filter wheel containing five NDACC filters.

### 3.1.2 Differences between the Karlsruhe instrumental setup and standard TCCON and NDACC FTIR instruments

The TCCON strives to attain the best site-to-site precision and accuracy achievable with the defined instrumentalities. Thus, the network sets guidelines for its partners to ensure consistency between different sites within the network. These guidelines include requirements demanding specific instrumental characteristics which limit the choice of acceptable FTIR instrumentations (Wunch et al., 2011; Washenfelder et al., 2006). The Bruker IFS 125HR spectrometer is currently one of the most stable stationary high-resolution FTIR instruments and therefore the preferred instrument within the network (Wunch et al., 2011). Standard TCCON instruments measure in the NIR spectral region which includes solar absorption bands of several trace gases of interest, the so called target gases, e.g. CO<sub>2</sub>, CH<sub>4</sub>, CO, N<sub>2</sub>O. Two detectors at room-temperature, an extended InGaAs and silicon (Si) detector cover the spectral range from 3800 to 15 500 cm<sup>-1</sup> in dual acquisition mode. The InGaAs detector covers the range from 3800 to 12 000 cm<sup>-1</sup> while the Si detector covers the 9500 to 30 000 cm<sup>-1</sup> range. A dichroic optic (Omega Optical Inc., USA) is installed with a cut-off wavenumber of 10 000 cm<sup>-1</sup>. An optical filter (Oriol Instruments, USA) with a cut-off wavenumber of 15 500 cm<sup>-1</sup> is mounted in front of the Si diode to block wavenumbers in the visible spectral range. This prevents aliasing of the visible spectrum into the NIR spectral domain. Retrievals from spectra recorded by the Si detector are not considered yet as official TCCON measurements but are of scientific interest for comparisons with satellite instruments which measure the  $b^1\Sigma_g^+(\nu=0) \leftarrow X^3\Sigma_g^-(\nu=0)$  transition in the oxygen A-Band ranging from 12 950 to 13 170 cm<sup>-1</sup>. Moreover, TCCON partners typically use very similar optical components (e.g. beam splitters, narrow band filters, mirror coating, etc.) to reduce differing optical component responses between globally distributed instruments (Wunch et al., 2011; Washenfelder et al., 2006). This approach of standardizing the optical components is imperfect, but the instrumental impact on measured solar spectra from different sites is generally small.

The Karlsruhe instrument differs from the standard TCCON instrumental requirements. The prototype instrumental setup is an extension over the standard TCCON setup as the dichroic optic allows measurements of solar spectra in the MIR and NIR spectral domains simultaneously, covering spectral regions down to 1900 cm<sup>-1</sup>. To measure all gases which are of interest for TCCON, the spectral range of the TCCON measurements have to include 3800 to 11 000 cm<sup>-1</sup>, only the oxygen A- and B-bands are measured on the Si detector above 11 000 cm<sup>-1</sup>. In Karlsruhe, instead of operating an extended InGaAs detector, the full spectral coverage from 3800 to 11 000 cm<sup>-1</sup> is covered by the simultaneous operation of an InGaAs and an InSb diode in combination with the dichroic beamsplitter and a narrowband

filter (see Fig. 3.4). Measurements from 5250 to 11 000  $\text{cm}^{-1}$  are performed similarly to standard TCCON instruments using the InGaAs detector. Target gases in this spectral region are  $\text{CH}_4$ ,  $\text{O}_2$ , and  $\text{CO}_2$ . For TCCON measurements of  $\text{CO}$ ,  $\text{N}_2\text{O}$  and  $\text{HF}$  which absorb in the 3800 to 4800  $\text{cm}^{-1}$  region, a narrowband spectral filter transmitting from 3800 to 5250  $\text{cm}^{-1}$  is mounted in front of the InSb diode, yielding higher signal-to-noise ratios and minimizing any detector nonlinearity. A typical Karlsruhe spectrum covering the full TCCON spectral range is depicted in Fig. 3.4. The cut-off wavenumber of the dichroic optic is 5250  $\text{cm}^{-1}$  and lies between two atmospheric windows separated by  $\text{H}_2\text{O}$  absorption lines. In the Earth's atmosphere, these lines are strongly saturated such that no loss of information arises by splitting the incoming beam into two parts at this wavenumber.

Whereas the Karlsruhe device differs from the standard TCCON setup, it is quite typical from the NDACC perspective. The InSb diode is typically used in conjunction with five optical filters as recommended by the NDACC (see Table 3.1). The filters define narrow absorption bands by limiting the wavenumber range of the recorded spectra and also increase the signal-to-noise ratio. Typical NDACC-style spectra are depicted in Fig. 3.5. This enables measurements in the MIR that are of scientific interest, but are not considered as TCCON measurements. These spectra are routinely measured by NDACC - Infrared Working Group (IRWG) stations and include solar absorption lines of various additional gases, e.g.  $\text{NO}$ ,  $\text{O}_3$ ,  $\text{HCl}$ ,  $\text{HCN}$ ,  $\text{C}_2\text{H}_2$ ,  $\text{C}_2\text{H}_4$ ,  $\text{NO}_2$  and  $\text{C}_2\text{H}_6$ . Additionally, the fundamental absorption bands of  $\text{OCS}$  and  $\text{CO}$  are in this region, making it the preferred spectral region for retrievals of these gases. The optical setup also provides spectra of  $\text{H}_2\text{O}$ ,  $\text{HDO}$ ,  $\text{CH}_4$  and  $\text{N}_2\text{O}$  in the MIR bands. Thus, the Karlsruhe TCCON instrument allows to make observations in the MIR region compatible with those routinely done by NDACC FTIR stations.

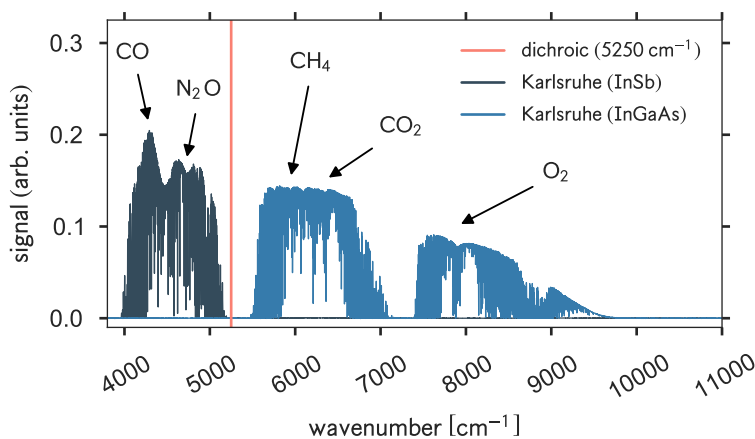


**Figure 3.4:** Typical Karlsruhe spectrum recorded by the InSb and InGaAs diode. The coverage of the full spectral range from 3800 to 11 000  $\text{cm}^{-1}$  is realized by the simultaneous operation of the two diodes.

Although the Karlsruhe instrument conforms to almost all of the NDACC criteria, it does not cover the full spectral range down to  $720\text{ cm}^{-1}$  due to the lack of a mercury cadmium telluride (MCT) detector. Typical NDACC instruments additionally operate an MCT detector which is sensitive to the range  $720$  to  $6000\text{ cm}^{-1}$ . Therefore, retrievals of, e.g.  $\text{O}_3$ , at  $1000\text{ cm}^{-1}$  are not performed in Karlsruhe. Consequently, the Karlsruhe FTIR site does not carry out a full operational NDACC-IRWG status. Still, all measurements in the MIR are performed and processed following the guidelines of the NDACC-IRWG.

Although other FTIR sites also perform NDACC and TCCON measurements using the same instrument (e.g. Izaña, Tenerife Island, Spain), the novel Karlsruhe instrumental setup is unique within the TCCON and the NDACC and is currently the only instrument which can perform measurements in the MIR and NIR simultaneously. So far, other FTIR sites which are affiliated with both, the NDACC and the TCCON, perform MIR and NIR measurements in a consecutive way. This requires a change of the beamsplitter when alternating between MIR and NIR measurements. Therefore, the Karlsruhe instrumental setup is a prototype of a merged NDACC and TCCON instrument and can be seen as a pilot project of both networks to extend their spectral coverages.

To account for deviations from the ILS due to small instrument misalignments or imperfections, the ILS is monitored on a regular base. For standard TCCON instruments, the ILS is monitored using a permanently mounted  $10\text{ cm}$  long low-pressure HCl cell ( $5.1\text{ hPa}$ ) in the

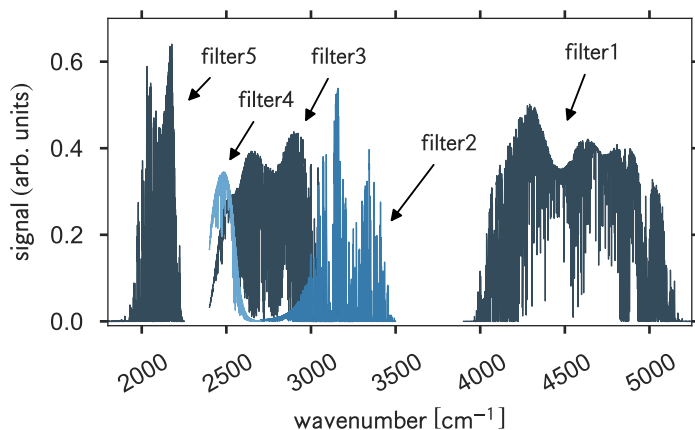


**Figure 3.5:** Typical Karlsruhe spectrum recorded by the InSb diode largely covering the MIR spectral range. Different optical filters define narrow absorption bands and are typically recorded in a consecutive way in parallel to measurements with the InGaAs diode.

NDACC filter	1	2	3	4	5
spectral range*	3950–5250	2700–3500	2400–3250	2400–2700	1800–2250

\*: given in  $\text{cm}^{-1}$

**Table 3.1:** Transmission ranges for the optical filters typically used within the NDACC which are also part of the Karlsruhe instrumental setup.

solar beam of the interferometer prior to the entrance field stop wheel. For standard NDACC instruments, low pressure gas cells filled with hydrogen bromide (HBr) are inserted in the beam of the instrument in the sample compartment. HBr spectra are measured approximately every two months using a laboratory mid-infrared source. To precisely determine the ILS, the HCl and HBr spectra measured by TCCON or NDACC instruments are analyzed by the LINEFIT algorithm (Hase et al., 1999). In comparison to standard TCCON sites, the Karlsruhe instrument does not contain a permanently mounted low-pressure HCl cell in the solar beam to monitor the ILS since measurements are also performed in the MIR where atmospheric HCl absorption lines are accessible and of scientific interest. Nevertheless, once a month, a low-pressure HCl cell is mounted into the beam of a laboratory lamp source and ILS measurements are performed. These measurements are performed on a regular base following an improved method which applies a sequence of measurements using different gas cells instead of one single calibration cell as done within the NDACC. For that, a refillable cell ( $C_2H_2$ ) with a pressure gauge is used. In Hase (2012) it was demonstrated that an ILS retrieval using refillable pressure monitored cells significantly improves the residual of the ILS retrieval over the current calibration cells used in both networks. This method is also used to uncover impurities of the sealed low-pressure HCl cells used by other TCCON stations to monitor the ILS. To date, the Karlsruhe instrument has been kept in near-perfect alignment.

Typical TCCON measurements are routinely recorded at a maximum optical path difference ( $OPD_{max}$ ) of 45 cm leading to a spectral resolution of  $0.02\text{ cm}^{-1}$ . Karlsruhe solar spectra are recorded at an  $OPD_{max}$  of 45 cm, 64 cm, and 120 cm leading to spectral resolutions of 0.02, 0.014, and  $0.0075\text{ cm}^{-1}$ , respectively. NDACC measurements in the MIR are always performed at an  $OPD_{max}$  of 180 cm leading to a spectral resolution of  $0.005\text{ cm}^{-1}$ . Typically, one measurement consists of two forward and two backward scans which are averaged. TCCON measurements at  $OPD_{max} = 64\text{ cm}$  and  $OPD_{max} = 120\text{ cm}$  are recorded approximately within 212 sec and 388 sec, respectively. The spectral collection time for NDACC measurements is 580 sec at 20 kHz laser fringe rate. Both, MIR and NIR measurements are controlled using the Optics User Software (OPUS) Version 7.0 provided by Bruker. Moreover, interferogram slices can be directly obtained via the web interface of the Bruker IFS 125HR instrument. The internal spectrometer software generates interferogram slices which represent a 10 cm optical path portion of an interferogram. These slices can be automatically transferred to the instrument and assembled in complete interferograms, making the data acquisition independent from the usage of proprietary commercial software. On average, measurements are performed on 130 days per year with about 100 recorded spectra per day requiring clear sky conditions.

## 3.2 Analysis of solar absorption FTIR spectra

Both, the TCCON and the NDACC use non-linear least-squares spectral fitting algorithms to analyze solar absorption spectra. However, different approaches are used for both networks concerning the retrieval procedure, preprocessing routines, the choice of spectral windows, spectroscopic parameters, a priori information and correction factors. In the next sections, the data processing and analysis for TCCON and NDACC measurements are described in more detail. Parts of the following sections are based on Wunch et al. (2011), Wunch et al. (2015) and Hase et al. (2004).

### 3.2.1 Analysis of TCCON data

The TCCON data processing is performed by a network wide software package named GGG Suite (Wunch et al., 2011). For public distribution of TCCON data sets, only measurements analyzed with this algorithm are accepted. All TCCON partners use the same retrieval analysis strategy to minimize algorithmic biases between sites and to provide a consistent primary long-term data sets of trace gas concentration records.

The GGG Software Suite includes a pre-processor which corrects the recorded interferograms for solar brightness fluctuations (SBF, Keppel-Aleks et al., 2007). A fast Fourier transform based on Bergland (1969) which also includes a phase correction routine (Forman et al., 1966) is performed to compute solar absorption spectra from raw interferograms. The GFIT algorithm is the main core of the GGG Suite and is a non-linear least-squares spectral fitting algorithm designed for the analyses of solar FTS spectra (Wunch et al., 2015). The algorithm was developed at the Jet Propulsion Laboratory, Pasadena, USA, and evolved from the ODS Software (Norton and Rinsland, 1991). GFIT has been widely used for analyses of MkIV spectra and ATMOS shuttle spectra (Irion et al., 2002). The algorithm is suitable to analyze spectra from multiple platforms including balloon and aircraft measurements and is used within the TCCON to analyze solar spectra obtained from stationary ground-based FTIR measurement. The GFIT algorithm scales an a priori VMR profile to generate the best spectral fit. The scaled profile is then integrated over height to compute the column abundance of a gas (Wunch et al., 2011). The algorithm basically consists of two parts, a forward and inverse model. The forward model calculates an atmospheric transmittance spectrum for a set of certain prescribed conditions. The inverse model compares the calculated spectrum with the measured spectrum and adjusts the retrieved parameters to obtain the best match. Most of the adjusted parameters are user-selectable, however, for standard TCCON data products, these choices are prescribed to ensure consistency between sites (Wunch et al., 2011). The GFIT algorithm does not perform profile retrievals (i.e. the gas concentrations at different altitudes are not scaled

independently to obtain the best fit to the spectrum). Instead, the algorithm scales an a priori VMR profile, which implies that the shape of the gas profile is well known. This approach is justified because the most important TCCON target gases are, e.g. CO<sub>2</sub> and O<sub>2</sub>, whose VMR profile shapes are well known and not highly variable with altitude (Wunch et al., 2011).

However, for gases like, e.g. CO, whose concentration is highly variable with altitude, the a priori knowledge of the shape of the VMR profile is important. Daily a priori VMR profiles used within the GGG Suite are generated by a set of empirical functions which are based on measurements from balloon-borne platforms [MkIV (Toon, 1991), AirCore (Karion et al., 2010), OMS (Daube et al., 2002)], aircraft [HIPPO (Wofsy, 2011), START-08 (Pan et al., 2010), INTEX-NA (Singh et al., 2006), IMECC (Messerschmidt et al., 2011; Geibel et al., 2012)], and satellites [ACE-FTS (Bernath et al., 2005), ATMOS (Irion et al., 2002)]. The empirical functions take into account inter hemispheric gradients, secular increases and variations due to the seasonal cycle. Most of the a priori profiles of gases of interest for the TCCON are derived from ACE FTS (Bernath et al., 2005) and MkIV FTS (Toon, 1991) solar occultation measurements. Stratospheric a priori VMR profiles of CH<sub>4</sub> and NO<sub>2</sub> are constrained by the nearly inverse relationship between profiles of HF and those of CH<sub>4</sub> and N<sub>2</sub>O (Washenfelder et al., 2003; Luo et al., 1995). The CO<sub>2</sub> a priori VMR profiles are based on the GLOBALVIEW data set (GLOBALVIEW-CO2, 2010) and vary with the time of year and the latitude of the site. The H<sub>2</sub>O a priori VMR profiles are derived from the National Centers for Environmental Prediction/National Center for Atmospheric Research (NCEP/NCAR) analyses (Kalnay et al., 1996).

Also, the NCEP/NCAR analysis product, together with measured surface pressure at the FTIR site, is used to generate daily pressure and temperature profiles. The surface pressure is taken from measurements obtained from instruments installed at the Karlsruhe meteorological tall tower (200 m) also located at the KIT - Campus North near the FTIR station. These and the a priori VMR profiles are the main site dependent inputs for the GGG Suite.

For TCCON retrievals, an adopted high-resolution transmission molecular absorption database, roughly based on HITRAN 2012 (Rothman et al., 2013) is used. This database provides spectroscopic parameters (e.g. line intensities, self-broadening coefficients, air-broadening coefficients, temperature-dependent coefficients) which are used by the GFIT algorithm. For H<sub>2</sub>O, many empirical changes were applied to the original HITRAN 2012 compilation throughout the 4000 to 6000 cm<sup>-1</sup> region based on fits made to Kitt Peak laboratory spectra (Wunch et al., 2015). Spectral lines centered around the 7885 cm<sup>-1</sup>

O<sub>2</sub> band are based on laboratory measurements of Newman et al. (1999) with modifications from Yang et al. (2005). This spectral O<sub>2</sub> band is highly affected by collision induced O<sub>2</sub> absorption, therefore a model based on laboratory measurements by Smith and Newnham (2000) is fitted in this region. Interfering solar lines are calculated from a tabulated solar line list, which was derived from MkIV balloon spectra in the MIR from 600 to 5600 cm<sup>-1</sup> and ground-based Kitt Peak spectra in the NIR and visible spectral region.

The retrieval strategy by TCCON prefers wide spectral fitting regions, which might encompass a whole molecular band of the target gas. This is a superior approach especially in the NIR because using whole absorption bands minimizes any temperature sensitivities, and for a given noise level in the spectrum, this approach significantly reduces the noise error of the retrieved column abundances because many absorption lines contribute. An excerpt of fitted spectral windows for the major TCCON target gases is given in Table 3.2. The official TCCON data products are provided as column averaged dry-air mole fractions (DMF, see Sect. 3.3.7).

gas		spectral window*	
target	interfering	center	width
CO <sub>2</sub>	H <sub>2</sub> O, HDO, CH <sub>4</sub>	6220.00	80.00
CO <sub>2</sub>	H <sub>2</sub> O, HDO	6339.50	85.00
CH <sub>4</sub>	HDO, CO <sub>2</sub>	5938.00	116.00
CH <sub>4</sub>	CO <sub>2</sub> , H <sub>2</sub> O, HDO,	6002.00	11.10
CH <sub>4</sub>	HDO, NO <sub>2</sub> , H <sub>2</sub> O	6076.00	138.00
N <sub>2</sub> O	CH <sub>4</sub> , H <sub>2</sub> O, HDO	4395.20	43.40
N <sub>2</sub> O	CH <sub>4</sub> , H <sub>2</sub> O, HDO, CO <sub>2</sub>	4430.10	23.10
CO	CH <sub>4</sub> , H <sub>2</sub> O, HDO	4233.00	48.60
CO	CH <sub>4</sub> , H <sub>2</sub> O, HDO	4290.40	56.80
HF	H <sub>2</sub> O	4038.95	0.32

\* given in cm<sup>-1</sup>

**Table 3.2:** Main target gases of the TCCON. In addition to the center and width of the spectral window, the interfering gases of the particular spectral windows are listed. Additionally, H<sub>2</sub>O and HDO are retrieved from several narrow spectral windows which are not listed here since they are not declared as official TCCON target gases.

Gas	CO <sub>2</sub>	CH <sub>4</sub>	N <sub>2</sub> O	CO
AI	$0.9898 \pm 0.0010$	$0.9765 \pm 0.0020$	$0.9638 \pm 0.0100$	$1.0672 \pm 0.0200$

**Table 3.3:** Airmass independent calibration factors (AI) for the main target gases of the TCCON. Retrieved column averaged dry-air mole fractions of the particular gas are divided by these constant AIs. For H<sub>2</sub>O, HDO, and HF, no AI is applied.

An additional post-processing algorithm applies empirical airmass correction and airmass-independent correction factors (obtained from in situ measurements) to the retrieved column averaged dry-air DMFs. Air-mass-dependent retrieval biases must be accounted for, as they can be aliased into the seasonal cycle. Most likely, they are caused by spectroscopic inadequacies, e.g. inconsistencies in the relative strengths of weak and strong absorption lines and incorrect line widths. TCCON retrieval results are tied to the WMO scale via aircraft and AirCore profiles measured over TCCON sites to account for biases that are consistent throughout the network (Washenfelder et al., 2006; Deutscher et al., 2010; Wunch et al., 2010; Messerschmidt et al., 2011; Geibel et al., 2012; Karion et al., 2010). Such a calibration is reasonable since the observations rely on spectroscopic parameters which might contain systematic biases. Today, vertical gas profiles over almost all TCCON sites have been measured and the empirical correction is applied by dividing the retrieved TCCON data by the obtained calibration factors. Table 3.3 summarizes the obtained calibration factors for the gases CO<sub>2</sub>, CH<sub>4</sub>, N<sub>2</sub>O, and CO.

### 3.2.2 Analysis of NDACC data

Currently there are two codes which are widely used for analyses of recorded NDACC spectra in the MIR, namely SFIT (Rinsland et al., 1998) and PROFFIT (Hase et al., 2004). The latter is used in this work to analyze spectra in the MIR. The PROFFIT algorithm was developed at the Karlsruhe Institute of Technology and is also used for analyses of low-resolution spectra as recorded with EM27/SUN spectrometers (Bruker Optics GmbH, Germany, Gisi et al., 2012; Hase et al., 2015; Frey et al., 2015; Klappenbach et al., 2015).

Before analyzing solar absorption spectra, raw interferograms are processed using the CALPY preprocessing algorithm. Within the frame of this work, the at KIT jointly developed algorithm CALPY was further evolved and utilized as a pre-processor for PROFFIT. The algorithm applies a quality check to recorded interferograms based on signal strengths. Moreover, the algorithm calculates the solar absorption spectrum from the raw interferogram. Similar to the GGG Suite pre-processor for NIR spectra, an SBF correction is applied to the raw MIR interferograms. SBFs occur due to clouds (e.g. variable cirrus clouds) and

may reduce the interferograms amplitude causing a distortion of the calculated spectrum (Keppel-Aleks et al., 2007). In general, SBFs introduce broadband oscillations in the raw interferogram with frequencies typically much lower compared to frequencies corresponding to the wanted spectral information of interest. The PROFFIT preprocessor separates these two parts. SBFs are estimated by applying a moving average over the raw interferogram, suppressing the high frequencies and results in a smoothed interferogram. Then, an SBF corrected interferogram is obtained from division of the raw interferogram by the smoothed interferogram where the low-frequency oscillations are minimized. However, interferograms with strong fractional SBFs of more than 10 % are discarded from the scientific data set by an automated quality filter in advance of the SBF correction algorithm. A fast Fourier transform using the Sande-Tukey algorithm computes the solar absorption spectrum from the raw interferogram which can directly be utilized by the retrieval algorithm PROFFIT.

The retrieval of gas abundances underlies the PROFFIT algorithm. The algorithm was systematically validated in Hase et al. (2004). PROFFIT is a non-linear least-squares fitting algorithm which analyzes solar absorption spectra on the basis of inversion methods. The algorithm can handle several spectral windows and target gases simultaneously.

The a priori VMR profiles are obtained from the Whole Atmospheric Chemistry Climate Model (WACCM, Garcia et al., 2007). One fixed a priori VMR profile is used per site which represents the climatological mean obtained from WACCM (Version 5) model runs for 40 years from 1980 – 2020. WACCM is a comprehensive numerical model, spanning the range of altitudes from the Earth’s surface to the thermosphere. It is a fully coupled chemistry climate model which simulates the entirety of the Earth’s atmosphere. WACCM unifies approaches of the upper, middle and tropospheric atmospheric modeling. A more detailed description is given in Marsh et al. (2013).

Further input for PROFFIT are pressure and temperature profiles allowing for intra day variability with a temporal resolution of up to 30 minutes. These profiles are taken from measurements obtained from instruments installed at the Karlsruhe meteorological tall tower and the Modern-era retrospective analysis for research and applications model data (MERRA, Rienecker et al., 2011) which provides temperature and pressure profiles on a  $1.25^\circ \times 1.25^\circ$  grid, from 1000 to 0.1 hPa for eight times per day. For each of the eight time points, the solar position is calculated and the pressure and temperature along the unrefracted path of the solar radiation is retrieved from the model data leading to three-dimensional pressure and temperature profiles with intra day variability (Gisi et al., 2012).

PROFFIT is utilized for a full profile retrieval using an inverse covariance matrix. For the efficient construction of simplified empirical covariances, the method described by Tikhonov and Phillips (Phillips, 1962) can be used. This allows for height-dependent constraints on the variability (Hase et al., 2004). Moreover, instead of using a priori covariances, the regularization term includes the discrete first order derivative operator. PROFFIT allows for inversions on a linear or a logarithmic scale. The latter approach forces the solution to physically meaningful positive values. The signal-to-noise ratio is empirically obtained from the fit residual (the difference between measured and simulated spectrum). The PROFFIT algorithm is suitable to analyze spectra recorded from nadir viewing satellites, for example the Infrared Atmospheric Sounding Interferometer (IASI, Wiegele et al., 2014). For retrievals following the NDACC-IRWG guidelines, the HITRAN line list from 2008 in its original form is used (Rothman et al., 2009). For H<sub>2</sub>O and HDO, the updated HITRAN 2009 line list is applied. Traditionally, the analysis of solar absorption spectra using the NDACC methodology relies on narrow spectral fitting regions, typically a couple of tenths up to several wavenumbers wide. The spectral window atlas edited by Meier et al. (2004) provides a comprehensive collection of spectral windows as used for the analysis of MIR spectra. An excerpt of several analyzed spectral windows used within the NDACC is summarized in Table 3.4.

In contrast to TCCON, the official data products provided by NDACC are vertical trace gas profiles instead of column averaged DMFs. However, total columns can be obtained from the integration of the retrieved vertical profile. Most of the NDACC sites do not operate an InGaAs detector which has access to the 7885 cm<sup>-1</sup> O<sub>2</sub> band in the NIR. However, DMFs can be calculated by utilizing the ground pressure and H<sub>2</sub>O total column to determine C<sub>dryair</sub> to calculate DMFs. However, the Karlsruhe FTIR instrument is currently the only instrument which can provide DMFs of gases in the MIR using spectroscopic O<sub>2</sub> measurements due to the simultaneous recording of MIR and NIR spectra. Also in contrast to TCCON, no post-processing routine is applied to the retrieval results and therefore no air mass correction or calibration to any in situ measurements is implemented in the retrieval post-processing routine.

gas		spectral window <sup>a</sup>	
target	interfering	center	width
O <sub>3</sub>	H <sub>2</sub> O, CO <sub>2</sub> , C <sub>2</sub> H <sub>4</sub>	1002.50	5.00
CH <sub>4</sub>	HDO, CO <sub>2</sub>	2614.55	1.70
CH <sub>4</sub>	HDO, N <sub>2</sub> O	2835.65	0.30
CH <sub>4</sub>	HDO, NO <sub>2</sub> , H <sub>2</sub> O	2921.30	0.60
N <sub>2</sub> O	H <sub>2</sub> O, CO <sub>2</sub> , O <sub>3</sub> , N <sub>2</sub> O, CH <sub>4</sub>	2481.95	1.30
CO	O <sub>3</sub> , CO <sub>2</sub> , OCS	2057.85	0.30
CO	O <sub>3</sub> , CO <sub>2</sub> , OCS	2069.66	0.20
CO	O <sub>3</sub> , CO <sub>2</sub> , N <sub>2</sub> O, H <sub>2</sub> O	2158.30	1.65
HF	H <sub>2</sub> O, HDO, CH <sub>4</sub>	4038.95	0.32
HCl	O <sub>3</sub> , HDO	2727.78	0.10
HCl	N <sub>2</sub> O, O <sub>3</sub>	2775.75	0.10
HCl	O <sub>3</sub> , CH <sub>4</sub> , NO <sub>2</sub>	2925.90	0.20
HNO <sub>3</sub>	H <sub>2</sub> O	868.52	2.95
C <sub>2</sub> H <sub>6</sub>	H <sub>2</sub> O, O <sub>3</sub> , CH <sub>4</sub>	2976.81	0.30
C <sub>2</sub> H <sub>6</sub>	H <sub>2</sub> O, O <sub>3</sub> , CH <sub>4</sub>	2984.9	0.35
HCN	H <sub>2</sub> O, C <sub>2</sub> H <sub>2</sub>	3268.22	0.35
HCN	H <sub>2</sub> O, CO <sub>2</sub> , C <sub>2</sub> H <sub>2</sub>	3287.22	0.25
HCN	H <sub>2</sub> O	3299.5	0.20
ClONO <sub>2</sub>	H <sub>2</sub> O	780.22	0.25

a: given in cm<sup>-1</sup>

**Table 3.4:** Excerpt of various NDACC target gases with corresponding interfering species and spectral windows. Spectral windows containing solar absorption lines of NO, NO<sub>2</sub>, and OCS are not listed, but are declared as official NDACC target gases. Measurements of O<sub>3</sub> at 1002.50 cm<sup>-1</sup> are not performed in Karlsruhe.

### 3.3 Discussion of error sources

Measurements of total column abundances of trace gases in the atmosphere are subject to a variety of restrictions of the remote-sensing technique. Several sources of uncertainty have to be taken into account which impact the accuracy of retrieved abundances from solar absorption spectra. Some errors are considered as systematic (e.g. spectroscopic parameters, detector nonlinearity, instrumental changes over time like ILS drifts) while others are of statistical behaviour (e.g. spectral noise). This section aims to give an brief overview of several sources of uncertainty which affect retrieved total column abundances.

#### 3.3.1 Spectral noise

Errors due to solar spectral photon noise are in general small for instruments with a direct solar viewing geometry. Moreover, most of the spectral windows considered by the NDACC and TCCON retrieval strategies contain strong spectral absorption lines. Spectral noise has a liberal effect on retrieved column abundances since it causes no significant bias. Assuming a retrieval strategy which performs a scaling retrieval, the spectral noise error is estimated via:

$$\epsilon_n = \frac{\sigma}{S\sqrt{N}} \quad (3.1)$$

Here,  $S$  represents the line intensity of the observed spectral absorption line,  $\sigma$  the standard deviation of the spectral noise and  $N$  the number of independent spectral grid points within the half width of the spectral line (Hase, 2000). The error which affects the retrieved total column is of the order of 0.03 % for CO<sub>2</sub> (Wunch et al., 2011; Dohe, 2013). Moreover, the signal-to-noise ratio (SNR) for a single spectrum (75 sec acquisition) recorded at 45 cm OPD<sub>max</sub> is approximately 750 : 1 in the region of 5000 cm<sup>-1</sup>.

#### 3.3.2 Detector nonlinearity

Detectors or electronic devices like pre-amplifier can have a non-linear frequency response and might cause zero-level offsets in the measured spectra (Abrams et al., 1994). Such offsets affect retrieved total columns since the line intensities in the spectra are not correct any more. For example, absorption lines which are strongly saturated in the atmosphere do not have a transmission of zero at the line centre. Therefore, intensities of all lines in the same spectral window are incorrectly calculated by the forward model. The induced error can be estimated as:

$$\epsilon_l = \frac{1}{1 - \Delta S/S} \quad (3.2)$$

Here,  $\Delta^S/s$  determines the offset in relation to the continuum (Hase, 2000). As described in the previous sections, the Karlsruhe instruments operates an InSb and an InGaAs detector to cover the full spectral range from 1900 to 11 000  $\text{cm}^{-1}$ . Both detectors are sufficiently linear that no offset correction has to be applied to the spectra and more importantly,  $\epsilon_l$  can be neglected for the Karlsruhe data set.

### 3.3.3 Pointing offset

Pointing offsets might cause errors in the assumed airmass which can be biased into retrieved total columns. Gisi et al. (2011) showed that for a tracking range from 0 to 80°, the airmass changes by up to 9.6 % per degree solar zenith angle (SZA) change. Therefore, a precise solar tracking is essential to determine the airmass along the line of sight. To achieve a total column precision of 0.05 % with regards to pointing offsets, a minimum tracking precision of at least 19 arcsec has to be achieved (Gisi et al., 2011). The camera based solar tracker which is used to guide solar radiation into the Karlsruhe FTS has a tracking accuracy of  $(-0.3 \pm 0.3)$  arc sec which satisfies this requirement. Moreover, the calculated measurement duration deviates from the true measurement duration since typically two or more interferograms are averaged for NDACC- and TCCON-style measurements. Such timing errors might cause an additional error in the retrieved total column (Gisi et al., 2011). Pointing errors can also cause systematic residuals in spectral fits due to Doppler-shifted solar lines and might lead to an error up to 0.05 % of the retrieved total column for small SZA of the order of 20° (Wunch et al., 2011).

### 3.3.4 A priori temperature

A good knowledge of a priori information is desirable to reduce inaccuracy of retrieved total columns. Analyzed absorption lines or entire absorption bands might be highly dependent on the temperature. Therefore, incorrect temperature profiles can induce errors in retrieved abundances. For the analyses of MIR spectra using PROFFIT, temperature profiles with intraday variability are used based on eight individual temperature profiles (see Sect. 3.2.2).

For the analysis of TCCON-style NIR spectra, the temperature profile is provided by the NCEP (Kalnay et al., 1996), which provides temperature values from the surface up to 45 km. For higher altitudes, the temperature profile is extrapolated using the US standard atmosphere (NOAA, 1976). A single profile is generated per day from the 6 hourly NCEP/NCAR data. One single temperature profile is used for TCCON retrievals, interpolated to local noon. The TCCON mainly uses spectral windows containing absorption bands with low temperature sensitivity, thus, the error induced due to systematic negligence

of intraday variable temperature profiles during a day is less than 0.1 % (Wunch et al., 2011).

#### 3.3.5 A priori pressure

Similar to the a priori temperature, the retrieval results are sensitive to the prior knowledge of the pressure profile during the time of a measurement. For both retrieval strategies in the MIR and NIR, surface pressure measurements are obtained from instruments installed at the Karlsruhe tall tower. Ten minute means of the surface pressure are obtained from instruments installed at the Karlsruhe tall tower and are used as auxiliary data. Wunch et al. (2011) showed that a change of 1 hPa in the surface pressure induces an error of about 0.04 % in the retrieved column. The retrieval algorithm GFIT uses the measured surface pressure to calculate a site pressure altitude for each recorded spectrum. This altitude deviates from the true site altitude by up to 0.1 km mainly because of errors in the pressure-temperature model (Wunch et al., 2011). For TCCON, it was empirically found that using the deviating site pressure altitude and a correct surface pressure leads to accurate results for gases of interest whose volume mixing ratio (VMR) profile can be considered as fairly constant in the troposphere (e.g. CO<sub>2</sub>, O<sub>2</sub>). Moreover, investigations by Gisi (2012) indicated that pressure (and temperature) profiles with intraday variability reduce the error in the intraday variability of the O<sub>2</sub> total column from 2 % to 0.1 %.

#### 3.3.6 Spectroscopic parameters

The spectroscopic line list parameters used for the NDACC retrieval strategy in the MIR is based on the HITRAN 2008 line list (Rothman et al., 2009). TCCON retrievals are based roughly on HITRAN 2012 (Rothman et al., 2013). The HITRAN spectroscopic line list database provides uncertainty codes for six parameters including line positions, air pressure induced line shifts, intensities, the half-width for self- and air-broadening, and temperature dependence. Nevertheless, these spectroscopic parameters might still contain systematic biases (currently approximately 1 %, Wunch et al., 2011). Therefore, TCCON retrieval results are tied to the WMO scale via aircraft campaigns to account for these biases as described in Sect. 3.2.1. The NDACC retrieval strategy does not correct such systematic biases. Moreover, empirical changes are applied to the spectroscopic line parameters. As described in Sect. 3.2.1, preliminary empirical changes are also applied to CH<sub>4</sub> absorption lines in the MIR region which are used in the MIR NDACC retrieval strategy.

### 3.3.7 Calculation of column averaged dry-air mole fractions

The necessity for a sufficiently high precision of retrieved total columns desires a minimization of potential error sources. For the trace gas CO<sub>2</sub>, a total column accuracy of at least 0.1 % is required to identify a CO<sub>2</sub> sink of about 1 GtC year<sup>-1</sup> in the northern hemisphere (Olsen and Randerson, 2004). Therefore, high effort is undertaken within both ground-based networks to minimize contributions of error sources to retrieved results, for example the regular monitoring of ILS measurements or calibrations against the WMO scale. Several of the aforementioned error sources can be minimized by converting the retrieved total columns into column averaged dry-air mole fractions (DMFs) using spectroscopically retrieved total columns of O<sub>2</sub>.

To calculate DMFs of a particular gas, namely  $X_{\text{gas}}$ , the retrieved total column amount of a gas ( $C_{\text{gas}}$ ) is divided by the total column of dry-air ( $C_{\text{dryair}}$ ):

$$X_{\text{gas}} = \frac{C_{\text{gas}}}{C_{\text{dryair}}} \quad (3.3)$$

For TCCON,  $C_{\text{dryair}}$  is determined via the total column of O<sub>2</sub> ( $C_{\text{O}_2}$ ) retrieved from the 7885 cm<sup>-1</sup> absorption band in the NIR divided by an assumed dry-air mole fraction of O<sub>2</sub> (0.2095):

$$C_{\text{dryair}} = \frac{C_{\text{O}_2}}{0.2095} \quad (3.4)$$

The advantage of this approach is that errors which are common to the gas of interest and O<sub>2</sub> are minimized in the column ratio, e.g. pointing offsets or zero-level offsets due to a nonlinear response of the electronics (Washenfelder et al., 2006). Moreover, the division removes variations due to surface pressure changes which also improves a direct comparison of retrieved results from different days or sites. Using the O<sub>2</sub> 7885 cm<sup>-1</sup> band also minimizes the effect of errors in retrieving the airmass for a particular spectrum because, again, this affects O<sub>2</sub> and the gas of interest in the same way. Therefore, within the TCCON, the total column of O<sub>2</sub> is used as an internal network wide standard, since the mixing ratio of O<sub>2</sub> is fairly constant in the homosphere and well known.

In general, standard NDACC instruments which only measure in the MIR do not have access to the O<sub>2</sub> absorption band in the NIR. Instead,  $C_{\text{dryair}}$  can be calculated on the basis of the ground pressure  $p_g$  and the total column of water vapor ( $C_{\text{H}_2\text{O}}$ ):

$$C_{\text{dryair}} = \frac{p_g}{g \cdot m_{\text{dryair}}} - \frac{C_{\text{H}_2\text{O}} \cdot m_{\text{H}_2\text{O}}}{m_{\text{dryair}}} \quad (3.5)$$

Here,  $g$  represents the surface gravitational acceleration whereas  $m_{\text{dryair}}$  and  $m_{\text{H}_2\text{O}}$  represent the molecular masses of dry-air and water vapor, respectively. However, applying Eq. (3.5) does not minimize errors which are common to the gas of interest and  $\text{O}_2$ . It is even more likely that errors are introduced due to uncertainties in the retrieval of the  $\text{H}_2\text{O}$  total column. However, due to the particular optical setup of the Karlsruhe FTS and the simultaneous recording of spectra in the MIR and NIR, the total column of  $\text{O}_2$  retrieved from the  $7885\text{ cm}^{-1}$  absorption band in the NIR can also be used to calculate DMFs for gases typically retrieved within the NDACC in the MIR spectral region. Therefore, for Karlsruhe data retrieved from the MIR spectral region, the division of the total column of the gas of interest by the total column of  $\text{O}_2$  also minimizes measurement and instrumental errors which are common to both gases and improves the precision of the measurement. This is an superior approach compared to standard NDACC instruments which in general do not have access to the oxygen absorption band located in the NIR. This approach also improves the comparability between data sets provided by both networks which is a valuable improvement when a harmonization between both data sets is targeted. For the retrieval of  $\text{O}_2$ , both retrieval algorithms, GFIT and PROFFIT, scale an altitude independent a priori VMR profile using the spectral window ranging from  $7765.0$  to  $8005\text{ cm}^{-1}$ . A more detailed investigation of  $\text{O}_2$  retrieved by both algorithms is provided in Sect. 5.4.

#### 3.3.8 Background continuum variations

Other possible error sources are variations in the background continuum of the measured spectrum. Continuum variations, the so called continuum curvatures, can be of atmospheric origin, e.g. due to collision induced absorption (CIA) as observed in the  $\text{O}_2$  spectral window centered at  $7885\text{ cm}^{-1}$  (Spiering and van der Zande, 2012). However, instrumental features can also give rise to background continuum variations in recorded spectra due to, e.g. spectral characteristics of a beamsplitter, the frequency dependent coating of mirrors, and optical filters with a wavy bandpass (Kiel et al., 2016b). Also, unaccounted SBFs and changes in the spectral response of operated detectors can induce continuum curvatures. These curvatures can affect retrieval results by airmass-dependent artefacts which can be aliased into the seasonal cycle of long-term monitored time series. TCCON and NDACC partners typically use very similar optical components and detectors with well-known properties to minimize continuum curvature in the measured spectra and thus maintain the best site-to-site precision and accuracy possible.

The Karlsruhe system, however, has a significant different optical setup, designed to allow for automated MIR NDACC and TCCON measurements to be made from the same instrument. As shown in the next sections, this unique optical setup induces significant larger variations in the background continuum than standard instrumental setups as used within the TCCON

and NDACC. The combined installation of the dichroic beamsplitter and several optical filters mounted in front of the InSb diode in the Karlsruhe setup induces variations in the continuum which are not true atmospheric signals. This behaviour is a potential error source in the retrieval of gas abundances and therefore requires special attention and is discussed in more detail in the following.

### 3.4 Impact of the Karlsruhe instrumental setup on background continuum variations

To qualitatively examine the impact of the unique Karlsruhe optical setup on measured spectra, one typical TCCON-style spectrum recorded in Karlsruhe (see Fig. 3.6, upper right panel) is compared to a reference spectrum recorded by an FTS which satisfies the instrumental requirements prescribed by the TCCON. The reference spectrum is obtained from the FTS site in Park Falls (Wisconsin, USA) which is part of TCCON since 2004. A detailed description of the instrumentation operated at this site is given in Washenfelder et al. (2006). This reference site covers the full spectral range from 3900 to 11 000  $\text{cm}^{-1}$ , which is necessary to measure all TCCON target gases by the operation of one single wide band InGaAs detector. A typical Park Falls spectrum is also shown in Fig. 3.6 (upper left panel).

Regarding the spectral region covered by the InSb detector (3900 to 5250  $\text{cm}^{-1}$ ), there are clear differences between the shapes of the spectra measured by the Karlsruhe instrument (see Fig. 3.6, center right) and the Park Falls instrument (see Fig. 3.6, center left). The Karlsruhe spectrum contains an oscillating overall envelope which is not present in standard TCCON spectra. These broadband oscillations significantly affect the Karlsruhe spectrum in the 4500 to 5250  $\text{cm}^{-1}$  region. Another major difference is the detector response in the lower wavenumber region between 3900 and 4500  $\text{cm}^{-1}$ . While the amplitude of the detected signal of the extended InGaAs diode (as used in Park Falls) decreases with decreasing wavenumbers, the InSb diode signal remains at a constant level with a high signal-to-noise ratio. These broadband oscillations are of such an obvious manner, that different atmospheric conditions at two locally apart sites can be excluded as their origins (see Sect. 3.5). Retrieved TCCON gases within this spectral region are CO (center wavenumber (cw) in  $\text{cm}^{-1}$ : 4233.0, 4290.4),  $\text{N}_2\text{O}$  (cw: 4395.2, 4430.1, 4719.5), HF (cw: 4038.95) and several  $\text{H}_2\text{O}$  and HDO narrow spectral windows.

Smaller but significant differences in the continuum are also present in the covered range by the InGaAs detector (see Fig. 3.6, lower left and right panel). From 5250 to 7500  $\text{cm}^{-1}$ ,

the Karlsruhe signal remains high forming a plateau region with narrowband oscillations whereas the Park Falls signal decreases smoothly with increasing wavenumbers. However, the flat plateau in the Karlsruhe signal might be superior for compensations of nonlinear artefacts in the spectrum. This spectral region contains wide spectral windows of the TCCON target gases  $\text{CO}_2$  and  $\text{CH}_4$ . Moreover, the region from 7500 to 11 000  $\text{cm}^{-1}$  shows clear differences. Whereas the differing signal responses in the 9500 to 10 000  $\text{cm}^{-1}$  do not affect typical spectral windows used by the TCCON, the region from 7500 to 9500  $\text{cm}^{-1}$  contains small differences in the background continuum which are of special concern since the  $\text{O}_2$  spectral window at 7885  $\text{cm}^{-1}$ , which is used to calculate DMFs of all TCCON target gases, lies in this region.

Variations of the background continuum are also identified in NDACC-style spectra recorded in the MIR spectral region. As described in Sect. 3.1.2, the InSb diode is typically used in conjunction with five optical filters which define narrow absorption bands covering different spectral ranges (see Table 3.1). For typical NDACC-style measurements, an automated filter-wheel containing the five different narrowband filters is shuffled resulting in five independent measured spectra for one complete measurement series. Karlsruhe MIR spectra are compared to NDACC MIR reference spectra recorded at Izaña, Tenerife Island, Spain. The Izaña FTIR site is part of the NDACC since 1999 and measurements are also acquired with a Bruker IFS 125HR instrument with an optical setup which is quite typical for an NDACC instrument. Figure 3.7 shows solar absorption spectra recorded by the Karlsruhe instrument and the Izaña instrument for the narrow band filters 1 through 5. Differences between the continua of the recorded spectra are present in all five filter regions. The largest differences in the background continuum are determined for filter 1 (see Fig. 3.7, upper panel). In Karlsruhe, filter 1 covers the entire 3950 to 5250  $\text{cm}^{-1}$  spectral range to satisfy TCCON recommendations whereas filter 1 in Izaña transmits only from 3950 to 4300  $\text{cm}^{-1}$ . Here again, the overlapping region from 3950 to 4300  $\text{cm}^{-1}$ , which is transmitted by both filters, indicates differences in the overall shape of the spectrum. In the Karlsruhe spectrum (see Fig. 3.7, upper right panel), the signal increases with increasing wavenumbers as already seen in the comparison between the Karlsruhe and Park Falls instrument. On the contrary, the signal in the Izaña spectrum increases with increasing wavenumbers until a plateau is reached where the signal remains stable. The signal starts to decrease for larger wavenumbers. In this spectral region, a spectral window containing HF absorption lines is analyzed within the NDACC retrieval routine. The spectral region beyond 4300  $\text{cm}^{-1}$  is not considered for standard NDACC retrievals and is only covered by the Karlsruhe filter to satisfy TCCON requirements.

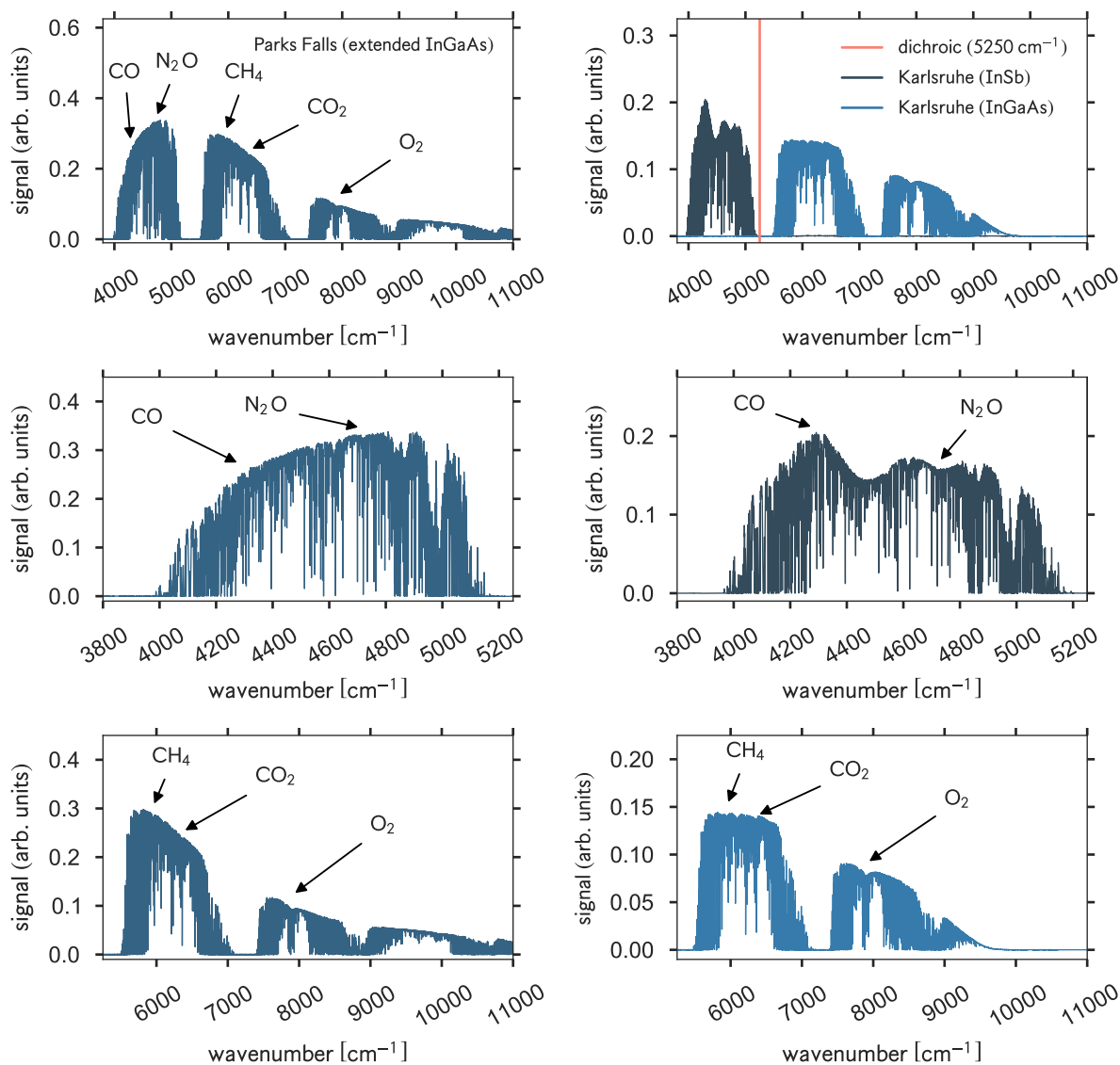
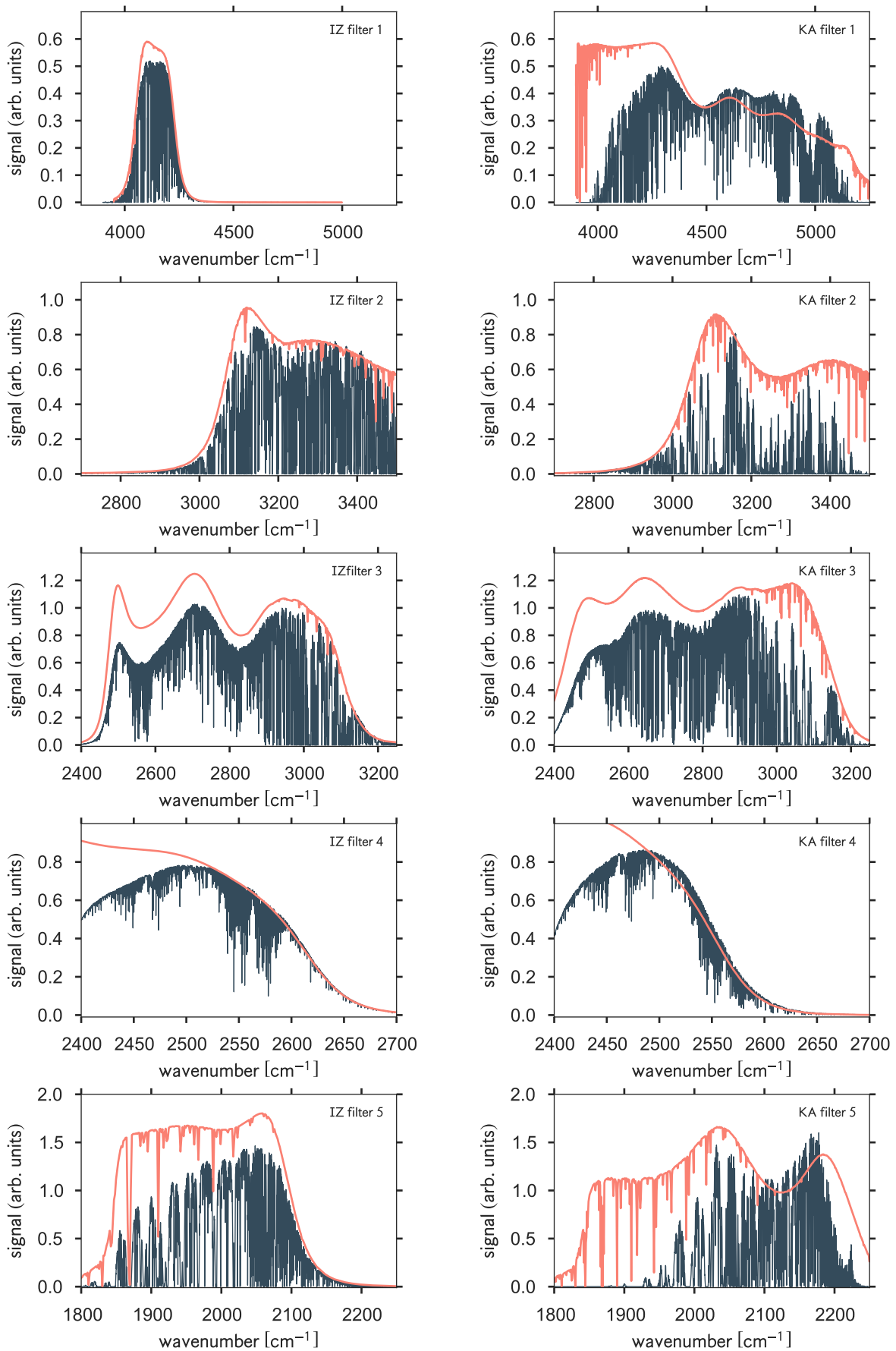


**Figure 3.6:** Spectra recorded by the Park Falls instrument (left column) and by the Karlsruhe FTS using the InSb and InGaAs detector to cover the entire TCCON spectral range from 3800 to 11 000  $\text{cm}^{-1}$  (right column). A comparison between the two separated spectral regions covered by the two different detectors in the Karlsruhe instrument (InSb: 3800 to 5250  $\text{cm}^{-1}$ , InGaAs: 5250 to 11 000  $\text{cm}^{-1}$ ) is given in the center and lower panel, respectively. Spectral windows for TCCON target gases are indicated in the spectra.

**Figure 3.7 (facing page):** NDACC-style recorded spectra in Izaña (left column) and Karlsruhe (right column) for the five different NDACC filters (every row indicates one filter) as given in Table 3.1. To rule out that different atmospheric conditions induce variations in the overall shape of the spectra, low resolution spectra using a black body cavity as a source are shown in orange (see Sect. 3.5).

### 3.4 Impact of the Karlsruhe instrumental setup on background continuum variations



Moreover, the spectral region from 1800 to 2200  $\text{cm}^{-1}$  which is covered by filter 5 also shows clear differences around 2100  $\text{cm}^{-1}$  between both background continua (see Fig. 3.7, fifth panel). In the Izaña spectrum, the signal shows a local maximum around 2050  $\text{cm}^{-1}$ , preceded by a plateau for smaller wavenumbers. The signal in the Karlsruhe spectrum shows an broad oscillating behaviour in this spectral region. The spectral window which is analyzed in the wavenumber region covered by filter 5 contains absorption lines of, e.g. CO. Moreover, there are also variations and differences in the background continuum when comparing the Karlsruhe and Izaña spectrum for filter 2 through filter 5. Analyzed spectral windows in these filter bands contain absorption lines of  $\text{CH}_4$ ,  $\text{H}_2\text{O}$ , HCl,  $\text{N}_2\text{O}$ , NO, and OCS.

In general, variations in the background continuum seem to be larger for spectra recorded by the InSb detector when Karlsruhe spectra are compared to reference spectra recorded by standard NDACC and TCCON instruments. This effect is explained by the fact, that in addition to the optical response curve of the dichroic, the optical response curve of the single filters also contributes to the total response curve which is detected at the InSb detector. This superposition of the response curves induces larger variation in the background continuum of spectra measured by the InSb detector than recorded by the InGaAs diode. Moreover, the response curve for the transmission and reflection of the dichroic for MIR and NIR radiation might differ and has a larger impact on reflected than transmitted radiation.

### **3.5 Impact of the background continuum variations on spectral fits in the NIR and MIR**

As discussed in Sect. 3.3.8, a varying continuum background is a potential error source in the retrieval of gas abundances and might affect the calculated total columns and DMFs. Not sufficiently well modelled background continua in the forward model of the retrieval algorithms can affect retrieval results by airmass dependent artefacts or biases. Spectral residuals can serve as an indicator for an inadequate treatment of background continuum variations by the retrieval algorithm. Typically, residuals should have no structure, and consist only of the random noise associated with the signal-to-noise ratio of the measured spectrum. Nevertheless, as seen from comparisons between Karlsruhe spectra and spectra recorded by standard NDACC and TCCON instruments, the continuum curvatures in MIR and NIR spectra recorded in Karlsruhe show a varying and oscillating behaviour which affects spectral fits and residuals in the affected regions, especially for wide spectral windows which encompass a whole molecular band of the target gas as used within the TCCON.

Moreover, a standardized retrieval routine as used within the TCCON is not favorable for sites which operate instruments with non-standard optical setups.

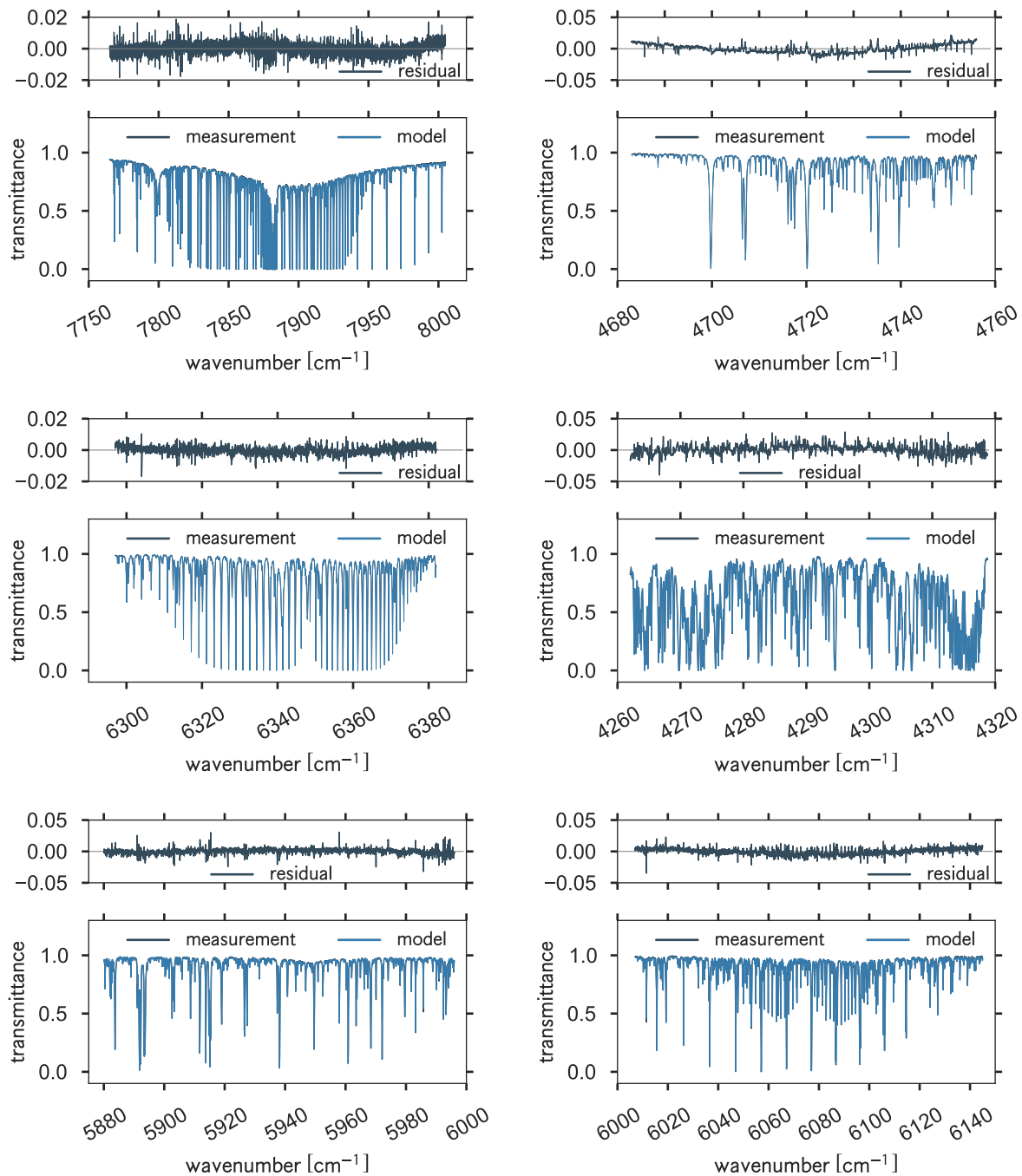


**Figure 3.8:** Spectral fits for the spectral windows whose residuals are affected by broadband variations (obtained from one typical Karlsruhe measurement). Shown is the measured atmospheric spectrum, the model calculation, and the residual is depicted in the upper part of the particular panel. Upper left,  $\text{O}_2$  (cw: 7885.0); upper right,  $\text{N}_2\text{O}$  (cw: 5719.5); center left:  $\text{CO}_2$  (cw: 6339.5); center right:  $\text{CO}$  (cw: 4290.4); lower left:  $\text{CH}_4$  (cw: 5938.0); lower right:  $\text{CH}_4$  (cw: 6076.0).

Following the standard TCCON retrieval strategy which, by default, fits only a scalar continuum level and linear continuum tilt, spectral residuals for several fitted spectral windows show significant broad varying and oscillating structures. Affected are spectral fits of several TCCON target gases, namely  $\text{CO}_2$ ,  $\text{CH}_4$ ,  $\text{CO}$ ,  $\text{N}_2\text{O}$ , and  $\text{O}_2$ . Gas abundances of these gases are retrieved from wide spectral windows up to  $240\text{ cm}^{-1}$  wide (see Table 3.2). Figure 3.8 shows spectral fits and residuals for these fitted spectral windows. The residuals for  $\text{CO}_2$ ,  $\text{N}_2\text{O}$ ,  $\text{CH}_4$  and  $\text{CO}$  have a single extremum (for the spectral windows with center wavenumbers (cw) at  $6339.5$ ,  $4720$ ,  $6076.0$ , and  $4290.0\text{ cm}^{-1}$ ). Moreover, the residual for  $\text{CH}_4$  (at  $5938\text{ cm}^{-1}$ ) has the shape of a higher order polynomial. For the  $\text{O}_2$  spectral window at  $7885\text{ cm}^{-1}$ , there is an underlying continuum absorption caused by collision-induced absorption (CIA). Although only the discrete  $\text{O}_2$  absorption lines in the  $7885\text{ cm}^{-1}$  range are used to calculate the  $\text{O}_2$  total column, an CIA continuum is modelled in the retrieval procedure to fit the continuum. However, also the residual of the  $\text{O}_2$  spectral windows follows the shape of a higher order polynomial. In contrast, for spectral fits of narrower spectral windows as used for, e.g.  $\text{H}_2\text{O}$  and  $\text{HDO}$ , no comparable broad structures in the residuals are identified. This is mainly caused by the choice of the narrow width of the spectral window, where potential curvatures are not detectable any more.

As claimed previously, the observed continuum variations in the residuals are related to the choice of optical filters and the dichroic, and are not of atmospheric origin. To demonstrate this, laboratory measurements using a black body cavity as a source are analyzed. Black body cavity measurements are generally free of atmospheric spectral signatures and spectral fits of such spectra can be used as an indicator whether variations in the spectral residuals are of atmospheric or instrumental origin. A typical black body cavity spectrum recorded at Karlsruhe is depicted in Fig. 3.9. The black body cavity was used at  $1000\text{ }^\circ\text{C}$  as a source. The Karlsruhe FTIR instrument is not evacuated, therefore Karlsruhe cavity measurements contain some atmospheric absorption lines, mainly from  $\text{H}_2\text{O}$  in the laboratory air (see Fig.

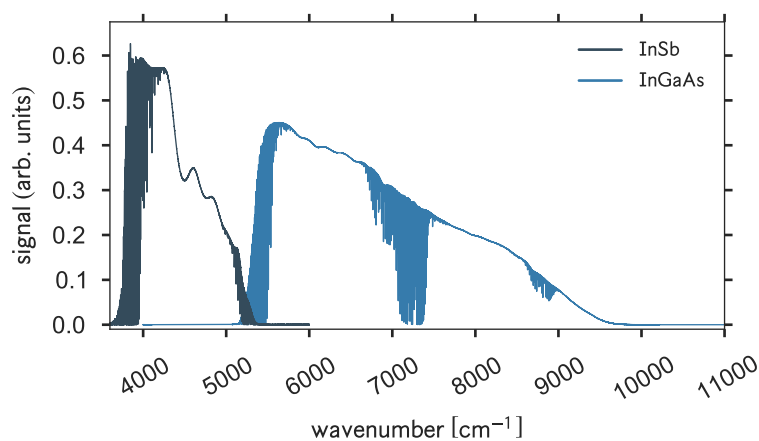


**Figure 3.9:** Low resolution Karlsruhe laboratory spectrum recorded by the InSb and InGaAs diode using a black body cavity ( $1000\text{ }^\circ\text{C}$ ) as source.

3.9). The identical TCCON retrieval setup (as applied for atmospheric measurements) is applied when analyzing the black body spectrum. Residuals of spectral fits from retrievals using the laboratory spectrum have a similar shape to residuals of the atmospheric measurements. Figure 3.10 shows spectral fits and residuals for all spectral windows whose residuals are affected by continuum variations when analyzing atmospheric spectra. Similar

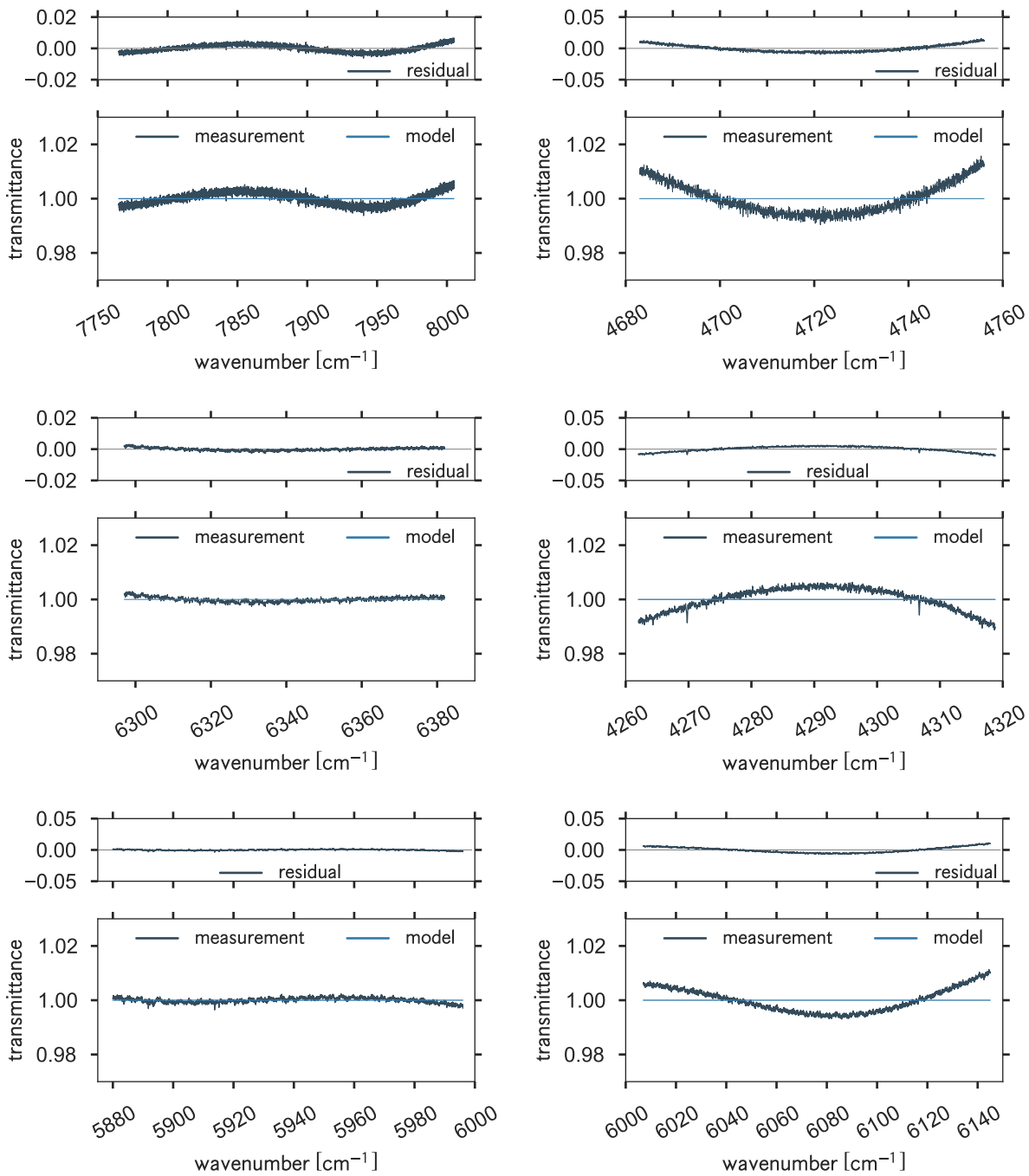


**Figure 3.10:** Same as Fig. 3.8 for Karlsruhe laboratory spectra using a black body cavity as source.

to the atmospheric spectra, the residuals from measurements using the black body cavity as source have a similar shape to residuals of the previously analyzed atmospheric measurements. For example, for  $\text{O}_2$ , residuals follow the shape of a higher-order polynomial as seen for atmospheric measurements (see Fig. 3.10, upper left). Residuals within the  $\text{N}_2\text{O}$  spectral range follow the same parabolic shape as for atmospheric measurements. This holds for all affected spectral windows (see Fig. 3.10, upper right) and proves that broadband variations in the residuals in the TCCON retrieval are due to instrumental features of the particular setup of the Karlsruhe FTIR spectrometer and not true atmospheric signals.

For the analysis of NDACC-style spectra recorded in the MIR, the PROFFIT retrieval algorithm is used to retrieve total column amounts of target gases by fitting quite narrow spectral windows, the so called microwindows. Narrow spectral windows are not expected to identify atypical shapes in the residuals of the fits since the analysis of TCCON spectral fits showed that the induced variations are typically broadband oscillations.

Typical widths of microwindows in the NDACC retrieval strategy are below one wavenumber wide, too narrow to identify potential broadband variations of the continuum background which are not sufficiently well modeled by the forward model. The widest microwindow in the standard NDACC retrieval routine is about  $6\text{ cm}^{-1}$  wide and includes spectral lines of  $\text{O}_3$ . This spectral range is not covered by the Karlsruhe instrument due to the lack of an MCT detector. One of the widest microwindows analyzed from Karlsruhe MIR spectra is  $5\text{ cm}^{-1}$  wide containing absorption lines of  $\text{H}_2\text{O}$ . Figure 3.11 shows a spectral fit and residual for that NDACC microwindow. In contrast to the wide spectral windows as used by TCCON, no atypical behaviour of the residuals is identified which also holds for all other spectral fits of the NDACC gases of interest.

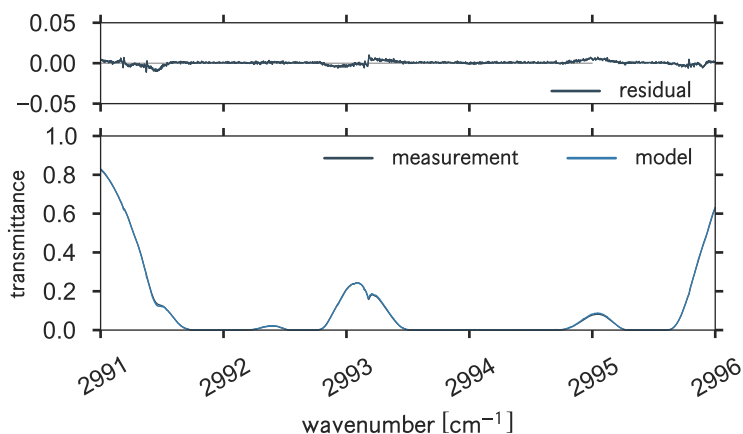


**Figure 3.11:** Spectral fit of a  $5\text{ cm}^{-1}$  wide microwindow used within the NDACC to retrieve total columns of  $\text{H}_2\text{O}$ . No broad variations or oscillations are identified in the residual. Variations in the residuals are mainly due to spectroscopic inadequacies.

Nonetheless, in contrast to the GGG retrieval algorithm which only fits a continuum level and continuum tilt, the PROFFIT retrieval approach includes a fit of the empirical background based on a user-selectable number of baseline points which are evenly distributed across the fitted spectral window. A single point is equivalent to a scaling factor, two points are used to create a linear fit, three or more points create a smooth background, very similar to a cubic spline fit through these guiding points (Dohe, 2013; Kiel et al., 2016b). This choice has been made because each associated derivative is spectrally localized, whereas the fitting of parameters, shaping a global polynomial fit across the spectral window, results in derivatives which are all strongly interwoven. Therefore, even for wide spectral windows as the O<sub>2</sub> spectral window, which is also analyzed by the PROFFIT algorithm in the later part of this work, no broad variations in the residuals are expected. This is demonstrated in Sect. 4.5.

# 4 Improvement of retrievals of gas abundances from TCCON measurements

In the previous chapter it was shown that instrumental features of the Karlsruhe FTS in combination with the deficiency of the uniform TCCON retrieval strategy to properly fit the background continuum, lead to variations in residuals of several spectral windows. In contrast, the NDACC retrieval strategy traditionally uses quite narrow microwindows where no variations are identified in its residuals. The broad spectral windows used by TCCON require special attention with respect to the background continuum, especially for the non-standard optical setup of the Karlsruhe FTS. The uniform TCCON retrieval strategy requires modifications which have to be specifically designed for the Karlsruhe data set. A modified retrieval approach for the analysis of Karlsruhe TCCON data is presented in this chapter. An intervention to the retrieval routine affects the retrieved DMFs and its airmass dependencies which are also subject of several investigations presented in the following sections. Furthermore, the consistency between data sets of the Karlsruhe and geographically nearby TCCON stations is tested after modifications to the uniform TCCON retrieval strategy are applied. The contents of this chapter are mainly based on Kiel et al. (2016b).

## 4.1 Fitting the background continuum

TCCON spectra are not radiometrically calibrated, therefore atmospheric spectra include the responses of the instrument in addition to the solar Planck function. This holds for spectra recorded at all sites affiliated with the network. However, as seen in the previous chapter, the instrumental response is particularly stronger pronounced in Karlsruhe spectra than for other TCCON instruments.

There are several options for an advanced treatment of the background continuum. As described later in Sect. 4.5, the PROFFIT retrieval algorithm, which is used in this work for the analysis of MIR spectra, includes a fit of the empirical background based on a

user-selectable number of baseline points which are evenly distributed across the fitted spectral window. Another option is to apply a black body cavity correction to atmospheric spectra. For that, atmospheric spectra are divided by a high signal-to-noise ratio, reduced-resolution ( $0.05 \text{ cm}^{-1}$ ) laboratory spectrum using a black body cavity operated at  $1000 \text{ }^\circ\text{C}$  as source. This ratioing eliminates broadband variations, caused by the optical elements, in the resulting calibrated atmospheric spectra. The main disadvantage of this method is that dividing an atmospheric spectrum by a cavity spectrum converts the white noise in the measured spectrum into non-white noise. The GGG forward model, however, assumes that the measured spectrum is only affected by white noise. This is likely a small effect in this case because the cavity spectra comprise many coadded spectra, significantly reducing its noise. Moreover, ratioing atmospheric spectra over black body cavity spectra for the retrieval routine involves a high expenditure of time and is not desirable as a uniform network wide retrieval strategy. In addition, only the minority of FTS sites affiliated with the TCCON measure laboratory spectra using a black body cavity as source on a regular base. Therefore, the following approach for the background continuum treatment is chosen.

To accommodate the unique setup of the Karlsruhe FTS, higher-order Legendre polynomials have been enabled in the TCCON retrieval algorithm to fit the background continuum. This continuum fit option is specifically meant to properly and robustly fit variations in the background continuum of a spectrum that are caused by instrumental features. This user-selectable option should not minimize spectroscopic errors which should be modeled separately (Wunch et al., 2011). This fitting option is not a standard parameter in the TCCON data processing within the GGG Suite. However, since all sites affiliated with the TCCON are obligated to use the conform GGG retrieval algorithm and strategy, this approach can be easily made available network wide. Its application can be performed without any further expense of additional measurements of black body cavity spectra. This approach can be applied at other TCCON sites when the change or replacement of optical components causes similar variations in spectra as observed in Karlsruhe.

In general, Legendre functions are solutions of the Legendre's differential equation which is a second-order ordinary differential equation of the form:

$$\frac{d}{dx} \left[ (1 - x^2) \frac{d}{dx} P_l(x) \right] + l(l + 1) P_l(x) = 0 \quad (4.1)$$

Equation (4.1) is a special case of the associated Legendre differential equation corresponding to the case  $m = 0$  when  $(-1)^m$  represents the Condon-Shortley phase as used in quantum mechanical literature (Abramowitz and Stegun, 1972). It has two linearly independent solutions, the Legendre function of the first kind and the Legendre function of the second

kind. For integer values of  $l$ , the Legendre function of the first kind becomes a polynomial, also called Legendre polynomial. For different orders  $l$ , it can be expressed by Rodrigue's formula (Rodriguez, 1840):

$$P_l(x) = \frac{1}{2^l l!} \frac{d^l}{dx^l} \left[ (x^2 - 1)^l \right], \quad l \in \mathbb{N}_0 \quad (4.2)$$

The Legendre polynomials for  $l = 0, 1, 2, \dots, 5$  are depicted in Fig. 4.1. These polynomials form a sequence of orthogonal polynomials. Therefore, Legendre polynomials make a fitting problem better posed leading to smaller condition numbers of the design matrix. The standard TCCON retrieval approach applies only fits of the orders  $l = 0$  and  $l = 1$  to the background continuum. In the following, the order of a Legendre polynomial fit is given by  $N = l + 1$ .

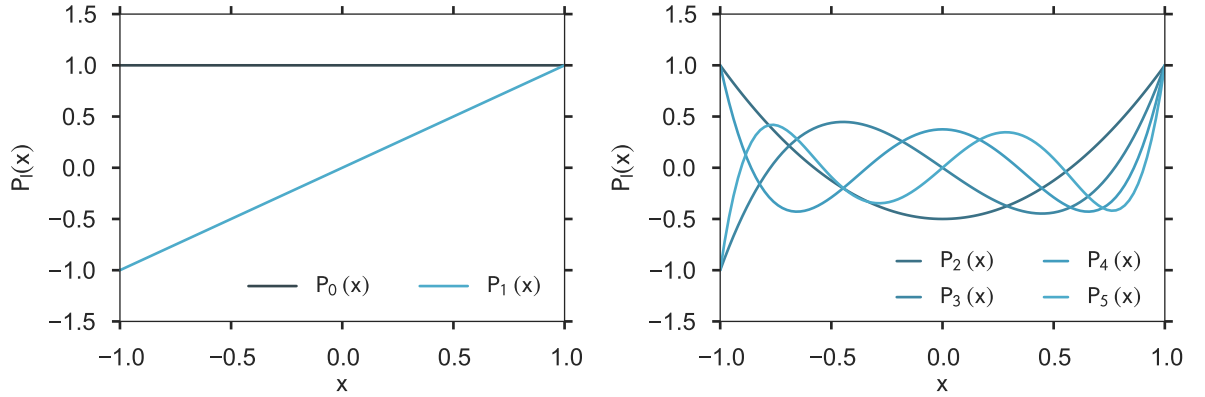


**Figure 4.1:** Illustration of the Legendre polynomials for the orders  $l = 0$  and  $l = 1$  which are fitted by default using the standard TCCON retrieval approach (left panel) and for the higher orders  $l = 2, \dots, 5$  (right panel).

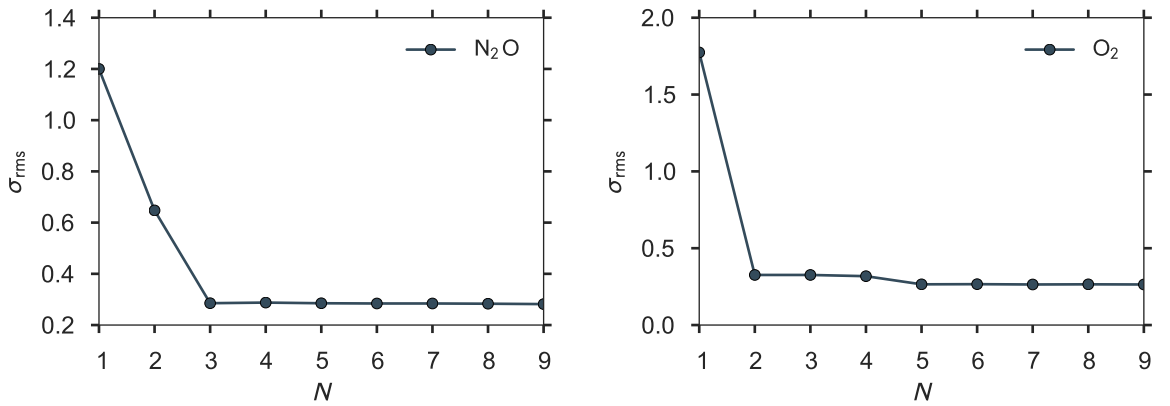


**Figure 4.2:** Left panel:  $\sigma_{\text{rms}}$  when different orders  $N$  of the Legendre polynomials are fitted to the background continuum for the  $\text{N}_2\text{O}$  and  $\text{O}_2$  spectral windows (right panel) using atmospheric spectra. A similar behaviour holds for black body cavity spectra.

Since black body cavity measurements are performed on a regular base in Karlsruhe, these laboratory spectra can be utilized to determine the order  $N$  for every affected spectral window individually which is needed to properly fit the background continuum in atmospheric spectra. Black body cavity measurements are free from atmospheric absorptions and basically reflect the instrumental response curve (see Sect. 3.5). To achieve the best fit in the continuum level, different polynomial orders are tested. It is expected, that the standard deviation of the quadratic mean ( $\sigma_{\text{rms}}$ ) for spectral fit residuals reaches a plateau if an order  $N$  is found that sufficiently well accounts for background continuum variations. For every affected spectral window, several orders  $N$  are tested. Figure 4.2 shows  $\sigma_{\text{rms}}$  as a function of the order  $N$  for the  $\text{N}_2\text{O}$  and  $\text{O}_2$  spectral window. For  $\text{N}_2\text{O}$ , a plateau is reached for  $N = 3$  and for  $\text{O}_2$  when  $N = 5$  is reached. In analogy,  $N$  is determined for all affected spectral windows. The corresponding spectral fits showing the residuals with reduced  $\sigma_{\text{rms}}$  are shown in Fig. 4.3.

The Karlsruhe FTIR instrument was initiated in 2009 and since the start of operation, three different narrow spectral filters were used in front of the InSb diode to perform TCCON-style measurements. Data discussed above is for the most recent filter, transmitting from 3800 to 5200  $\text{cm}^{-1}$ . Earlier filters differ basically by varying transmission ranges: filter 1a, used until 15 November 2011, transmitting from 3800 to 4500  $\text{cm}^{-1}$ ; filter 1b, used until 10 August 2012, transmitting from 3800 to 4600  $\text{cm}^{-1}$  and the most recent filter 1c transmitting from 3800 to 5250  $\text{cm}^{-1}$ . A depiction of the spectral region from 3800 to 5250  $\text{cm}^{-1}$  for the three different filters is given in Fig. 4.4. As expected, the different narrowband filters have different optical properties which affect the spectral fits of several spectral windows in a different way. Therefore, three slightly different retrieval approaches are applied for the three different time periods. Again, the same approach using black body cavity spectra to determine the polynomial order,  $N$ , for affected spectral windows for the different filters, is followed. In comparison to filter 1c, one additional spectral window is affected for filter 1b, namely  $\text{N}_2\text{O}$  (cw: 4395.2) and for filter 1c, two more spectral windows are affected, namely CO (cw: 4233.0) and  $\text{N}_2\text{O}$  (cw: 4330.1). In addition, the TCCON standard retrieval contains one spectral window in the 4700  $\text{cm}^{-1}$  range, namely  $\text{N}_2\text{O}$  (cw: 4719.5) which is not covered by the InSb diode using filter 1a and 1b. Therefore, this spectral window is omitted in the Karlsruhe TCCON GGG analysis. An overview of the empirically determined orders of the Legendre polynomials for all affected spectral windows is summarized in Table 4.1. Spectral windows which are not listed in Table 4.1 remain unchanged and do not need a special treatment with regard to the background continuum. For these unaffected spectral windows only a continuum tilt and continuum level is fitted to account for background continuum variations. Despite the improvement of the spectral fits, the fitting of the continuum background induces changes in the retrieved total columns and

their airmass dependencies. In the following sections, the impact of the continuum fitting on the airmass dependencies and on retrieved DMFs is analyzed in more detail.

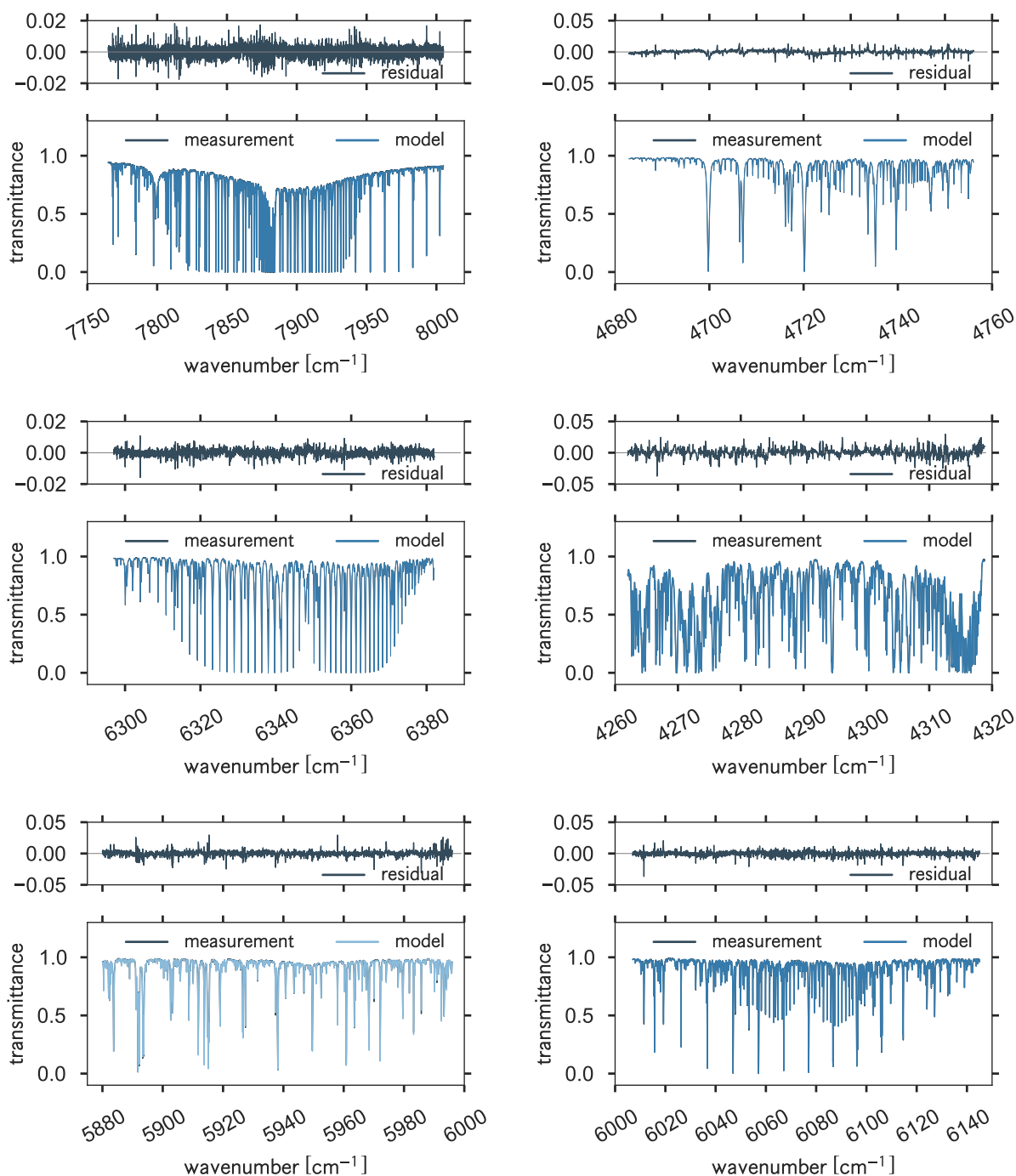


**Figure 4.3:** Spectral fits for one typical Karlsruhe spectrum using Legendre polynomials to fit the background continuum. Upper left,  $\text{O}_2$  (cw: 7885.0),  $N = 5$  was used for the background continuum fit; upper right,  $\text{N}_2\text{O}$  (cw: 5719.5,  $N = 3$ ); center left:  $\text{CO}_2$  (cw: 6339.5,  $N = 3$ ); center right:  $\text{CO}$  (cw: 4290.4,  $N = 4$ ); lower left:  $\text{CH}_4$  (cw: 5938.0,  $N = 4$ ); lower right:  $\text{CH}_4$  (cw: 6076.0,  $N = 5$ ). All of the spectral fits show reduced variations in the residuals.

applied order $N$ for Karlsruhe TCCON retrieval					
detector		InGaAs diode		InSb diode	
filter		Si filter	filter 1c	filter 1b	filter 1a
gas	center wavenumber <sup>a</sup>	19 Apr 2010– now	10 Aug 2012– now	22 Nov 2011– 10 Aug 2012	19 Apr 2010– 15 Nov 2011
CH <sub>4</sub>	5938.0	4			
CH <sub>4</sub>	6076.0	5			
CO <sub>2</sub>	6339.5	3			
CO	4233.0		2 <sup>b</sup>	2 <sup>b</sup>	3
CO	4290.4		4	3	4
N <sub>2</sub> O	4395.2		2 <sup>b</sup>	3	3
N <sub>2</sub> O	4430.1		2 <sup>b</sup>	2 <sup>b</sup>	3
N <sub>2</sub> O	4719.5		3	$\chi^c$	$\chi^c$
O <sub>2</sub>	7885.0	5			

<sup>a</sup> Given in  $\text{cm}^{-1}$ , <sup>b</sup> Corresponds to the standard TCCON GGG retrieval strategy where a continuum level and tilt is fitted by default, <sup>c</sup> Not available in this wavenumber region.

**Table 4.1:** Changes for the new Karlsruhe retrieval strategy. Not listed spectral windows are retrieved by the recommended TCCON retrieval strategy. The three different time periods for the InSb diode correspond to the usage of three different narrowband filters in front of this detector since the instrument was initiated.

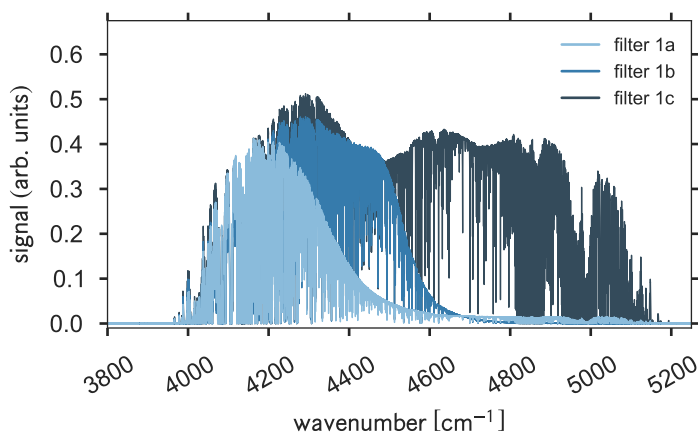


**Figure 4.4:** Karlsruhe spectra recorded by the InSb diode for the three different spectral filters which were mounted in front of the detector since FTS measurements started in 2009.

## 4.2 Impact of background continuum fitting on airmass dependence of DMFs

In general, TCCON data of all gases of interest show airmass dependent artefacts. Retrieved DMFs of gases are systematically varying for different solar zenith angles (SZAs). For example for CO<sub>2</sub>, this effect reaches a variation of about 1% when comparing measurements recorded at noon and sunset (Wunch et al., 2011). Since the mean SZA varies with seasonality and latitude, airmass dependent retrieval biases must be accounted for. The biases can be aliased into the seasonal cycle and affect the time series from different sites at different latitudes differently. For CO<sub>2</sub>, this effect can be easily identified in the southern hemisphere where the amplitude of the seasonal cycle is rather small (Wunch et al., 2011). There are numerous factors that induce airmass dependent artefacts, including spectroscopic inadequacies and instrumental features as seen for the Karlsruhe FTS.

The GGG algorithm applies a single empirical correction that accounts for all the aforementioned causes. Briefly summarized, the diurnal airmass dependence can be split in a symmetric and antisymmetric component of the retrieved column averaged DMF around local noon. Whereas the antisymmetric component is considered to be a real atmospheric signal, the symmetric component is considered as an airmass dependent artefact which is spurious and mainly introduced due to the aforementioned reasons (Wunch et al., 2011). The correction term consisting of the antisymmetric component is empirically obtained from the TCCON data recorded at the sites Park Falls (Wisconsin, USA), Lauder (New Zealand), Lamont (Oklahoma, USA) and Darwin (Australia). A detailed description of the formulation how the airmass dependent correction factor is obtained is given in Wunch et al. (2011). Since the TCCON tries to maintain consistency between all partners, the median value of the correction term derived from these sites is used for all stations affiliated with the TCCON. This seems reasonable when the airmass dependent artefacts arise from spectroscopic inadequacies. For SZAs larger than 85°, no airmass correction factor is applied to the retrieved DMFs since the derived airmass correction term for such large SZAs is not consistent any more for different sites (Wunch et al., 2011). Retrieval results for SZAs larger than 85° are not publicly released and are not an official TCCON data product. In addition to spectroscopic inadequacies, Karlsruhe TCCON data is subject to airmass dependent artefacts induced by the particular instrumental setup and varying continuum curvature in the spectra. The fitting of the background continuum by a higher-order continuum level fit changes the airmass dependence for most of the target gases whose residuals are largely affected by curvatures. It is important to analyze whether the airmass dependence changes when the retrieval strategy with a higher order continuum level fit compared to the network wide standard GGG retrieval strategy. Using cavity-ratioed spectra as a reference, it can be

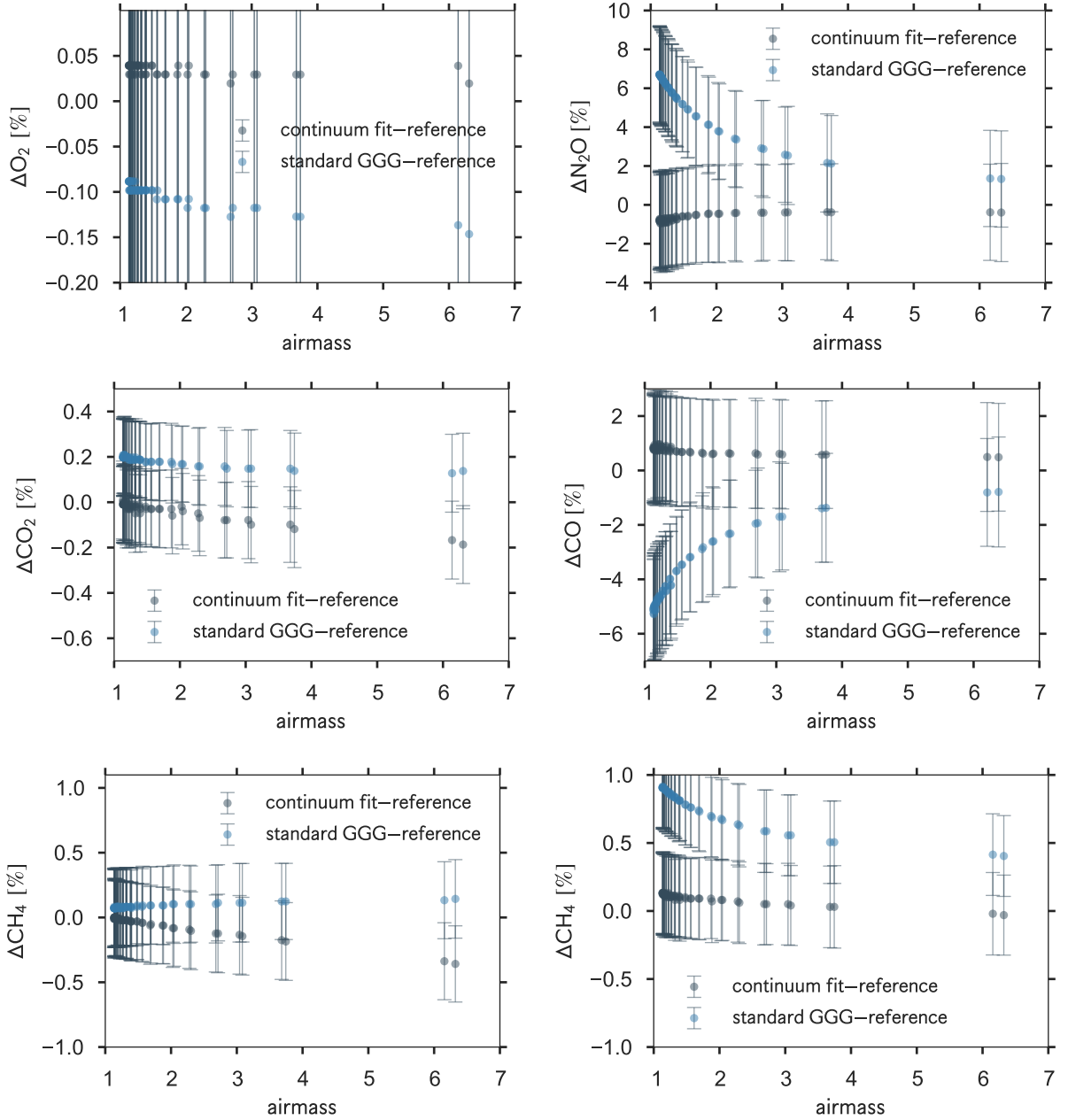
shown that implementing the new retrieval approach with an continuum curvature fitting scheme using higher order Legendre polynomials significantly reduces airmass dependent biases in the Karlsruhe TCCON data set. Cavity-ratioed reference spectra are produced as described in the above section recorded by the InGaAs and InSb detector. The impact of a continuum level fit on the airmass dependence is elaborated via a case study using Karlsruhe TCCON data on 18 May 2014 when high airmass values up to seven are reached during the measurement day.

Figure 4.5 (upper left panel) depicts the airmass dependence of  $O_2$  retrieved by the Karlsruhe approach compared to the reference retrieval using cavity-ratioed atmospheric spectra. Applying the standard TCCON retrieval strategy (fitting only the continuum level and tilt), an overall bias of  $-0.10\%$  results along with an airmass dependence leading to a relative difference of  $-0.15\%$  between the reference run and the standard TCCON retrieval strategy for airmass values between six and seven. In comparison, the airmass dependence for column abundances from the retrieval when a higher-order continuum fit is applied shows neither a significant airmass dependence nor a significant bias ( $0.04\%$ ). The reduction of the airmass dependence for the  $O_2$  spectral window ensures that no airmass dependence is induced to all other DMFs provided by the TCCON which are calculated by dividing by the  $O_2$  total column.

In general, applying a higher-order Legendre polynomial fit improves the airmass dependence for  $CO_2$ ,  $CO$ ,  $N_2O$ , and  $CH_4$  retrieved from the  $6076.0\text{ cm}^{-1}$  spectral window (see Fig. 4.5). Especially for  $CO$ , an initially large deviation of about  $-5\%$  from the retrieval using the reference spectra and the standard TCCON retrieval was minimized to  $1\%$  and simultaneously the airmass dependence was reduced. This is indicated by a largely constant difference over the entire airmass values covered by this study. The same holds for  $N_2O$ , where an initial difference of about  $7\%$  between the standard GGG retrieval strategy and the adopted strategy using reference spectra was reduced to  $1\%$  converging towards zero for larger airmasses when using the modified GGG retrieval strategy including the empirical continuum curvature fit. Standard GGG retrievals from spectral regions covered by the InSb detector suffer stronger from the impact of the instrumental setup on the spectra than retrievals performed in the NIR from spectra recorded by the InGaAs detector. This confirms that the usage of an optical narrow band filter mounted in front of the InSb detector in combination with the dichroic beamsplitter enhances the effect of airmass dependencies of retrieved total columns.

Even though the retrieval strategy using a continuum fit improved the airmass dependence for retrievals of  $CO_2$ ,  $CO$ ,  $N_2O$ , and  $CH_4$  retrieved from the  $6076.0\text{ cm}^{-1}$  spectral window,

there is no clear improvement for  $\text{CH}_4$  retrieved in the  $5938.0 \text{ cm}^{-1}$  region (see Fig. 4.5, lower left). On the one hand, the overall bias is reduced for small airmass values. On the other hand, a stronger airmass dependence is induced by applying the higher-order continuum level fit. Nevertheless, since the majority of the Karlsruhe measurements are



**Figure 4.5:** Airmass dependence of DMFs for all affected spectral windows retrieved by the standard GGG TCCON retrieval strategy and using a higher-order continuum fit. As a reference, cavity-ratioed atmospheric spectra are used for the standard GGG retrieval setup. Upper left,  $\text{O}_2$  (cw: 7885.0,  $N = 5$  was used for the background continuum fit); upper right,  $\text{N}_2\text{O}$  (cw: 5719.5,  $N = 3$ ); center left:  $\text{CO}_2$  (cw: 6339.5,  $N = 3$ ); center right:  $\text{CO}$  (cw: 4290.4,  $N = 4$ ); lower left:  $\text{CH}_4$  (cw: 5938.0,  $N = 4$ ); lower right:  $\text{CH}_4$  (cw: 6076.0,  $N = 5$ ).

recorded between airmass values of one and two, the retrieval strategy with a higher-order continuum fit still seems to improve the airmass dependence compared to the standard GGG retrieval. The remaining airmass dependence for all retrieved total columns is most likely due to spectroscopic errors.

### 4.3 Impact of background continuum fitting on column averaged DMFs

The higher-order background continuum fit improves spectral fits as well as the airmass dependence for spectra recorded in Karlsruhe. It is also important to note that the amount of column averaged DMFs change. DMFs are computed by ratioing the column abundance of the gas of interest by  $O_2$ , and multiplying by the assumed atmospheric DMF of  $O_2$  (0.2095) (see Sect. 3.3.7). Since residuals of spectral fits of  $O_2$  are significantly impacted by continuum curvature, the DMFs of all gases change when fitting the background continuum curvature by Legendre polynomials compared to the standard TCCON retrieval strategy. To analyze the impact of continuum fits on column averaged DMFs, the standard GGG retrieval strategy and the new retrieval approach is applied. This assigns a higher-order continuum fit for gases listed in Table 4.1 using the corresponding order of the Legendre polynomials. For the intercomparison, one year of Karlsruhe TCCON data covering large parts of the year 2014 are used.

Analyzing the impact of the continuum fit on the retrieved  $O_2$  total columns shows a relative mean difference between both retrieval strategies of  $(0.132 \pm 0.010) \%$ . The  $O_2$  total column is slightly higher when following the retrieval strategy using a higher-order continuum fit. Therefore, DMFs of target gases change by 0.132 % when no higher-order continuum fit is required. This is the case for spectral windows used to retrieve  $H_2O$ ,  $HF$ , and  $HCl$ . For all

Gas	abs. mean diff.	std. deviation	change from $O_2$	rel. mean diff. [%]
$O_2$	$6.007 \times 10^{21c}$	$0.453 \times 10^{21c}$		$0.132 \pm 0.010$
$XCH_4$	$-2.450^b$	$0.741^b$	$-2.376^b$	$-0.136 \pm 0.041$
$XCO_2$	$-0.918^a$	$0.062^a$	$-0.528^a$	$-0.232 \pm 0.016$
$XCO$	$1.595^b$	$0.490^b$	$-0.132^b$	$2.009 \pm 0.674$
$XN_2O$	$-2.203^b$	$0.770^b$	$-0.422^b$	$-0.699 \pm 0.245$

<sup>a</sup>: given in ppm, <sup>b</sup>: given in ppb, <sup>c</sup>: given in molec  $cm^{-2}$ ,

**Table 4.2:** Absolute and relative mean differences of retrieved TCCON target gases with and without a higher-order background continuum fit.

other target gases, any differences are due to the change in retrieved O<sub>2</sub> abundances and changes in abundances retrieved of the target gas itself. The corresponding mean absolute and relative differences for XCO<sub>2</sub>, XCO, XN<sub>2</sub>O, and XCH<sub>4</sub> are given in Table 4.2. The largest change is found for XCO (about 2%) followed by XN<sub>2</sub>O with a change of about -0.7%. The change of XCO<sub>2</sub> is -0.2% and corresponds to an mean absolute decrease of about 0.9 ppm.

## 4.4 Karlsruhe data in context of other TCCON stations

Differences in DMFs retrieved with the standard TCCON retrieval strategy and the strategy when a higher order continuum level fit is applied to the background continuum, range between -0.7% and 2.0% for the particular gases. Thus, in this section, the consistency of the Karlsruhe data set with other TCCON sites is reviewed. A method to investigate the consistency between data sets recorded at different TCCON sites is given by the calibration curves derived from in situ aircraft measurements flown over TCCON sites which are also used to determine the calibration factor to tie the ground-based data sets to the WMO reference scale (see Sect. 3.2.1). Typically, such calibration curves show a significant bias but a good correlation (Wunch et al., 2010).

The calibration curves contain TCCON and in situ data from a variety of globally distributed sites. These graphs are utilized as an indicator for the consistency of the Karlsruhe data set with other sites since the difference between the data derived from the in situ measurements and the TCCON data set should basically be comparable for different sites. Differences are mainly driven by spectroscopic uncertainties rather than instrumental features. In this section it is shown that the modified Karlsruhe retrieval strategy improves the consistency between geographically nearby TCCON stations on the European continent.

The first calibration campaign of a TCCON site is described by Washenfelder et al. (2006) for the Park Falls instrument. In 2004, during the Intercontinental Chemical Transport Experiment–North America (INTAX-NA) and CO<sub>2</sub> Boundary Layer Regional Airborne Experiment (COBRA) campaigns, a research aircraft recorded several in situ CO<sub>2</sub> vertical profiles over this TCCON site. Comparison of the integrated aircraft profiles and CO<sub>2</sub> column abundances were used to calibrate the Park Falls TCCON data set to the WMO scale. Several calibration campaigns followed for sites in Australia and the United States of America, Japan and New Zealand which are today jointly used to derive a global calibration factor to tie TCCON data to the WMO scale (Deutscher et al., 2010; Messerschmidt et al., 2011; Wunch et al., 2010; Washenfelder et al., 2006). Karlsruhe TCCON data sets were used to compare vertical gas profiles obtained from aircraft overflights as part of the

Infrastructure for Measurement of the European Carbon Cycle (IMECC) project in 2009. IMECC was the first airborne campaign to calibrate the European TCCON FTIR sites with respect to the WMO standards (Wunch et al., 2010; Messerschmidt et al., 2011; Geibel et al., 2012).

Here, Karlsruhe TCCON data are compared to data obtained from these overflights to provide evidence that the higher-order continuum level fit option improves the consistency of the Karlsruhe data set with other TCCON sites. The focus of this study lies on the correlation between other geographically nearby stations rather than on the overall calibration factor. The following comparison relies on IMECC and TCCON data which is presented in detail in, e.g., Wunch et al. (2010), Messerschmidt et al. (2011) and Geibel et al. (2012), where numerous CO<sub>2</sub> and CH<sub>4</sub> in situ profiles were obtained via instruments on an aircraft and compared to CO<sub>2</sub> and CH<sub>4</sub> column amounts from TCCON spectrometers. A detailed description of the aircraft instrumentation, the numerical integration of aircraft in situ profiles and the uncertainty discussion can also be found in Deutscher et al. (2010); Messerschmidt et al. (2011) and Washenfelder et al. (2006). TCCON data for CO and N<sub>2</sub>O for 2 October, 2009 when the aircraft overflight took place in Karlsruhe are not available. The FTS instrument has become operational just before the IMECC campaign took place and the InSb detector which covers the CO and N<sub>2</sub>O spectral window was not fully operational at that time. Therefore, this study is restricted to CO<sub>2</sub> and CH<sub>4</sub> whose spectral windows are accessible in spectra recorded by the InGaAs detector.

An update of the calibration curve for CO<sub>2</sub> with combined results using the IMECC campaign and other aircraft profiles is shown in Fig. 4.6. The calibration curve contains North American, Australian, Asian and European TCCON sites (see legend within Fig. 4.6). In the updated calibration curve in the left panel of Fig. 4.6, Karlsruhe data is already retrieved following the higher order continuum fit approach for XCO<sub>2</sub>. The GGG retrieval method is predicted to be both linear and has no intercept (Wunch et al., 2011). The data is fitted with a linear least-squares and a zero ordinate intercept is forced. For XCO<sub>2</sub>, there is a bias of about  $(1.03 \pm 0.04)$  % between the Karlsruhe data and the aircraft data when comparing the integrated in situ profiles and the Karlsruhe TCCON data (with the higher-order continuum fit option). The Karlsruhe XCO<sub>2</sub> reaches  $(380.03 \pm 0.32)$  ppm whereas the integrated in situ profile provides a total column dry-air mole fraction of  $(384.35 \pm 0.20)$  ppm. Nevertheless, Karlsruhe XCO<sub>2</sub> data is in good agreement with the other geographically nearby TCCON stations of Orleans (France), Bialystok (Poland), Jena and Garmisch-Partenkirchen (both Germany) and is in good agreement with the network wide calibration factor of  $0.9898 \pm 0.0010$  obtained from all available in situ measurements worldwide (see Fig. 4.7, left panel). Without the higher-order continuum fit, Karlsruhe

XCO<sub>2</sub> data is slightly elevated and exhibits an overestimation with respect to the best fit as seen in Fig. 4.6, right panel. The correlation coefficient slightly improves from 0.993 (for the standard GGG retrieval) to 0.994 (for the retrieval including the higher order continuum fit). The slope of the fit is found to be  $0.9897 \pm 0.0005$ .

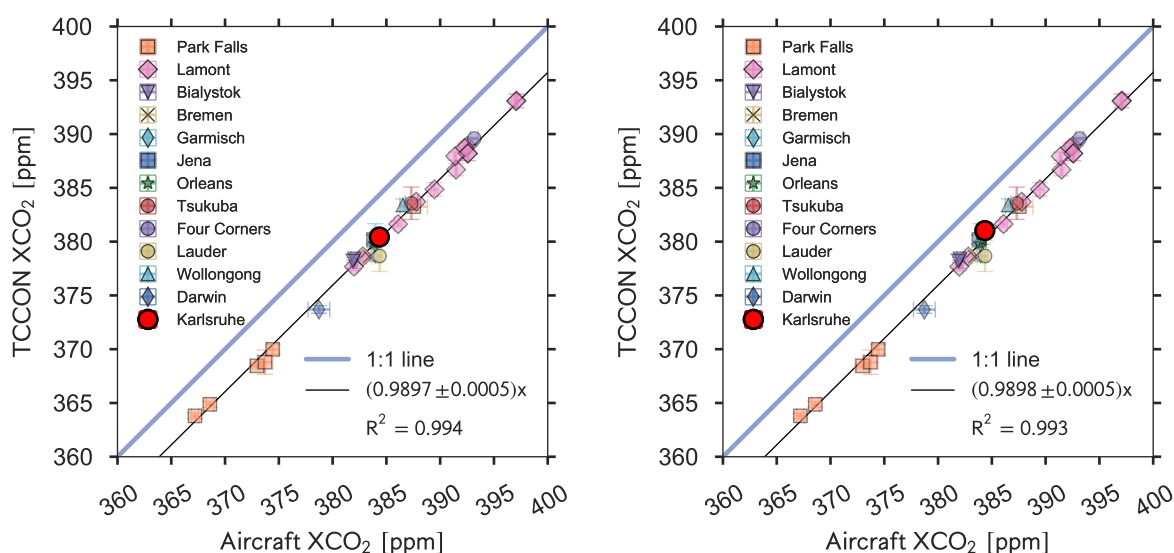


**Figure 4.6:** Update of the XCO<sub>2</sub> calibration curve which is discussed in detail in, e.g. Wunch et al. (2010), Messerschmidt et al. (2011) and Geibel et al. (2012) using the continuum fit option (left panel) and the standard GGG retrieval strategy (right panel) for the Karlsruhe TCCON data.

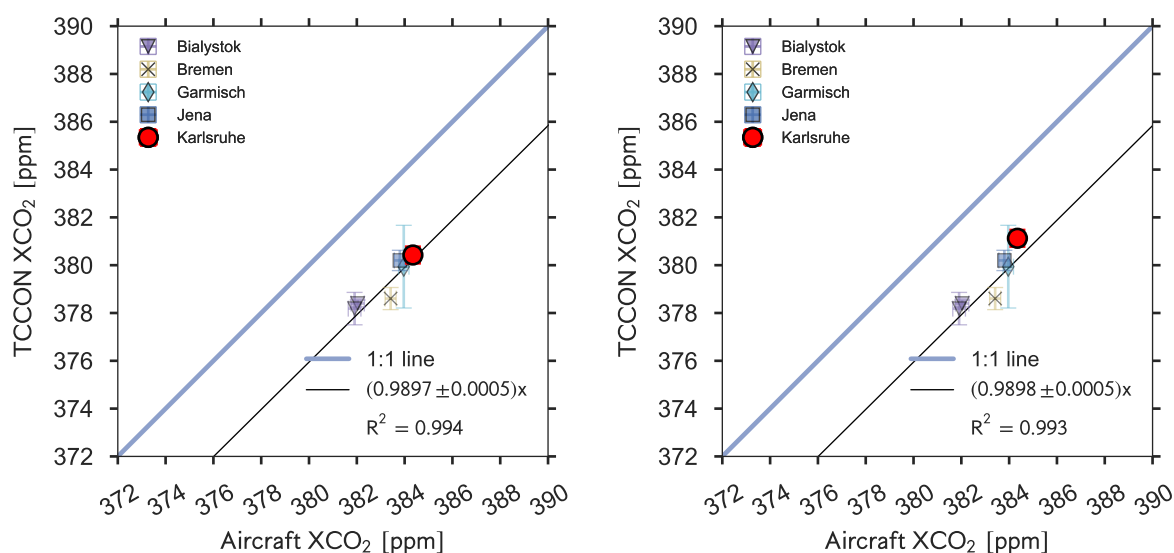


**Figure 4.7:** Same as Fig. 4.6 just for geographically nearby European stations Bialystok, Bremen, Garmisch-Partenkirchen, and Jena.

In analogy to the  $\text{XCO}_2$  calibration curve, an update of the correlation graph for  $\text{XCH}_4$  is shown in Fig. 4.8 (left panel). Again, the higher order continuum retrieval strategy is already applied to the Karlsruhe data. The Karlsruhe TCCON  $\text{XCH}_4$  reaches  $(1750.81 \pm 1.325)$  ppb whereas the integrated in situ  $\text{CH}_4$  profile provides a DMF of  $(1793.32 \pm 18.987)$  ppb. This corresponds to a relative difference of about  $(2.3 \pm 0.9)\%$ . As seen for  $\text{XCO}_2$ , the agreement of Karlsruhe TCCON  $\text{XCH}_4$  data with other geographically nearby TCCON stations improves when the higher order continuum fit retrieval strategy is applied. For the standard TCCON retrieval strategy, the relative difference of about 2 % between TCCON  $\text{XCH}_4$  and the aircraft  $\text{XCH}_4$  was slightly smaller but the consistency with other European TCCON stations downgraded, as can be seen in Fig. 4.8 (right panel). The TCCON DMF of  $\text{XCH}_4$  reaches  $(1756.87 \pm 1.66)$  ppb when no higher order continuum fit is applied. The correlation coefficient remains the same for both retrieval strategies ( $0.9631$ ). Also the slope of the linear fit forced through zero does not change significantly ( $0.9760 \pm 0.001$ ).

In order to test how DMFs from other sites are affected when a higher-order continuum fit in the retrieval strategy is applied, the calibration curve is updated using the Karlsruhe retrieval approach to process data of the other TCCON stations which contribute to the TCCON  $\text{XCO}_2$  and  $\text{XCH}_4$  calibration curves (of the particular day of the aircraft overflight). The differences between  $\text{XCO}_2$  retrieved from both retrieval strategies are depicted in Fig. 4.10 (left panel). The change in  $\text{XCO}_2$  for Karlsruhe is about three times larger than for the other TCCON sites. This shows that a continuum fit to the Karlsruhe spectra is

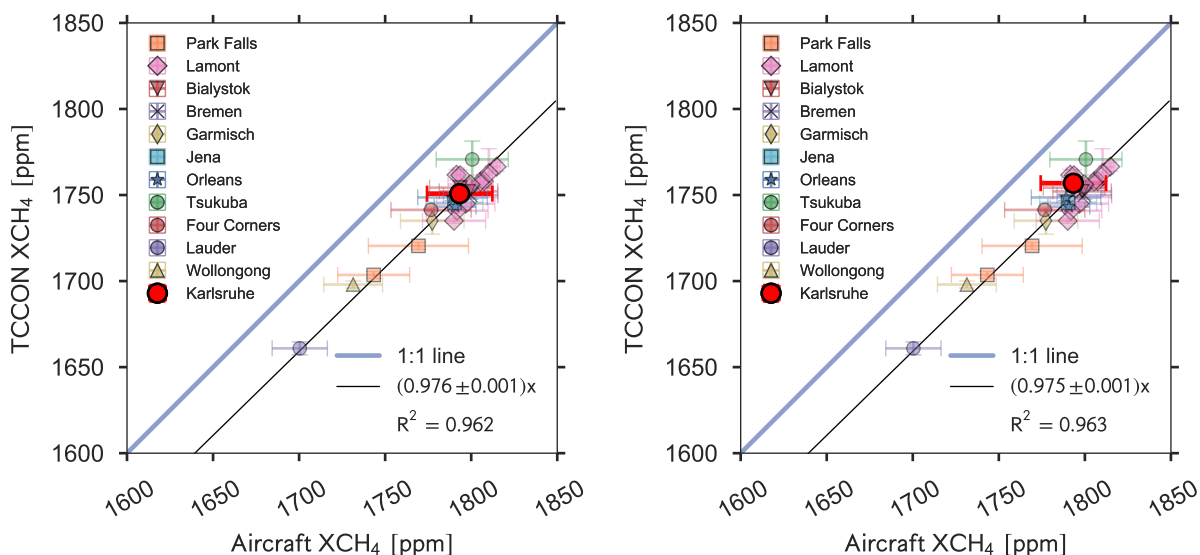


**Figure 4.8:** Update of the  $\text{XCH}_4$  calibration curve which is discussed in detail in, e.g. Wunch et al. (2010), Messerschmidt et al. (2011) and Geibel et al. (2012) using the continuum fit option (left panel) and the standard GGG retrieval strategy (right panel) for the Karlsruhe TCCON data.

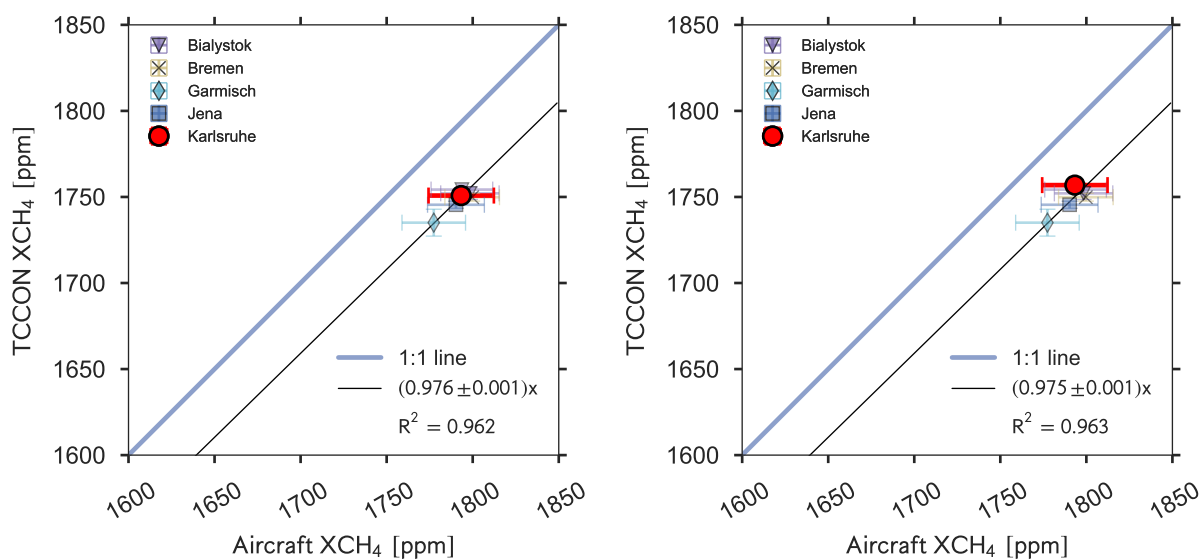


**Figure 4.9:** Same as Fig. 4.8 just for geographically nearby European stations Bialystok, Bremen, Garmisch-Partenkirchen, and Jena.

required to improve its consistency with the other TCCON data. The change in  $XCO_2$  is not negligible for the other stations which mainly follow the standard FTIR instrumental setup as recommended by TCCON. The changes are consistent (within about 0.1 ppm) for all other TCCON sites, suggesting that the addition of higher-order continuum terms is likely accommodating errors that are common across the network. Such errors are currently accounted for by scaling to the aircraft profiles and thus do not impact the overall accuracy of the TCCON. The variation in the  $XCO_2$  change of about  $-0.4$  ppm for Lamont are largely due to airmass dependencies that are not accounted for since applying the Karlsruhe approach to other stations does not automatically change the applied global airmass correction factors which are obtained from retrievals where only a continuum level and tilt is fitted for the sites Lamont, Lauder, Parks Falls, and Darwin.

The higher order fit retrieval strategy as used for Karlsruhe TCCON  $XCH_4$  data is applied to TCCON data of all other stations which contribute to the TCCON  $CH_4$  calibration curve. The absolute differences between both retrieval approaches are depicted in Fig. 4.10 (right panel). Compared to the other European TCCON stations Bialystok, Bremen, Garmisch-Partenkirchen, Jena and Orleans, the change in Karlsruhe  $XCH_4$  is about six times larger. As already seen for  $XCO_2$ , the change in  $XCH_4$  for the other TCCON stations is not negligible. The change in  $XCH_4$  for the European sites differ by about 1 ppb when the continuum fit is applied but are in general consistent to within 1 ppb, especially when comparing measurements at similar SZAs.

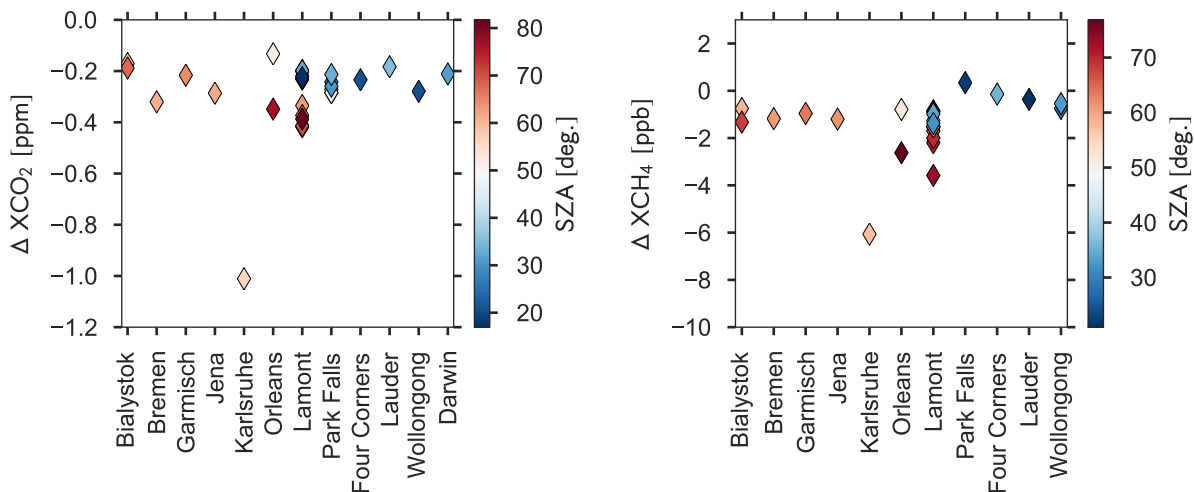


**Figure 4.10:** Differences in XCO<sub>2</sub> (left panel) and XCH<sub>4</sub> (right panel) if the Karlsruhe retrieval strategy is applied to data of all TCCON stations which contribute to the XCO<sub>2</sub> and XCH<sub>4</sub> aircraft calibration curve. Corresponding solar zenith angles (SZA) of the particular measurement are color coded. For reason of comparability, no error bars are depicted.

## 4.5 Airmass dependence of O<sub>2</sub> retrievals in the MIR

For the calculation of DMFs of gases retrieved from MIR spectra, the 7885 cm<sup>-1</sup> O<sub>2</sub> absorption window is analyzed using the PROFFIT retrieval algorithm. Since the O<sub>2</sub> spectral window is wide compared to the usual spectral microwindows analyzed by PROFFIT for the NDACC, the handling of background continuum curvatures as performed by PROFFIT is described in this section in more detail. In general, the results achieved with the modified TCCON retrieval setup developed for Karlsruhe in this work indicate that the spurious airmass dependence of O<sub>2</sub> retrievals is mainly induced by the overlaying collision-induced absorption (CIA) in combination with continuum curvatures induced by instrumental features. This corroborates earlier studies by Dohe (2013) using the PROFFIT algorithm, which also indicated reduced airmass dependence when using a refined treatment of the background continuum level. As already mentioned in Sect. 4.1, the PROFFIT approach includes a fit of the empirical background based on a user-selectable number of baseline guiding points which are evenly distributed across the fitted spectral window.

Dohe (2013) demonstrated that a detailed model of the O<sub>2</sub> CIA which overlaps the 1.26 μm absorption band is not required if a sufficiently flexible empirical background fit is included in the fit. Here, the O<sub>2</sub> spectral window (cw: 7885.0) is revisited and the impact of the number of guiding points,  $G$ , on the retrieved column of molecular oxygen is investigated in greater detail using the PROFFIT algorithm.

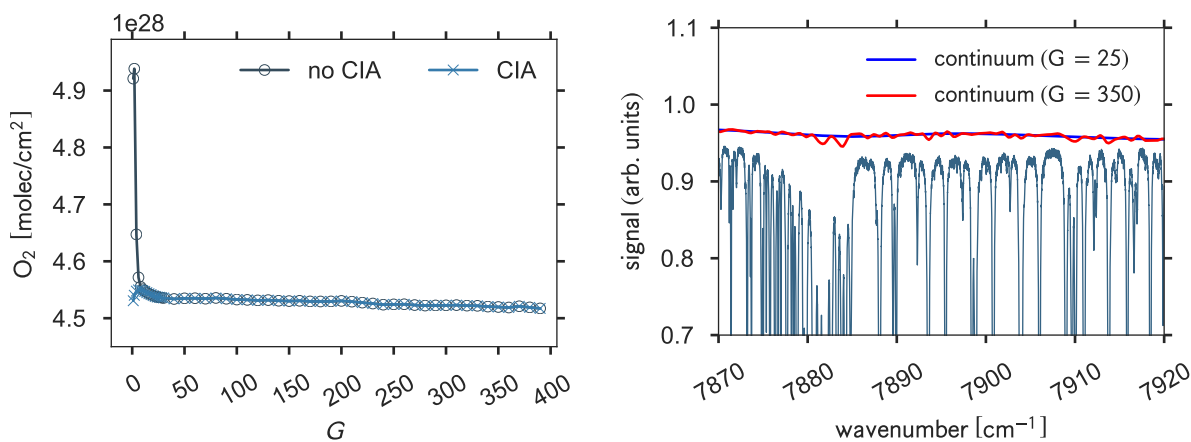


**Figure 4.11:** Left panel: Retrieved total column of O<sub>2</sub> with respect to the number of guiding points  $G$  without (no CIA) and with modeling of the collision-induced absorption (CIA). Right panel: Excerpt of the Q-branch in the O<sub>2</sub> spectral window. For  $G = 350$ , the continuum starts to curve into broad solar absorption lines. Due to the high density of guiding points, no error bars are depicted (left panel).

It is expected that a small number of guiding points requires explicit modeling of the CIA (mainly based on Chagas et al. (2002)), and that a rather flat plateau area is reached for a larger number of guiding points where fits with or without taking CIA into account are essentially equivalent until a further increase finally results in an empirical continuum so flexible that it starts to interact with individual spectral lines, spoiling the retrieved column. The result of this investigation is shown in Fig. 4.11 (left panel). The flat plateau area extends at least up to  $G = 400$ , at this value the dimension of the state vector becomes so large that the executable exceeds the memory boundaries. The retrieved column is slightly decreasing with increasing  $G$ , probably due to the fact that the continuum starts to curve into some broader absorption bands, as the solar H absorption line or the Q-branch of the O<sub>2</sub> band (see Fig. 4.11, right panel). A further improvement of the approach might be achievable by allowing for a variable spacing of guiding points, allowing for a higher degree of flexibility as function of the position in the spectral window. Although the retrieval seems stable for up to the maximum number of guiding points applied in this investigation, a small number of guiding points is clearly preferable from the technical point of view. In the standard PROFFIT setup for this window  $G = 25$  is used (this setup is currently used for the analysis of low-resolution spectra as recorded with the EM27/SUN, Gisi et al. (2012)).

The required polynomial order empirically determined for the operational TCCON retrieval is smaller (e.g.,  $N = 5$  for the O<sub>2</sub> spectral window) than the number of guiding points required for PROFFIT (larger than 20). This discrepancy might be due to the use of a superior model of the CIA in the GGG Software Suite and due to the fact that the

retrieval strategy differs: both algorithms retrieve the O<sub>2</sub> column from the line absorption alone, but the GGG algorithm in addition allows a scaling of the CIA, whereas PROFFIT only performs a forward calculation of the CIA without any further adjustments of this absorption contribution in the retrieval. In the future, selection of wider spectral windows might prove useful for NDACC applications as well.

## 4.6 Conclusions

The TCCON strives to attain the best precision and accuracy possible between different sites and therefore sets guidelines to ensure that the instrumentation at each site is as similar as possible and that the retrieval algorithm is identical for each site (Wunch et al., 2011). However, degradation in the networks consistency can be caused by several site-specific differences including differing optical component responses between instruments (beam splitters, detectors, filters, mirror coatings, etc.). The approach of the TCCON to homogenize the optical components leads to typically small differences between spectra from different sites. The particular optical setup of the Karlsruhe instrument induces stronger variations of the spectrum continuum that are not sufficiently well fitted by the standard TCCON retrieval strategy. These variations in the background continuum are not of atmospheric origin as proofed by the analysis of black body cavity spectra. In general, different approaches are possible to reduce such effects, for example an empirical fit as used by the PROFFIT algorithm or a ratioing by black body cavity laboratory spectra.

For the Karlsruhe TCCON data set, a modified retrieval strategy is developed which accounts for the aforementioned difficulties. In addition to a continuum tilt and continuum level, higher-order Legendre polynomials are used to fit the varying background continuum. This improves spectral fits and airmass dependencies for affected spectral windows. Moreover, on average, DMFs change by about  $(0.132 \pm 0.010)$  % for O<sub>2</sub>, which affects all other target gases by the calculation of DMFs, even those whose spectral windows are not affected by varying residuals. DMFs change by about  $(-0.232 \pm 0.016)$  % for CO<sub>2</sub>,  $(-0.136 \pm 0.041)$  % for CH<sub>4</sub>,  $(2.009 \pm 0.674)$  % for CO, and  $(-0.699 \pm 0.245)$  % for N<sub>2</sub>O. CO<sub>2</sub> and CH<sub>4</sub> are more consistent with the other European TCCON sites as obtained from the analysis of the aircraft calibration curves when a higher order continuum fit strategy is applied for the retrievals. Applying the modified retrieval approach to other TCCON sites, changes in DMFs are identified in the range of  $-0.3$  % for CO<sub>2</sub> and  $-0.4$  % for CH<sub>4</sub>.

As widths of fitting windows might increase, and the spectroscopic line lists improve in the future, small continuum curvature will become more apparent in spectral fits. Therefore, the TCCON and its partners seek to produce a uniform recommendation for fitting the

continuum that will accommodate the unique aspects of the Karlsruhe implementation. Hence, the pioneering setup of the Karlsruhe instrument provides valuable findings for the entire network. Moreover this work might be useful for future NDACC work also when fits over wider spectral regions are attempted.



# 5 Harmonization of XCO abundances from Karlsruhe NDACC and TCCON measurements

In the last years, several satellite missions were launched to provide long-term observations of trace gas abundances in the Earth's atmosphere including the monitoring of global CO concentrations (e.g. Buchwitz et al., 2007; Deeter et al., 2003; Clerbaux et al., 2008). These measurements provide valuable data records of global trace gas distributions in the Earth's atmosphere which are of uttermost significance to investigate and understand the impact of trace gases on the Earth's climate and potential future climate scenarios. Space-based data records are validated through comparisons with ground-based remote sensing observations which provide comparable quantities as satellite instruments, typically column averaged abundances of trace gases (de Laat et al., 2010). These ground-based column measurements complement sparse but highly precise surface in situ data records. The latter are representative for specific locations which, in general, are influenced by local sources and sinks. In contrast, total column measurements contain information of larger geographical areas (Keppel-Aleks et al., 2011) and reflect the exchange processes between the atmosphere and surface on regional and global scales.

In the recent past, ground-based FTS data records, either from the TCCON or the NDACC, were utilized to validate and confirm satellite measurements of various trace gases. For example, TCCON data sets were used to validate the GOSAT XCO<sub>2</sub> and XCH<sub>4</sub> data product (e.g. Yoshida et al., 2013; Zhou et al., 2016; Inoue et al., 2016), and NDACC data were used for, e.g. SCIAMACHY CO comparisons (de Laat et al., 2010). Typically, validation studies use data records from either one or the other ground-based network. However, an harmonized data set consisting of total column measurements from both ground-based FTS networks would improve the spatial coverage over each individual network, providing an extended data set. This is highly desirable for future validation and model studies as well as for long-term trend analyses. Nevertheless, measurements from different spectral regions and distinct retrieval approaches make a joint use of both ground-based data sets challenging. Different vertical sensitivities, spectroscopic parameters, differing retrieval

approaches, and different error budgets (e.g. due to temperature dependencies of analyzed spectral lines) might induce biases which exceed the network's precision. It is therefore essential to identify and quantify differences (e.g. bias, seasonal variations, etc.) between NDACC and TCCON measurements when aiming at harmonizing both data sets. A joint use of both data records would not only lead towards an improved spatial coverage of ground-based column measurements, but would also allow for trend analyses dating back 15 years before the TCCON network was established.

Since the Karlsruhe FTS merges an NDACC and TCCON spectrometer in one device, this site is favorable to study trace gas measurements from different spectral regions. Moreover, the simultaneous measurement of MIR and NIR spectra allows to use the O<sub>2</sub> total column from the 7885 cm<sup>-1</sup> spectral region to obtain DMFs of gases retrieved in the MIR, in analogy to the TCCON approach of constructing DMF products. In the following, carbon monoxide (CO) concentrations measured in the MIR and NIR spectral regions are analyzed. CO is an air pollutant which directly affects human health due to its toxicity. Moreover, it affects concentrations of other potent GHGs due to its reaction with the hydroxyl radical OH. Its vertical concentration profile is highly variable. NDACC CO retrievals are done from the fundamental absorption band in the MIR at 4.7 μm. TCCON CO retrievals are done from the 2.3 μm overtone band. Measurements in both spectral regions reveal significant differences in their vertical sensitivities.

In this chapter, sources and sinks of atmospheric CO are reviewed, followed by a summary of the retrieval approaches for NDACC and TCCON XCO measurements. Differences between both retrieved abundances are identified and quantified. This study aims at harmonizing both data sets. The contents of this chapter are mainly based on Kiel et al. (2016a).

## 5.1 Atmospheric carbon monoxide

Carbon Monoxide (CO) is an atmospheric trace gas which is of utmost importance for air quality studies. It is a commonly occurring air pollutant which affects human health due to its toxicity. The significance of CO for the formation of O<sub>3</sub> directly influences the air quality in the troposphere and stratosphere (Seiler and Fishman, 1981). Moreover, reactions with OH also influence concentrations of other atmospheric trace gases including GHGs and other near-term climate forcers. Typical concentrations in the northern hemisphere exceed 100 ppb in continental airmasses (Logan et al., 1981; Thompson, 1992). Natural sources of CO in the troposphere are natural bush and forest fires and the oceans. It is also directly released from vegetation and soils. Moreover, the oxidation of CH<sub>4</sub> is a key driver in the

production of atmospheric CO (Daniel and Solomon, 1998).

The principal oxidation reaction of CH<sub>4</sub> including the OH radical is:



The methyl radical (CH<sub>3</sub>) instantaneously reacts with O<sub>2</sub>, creating a methyl peroxy radical (CH<sub>3</sub>O<sub>2</sub>). Therefore reaction R 5.1 can directly be written as:



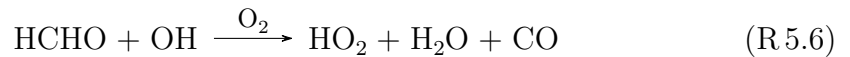
The methyl peroxy radical reacts with NO to:



Moreover, the produced CH<sub>3</sub>O rapidly reacts with O<sub>2</sub> and forms formaldehyde (HCHO) and HO<sub>2</sub>. It can directly be written as:



Formaldehyde underlies two main reactions in the atmosphere, photolysis and the reaction with OH, leading to three different reactions which produce CO:



For the latter, the following reaction was used:



The fractional contributions of the reaction R 5.5, R 5.6, and R 5.7 are roughly 55 %, 25 % and 25 %, respectively (Crutzen, 1988). In addition, CO is also created from oxidation processes with other non-methane hydrocarbons (NMHC). In the mesosphere, CO is produced by photodissociation of CO<sub>2</sub>. Major anthropogenic sources are incomplete combustion of fossil fuels, industrial processes, technological sources and biomass burning. About half of the emissions are of anthropogenic origin.

The primary sink of CO is the oxidation with OH (Spivakovsky et al., 2000) in the troposphere following the reaction:



Hence, CO is also a major sink for OH. OH reduces the lifetime of potent GHGs like, e.g. CH<sub>4</sub>, and therefore, elevated global concentrations of CO indirectly affect global warming (Daniel and Solomon, 1998) and are of interest in today's environmental sciences.

## 5.2 XCO retrieved from NDACC and TCCON measurements in Karlsruhe

Retrievals of CO from MIR spectra are performed following the NDACC – IRWG retrieval parameter guidelines. For that, spectral absorption lines from the CO fundamental band at 4.7 μm are analyzed whereas for NIR spectra, two broad spectral windows lying in the CO first overtone band are analyzed using the GFIT algorithm according to TCCON requirements. Retrievals in the NIR are performed using the modified TCCON retrieval strategy which compensates for spectral baseline modulations which are introduced by instrumental features of the Karlsruhe FTS setup (see Chap. 4 and Kiel et al., 2016b).

### 5.2.1 NDACC CO retrievals in the MIR spectral region

For the retrieval of total columns of CO in the MIR spectral range, Karlsruhe spectra recorded by the InSb detector using the NDACC filter 5 are analyzed. Three narrow spectral windows in the CO fundamental absorption band ranging from 2057.5 to 2058.2 cm<sup>-1</sup>, 2069.4 to 2069.9 cm<sup>-1</sup>, and 2140.4 to 2141.4 cm<sup>-1</sup> are fitted (Kramer, 2007). The NDACC CO retrieval is a constrained full profile retrieval similar to the retrieval approach described by Sussmann et al. (2011) for CH<sub>4</sub>. Here, a first order Tikhonov-Phillips regularization ( $\mathbf{L}_1$ ) on a logarithmic scale is applied (Hase et al., 2004; Schneider et al., 2006). In contrast to the classical approach using diagonal a priori covariance matrices with tuned variances which tend to generate VMR profile oscillations, the regularization term is chosen to be  $\mathbf{W} = \gamma \mathbf{L}_1^\top \mathbf{L}_1$  with  $\gamma$  the regularization strength and  $\mathbf{L}_1$  the discrete first order derivative operator:

$$\mathbf{L}_1 = \begin{pmatrix} -1 & 1 & 0 & \cdots & 0 \\ 0 & -1 & 1 & \ddots & \vdots \\ \vdots & \ddots & \ddots & \ddots & 0 \\ 0 & \cdots & 0 & -1 & 1 \end{pmatrix} \quad (5.1)$$

This regularization matrix allows for a constrained degree of flexibility in the VMR profile shape which can be adjusted. Here, the regularization strength  $\gamma$  is tuned that about three degrees of freedom are reached (obtained from the trace of the averaging kernel matrix). The signal-to-noise ratio used for the evaluation of the cost function is empirically obtained from the fit residual. All three spectral windows are fitted simultaneously. The a priori VMR profile is obtained from WACCM (Garcia et al., 2007) simulations as recommended by the NDACC. One fixed a priori VMR profile, which represents the average obtained from model runs from 1980 to 2020 for the Karlsruhe geolocation, is applied for the entire temporal range of this study (see Fig. 5.1, left panel). The HITRAN line list from 2008 (Rothman et al., 2009) is used in its original form for CO. The same HITRAN version is also used for the interfering gases CO<sub>2</sub>, OCS, O<sub>3</sub>, and N<sub>2</sub>O. For H<sub>2</sub>O and HDO, the HITRAN line list update from 2009 is used. The a priori pressure and temperature profiles allow for intra day variability based on eight individual profiles for one measurement day (see Sect. 3.2.2). Table 5.1 summarizes the NDACC retrieval approach. Spectral fits and residuals for all three spectral windows for a typical Karlsruhe measurement in the MIR are depicted in Fig. 5.2.

	NDACC retrieval	TCCON retrieval
spectral windows [cm <sup>-1</sup> ]	2057.5 – 2058.2 2069.4 – 2069.9 2157.5 – 2159.2	4208.7 – 4257.3 4262.0 – 4318.8
interfering gases	CO <sub>2</sub> , OCS, O <sub>3</sub> , N <sub>2</sub> O, H <sub>2</sub> O	CH <sub>4</sub> , H <sub>2</sub> O, HDO
retrieval algorithm	PROFFIT V9.6	GGG2014 (GFIT)
line list	HITRAN 2008, HITRAN 2009 (H <sub>2</sub> O, HDO)	based on HITRAN 2012
retrieval constraint	Tikhonov-Phillips $L_1$ regularization (DOF* $\approx$ 3.0)	scaling of a priori VMR profile
a priori VMR profile	WACCM V.6 (fixed)	based on in situ measurements (daily)

\*: mean degree of freedom obtained from the trace of the averaging kernel matrix

**Table 5.1:** Summary of the NDACC and TCCON retrieval approaches for CO. NDACC uses spectral absorption lines in the fundamental band in the MIR spectral region to retrieve total columns of atmospheric CO whereas the TCCON uses the first overtone band in the NIR spectral range. Spectral CO lines in the NIR are strongly overlaid by lines of the interfering species CH<sub>4</sub>, H<sub>2</sub>O, and HDO as depicted in Fig. 5.4.

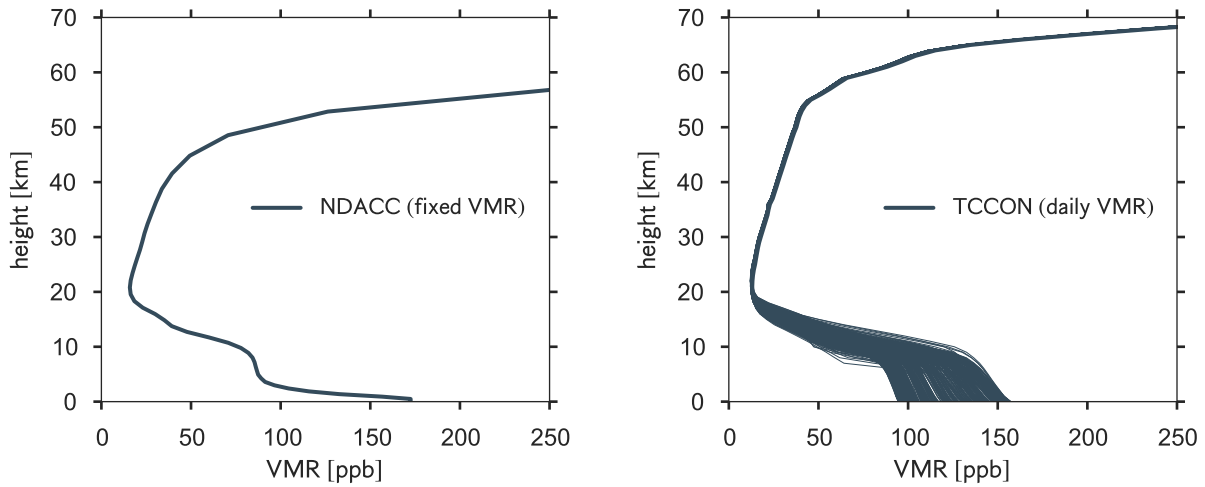


**Figure 5.1:** A priori CO VMR profiles used in this study for the NDACC CO retrieval from MIR spectra (one fixed profile obtained from WACCM simulations, left panel) and for the TCCON CO retrieval from NIR spectra (daily varying profiles, right panel). The slope of the profiles in the lower troposphere is significantly different.

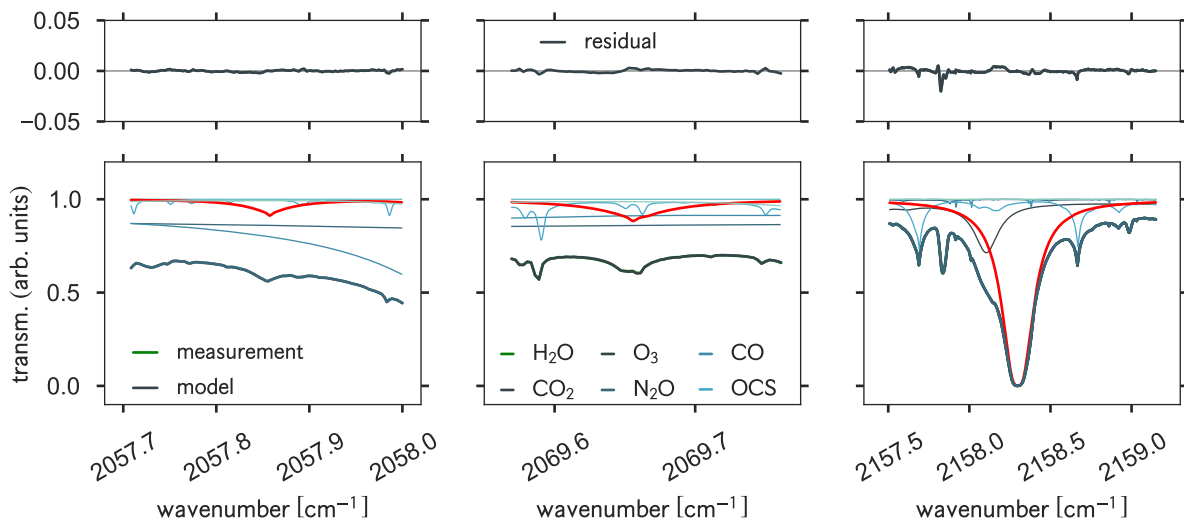


**Figure 5.2:** Spectral fits (lower panels) and residuals (upper panels) for one typical Karlsruhe spectrum for all three narrow microwindows which are fitted for the retrieval of CO from MIR spectra. Atmospheric CO lines are marked red, whereas the interfering species are colored as stated in the legend. The peak in the residual in the right panel is caused by a solar line.

## 5.2.2 TCCON CO retrievals in the NIR spectral range

For TCCON measurements in the NIR, the recorded interferograms are analyzed with the GGG Software Suite including GFIT and applying the modified retrieval methodology as described in Chap. 4 for the non-standard Karlsruhe FTS setup. Total columns of CO are retrieved by scaling of an a priori VMR profile to generate the best spectral fit. The scaled profile is integrated over height to compute the total column abundance. GFIT uses daily a priori VMR profiles which are generated by a set of empirical functions that are optimized to fit in situ measurements (e.g. Toon, 1991; Messerschmidt et al., 2011; Geibel et al., 2012; Karion et al., 2010; Wofsy, 2011). The TCCON a priori VMR profiles used in this study are depicted in Fig. 5.1 (right panel) and cover the time period from April 2010 to December 2014. To retrieve total columns of CO from NIR spectra, two broad spectral windows in the first CO overtone absorption band ranging from 4208.7 to 4257.3  $\text{cm}^{-1}$  and 4262.0 to 4318.8  $\text{cm}^{-1}$  are fitted. Interfering species are  $\text{CH}_4$ ,  $\text{H}_2\text{O}$ , and HDO. For TCCON CO retrievals, an adopted HITRAN 2012 line list (Rothman et al., 2013) is used as discussed in Sect. 3.2.1. Ten minute means of the ground pressure and surface temperature obtained from the Karlsruhe tall tower are used as auxiliary data for the Karlsruhe TCCON retrievals. Spectral fits for CO for a typical measurement in the NIR are depicted in Fig. 5.3. The spectral fit of the individual interfering gases is shown in Fig. 5.4. A comparison of both retrieval approaches for MIR and NIR measurements is given in Table 5.1.

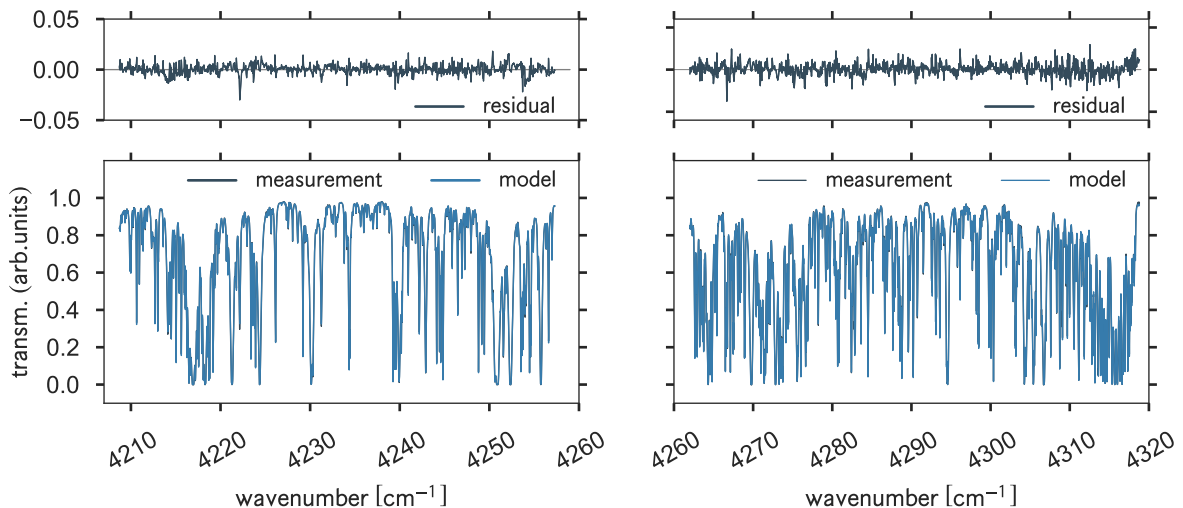


**Figure 5.3:** Spectral fits (lower panels) and residuals (upper panels) for one typical Karlsruhe spectrum for the 4208.7 to 4257.3  $\text{cm}^{-1}$  (left panel) and 4262.0 to 4318.8  $\text{cm}^{-1}$  (right panel) spectral windows which are used to retrieve total columns of CO from TCCON measurements in the NIR spectral range.

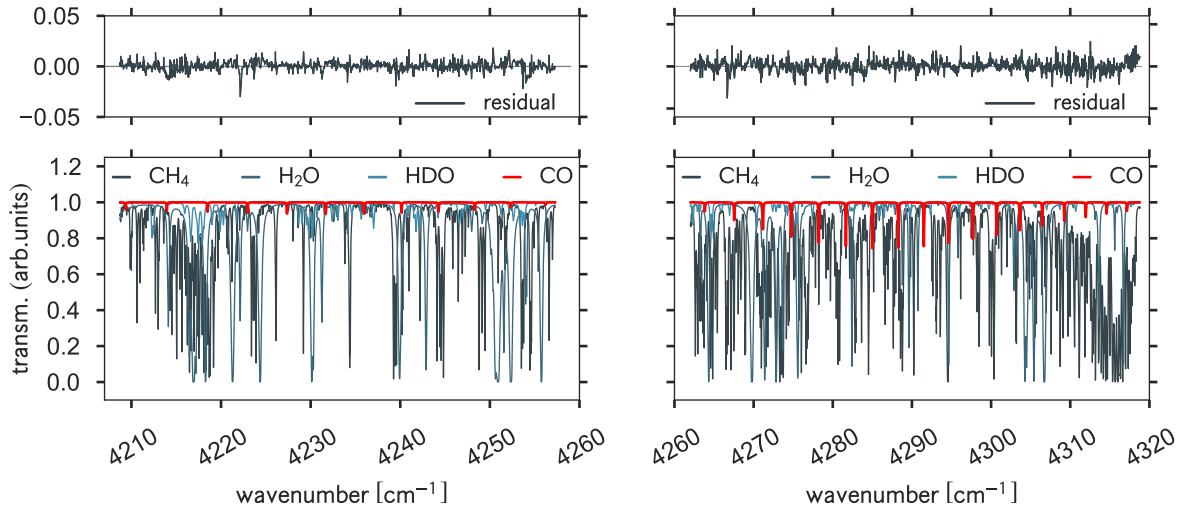


**Figure 5.4:** Same as Fig. 5.3, but absorption lines of the interfering gases are identified for both spectral windows. The CO absorption lines are marked red and are mainly overlaid by atmospheric CH<sub>4</sub> and H<sub>2</sub>O absorption lines. Absorption lines of interfering gases are colored as stated in the legend.

## 5.3 Theoretical error estimation for CO retrievals from MIR and NIR spectral regions

In this section, a quality assessment for the CO data product retrieved from MIR and NIR spectra is given. For that, the error calculation routine implemented in the retrieval algorithm PROFFIT is utilized for estimating errors in retrieved total columns and VMR profiles of CO from both spectral regions. For reasons of consistency, the CO retrieval approach as used for the TCCON is implemented into the PROFFIT algorithm. The error estimation is performed for one Karlsruhe measurement on 17 June 2014 around local noon.

### 5.3.1 Vertical profile and total column error estimation

For the error estimation, the analytical method suggested by Rodgers (2000) is utilized. The error, the difference between the retrieved and the true atmospheric VMR CO profile, is linearized about a mean profile, the estimated model parameters and the measurement noise:

$$\vec{x} - \vec{x}_{\text{true}} = (\mathbf{A} - \mathbf{1})(\vec{x}_{\text{true}} - \vec{x}_{\text{apriori}}) + \mathbf{G}\mathbf{K}_p(\vec{p} - \vec{p}_{\text{true}}) + \mathbf{G}\vec{\epsilon} \quad (5.2)$$

Here,  $\vec{x}$  represents the retrieved VMR profile,  $\vec{x}_{\text{true}}$  the true atmospheric VMR profile,  $\vec{x}_{\text{apriori}}$  the applied a priori VMR profile,  $\vec{p}$  the estimated model parameters,  $\vec{p}_{\text{true}}$  the real model parameters, and  $\vec{\epsilon}$  the measurement noise. Moreover,  $\mathbf{A}$  represents the averaging kernel

matrix,  $\mathbf{G}$  the gain matrix as defined in Eq. (2.87),  $\mathbf{K}_p$  the Jacobian matrix with respect to the model parameters, and  $\mathbf{1}$  the identity matrix. Equation (5.2) identifies three error classes: (1) the smoothing error, (2) errors due to uncertainties in the model parameters, and (3) errors due to measurement noise.

The error estimation performed in this study distinguishes between statistical and systematic error sources. However, several uncertainties are assumed to contribute to both, the statistical and systematic error budget. Uncertainties in the baseline of the spectrum (intensity offset), the ILS (modulation efficiency and phase error), the line of sight (LOS), solar lines (line intensity and spectral position), and spectroscopic parameters (line intensity and pressure broadening coefficient) are assumed as potential error sources. The uncertainty in the temperature profile is separated into three components: the lower and middle troposphere ( $< 10$  km) with an uncertainty of 1 K, in the lower stratosphere ( $< 35$  km) with an uncertainty of 2 K, and above ( $> 35$  km) with an uncertainty of 5 K. All assumed parameter uncertainties,  $\vec{p} - \vec{p}_{\text{true}}$ , are given in Table 5.2.

The total relative statistical profile error for NDACC CO retrieved from MIR spectra is shown in Fig. 5.5 (left panel). In the lower troposphere, the leading error sources are uncertainties in the ILS, LOS, and the temperature profile, whereas in the stratosphere, the measurement noise is the leading error source. The total relative systematic profile error is mainly driven by uncertainties in spectroscopic parameters throughout the entire troposphere and stratosphere (see Fig. 5.5, right panel). The relative error of about 10 % due to spectroscopic parameters exceeds the spectroscopic error in the NIR (see Fig. 5.6, right panel) due to the full profile retrieval which is the preferred approach for CO retrievals from the MIR spectral region.

Error source	acronym	uncertainty	stat./sys.
baseline (offset)	BAS	0.1 %	50/50
modulation (efficiency & phase error)	ILS	10 % & 0.1 rad	50/50
line of sight	LOS	0.1°	90/10
solar lines (intensity & wavenumber)	SOL	1 % & $10^{-6}$	80/20
temperature profile	TEMP	1–5 K	70/30
spec. para. (intensity & broadening)	SPEC	2 % & 5 %	0/100
measurement noise	NOI		100/0

**Table 5.2:** Estimated uncertainties for the various assumed error sources. The uncertainty in the temperature profile is estimated to vary with altitude, ranging between 1 and 5 K.

For the scaling retrieval in the NIR using the PROFFIT algorithm, the relative error contributions are constant throughout the vertical layers as depicted in Fig. 5.6. The absolute profile error typically reflects the shape of the retrieved VMR profile scaled by an error factor. This leads to a constant vertical profile error in relative units. The leading statistical error source is the measurement noise followed by uncertainties in the baseline (see Fig. 5.6, left panel). Similar to the retrieval in the MIR, the leading systematic error source is the uncertainty in spectroscopic parameters (see Fig. 5.6, right panel).

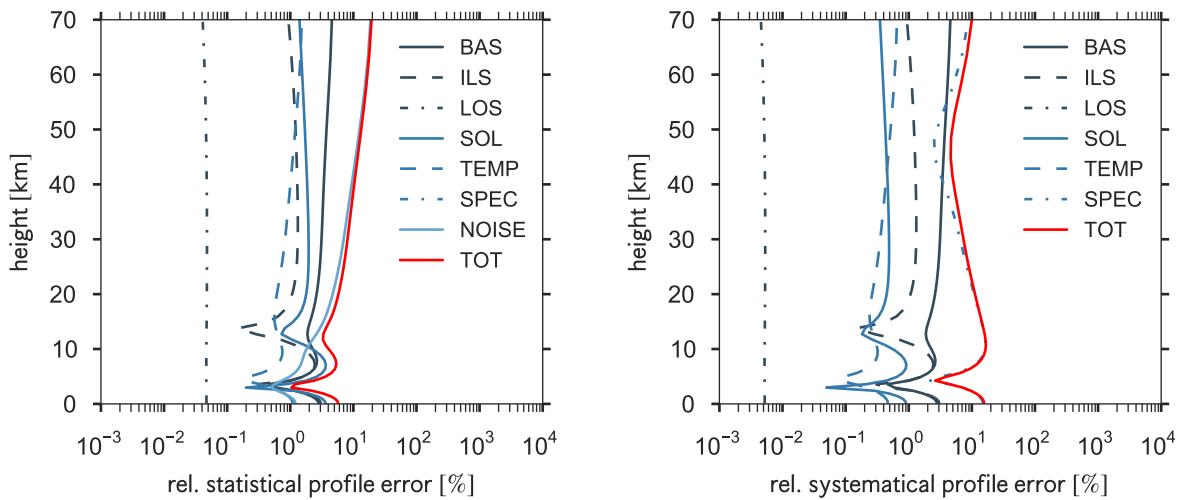


**Figure 5.5:** Relative statistical (left panel) and systematical (right panel) profile error for the full profile CO retrieval in the MIR spectral region.

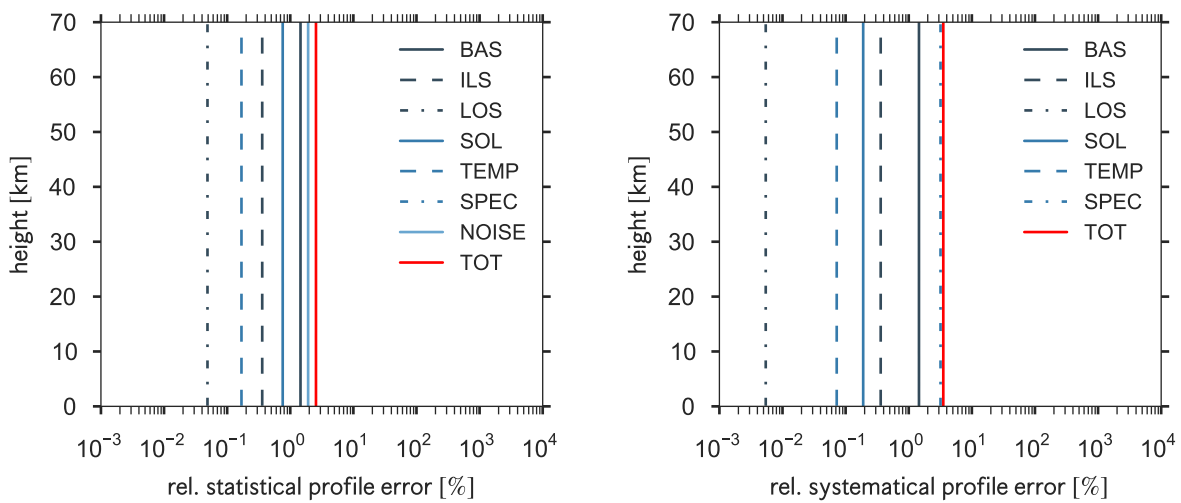


**Figure 5.6:** Relative statistical (left panel) and systematical (right panel) profile error for the scaling retrieval of CO in the NIR spectral region using the PROFFIT algorithm.

The estimated total column error for both retrieval strategies is given in Table 5.3. The total statistical error, given by the root-squares-sum of the individual errors, is 0.50 % for the total column of CO retrieved in the MIR spectral range. The noise error of 0.27 % provides the largest contribution to the total error. The total systematic error is estimated by 2.07 %, mainly driven by the uncertainty of spectroscopic parameters. For the NIR retrieval, the total statistical error reaches 1.03 %, mainly driven by uncertainties in solar lines. However, the TCCON final data product are column averaged DMFs. The calculation of DMFs leads to a minimization of several error sources including ILS, baseline and LOS errors. Therefore, it is expected that ratioing over O<sub>2</sub> reduces the error in DMFs of CO. Nevertheless, the ratioing over O<sub>2</sub> still might induce further uncertainties regarding the temperature or spectroscopic error. Similar to the systematical error in the MIR, the total systematical error is mainly driven by uncertainties in the spectroscopic parameters. The estimated smoothing error is about 0.4 % for the CO retrieval using MIR spectra and about 1.6 % for retrievals in the NIR.

Error source	MIR		NIR	
	stat.	sys.	stat.	sys.
BAS	0.22 %	0.22 %	0.15 %	0.15 %
ILS	0.21 %	0.21 %	0.51 %	0.51 %
LOS	0.05 %	0.02 %	0.05 %	0.02 %
SOL	0.18 %	0.09 %	0.80 %	0.40 %
TEMP	0.23 %	0.15 %	0.20 %	0.13 %
SPEC	–*	2.04 %	–*	3.19 %
NOI	0.27 %	–*	0.31 %	–*
TOT	0.50 %	2.07 %	1.03 %	3.26 %

\*: not considered as statistical or systematical error

**Table 5.3:** Total column error separated into different error sources for the MIR and NIR retrieval approach. The uncertainties for different error sources are separated in statistical and systematical error contributions. The total error (TOT) is given by the root-squares-sum of the individual errors.

## 5.4 Calculation of column averaged DMFs

To calculate column averaged DMFs of CO (XCO), the total column amount of CO ( $C_{\text{CO}}$ ) is divided by the total column of dry-air ( $C_{\text{dryair}}$ ). As seen in Sect. 3.3.7, for TCCON, the spectroscopically measured total column of O<sub>2</sub> ( $C_{\text{O}_2}$ ) retrieved from the 7885 cm<sup>-1</sup> absorption band in the NIR is used for deriving  $C_{\text{dryair}}$ :

$$C_{\text{dryair}} = \frac{C_{\text{O}_2}}{0.2095} \quad (5.3)$$

Here, 0.2095 is the assumed dry-air mole of O<sub>2</sub>. Alternatively, if instruments do not have access to the O<sub>2</sub> absorption band in the NIR,  $C_{\text{dryair}}$  can be determined via:

$$C_{\text{dryair}} = \frac{p_g}{g \cdot m_{\text{dryair}}} - \frac{C_{\text{H}_2\text{O}} \cdot m_{\text{H}_2\text{O}}}{m_{\text{dryair}}} \quad (5.4)$$

Here,  $g$  represents the gravitational acceleration whereas  $m_{\text{dryair}}$  and  $m_{\text{H}_2\text{O}}$  represent the molecular masses of dry-air and water vapor, respectively. The ground pressure is given by  $p_g$  and the total column of water vapor is  $C_{\text{H}_2\text{O}}$ . Since the Karlsruhe FTS setup allows to record spectra in the MIR and NIR simultaneously, Eq. (5.3) is also used to calculate XCO from MIR spectra. For the retrieval of O<sub>2</sub>, both retrieval algorithms, GFIT and PROFFIT, scale an altitude independent a priori VMR profile using the spectral window ranging from 7765.0 to 8005 cm<sup>-1</sup>. The corresponding spectral fits retrieved by GFIT and PROFFIT are depicted in Fig. 5.7.

Both time series of  $C_{\text{O}_2}$  retrieved with the GFIT and PROFFIT algorithm are in good agreement as depicted in Fig. 5.8. A bias of  $(0.04 \pm 0.02)$  % is identified in the relative difference time series with a standard deviation of 0.09 %. Using Eq. (5.4) to determine  $C_{\text{dryair}}$  from MIR spectra (when using the PROFFIT algorithm for the H<sub>2</sub>O retrieval) indicates a bias of  $(-2.28 \pm 0.01)$  % with a standard deviation of 0.13 % when compared with spectroscopically retrieved  $C_{\text{dryair}}$  using the GFIT algorithm (see Fig. 5.9). The mean bias of  $-2.28$  % is mainly due to spectroscopic inadequacies attributed to oxygen line intensity errors and is in good agreement with a bias of  $-2.27$  % observed by Washenfelder et al. (2006). Nevertheless, the spectroscopically derived  $C_{\text{dryair}}$  is used to calculate XCO from MIR spectra to achieve a more consistent comparison to TCCON measurements. However, despite the constant bias, the advantage of Eq. (5.3) is that errors in retrieved total columns of H<sub>2</sub>O and also rare but still possible inadequacies in measurements of the ground pressure due to instrument failure do not contribute to the total dry-air column. The aforementioned errors that are common to CO and O<sub>2</sub> are minimized.

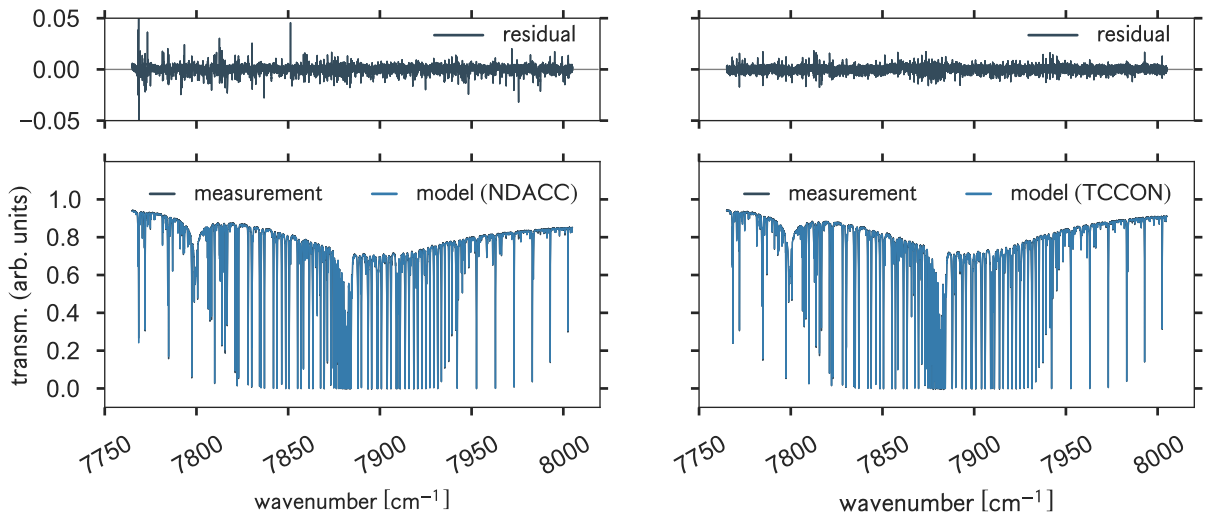


**Figure 5.7:** Spectral fits (lower panels) and residuals (upper panels) for the  $\text{O}_2$  spectral window lying at  $7885 \text{ cm}^{-1}$  for one typical Karlsruhe spectrum using the PROFFIT retrieval algorithm (left panel) and the GFIT retrieval algorithm (right panel). Residuals achieved with GFIT are smaller due to ad-hoc adjustments of  $\text{H}_2\text{O}$  absorption line parameters in the line list used for the TCCON retrieval.

## 5.5 Impact of a priori information on retrieved XCO

There are several factors which influence a direct comparison of retrieved total columns including the choice of different spectral regions, differing a priori information, spectroscopic parameters and the difference in the utilized retrieval algorithms. The latter was investigated by Dohe (2013), where an extensive cross-validation between the GFIT and PROFFIT

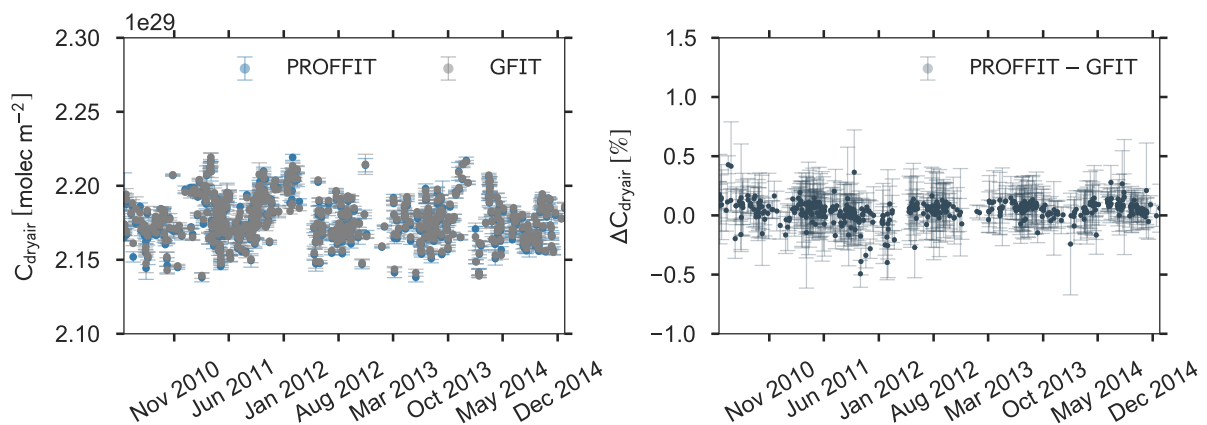


**Figure 5.8:** Spectroscopically retrieved daily mean time series of  $C_{\text{dryair}}$  using the  $\text{O}_2$   $7885 \text{ cm}^{-1}$  absorption band and utilizing the PROFFIT and GFIT retrieval algorithm (left panel). The relative difference time series (PROFFIT – GFIT) is shown in the right panel. Error bars represent the diurnal variation of  $C_{\text{dryair}}$ .

algorithm was performed for XCO<sub>2</sub> retrieved from the same spectral region in the NIR using two spectral windows ranging from 6180 to 6260 cm<sup>-1</sup> and 6310 to 6380 cm<sup>-1</sup>. It is expected that modifications within the PROFFIT retrieval strategy including, e.g. improvements of the O<sub>2</sub> and solar line parameters, implementation of TCCON a priori VMR profiles etc., improve the comparability between both retrieval algorithms. The overall bias between XCO<sub>2</sub> retrieved by the GFIT and PROFFIT algorithm from Karlsruhe NIR spectra is about 0.03 % (Dohe, 2013). This indicates a good agreement between both algorithms when same auxiliary data sets are used and therefore is not analyzed in more detail in the present study.

A comparison of data from two different spectral regions is not as straightforward as the analysis performed by Dohe (2013). Indeed, a priori information like temperature and pressure profiles are independent of the chosen spectral regions and can be used for both retrieval strategies in the MIR and NIR. However, line list parameters differ for different spectral regions and might be more adequate for one spectral region than for the other. Moreover, following the NDACC retrieval strategy, a full profile retrieval is applied in the MIR whereas in the NIR, a scaling retrieval is preferred by the TCCON retrieval approach. This seems to be reasonable since spectral absorption lines in the NIR are weaker and strongly Doppler broadened leading to less DOFs in the NIR when a full profile retrieval is applied. However, a scaling retrieval is strongly dependent on the shape of the a priori VMR profile. These substantially different retrieval approaches make a direct comparison of TCCON and NDACC XCO challenging. Therefore, the focus of the next sections lies on the impact of the a priori VMR profile and line list parameters choice on retrieved XCO using the NDACC and TCCON retrieval strategies.

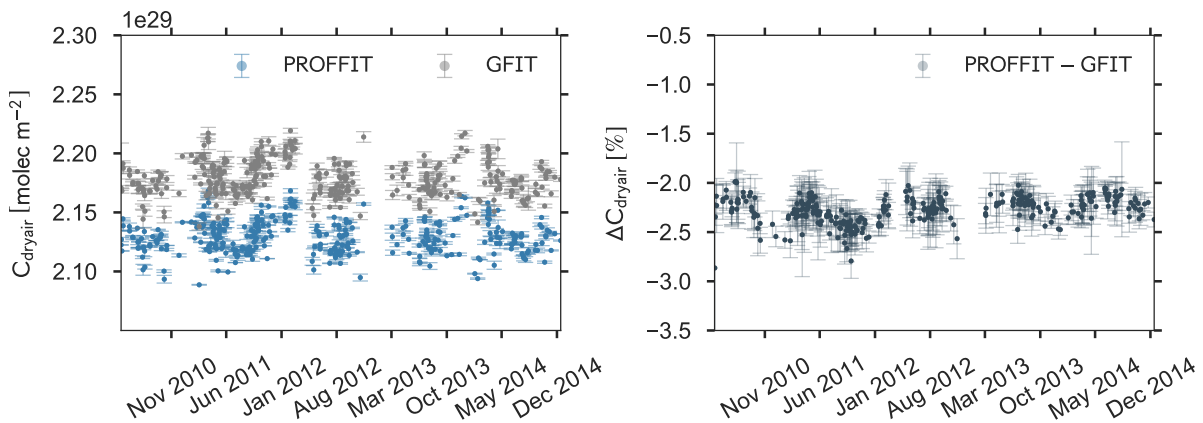


**Figure 5.9:**  $C_{\text{dryair}}$  spectroscopically retrieved with GFIT and using Eq. (5.4) utilizing the PROFFIT algorithm for the H<sub>2</sub>O retrieval. The right panel shows the relative difference time series. Error bars represent the diurnal variation of  $C_{\text{dryair}}$ .

### 5.5.1 Impact of a priori VMR profiles on retrieved XCO

The choice of a priori information influences the retrieved column abundances and has to be taken into account for an intercomparison of different soundings (Rodgers and Connor, 2003). Even though Karlsruhe spectra are recorded with one single instrument which allows for simultaneous measurements in the MIR and NIR, spectra from both spectral regions have to be treated as obtained by two different remote sounders since different detectors are operated and the optical filter and dichroic response curves are significantly different for MIR and NIR measurements. The TCCON and NDACC prescribe the CO VMR profiles which are used for the particular retrieval strategies. Here, the impact of the choice of the a priori VMR profile on retrieved DMFs of CO is analyzed. The MIR and NIR retrieval strategies are followed with (1) the standard a priori VMR profiles and (2) switched a priori VMR profiles for both retrieval approaches. For this analysis, Karlsruhe data from April 2010 to December 2014 is used and daily means for days with two or more measurements are calculated (see Fig. 5.10, left panel). Figure 5.10 (right panel) shows the absolute difference time series when XCO is retrieved with switched a priori VMR profiles. A bias of  $(-0.20 \pm 0.18)$  ppb is induced in the absolute difference time series in addition to a seasonal cycle with a standard deviation of 0.39 ppb. This corresponds to a relative difference of  $(-0.18 \pm 0.18)$  % for the bias and 0.39 % for the standard deviation of the seasonal variation.

The absolute difference time series for the XCO TCCON scaling retrieval using different a priori VMR profiles is shown in Fig. 5.11 (left panel). The number of daily means is larger in the TCCON time series (487 days) than in the NDACC time series (295 days). The spectral regions for the CO retrieval for TCCON and NDACC are both recorded by the

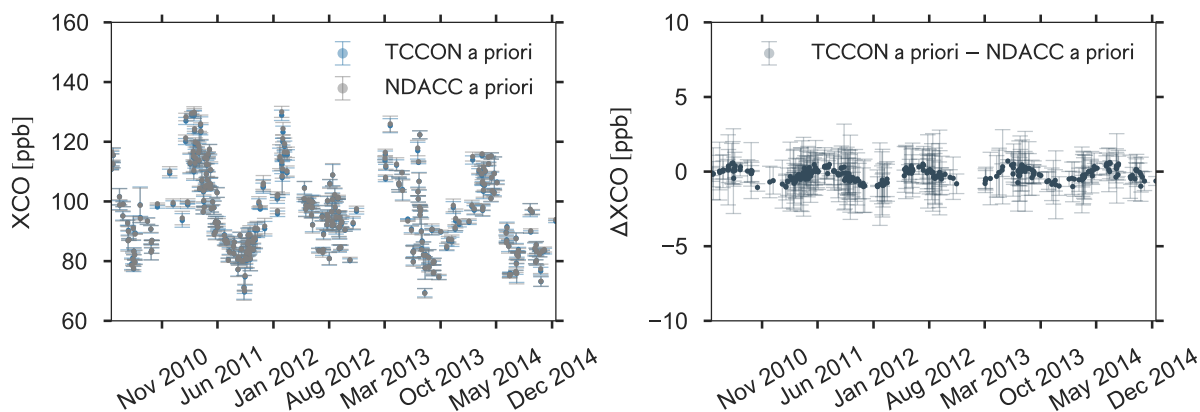


**Figure 5.10:** Daily mean time series of XCO retrieved from MIR spectra following the NDACC retrieval approach with different a priori VMR profiles (left panel). The absolute difference time series shows the impact of changing the a priori profiles on the retrieved column averaged XCO (right panel). Error bars represent the diurnal variation of XCO.

InSb diode. The narrow band filters which are mounted in an automated filter wheel in front of the InSb diode are shuffled in an order that every other spectrum covers the CO first overtone band (filter 1) leading to a larger number of TCCON-style CO measurements than NDACC-style measurements covering the fundamental band (filter 5). The recording by the InGaAs diode is independent of the filter wheel such that O<sub>2</sub> measurements in the NIR are available at the same time for both measurements using filter 1 and filter 5 in the MIR.

A significant bias of  $(0.30 \pm 0.12)$  ppb with a standard deviation of 1.15 ppb in the seasonal variation is identified in the absolute difference XCO time series (see Fig. 5.11, right panel). This corresponds to a relative difference of  $(-0.39 \pm 0.13)$  % for the bias with a standard deviation of 1.27 % for the seasonal variation. In general, it is a poor choice to use only one fixed a priori VMR profile for a scaling retrieval since a scaling retrieval approach basically relies on the knowledge of the shape of the VMR profile which, in general, changes over the year and seasons. Therefore, it is indispensable to use variable daily VMR profiles when performing a scaling retrieval of gases whose VMR profiles are not fairly constant over the year. Moreover, it is favourable to use identical a priori VMR profiles when comparing two different remote sounders. The retrieved profile  $\vec{x}$  can be expressed as:

$$\vec{x} - \vec{x}_{\text{apriori}} = \mathbf{A} (\vec{x}_{\text{true}} - \vec{x}_{\text{apriori}}) + \vec{\epsilon} \quad (5.5)$$

Here,  $\vec{x}_{\text{true}}$  represents the true atmospheric profile,  $\vec{x}_{\text{apriori}}$  the applied a priori VMR profile,  $\vec{\epsilon}$  the random and systematic error term, and  $\mathbf{A}$  the averaging kernel matrix. Therefore, using a common a priori profile leads to the same value for the difference  $(\vec{x}_{\text{true}} - \vec{x}_{\text{apriori}})$  for both retrieval strategies and eliminates differences in a direct comparison of TCCON and NDACC

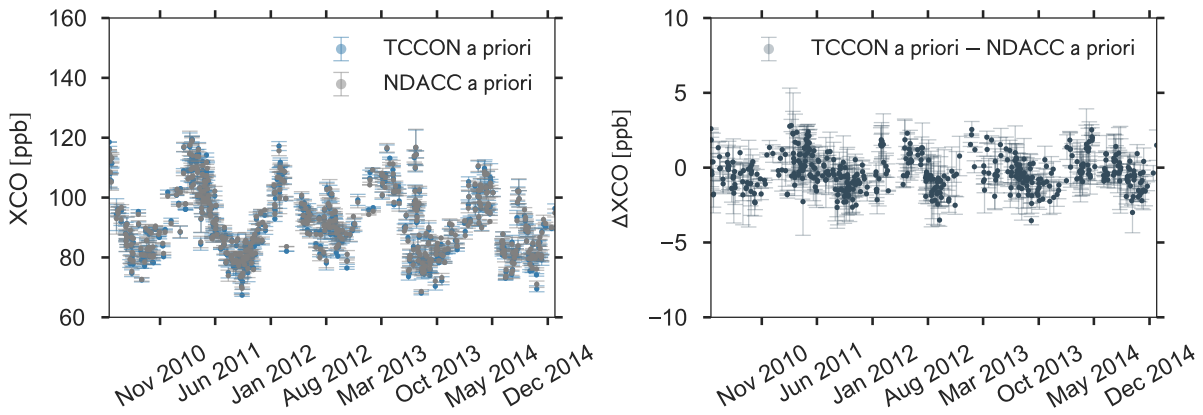


**Figure 5.11:** Same as Fig. 5.10 for XCO retrieved from NIR spectra using the TCCON retrieval approach with changed a priori VMR profiles.

data due to differing a priori VMR profiles. Nevertheless, the term  $\mathbf{A}(\vec{x}_{\text{true}} - \vec{x}_{\text{apriori}})$  in Eq. (5.5), here referred to as smoothing effect, has still to be taken into account for an intercomparison. Typically,  $\mathbf{A}$  is different for different remote sounders and also influences a direct comparison (see Sect. 5.8).

### 5.5.2 Impact of spectroscopic parameters on retrieved XCO

The HITRAN compilation (Rothman et al., 2009, 2013) provides spectroscopic parameters (e.g. line intensities, self-broadening coefficients, air-broadening coefficients, temperature-dependent coefficients, etc.) which are used by both retrieval algorithms (GFIT and PROFFIT) for the forward simulation. The impact of the spectroscopic parameters on the retrieval is not directly comparable since the TCCON and NDACC retrieval approaches use different spectral regions. For CO retrievals, the TCCON uses spectroscopic parameters which are based on the HITRAN 2012 line list (Rothman et al., 2013) whereas the NDACC uses the older HITRAN 2008 compilation (Rothman et al., 2009). The NDACC XCO time series retrieved with the HITRAN line lists from 2008 and 2012 are shown in Fig. 5.12 (upper left panel). The center left panel of Fig. 5.12 shows the absolute difference time series of both retrieved data products and indicates a bias of  $(0.05 \pm 0.17)$  ppb with a standard deviation of 0.03 ppb in the seasonal variation. This corresponds to a relative difference of  $(0.04 \pm 0.18)$  % for the bias and a standard deviation of 0.03 % in seasonal variation. The periodic maxima in  $\Delta\text{XCO}$  during the winter months (see Fig. 5.12, lower left panel, zoomed section) are mainly due to changes in the HITRAN line parameters from the 2008 to 2012 version. Compared to HITRAN 2008, the HITRAN 2012 compilation contains non-zero air-pressure induced lineshift parameters for the spectral absorption lines which are used for the NDACC CO retrieval. At the same time, the pressure broadening parameters remain unchanged. This generates an additional smear of the absorption along the spectral abscissa since an observed spectral line contains absorption contributions from many different altitudes. As a consequence, in case of an optically thick line, for example for large SZA, a smaller number of molecules achieves the same attenuation of the solar radiation (spectrally integrated over the entire line of sight). This slightly reduces the retrieved XCO values when the HITRAN 2012 line list is used. The effect is revealed in Fig. 5.12 (right column) where the slant column of CO is depicted when the two different line lists are used. The maxima in the difference time series (marked as red areas) are in phase with the maxima in the slant column time series of CO. Nevertheless, changes between retrieved CO total columns using the HITRAN 2008 and HITRAN 2012 line lists are in general small. Therefore, using the updated spectroscopic parameter list from 2012 to be conform with the TCCON line list which is based on the 2012 version, has a rather small impact of about 0.03 % on the comparison of NDACC and TCCON XCO data records.

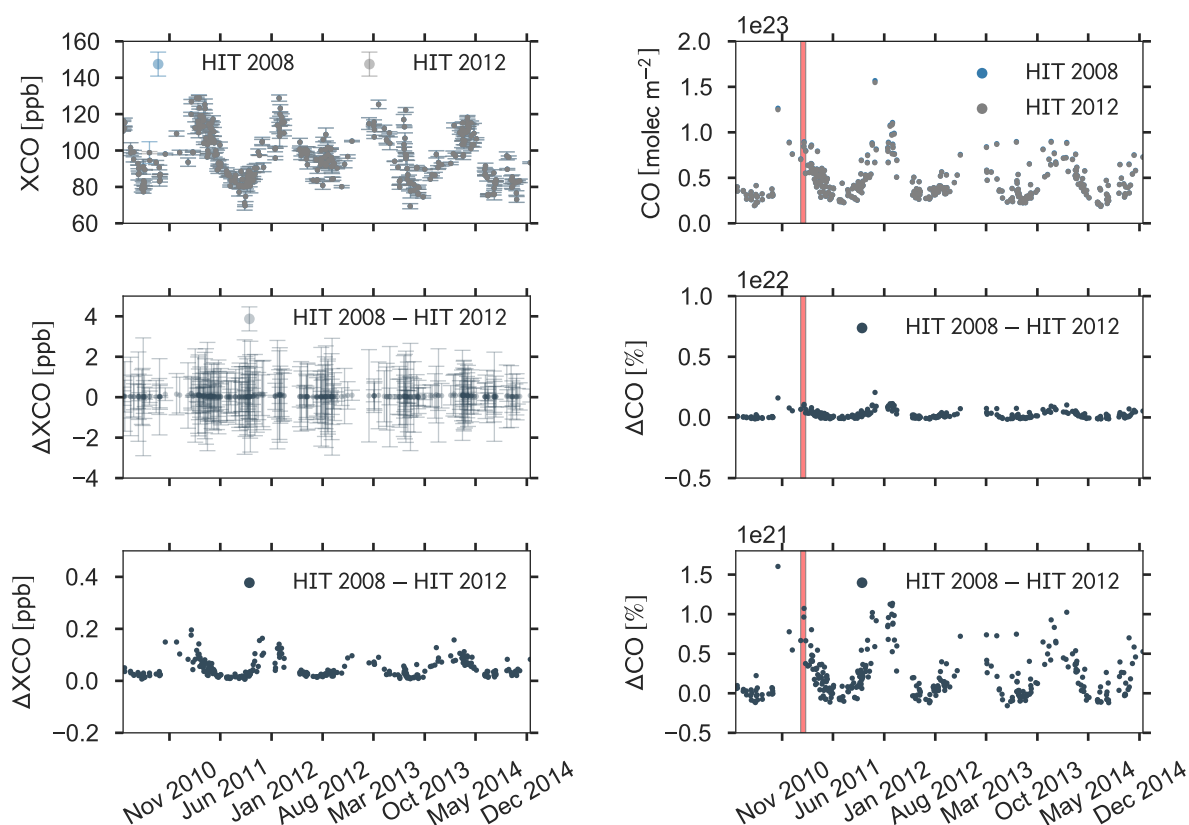


**Figure 5.12:** XCO daily mean time series following the NDACC retrieval methodology for the HITRAN 2008 (HIT 2008) and HITRAN 2012 (HIT 2012) line list parameters (left column, upper panel). The absolute difference time series (HITRAN 2008 – HITRAN 2012) is shown in the center panel and lower panel (zoomed) of the left column. Panels in the right column represent the same time period for retrieved slant columns of CO for the two different line parameter compilations. The phase of the maxima in the slant column and difference time series is marked as red area. For reasons of visibility, partly no error bars are shown.

## 5.6 Identification of differences between NDACC and TCCON XCO

A direct comparison of NDACC and TCCON XCO is essential to achieve a harmonization between both data products which are obtained by substantially different retrieval approaches. XCO time series retrieved as described in Table 5.1 and in addition following the modified TCCON retrieval strategy as described in Chap. 4 are shown in Fig. 5.13 (left panel), covering the time period ranging from August 2010 to August 2014. Typical values for XCO in Karlsruhe fluctuate around 100 ppb. Abundances of XCO decrease in spring followed by an increase in late summer. Maximum values occur around February to March (reaching up to 130 ppb) and lower values in the summer months August and September (minimum values as low as 65 ppb). The observed seasonal cycle is mainly driven by the seasonal variation in OH concentrations which acts as a CO sink in the troposphere, especially in the summer

months due to the increasing concentrations of the OH radicals. Sources for increasing abundances in the late summer are natural and anthropogenic emissions such as incomplete combustion of fossil-fuels and large-scale transports of CO. Furthermore, plumes containing combustion by-products usually increase CO concentrations in the northern hemisphere summer during the dry season as identified by the sharp peak in August 2012 and July 2013. Both time series agree with observed seasonal cycles from purely tropospheric CO columns in the northern hemisphere where maxima were also identified between February and April (Zbinden et al., 2013). A direct comparison is given in Fig. 5.13 (right panel) which shows a correlation graph of the NDACC and TCCON daily means from April 2010 to December 2014. The slope of  $0.952 \pm 0.007$  obtained from a linear fit forced through zero is significantly different from one and corresponds to a bias between both time series. The absolute difference time series (NDACC – TCCON) for the same data is shown in Fig. 5.14 (first panel). An absolute bias of  $(4.47 \pm 0.17)$  ppb is identified with a clear difference in the seasonality (standard deviation of 2.06 ppb). This corresponds to a relative bias of  $(4.76 \pm 0.18)$  % with a standard deviation of 2.28 %. This bias is in good agreement with the observed bias of about 4 ppb between globally distributed NDACC and TCCON XCO data products (Borsdorff et al., 2016). In the next sections, the origin of the bias and seasonality between TCCON and NDACC XCO data is identified and quantified in more detail which is indispensable towards a harmonization of both data sets.

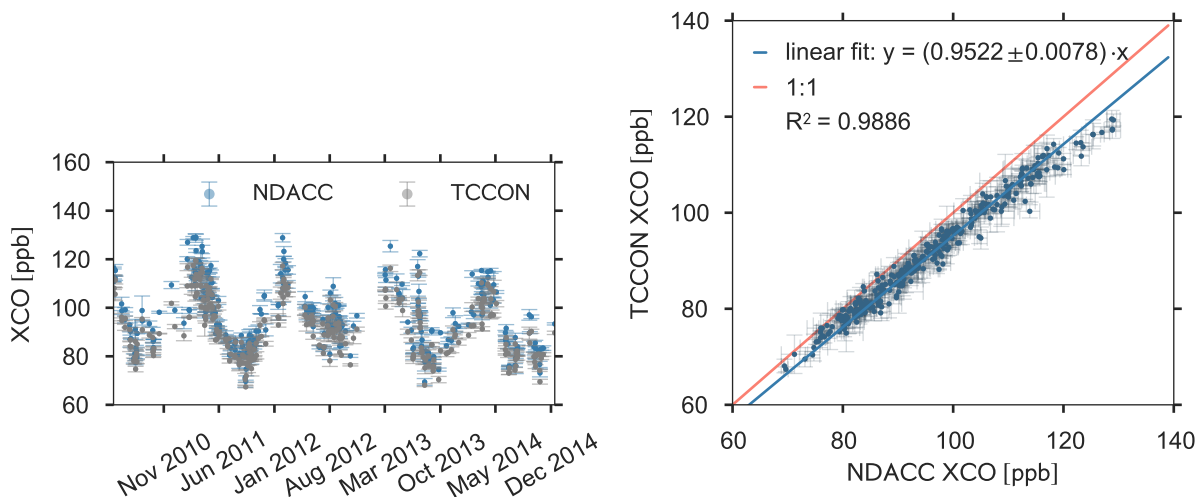


**Figure 5.13:** Daily mean time series of NDACC and TCCON XCO (left panel). The right panel shows the corresponding scatter graph. The slope is obtained from a linear fit forced through zero. Error bars represent the diurnal variation of XCO.

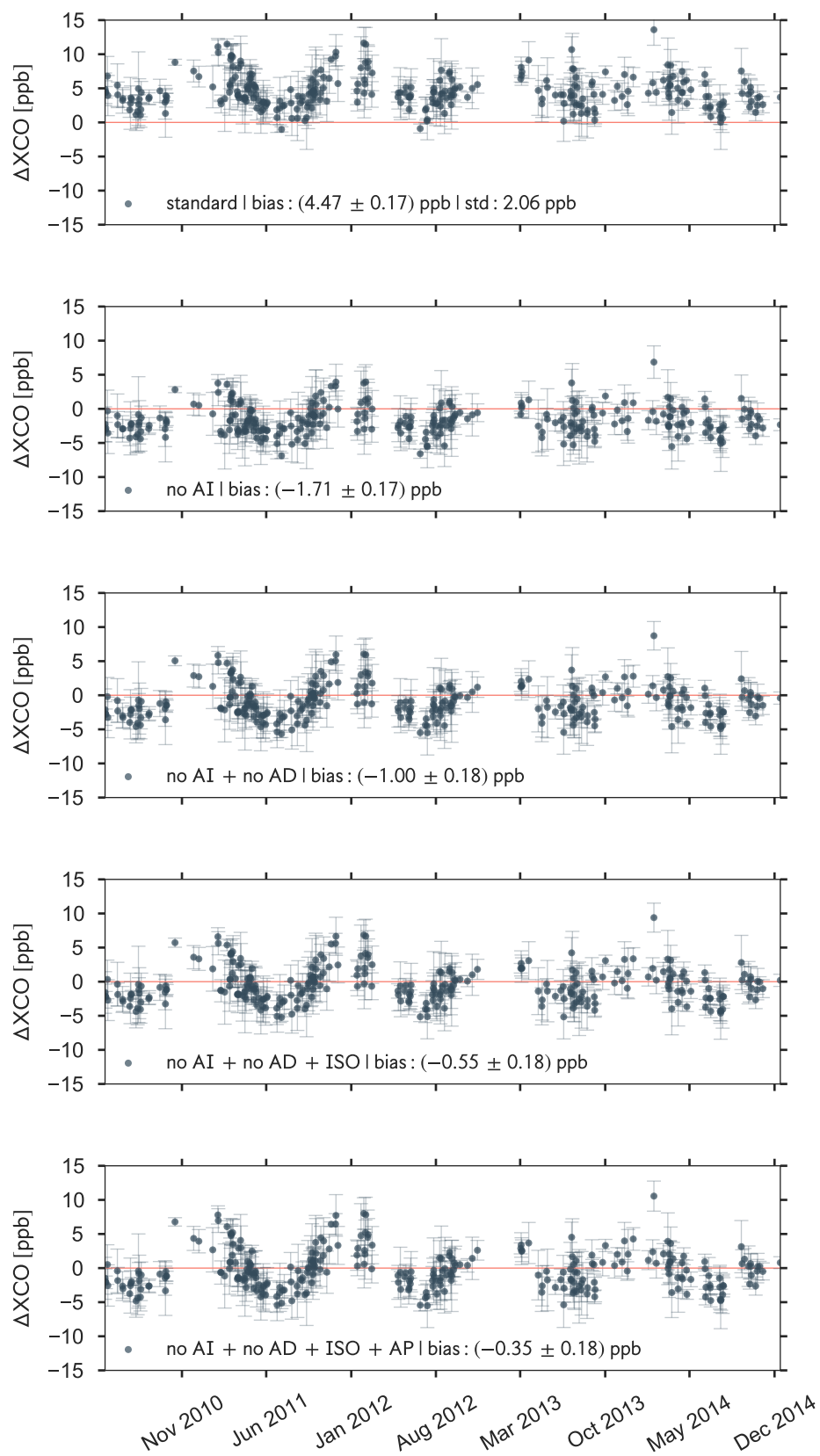
## 5.7 Analysis of bias

### 5.7.1 Impact of the air mass independent calibration factor

The observed bias between TCCON and NDACC XCO is mainly induced by the scaling of the TCCON data to the WMO scale. To account for spectroscopic inadequacies, TCCON measurements are tied to the WMO scale by dividing DMFs of the target gas by an air mass independent correction factor (AI) obtained from in situ measurements over several TCCON sites. This correction factor is  $1.0672 \pm 0.0200$  for XCO and by far the largest factor compared to the other correction terms for XCO<sub>2</sub>, XCH<sub>4</sub>, and XN<sub>2</sub>O (see Sect. 3.2.1, Table 3.3). This indicates that the spectroscopic parameters for CO around the 4250 cm<sup>-1</sup> spectral region are the origin of this deviation (Wunch et al., 2011) even though a difference of about 2 % is contributed by spectroscopic inadequacies from O<sub>2</sub>. In contrast, the NDACC data products are not tied to the WMO scale and therefore NDACC XCO is not scaled in any post-processing routine. To quantify the impact of the air mass independent calibration factor, the absolute difference time series (NDACC – TCCON) without applying AI to TCCON XCO is shown in Fig. 5.14 (second panel). The mean offset is reduced to  $(-1.71 \pm 0.17)$  ppb. Therefore, not applying AI reduces the bias, but changes sign. For future studies, it would be also favorable to tie the NDACC XCO data set to the WMO scale. Such an in situ calibration for NDACC XCO data will most likely minimize the bias between NDACC and TCCON XCO and therefore will improve a joint use of both data sets. Since an aircraft overflight can be a very involved and expensive undertaking, for the moment, NDACC XCO data might be scaled to the TCCON XCO data using the TCCON data set as a transfer standard to calibrate NDACC XCO to the WMO scale. Such a constant inter calibration factor can be determined from the mean bias between both data sets. For Karlsruhe, a factor of 1.048 with an corresponding error of 0.002 is determined if data from April 2010 to December 2014 is taken into account. For the moment, if Karlsruhe MIR and NIR XCO are jointly used for scientific studies or validation purposes, it is recommended to divide NDACC XCO by this inter calibration factor. Moreover, a global multi-station inter calibration factor for NDACC and TCCON XCO is desirable to further support the results in this study and the study by Borsdorff et al. (2016).

---

**Figure 5.14 (facing page):** Daily mean absolute difference time series (NDACC – TCCON) of XCO as retrieved following the NDACC and TCCON retrieval approaches (first panel, labelled as 'standard'), when no air mass independent correction factor (AI) is applied in the TCCON retrieval strategy (second panel), when no air mass dependent correction factor (AD) is applied in the TCCON retrieval strategy (third panel), when a modified treatment of isotopic identities is applied for the MIR NDACC retrieval approach (ISO, fourth panel), and when common a priori (AP) VMR profiles are used (fifth panel). Error bars are obtained from the diurnal variation of XCO. Zero lines are marked red and are for eye-guidance only.



### 5.7.2 Impact of the airmass dependent correction factor

As part of the post-processing routine, TCCON XCO is also corrected for airmass dependent artefacts. As described in Sect. 4.2, Wunch et al. (2011) and Wunch et al. (2015), the airmass dependent correction factor (AD) is determined from the symmetric component of the diurnal variation. Here, the impact of applying AD on retrieved TCCON XCO data is analyzed. TCCON XCO retrieved with and without AD with respect to the SZA for different months is depicted in Fig. 5.15. If AD is applied, XCO is elevated for large SZA between  $60^\circ$  and  $80^\circ$  by about 2 ppb, obtained from the mean enhancement of all months in this SZA region. This shift of XCO abundances for large SZAs corrects for airmass dependent artefacts affecting the TCCON data product. The change in XCO due to AD and the difference between TCCON and NDACC XCO is shown in Fig. 5.16.  $\Delta XCO$  between NDACC and TCCON is closer to zero for large SZA ( $> 50^\circ$ ) when no AD is applied, whereas applying AD reduces the SZA dependence which leads to a constant offset between NDACC and TCCON XCO for all SZA. Therefore, applying the airmass dependent

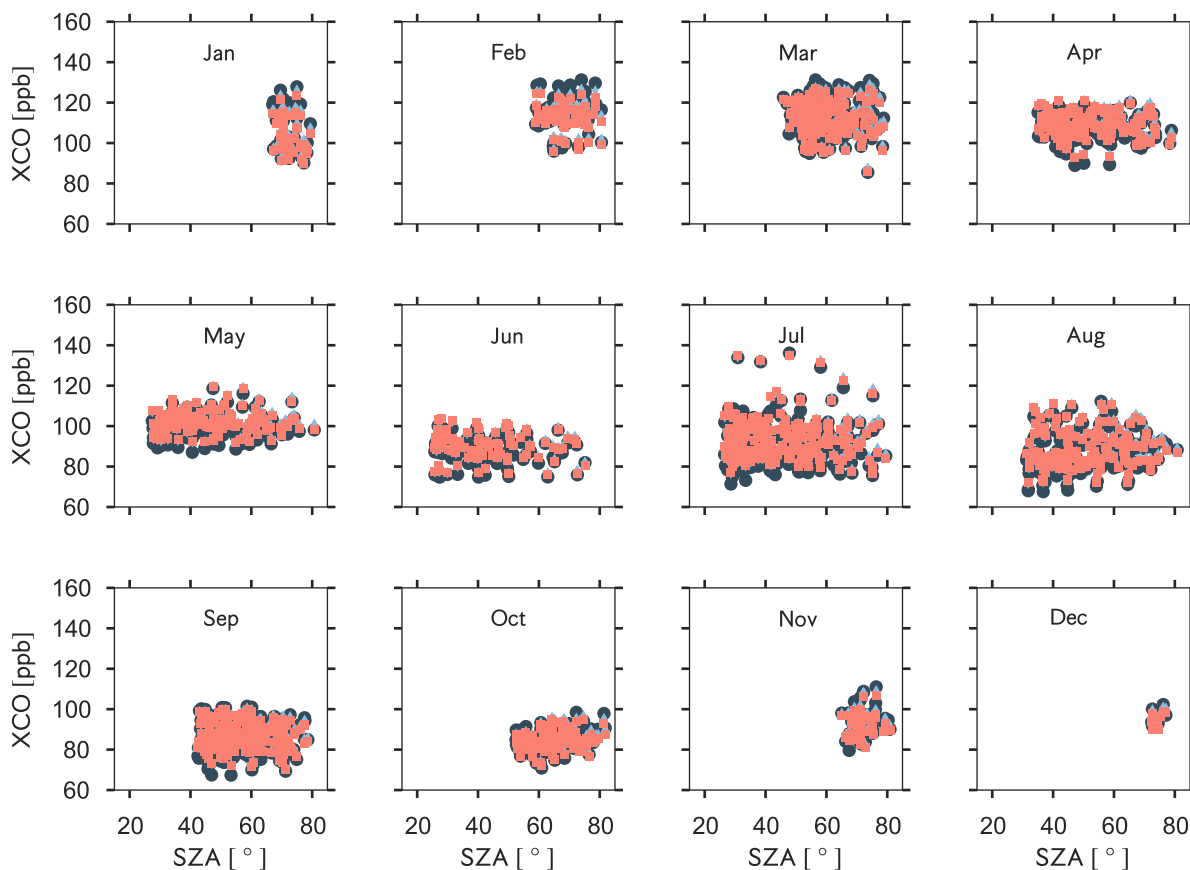


**Figure 5.15:** Monthly airmass dependence of XCO for NDACC XCO (dark blue circles), for TCCON XCO with AD applied (light blue diamonds), and without airmass dependent correction factor applied (orange squares). For reasons of visibility, no error bars are shown.

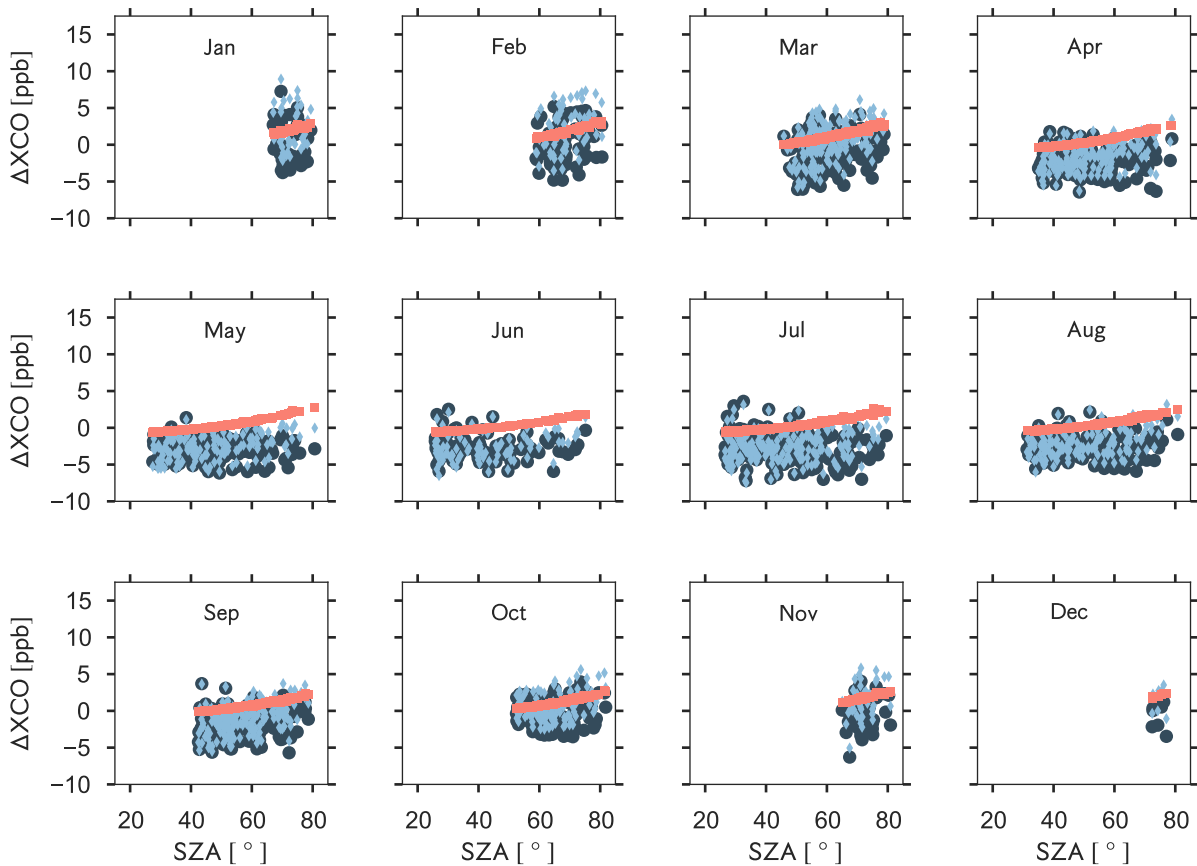


**Figure 5.16:** Monthly air mass dependent XCO differences between NDACC XCO and TCCON XCO with AD applied (dark blue circles), between NDACC XCO and TCCON XCO without air mass dependent correction factor applied (light blue diamonds), and the direct impact of AD on retrieved TCCON CO (orange squares). For reasons of visibility, no error bars are shown.

correction factor results in two effects: (1) compensating air mass dependent artefacts in the TCCON XCO time series and as a consequence (2) enlarging the bias between TCCON and NDACC daily mean XCO, especially for large SZAs. The latter is seen in the difference time series (see Fig. 5.14, third panel). The bias is further reduced to a mean value of  $(-1.00 \pm 0.18)$  ppb when no air mass dependent correction factor is applied to TCCON XCO. For NDACC, no clear air mass dependence is observed, for example as seen in Fig. 5.15 for the months November, December, and January, where the corrected TCCON XCO data fairly agrees with the NDACC XCO data for large SZAs.

### 5.7.3 Impact of different isotopic identities

The observed bias is also driven by the isotopic identities of the spectral absorption lines analyzed within the spectral windows used for TCCON and NDACC retrievals. The line intensity parameter provided by HITRAN is typically multiplied by the standard isotopic abundances derived from De Bièvre et al. (1984). Hence, when the HITRAN line lists

are used as spectroscopic auxiliary data to retrieve CO concentrations, the corresponding retrieval algorithm returns the total VMR of CO regardless of the isotopic identity of the spectral lines. The wide spectral windows as used for the TCCON retrieval contain a variety of spectral lines from the two most abundant CO isotopologues  $^{12}\text{C}^{16}\text{O}$  and  $^{13}\text{C}^{16}\text{O}$ . The same holds for the narrow microwindow as used for the NDACC retrieval strategy. The three microwindows contain absorption lines from the isotopologues  $^{12}\text{C}^{16}\text{O}$  at  $2158.3\text{ cm}^{-1}$  and from  $^{13}\text{C}^{16}\text{O}$  at  $2057.86\text{ cm}^{-1}$  and at  $2069.66\text{ cm}^{-1}$ . If atmospheric isotopic ratios deviate from the De Bièvre et al. (1984) reference values, the GFIT algorithm parameterizes the atmospheric fractionation using improved values. For  $^{12}\text{C}^{16}\text{O}$  and  $^{13}\text{C}^{16}\text{O}$ , the GFIT algorithm uses an altitude independent  $\delta^{13}\text{C}(\text{CO})$  value (the ratio of the isotopologues  $^{13}\text{C}^{16}\text{O}$  and  $^{12}\text{C}^{16}\text{O}$ ) of  $-27\text{ ‰}$  (Wang et al., 2012). This parameter mainly accounts for spectroscopic biases between different isotopologues and therefore corrects spectroscopic inconsistencies in the HITRAN line lists. Even though the microwindows for the MIR retrieval also contain spectral absorption lines of  $^{12}\text{C}^{16}\text{O}$  and  $^{13}\text{C}^{16}\text{O}$ , such a correction is not taken into account. Thus, the same isotopic treatment for  $^{12}\text{C}^{16}\text{O}$  and  $^{13}\text{C}^{16}\text{O}$  has been implemented into the NDACC retrieval strategy by adjusting the reported line strengths. Figure 5.14 (fourth panel) shows the difference time series when the modified treatment of isotopic identities in the MIR is applied. A reduction of the mean bias to an overall value of  $(-0.55 \pm 0.18)$  ppb between both data sets is observed. Therefore, for future updates of the NDACC retrieval strategy, it might be favorable to choose a modified treatment of different isotopic identities.

#### 5.7.4 Impact of differing a priori VMR profiles

As seen in Sect. 5.5.1, the choice of the a priori VMR profiles has a non-negligible impact on retrieved XCO data from both networks. To eliminate the impact of differing a priori VMR profiles, the daily a priori VMR profiles as used by TCCON are utilized as a priori information for the NDACC retrieval. As seen in Sect. 5.5.1, the mean bias of NDACC XCO changes by about 0.18%. Fig. 5.14 (fifth panel) shows the absolute difference time series using common a priori VMR profiles for both retrievals in the MIR and NIR. The mean bias is further reduced to  $(-0.35 \pm 0.18)$  ppb.

#### 5.7.5 Remaining bias

Although the largest proportions contributing to the observed overall mean bias between NDACC and TCCON XCO data is identified, a bias of about  $-0.35$  ppb remains between both data sets. Differences induced by the retrieval algorithms (e.g. numerical calculations etc.) can be largely ruled out as seen in Sect. 5.5 and in Dohe (2013). Findings from Sect.

5.4 also reveal that the total column of O<sub>2</sub> retrieved from both algorithms, which is used to calculate column averaged DMFs of CO, are in good agreement and have negligible impact on the observed bias. Differences might be induced by inconsistencies in spectroscopic parameters for MIR and NIR spectral ranges. The TCCON uses a modified line list based on HITRAN 2012 in the NIR whereas NDACC maintains the HITRAN 2008 line list in its original form for CO retrievals. Inter alia, major changes from HITRAN 2008 to HITRAN 2012 were applied to the spectral region covering the CO overtone absorption band in the NIR (e.g. line intensities, self- and air-broadening parameters, temperature dependence and air-induced line shifts) while line intensities, temperature dependence, etc. remained unchanged in the spectral domain where the CO fundamental band is located. In this study, the largest proportions of the observed bias has been identified and quantified which improves a future common usage of both data sets for scientific studies and validation purposes.

## 5.8 Analysis of seasonal variations between NDACC and TCCON XCO

The direct comparison between TCCON and NDACC XCO shows a seasonal variation in the difference time series. TCCON XCO data are larger from February through mid of October whereas NDACC data is consistently larger from mid of October through January. The comparison shows a standard deviation of 2.06 ppb in the difference time series. This corresponds to a relative variation of 2.28 %. Whereas a bias between two time series can be corrected by the scaling of the time series by an empirically determined constant factor, a seasonal variation usually cannot be accounted for by applying a single correction term. The observed seasonality is related to differing averaging kernels (AVK) in the MIR and NIR. Retrieved DMFs from both networks are subject to the usual restrictions of the remote-sensing technique including differing and non-perfect AVKs. Typically AVKs are functions of pressure, slant column, and SZA and therefore variable with season. Moreover, measurements in the MIR and NIR should be considered as done by different observing systems with different instrumental characteristics. In the next sections, the impact of the smoothing effect on the comparison between NDACC and TCCON XCO is analyzed using model simulations for CO to account for different smoothing functions induced by different AVKs in the MIR and NIR. For this analysis, NDACC and TCCON XCO retrievals are performed using common a priori VMR profiles (daily TCCON a priori VMR profiles) to eliminate the effect of differing prior information (see Sect. 5.5.1).

### 5.8.1 Applying averaging kernels to model data

Following Rodgers (2000) and Rodgers and Connor (2003), the retrieved VMR profile  $\vec{x}$  of a gas is related to the true atmospheric VMR profile and the a priori VMR profile by:

$$\vec{x} - \vec{x}_{\text{apriori}} = \mathbf{A} (\vec{x}_{\text{true}} - \vec{x}_{\text{apriori}}) + \vec{\epsilon} \quad (5.6)$$

Again,  $\vec{x}_{\text{true}}$  represents the true atmospheric profile,  $\vec{x}_{\text{apriori}}$  the applied a priori VMR profile,  $\vec{\epsilon}$  the random and systematic error in the measurement and forward model, and  $\mathbf{A}$  the averaging kernel matrix. Its row vectors are typically peaked functions which describe the vertical resolution of the retrieval in a qualitative way (Rodgers and Connor, 2003). A smoothed profile  $\vec{x}_s$  can be computed when assuming a modeled VMR profile  $\vec{x}_{\text{model}}$  as an ideal measurement or true atmospheric profile. When neglecting the measurement noise, this leads to:

$$\vec{x}_s = \mathbf{A} (\vec{x}_{\text{model}} - \vec{x}_{\text{apriori}}) + \vec{x}_{\text{apriori}} \quad (5.7)$$

The smoothed profile  $\vec{x}_s$  represents the profile which would be retrieved if the assumed true atmospheric profile would be measured by an remote sensing instrument, e.g. the Karlsruhe FTS with the corresponding AVKs. The difference  $\Delta\vec{x}_s$  between smoothed profiles using differing MIR and NIR AVKs is given by:

$$\Delta\vec{x}_s = (\mathbf{A}_{\text{MIR}} - \mathbf{A}_{\text{NIR}}) (\vec{x}_{\text{model}} - \vec{x}_{\text{apriori}}) \quad (5.8)$$

Here,  $\mathbf{A}_{\text{MIR}}$  and  $\mathbf{A}_{\text{NIR}}$  represent the AVKs from the MIR and NIR retrieval, respectively. Moreover, same a priori VMR profiles are assumed. Equation (5.8) describes the impact of differing AVKs on retrieved total columns when  $\Delta\vec{x}_s$  is integrated over pressure layers which is of major interest in this analysis. Therefore, if the seasonal variation in the absolute difference time series between TCCON and NDACC XCO is driven by the smoothing effect, it is expected to see a similar seasonality (with a comparable amplitude and phase) in the residual of the smoothed model data.

### 5.8.2 ECHAM/MESSy Atmospheric Chemistry model data

The modeled CO VMR profiles which are utilized as true atmospheric VMR profiles to estimate the smoothing error in the comparison between MIR and NIR XCO are obtained from the ECHAM/MESSy Atmospheric Chemistry (EMAC) model. This description of the EMAC model is based on Kirner et al. (2011). EMAC is a numerical chemistry and climate simulation system that uses the 5th generation European Centre Hamburg general circulation model (ECHAM5, Roeckner et al., 2006) as the base layer model. EMAC includes a variety of submodels for the description of processes in the troposphere and

middle atmosphere including their interactions with land, oceans, and human impacts (Jöckel et al., 2006). The EMAC model uses the second version of the Modular Earth Submodel System (MESSy2) as a framework to link multi-institutional computer codes (Jöckel et al., 2010).

For this investigation, EMAC was applied in the T42L39MA-resolution using the ECHAM5 version 5.3.02 and MESSy version 2.50. The simulation was performed with a spherical truncation of T42 which corresponds to a grid box of  $2.8^\circ$  by  $2.8^\circ$  in longitude and latitude with 39 vertical hybrid pressure levels up to 0.01 hPa (approx. 80 km). The time integration step is 10 minutes. In this study, the output of CO VMR profiles is done at local noon at 12:00:00. In the stratosphere, the vertical resolution lies between 1.5 and 2.5 km and decreases with increasing altitude.

The simulation includes a comprehensive chemistry set-up from the troposphere to the lower mesosphere. Gas phase chemistry and heterogeneous reactions are calculated using the submodel Module Efficiently Calculating the Chemistry of the Atmosphere (MECCA, Sander et al., 2005) and the Multiphase Stratospheric Box Model (MSBM, Kirner et al., 2011). Absorption cross sections for photolysis are taken from Sander et al. (2011) whereas gas phase reaction rate coefficients are derived from Atkinson et al. (2007). ERA-Interim reanalysis (Dee et al., 2011) from the European Centre for Medium-range Weather Forecasts (ECMWF) is used in this simulation to nudge the simulations between the boundary layer and below 1 hPa to reproduce realistic synoptic conditions. For this, a Newtonian relaxation technique for the prognostic variables temperature, vorticity, divergence, and the surface pressure is implemented in EMAC.

### 5.8.3 Estimation of the smoothing effect

To estimate the impact of the smoothing effect on the seasonal variation in the direct comparison between NDACC and TCCON XCO, the modeled CO profiles are smoothed using the AVKs from both retrieval strategies. The modeled CO profiles are interpolated to the same height levels as used in the corresponding retrieval strategies. One CO profile per day at 12:00:00 UTC simulated by the EMAC model is used in this analysis. The modeled CO profiles for the time period April 2010 to December 2014 are shown in Fig. 5.17. The model resolution of approximately  $2.8^\circ$  by  $2.8^\circ$  in latitude and longitude covers an area which includes the coordinates  $49.1^\circ$  N,  $8.4^\circ$  E where the Karlsruhe FTS is located.

In general, the AVK matrix element  $\mathbf{A}_{m,n}$  represents the change in the retrieved VMR profile at an altitude level  $m$  when the true atmospheric VMR profile is perturbed at an altitude level  $n$ . For a scaling retrieval as used within the TCCON, the rows of the AVK

matrix have the same shape, only the amplitudes differ by a constant factor for all altitudes. For a full profile retrieval as applied for NDACC analyses, every row contains an individual response. An AVK matrix can be transferred into a dimensionless column averaging kernel, which represents the sensitivity of the retrieved total column to a perturbation of the partial column at a certain altitude. Figure 5.18 shows the NDACC and TCCON column averaging kernels for CO for different SZA. The MIR column averaging kernels fluctuate around 1.0 with a sensitivity between 0.9 and 1.1 for the lower and middle troposphere whereas for larger altitudes, the fluctuation becomes slightly larger. The NIR column averaging kernels strongly deviate from one in the stratosphere reaching values of up to 2.0 for small SZA. In general, in the NIR spectral range, the spectral line broadening is stronger affected by the Doppler broadening mechanism than in the MIR. This leads to less information which can be retrieved from the observed line shape. Figure 5.19 (left panel) shows XCO obtained from smoothed CO model VMR profiles when applying Eq. (5.7) and using the MIR and NIR AVKs. These two smoothed time series are utilized to estimate the smoothing effect in the absolute difference time series between NDACC and TCCON XCO. The residual of the smoothed time series (see Fig. 5.19, right panel) shows an oscillating behaviour with a standard deviation of 1.65 ppb in seasonality, similar to the seasonal variation observed in the absolute difference time series between NDACC and TCCON XCO. This estimation shows that the smoothing effect induced due to differing AVKs is not negligible when comparing NDACC and TCCON XCO, even though spectra in both spectral regions are recorded by the same instrument. The phase and amplitude of the oscillation is comparable to the seasonality of the originally retrieved difference between TCCON and NDACC XCO which is also depicted in Fig. 5.19 (right panel).

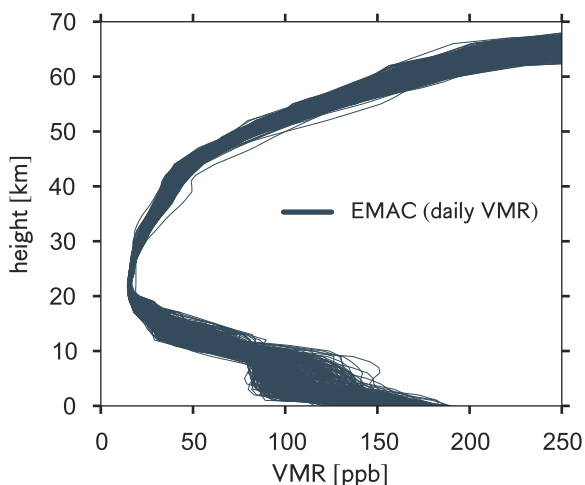


**Figure 5.17:** Simulated EMAC CO VMR profiles from April 2010 to December 2014 which are used in this study to estimate the smoothing effect between retrieved XCO from NDACC MIR and TCCON NIR measurements.

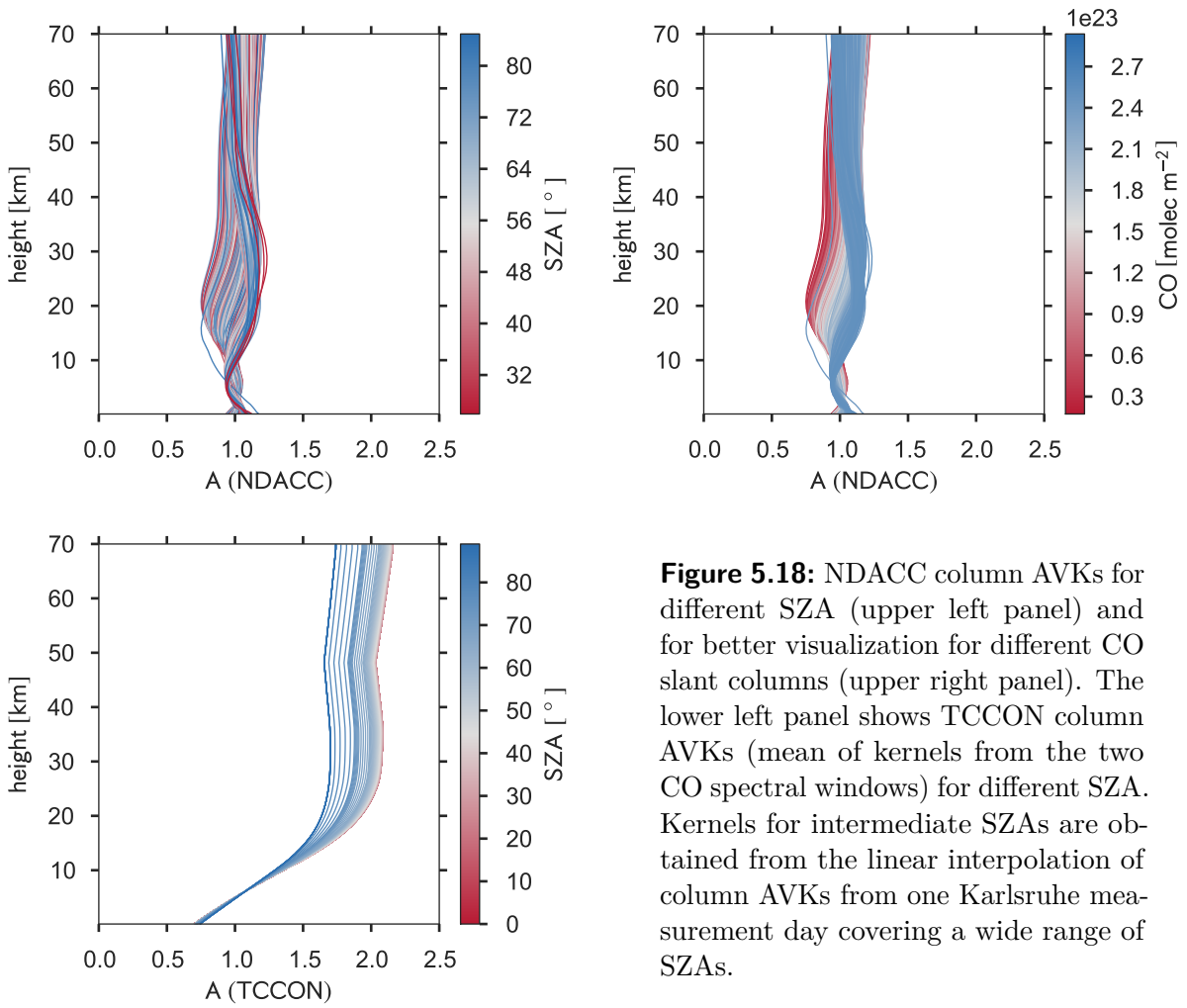


**Figure 5.18:** NDACC column AVKs for different SZA (upper left panel) and for better visualization for different CO slant columns (upper right panel). The lower left panel shows TCCON column AVKs (mean of kernels from the two CO spectral windows) for different SZA. Kernels for intermediate SZAs are obtained from the linear interpolation of column AVKs from one Karlsruhe measurement day covering a wide range of SZAs.

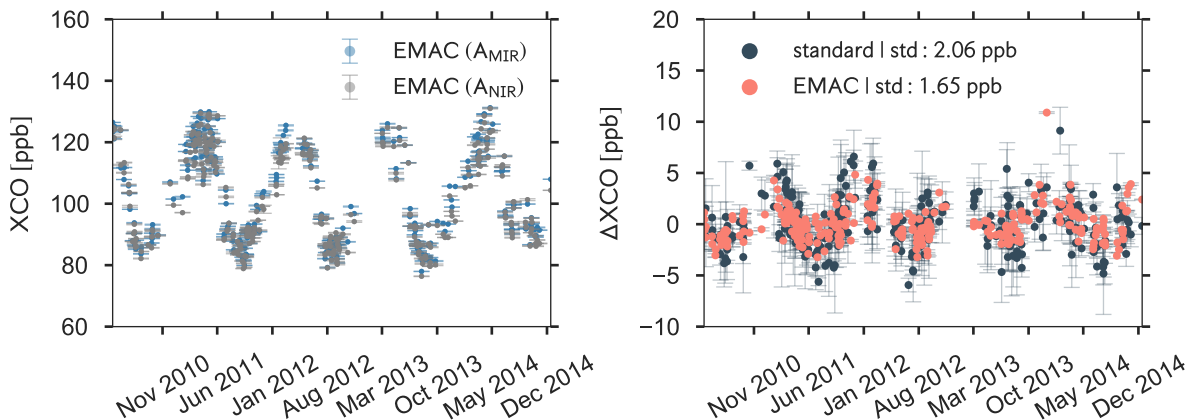


**Figure 5.19:** Smoothed daily mean XCO time series using NDACC and TCCON column AVKs and simulated EMAC VMR profiles (left panel). The absolute difference time series (right panel) is an estimate for the smoothing effect which is observed when the standard NDACC and TCCON retrieval approach is applied. Error bars indicate the diurnal variation of XCO. For reasons of visualisation, the bias is removed in the right panel.

Therefore, the seasonal variation in the comparison of NDACC and TCCON XCO data can be largely explained by smoothing effects induced by differing AVKs from differing vertical sensitivities of the retrievals in the MIR and NIR. For the harmonization and potential joint use of XCO from NDACC and TCCON as a validation data set, it is important to note that  $\Delta XCO$  changes in sign with seasonality. Therefore, the impact of the smoothing effect from differing MIR and NIR AVKs has to be taken into account in addition to the scaling factor to account for the bias when using NDACC and TCCON XCO as a joint data set for scientific studies and validation purposes.

## 5.9 Conclusions

In this study, a comparison between Karlsruhe NDACC and TCCON XCO retrievals from April 2010 to December 2014 from the fundamental absorption band ( $4.7 \mu\text{m}$ ) in the MIR and the first overtone absorption band ( $2.3 \mu\text{m}$ ) in the NIR was performed. A bias of  $(4.47 \pm 0.17)$  ppb between XCO retrieved from NDACC and TCCON using different retrieval algorithms and retrieval approaches is observed with a standard deviation of 2.06 ppb in the seasonal variation. Different sources which contribute to the observed bias are identified and quantified.

The airmass independent correction factor (1.0672) which is applied to TCCON XCO to correct the retrieved DMFs for inadequacies in spectroscopic parameters is the main source of the observed bias. The bias is reduced to  $(-1.71 \pm 0.17)$  ppb when this factor is not applied to TCCON XCO data. An additional component which contributes to the overall bias is the airmass dependent correction factor (contributing with 0.71 ppb) whereas a TCCON compatible treatment of different isotopic identities in the MIR retrieval strategy reduces the bias by 0.45 ppb. The choice of differing spectroscopic line lists in the MIR has minor influence on the overall bias (0.05 ppb). The impact of different a priori VMR profiles for the MIR and NIR retrievals contributes with 0.20 ppb to the observed bias. The remaining bias of  $(-0.35 \pm 0.18)$  ppb might be subject to imperfect knowledge of the spectroscopic parameters in the MIR and NIR. The impact due to deviations in the total column of  $O_2$  for the calculation of XCO is negligible with  $(0.04 \pm 0.02)$  ppb. This also holds for the impact of using different retrieval algorithms as already shown by Dohe (2013) when same retrieval strategies are followed by both algorithms.

The seasonal variation in the bias (standard deviation of 2.06 ppb) between both XCO data products is estimated using simulated CO VMR profiles by the EMAC model. It is shown that the smoothing effect, caused by differing AVK in the MIR and NIR, is the key

driver of the seasonality in the difference time series.

For a potential synergetic use of Karlsruhe XCO from TCCON and NDACC, it is necessary to apply the obtained inter calibration factor of 1.048 to the NDACC XCO to tie the MIR data set to the WMO scale using the TCCON data product as a transfer standard. This inter calibration accounts for the observed constant bias. Moreover, different vertical sensitivities for both retrievals have to be taken into account for a harmonization of both data sets. To utilize both data sets as one joint primary data record, satellite validations would need to include same a priori VMR profiles as used by both networks (or apply an a posteriori conversion) and also account for different averaging kernels. For the latter, models can be used as a transfer standard between MIR and NIR column retrievals to account for seasonal variations in the bias. If NDACC and TCCON XCO data is desired to be jointly used, it is critical to be aware of these effects. Moreover, for the future use of XCO from NDACC and TCCON as a joint validation data set, it is desirable to obtain an airmass independent correction factor for NDACC XCO retrievals from aircraft overflights to improve the comparability between both XCO time series.



## 6 Summary and Outlook

In this work, trace gas measurements from different spectral regions using FTIR spectroscopy were analyzed. Instrumental influences on measured total columns were identified and corrected. A comparison between column averaged dry-air mole fractions of carbon monoxide measured in different spectral regions has been performed. Differences were identified and quantified, aiming at a harmonization of NDACC and TCCON data records. A combined primary validation data set will provide a wider spatial and temporal coverage than either network individually. This is highly desirable for future satellite validations and model studies.

The Karlsruhe FTS is an extension over standard NDACC and TCCON instruments. The instrumental prototype setup allows for simultaneous measurements in the MIR and NIR spectral regions. This unique optical setup induces broad variations in the background continuum of measured spectra. These variations account for differences in column averaged dry-air mole fractions which exceed the network's precision (e.g. 1 ppm for XCO<sub>2</sub>). In this work, a new analysis approach has been developed, allowing for an appropriate treatment of the background continuum variations. A higher order Legendre polynomial fit has been enabled to properly fit the background continuum. The order of the fit is determined by the analysis of black body cavity spectra. The new retrieval strategy significantly improves the root mean square for residuals of the most important TCCON target gases CO<sub>2</sub>, CO, CH<sub>4</sub>, and N<sub>2</sub>O. Moreover, airmass dependent artefacts are minimized. The new modified retrieval strategy improves Karlsruhe TCCON data in context of other TCCON stations and reduces a site-specific bias at Karlsruhe. DMFs of CO<sub>2</sub> changed by 0.2 %, CH<sub>4</sub> by 0.1 %, CO by 2.0 %, and N<sub>2</sub>O by 0.7 %. Applying the developed analysis strategy to other TCCON stations, the change in XCO<sub>2</sub> (about 0.3 ppm) and XCH<sub>4</sub> (about 1.0 ppb) is not negligible. These findings are highly valuable to further improve the consistency of the TCCON and are published in Kiel et al. (2016b). In the future release of the TCCON retrieval algorithm, the California Institute of Technology and KIT will seek to produce a uniform recommendation for modelling the background continuum for stations other than Karlsruhe.

---

Due to its unique instrumental setup, Karlsruhe is a favorable FTS site to compare differences between gas abundances measured in different spectral regions. XCO retrieved from the fundamental band in the MIR at  $4.7\ \mu\text{m}$  and from the first overtone band in the NIR at  $2.3\ \mu\text{m}$  were compared. A constant bias of about 4.5 ppb has been identified with a seasonal variation of about 2.1 ppb. Contributions to the constant bias were identified and quantified. The bias is mainly induced by a posteriori corrections to TCCON XCO data. The airmass independent correction factor (1.0672) obtained from aircraft/AirCore in situ measurements over TCCON stations changes XCO by about 6.1 ppm in Karlsruhe. The absolute bias was reduced to 1.7 ppb when this factor was not taken into account. Several other factors contribute to the overall bias. These include the TCCON airmass dependent correction factor (0.7 ppb), a modified treatment of different isotopic identities for the retrieval in the MIR spectral range (0.4 ppb), and different a priori VMR profiles and spectroscopic line parameters (0.3 ppb). The remaining bias of about 0.4 ppb might be caused by imperfect knowledge of the spectroscopic parameters in the MIR and NIR. The seasonal variation in the comparison between NDACC and TCCON XCO was estimated by the smoothing effect. Differing vertical resolutions for measurements in the MIR and NIR are characterized by the column averaging kernels. Assuming simulated CO profiles from the ECHAM/MESy Atmospheric Chemistry model as the true atmospheric state, the seasonal variation was largely explained by the smoothing effect. For the future use of Karlsruhe XCO from NDACC and TCCON as a joint validation data set, it is favorable to intercalibrate NDACC XCO to the WMO scale using the TCCON XCO data record as a transfer standard. The intercalibration factor of 1.048 is obtained from the direct comparison of NDACC and TCCON XCO and is published in Kiel et al. (2016a).

The study of instrumental influences on measured spectra in different spectral regions can be seen as a pilot project from both networks to expand their spectral coverages. This study helps to identify potential present and future inconsistencies within both networks. Several TCCON stations plan to expand their spectral coverage towards the MIR. The presented work helps overcoming instrumental influences and at the same time maintaining the network's precision and consistency. The expansion of spectral coverages will merge both networks in the near future, making a harmonization of both data sets indispensable. Different vertical sensitivities of measurements in the MIR and NIR, temperature dependencies of the chosen spectral windows, different spectroscopic line parameter and assumptions about the error budget will make the use of one joint primary data record challenging. A harmonization procedures as presented in this work will become crucial for gases which are accessible in the MIR and NIR spectral region. Moreover, the Karlsruhe data record can be utilized for a synthesis of retrievals in the MIR and NIR,

combining the advantages of both spectral regions. This will improve the vertical sensitivity of the measurement which is highly desirable for gases with high vertical variabilities.



## 7 Bibliography

- Abramowitz, M. and Stegun, I. A.: Handbook of Mathematical Functions with Formulas, Graphs, and Mathematical Tables, Vol. 9, United States Department of Commerce, National Bureau of Standards (NBS), New York, 1972.
- Abrams, M. C., Toon, G. C., and Schindler, R. A.: Practical example of the correction of Fourier-transform spectra for detector nonlinearity, *Appl. Opt.*, 33, 6307–6314, doi:10.1364/AO.33.006307, 1994.
- Atkinson, R., Baulch, D. L., Cox, R. A., Crowley, J. N., Hampson, R. F., Hynes, R. G., Jenkin, M. E., Rossi, M. J., and Troe, J.: Evaluated kinetic and photochemical data for atmospheric chemistry: Volume III – gas phase reactions of inorganic halogens, *Atmos. Chem. Phys.*, 7, 981–1191, doi:10.5194/acp-7-981-2007, 2007.
- Bala, G., Caldeira, K., Wickett, M., Phillips, T. J., Lobell, D. B., Delire, C., and Mirin, A.: Combined climate and carbon-cycle effects of large-scale deforestation, *Proceedings of the National Academy of Sciences*, 104, 6550–6555, doi:10.1073/pnas.0608998104, 2007.
- Beer, R.: *Remote Sensing by Fourier Transform Spectrometry*, Wiley Interscience publication, Wiley & Sons, New York, 1992.
- Bengtsson, L.: The global atmospheric water cycle, *Environmental Research Letters*, 5, 025 202, doi:10.1088/1748-9326/5/2/025002, 2010.
- Bergland, G.: A radix-eight fast Fourier transform subroutine for real-valued series, *IEEE Transactions on Audio and Electroacoustics*, 17, 138–144, doi:10.1109/TAU.1969.1162043, 1969.
- Bernath, P. F., McElroy, C. T., Abrams, M. C., Boone, C. D., Butler, M., Camy-Peyret, C., Carleer, M., Clerbaux, C., Coheur, P.-F., Colin, R., DeCola, P., DeMazière, M., Drummond, J. R., Dufour, D., Evans, W. F. J., Fast, H., Fussen, D., Gilbert, K., Jennings, D. E., Llewellyn, E. J., Lowe, R. P., Mahieu, E., McConnell, J. C., McHugh, M., McLeod, S. D., Michaud, R., Midwinter, C., Nassar, R., Nichitiu, F., Nowlan, C., Rinsland, C. P., Rochon, Y. J., Rowlands, N., Semeniuk, K., Simon, P., Skelton, R., Sloan, J. J., Soucy, M.-A., Strong, K., Tremblay, P., Turnbull, D., Walker, K. A., Walkty, I., Wardle, D. A.,

- Wehrle, V., Zander, R., and Zou, J.: Atmospheric Chemistry Experiment (ACE): Mission overview, *Geophysical Research Letters*, 32, doi:10.1029/2005GL022386, 115S01, 2005.
- Born, M. and Oppenheimer, R.: Zur Quantentheorie der Molekeln, *Annalen der Physik*, 84, 457–484, doi:10.1002/andp.19273892002, 1927.
- Borsdorff, T., Tol, P., Williams, J. E., de Laat, J., aan de Brugh, J., Nédélec, P., Aben, I., and Landgraf, J.: Carbon monoxide total columns from SCIAMACHY 2.3  $\mu\text{m}$  atmospheric reflectance measurements: towards a full-mission data product (2003–2012), *Atmos. Meas. Tech.*, 9, 227–248, doi:10.5194/amt-9-227-2016, 2016.
- Buchwitz, M., Khlystova, I., Bovensmann, H., and Burrows, J. P.: Three years of global carbon monoxide from SCIAMACHY: comparison with MOPITT and first results related to the detection of enhanced CO over cities, *Atmos. Chem. Phys.*, 7, 2399–2411, 2007.
- Chagas, J. C. S., Newnham, D. A., Smith, K. M., and Shine, K. P.: Impact of new measurements of oxygen collision-induced absorption on estimates of short-wave atmospheric absorption, *Quarterly Journal of the Royal Meteorological Society*, 128, 2377–2396, doi:10.1256/qj.01.159, 2002.
- Clerbaux, C., George, M., Turquety, S., Walker, K. A., Barret, B., Bernath, P., Boone, C., Borsdorff, T., Cammas, J. P., Catoire, V., Coffey, M., Coheur, P.-F., Deeter, M., De Mazière, M., Drummond, J., Duchatelet, P., Dupuy, E., de Zafra, R., Eddounia, F., Edwards, D. P., Emmons, L., Funke, B., Gille, J., Griffith, D. W. T., Hannigan, J., Hase, F., Höpfner, M., Jones, N., Kagawa, A., Kasai, Y., Kramer, I., Le Flochmoën, E., Livesey, N. J., López-Puertas, M., Luo, M., Mahieu, E., Murtagh, D., Nédélec, P., Pazmino, A., Pumphrey, H., Ricaud, P., Rinsland, C. P., Robert, C., Schneider, M., Senten, C., Stiller, G., Strandberg, A., Strong, K., Sussmann, R., Thouret, V., Urban, J., and Wiacek, A.: CO measurements from the ACE-FTS satellite instrument: data analysis and validation using ground-based, airborne and spaceborne observations, *Atmos. Chem. Phys.*, 8, 2569–2594, doi:10.5194/acp-8-2569-2008, 2008.
- Crutzen, P. J.: Tropospheric Ozone: Regional and Global Scale Interactions, Chap. Tropospheric Ozone: An Overview, 3–32, Springer Netherlands, Dordrecht, doi:10.1007/978-94-009-2913-5\_1, 1988.
- Daniel, J. S. and Solomon, S.: On the climate forcing of carbon monoxide, *Journal of Geophysical Research: Atmospheres*, 103, 13 249–13 260, doi:10.1029/98JD00822, 1998.
- Daube, B. C. J., Boering, K. A., Andrews, A. E., and Wofsy, S. C.: A High-Precision Fast-Response Airborne CO<sub>2</sub> Analyzer for In Situ Sampling from the Surface to the

- Middle Stratosphere, *Journal of Atmospheric and Oceanic Technology*, 19, 1532–1543, doi:10.1175/1520-0426(2002)019<1532:AHPFRA>2.0.CO;2, 2002.
- De Bièvre, P., Gallet, M., Holden, N. E., and Barnes, I. L.: Isotopic Abundances and Atomic Weights of the Elements, *Journal of Physical and Chemical Reference Data*, 13, 809–891, doi:10.1063/1.555720, 1984.
- de Laat, A. T. J., Gloudemans, A. M. S., Schrijver, H., Aben, I., Nagahama, Y., Suzuki, K., Mahieu, E., Jones, N. B., Paton-Walsh, C., Deutscher, N. M., Griffith, D. W. T., De Mazière, M., Mittermeier, R. L., Fast, H., Notholt, J., Palm, M., Hawat, T., Blumenstock, T., Hase, F., Schneider, M., Rinsland, C., Dzhola, A. V., Grechko, E. I., Poberovskii, A. M., Makarova, M. V., Mellqvist, J., Strandberg, A., Sussmann, R., Borsdorff, T., and Rettinger, M.: Validation of five years (2003–2007) of SCIAMACHY CO total column measurements using ground-based spectrometer observations, *Atmos. Meas. Tech.*, 3, 1457–1471, doi:10.5194/amt-3-1457-2010, 2010.
- Dee, D. P., Uppala, S. M., Simmons, A. J., Berrisford, P., Poli, P., Kobayashi, S., Andrae, U., Balmaseda, M. A., Balsamo, G., Bauer, P., Bechtold, P., Beljaars, A. C. M., van de Berg, L., Bidlot, J., Bormann, N., Delsol, C., Dragani, R., Fuentes, M., Geer, A. J., Haimberger, L., Healy, S. B., Hersbach, H., Hólm, E. V., Isaksen, L., Kållberg, P., Köhler, M., Matricardi, M., McNally, A. P., Monge-Sanz, B. M., Morcrette, J.-J., Park, B.-K., Peubey, C., de Rosnay, P., Tavolato, C., Thépaut, J.-N., and Vitart, F.: The ERA-Interim reanalysis: configuration and performance of the data assimilation system, *Quarterly Journal of the Royal Meteorological Society*, 137, 553–597, doi:10.1002/qj.828, 2011.
- Deeter, M. N., Emmons, L. K., Francis, G. L., Edwards, D. P., Gille, J. C., Warner, J. X., Khattatov, B., Ziskin, D., Lamarque, J.-F., Ho, S.-P., Yudin, V., Attié, J.-L., Packman, D., Chen, J., Mao, D., and Drummond, J. R.: Operational carbon monoxide retrieval algorithm and selected results for the MOPITT instrument, *Journal of Geophysical Research: Atmospheres*, 108, doi:10.1029/2002JD003186, 4399, 2003.
- Demtröder, W.: *Experimentalphysik 3: Atome, Moleküle und Festkörper*, Chap. Moleküle, 297–359, Springer Berlin Heidelberg, Berlin, Heidelberg, doi:10.1007/978-3-642-03911-9\_9, 2010.
- Deutscher, N. M., Griffith, D. W. T., Bryant, G. W., Wennberg, P. O., Toon, G. C., Washenfelder, R. A., Keppel-Aleks, G., Wunch, D., Yavin, Y., Allen, N. T., Blavier, J.-F., Jiménez, R., Daube, B. C., Bright, A. V., Matross, D. M., Wofsy, S. C., and Park, S.: Total column CO<sub>2</sub> measurements at Darwin, Australia – site description and calibration against in situ aircraft profiles, *Atmos. Meas. Tech.*, 3, 947–958, doi:10.5194/amt-3-947-2010, 2010.

- Dlugokencky, E. J., Bruhwiler, L., White, J. W. C., Emmons, L. K., Novelli, P. C., Montzka, S. A., Masarie, K. A., Lang, P. M., Crotwell, A. M., Miller, J. B., and Gatti, L. V.: Observational constraints on recent increases in the atmospheric CH<sub>4</sub> burden, *Geophysical Research Letters*, 36, doi:10.1029/2009GL039780, 118803, 2009.
- Dohe, S.: Measurements of atmospheric CO<sub>2</sub> columns using ground-based FTIR spectra, Ph.D. thesis, Karlsruhe Institute of Technology, 2013.
- Dörnbrack, A.: Atmospheric Physics: Background – Methods – Trends, Chap. The Atmosphere: Vast, Shallow, and Full of Subtleties, 3–16, Springer Berlin Heidelberg, Berlin, Heidelberg, doi:10.1007/978-3-642-30183-4\_1, 2012.
- Elkins, J. and Dutton, G.: Nitrous oxide and sulfur hexafluoride, *Bull. Am. Meteorol. Soc.*, 90, 38–39, 2009.
- Fellgett, P. B.: On the Ultimate Sensitivity and Practical Performance of Radiation Detectors, *J. Opt. Soc. Am.*, 39, 970–976, doi:10.1364/JOSA.39.000970, 1949.
- Forman, M. L., Steel, W. H., and Vanasse, G. A.: Correction of Asymmetric Interferograms Obtained in Fourier Spectroscopy, *J. Opt. Soc. Am.*, 56, 59–63, doi:10.1364/JOSA.56.000059, 1966.
- Fowler, D., Pilegaard, K., Sutton, M., Ambus, P., Raivonen, M., Duyzer, J., Simpson, D., Fagerli, H., Fuzzi, S., Schjoerring, J., Granier, C., Nefstel, A., Isaksen, I., Laj, P., Maione, M., Monks, P., Burkhardt, J., Daemmgen, U., Neiryneck, J., Personne, E., Wichink-Kruit, R., Butterbach-Bahl, K., Flechard, C., Tuovinen, J., Coyle, M., Gerosa, G., Loubet, B., Altimir, N., Gruenhage, L., Ammann, C., Cieslik, S., Paoletti, E., Mikkelsen, T., Ro-Poulsen, H., Cellier, P., Cape, J., Horv ath, L., Loreto, F., Niinemets,  ., Palmer, P., Rinne, J., Misztal, P., Nemitz, E., Nilsson, D., Pryor, S., Gallagher, M., Vesala, T., Skiba, U., Br uggemann, N., Zechmeister-Boltenstern, S., Williams, J., O’Dowd, C., Facchini, M., de Leeuw, G., Flossman, A., Chaumerliac, N., and Erisman, J.: Atmospheric composition change: Ecosystems–Atmosphere interactions, *Atmospheric Environment*, 43, 5193 – 5267, doi:http://dx.doi.org/10.1016/j.atmosenv.2009.07.068, 2009.
- Frankenberg, C., Meirink, J. F., Bergamaschi, P., Goede, A. P. H., Heimann, M., K rner, S., Platt, U., van Weele, M., and Wagner, T.: Satellite cartography of atmospheric methane from SCIAMACHY on board ENVISAT: Analysis of the years 2003 and 2004, *Journal of Geophysical Research: Atmospheres*, 111, doi:10.1029/2005JD006235, d07303, 2006.
- Frankenberg, C., Pollock, R., Lee, R. A. M., Rosenberg, R., Blavier, J.-F., Crisp, D., O’Dell, C. W., Osterman, G. B., Roehl, C., Wennberg, P. O., and Wunch, D.: The Orbiting

- Carbon Observatory (OCO-2): spectrometer performance evaluation using pre-launch direct sun measurements, *Atmos. Meas. Tech.*, 8, 301–313, doi:10.5194/amt-8-301-2015, 2015.
- Frey, M., Hase, F., Blumenstock, T., Groß, J., Kiel, M., Mengistu Tsidu, G., Schäfer, K., Sha, M. K., and Orphal, J.: Calibration and instrumental line shape characterization of a set of portable FTIR spectrometers for detecting greenhouse gas emissions, *Atmos. Meas. Tech.*, 8, 3047–3057, doi:10.5194/amt-8-3047-2015, 2015.
- Garcia, R. R., Marsh, D. R., Kinnison, D. E., Boville, B. A., and Sassi, F.: Simulation of secular trends in the middle atmosphere, 1950–2003, *Journal of Geophysical Research: Atmospheres*, 112, doi:10.1029/2006JD007485, d09301, 2007.
- Geibel, M. C., Messerschmidt, J., Gerbig, C., Blumenstock, T., Chen, H., Hase, F., Kolle, O., Lavrič, J. V., Notholt, J., Palm, M., Rettinger, M., Schmidt, M., Sussmann, R., Warneke, T., and Feist, D. G.: Calibration of column-averaged CH<sub>4</sub> over European TCCON FTS sites with airborne in-situ measurements, *Atmos. Chem. Phys.*, 12, 8763–8775, doi:10.5194/acp-12-8763-2012, 2012.
- Gisi, M.: Setup of precise camera based solar tracker systems and greenhouse gas measurements using a modified portable spectrometer, Ph.D. thesis, Karlsruhe Institute of Technology, 2012.
- Gisi, M., Hase, F., Dohe, S., and Blumenstock, T.: Camtracker: a new camera controlled high precision solar tracker system for FTIR-spectrometers, *Atmos. Meas. Tech.*, 4, 47–54, doi:10.5194/amt-4-47-2011, 2011.
- Gisi, M., Hase, F., Dohe, S., Blumenstock, T., Simon, A., and Keens, A.: XCO<sub>2</sub>-measurements with a tabletop FTS using solar absorption spectroscopy, *Atmos. Meas. Tech.*, 5, 2969–2980, doi:10.5194/amt-5-2969-2012, 2012.
- GLOBALVIEW-CO<sub>2</sub>: Cooperative Atmospheric Data Integration Project – Carbon Dioxide, CD-ROM, NOAA-ESRL, Boulder, Colorado, 2010.
- Haken, H. and Wolf, C.: Molekülphysik und Quantenchemie: Einführung in die experimentellen und theoretischen Grundlagen, Chap. Rotationsspektren, 159–177, Springer Berlin Heidelberg, Berlin, Heidelberg, doi:10.1007/3-540-30315-4\_9, 2006a.
- Haken, H. and Wolf, C.: Molekülphysik und Quantenchemie: Einführung in die experimentellen und theoretischen Grundlagen, Chap. Schwingungsspektren, 179–207, Springer Berlin Heidelberg, Berlin, Heidelberg, doi:10.1007/3-540-30315-4\_10, 2006b.

- Hansen, J., Ruedy, R., Sato, M., and Lo, K.: GLOBAL SURFACE TEMPERATURE CHANGE, *Reviews of Geophysics*, 48, doi:10.1029/2010RG000345, rG4004, 2010.
- Hase, F.: Inversion von Spurengasprofilen aus hochaufgelösten bodengebundenen FTIR-Messungen in Absorption, Ph.D. thesis, Forschungszentrum Karlsruhe, 2000.
- Hase, F.: Improved instrumental line shape monitoring for the ground-based, high-resolution FTIR spectrometers of the Network for the Detection of Atmospheric Composition Change, *Atmos. Meas. Tech.*, 5, 603–610, doi:10.5194/amt-5-603-2012, 2012.
- Hase, F., Blumenstock, T., and Paton-Walsh, C.: Analysis of the instrumental line shape of high-resolution Fourier transform IR spectrometers with gas cell measurements and new retrieval software, *Appl. Opt.*, 38, 3417–3422, doi:10.1364/AO.38.003417, 1999.
- Hase, F., Hannigan, J., Coffey, M., Goldman, A., Höpfner, M., Jones, N., Rinsland, C., and Wood, S.: Intercomparison of retrieval codes used for the analysis of high-resolution, ground-based FTIR measurements, *Journal of Quantitative Spectroscopy and Radiative Transfer*, 87, 25–52, doi:10.1016/j.jqsrt.2003.12.008, 2004.
- Hase, F., Frey, M., Blumenstock, T., Groß, J., Kiel, M., Kohlhepp, R., Mengistu Tsidu, G., Schäfer, K., Sha, M. K., and Orphal, J.: Application of portable FTIR spectrometers for detecting greenhouse gas emissions of the major city Berlin, *Atmos. Meas. Tech.*, 8, 3059–3068, doi:10.5194/amt-8-3059-2015, 2015.
- Hausmann, P., Sussmann, R., and Smale, D.: Contribution of oil and natural gas production to renewed increase in atmospheric methane (2007-2014): top-down estimate from ethane and methane column observations, *Atmospheric Chemistry and Physics*, 16, 3227–3244, doi:10.5194/acp-16-3227-2016, 2016.
- Held, I. M. and Soden, B. J.: Robust Responses of the Hydrological Cycle to Global Warming, *Journal of Climate*, 19, 5686–5699, doi:10.1175/JCLI3990.1, 2006.
- Höpfner, M., Glatthor, N., Grabowski, U., Kellmann, S., Kiefer, M., Linden, A., Orphal, J., Stiller, G., von Clarmann, T., Funke, B., and Boone, C. D.: Sulfur dioxide (SO<sub>2</sub>) as observed by MIPAS/Envisat: temporal development and spatial distribution at 15–45 km altitude, *Atmospheric Chemistry and Physics*, 13, 10 405–10 423, doi:10.5194/acp-13-10405-2013, 2013.
- Höpfner, M., Volkamer, R., Grabowski, U., Grutter, M., Orphal, J., Stiller, G., von Clarmann, T., and Wetzal, G.: First detection of ammonia (NH<sub>3</sub>) in the Asian monsoon upper troposphere, *Atmospheric Chemistry and Physics Discussions*, 2016, 1–22, doi: 10.5194/acp-2016-392, 2016.

- Inoue, M., Morino, I., Uchino, O., Nakatsuru, T., Yoshida, Y., Yokota, T., Wunch, D., Wennberg, P. O., Roehl, C. M., Griffith, D. W. T., Velasco, V. A., Deutscher, N. M., Warneke, T., Notholt, J., Robinson, J., Sherlock, V., Hase, F., Blumenstock, T., Rettinger, M., Sussmann, R., Kyrö, E., Kivi, R., Shiomi, K., Kawakami, S., De Mazière, M., Arnold, S. G., Feist, D. G., Barrow, E. A., Barney, J., Dubey, M., Schneider, M., Iraci, L., Podolske, J. R., Hillyard, P., Machida, T., Sawa, Y., Tsuboi, K., Matsueda, H., Sweeney, C., Tans, P. P., Andrews, A. E., Biraud, S. C., Fukuyama, Y., Pittman, J. V., Kort, E. A., and Tanaka, T.: Bias corrections of GOSAT SWIR XCO<sub>2</sub> and XCH<sub>4</sub> with TCCON data and their evaluation using aircraft measurement data, *Atmospheric Measurement Techniques Discussions*, 2016, 1–49, doi:10.5194/amt-2015-366, 2016.
- IPCC: Climate Change 2007: The Physical Science Basis. Contribution of Working Group I to the Fourth Assessment Report of the Intergovernmental Panel on Climate Change, Cambridge University Press, Cambridge, United Kingdom and New York, NY, USA, 2007.
- IPCC: Climate Change 2013: The Physical Science Basis. Contribution of Working Group I to the Fifth Assessment Report of the Intergovernmental Panel on Climate Change, Cambridge University Press, Cambridge, United Kingdom and New York, NY, USA, doi:10.1017/CBO9781107415324, 2013.
- Irion, F. W., Gunson, M. R., Toon, G. C., Chang, A. Y., Eldering, A., Mahieu, E., Manney, G. L., Michelsen, H. A., Moyer, E. J., Newchurch, M. J., Osterman, G. B., Rinsland, C. P., Salawitch, R. J., Sen, B., Yung, Y. L., and Zander, R.: Atmospheric Trace Molecule Spectroscopy (ATMOS) Experiment Version 3 data retrievals, *Appl. Opt.*, 41, 6968–6979, doi:10.1364/AO.41.006968, 2002.
- Jöckel, P., Tost, H., Pozzer, A., Brühl, C., Buchholz, J., Ganzeveld, L., Hoor, P., Kerkweg, A., Lawrence, M., Sander, R., Steil, B., Stiller, G., Tanarhte, M., Taraborrelli, D., van Aardenne, J., and Lelieveld, J.: The atmospheric chemistry general circulation model ECHAM5/MESy1: consistent simulation of ozone from the surface to the mesosphere, *Atmos. Chem. Phys.*, 6, 5067–5104, doi:10.5194/acp-6-5067-2006, 2006.
- Jöckel, P., Kerkweg, A., Pozzer, A., Sander, R., Tost, H., Riede, H., Baumgaertner, A., Gromov, S., and Kern, B.: Development cycle 2 of the Modular Earth Submodel System (MESy2), *Geosci. Model Dev.*, 3, 717–752, doi:10.5194/gmd-3-717-2010, 2010.
- Jones, P. D., New, M., Parker, D. E., Martin, S., and Rigor, I. G.: Surface air temperature and its changes over the past 150 years, *Reviews of Geophysics*, 37, 173–199, doi:10.1029/1999RG900002, 1999.

- Kalnay, E., Kanamitsu, M., Kistler, R., Collins, W., Deaven, D., Gandin, L., Iredell, M., Saha, S., White, G., Woollen, J., Zhu, Y., Leetmaa, A., Reynolds, R., Cheliah, M., Ebisuzaki, W., Higgins, W., Janowiak, J., Mo, K. C., Ropelewski, C., Wang, J., Jenne, R., and Joseph, D.: The NCEP/NCAR 40-Year Reanalysis Project, *Bulletin of the American Meteorological Society*, 77, 437–471, doi:10.1175/1520-0477(1996)077<0437:TNYRP>2.0.CO;2, 1996.
- Karion, A., Sweeney, C., Tans, P., and Newberger, T.: AirCore: An Innovative Atmospheric Sampling System, *Journal of Atmospheric and Oceanic Technology*, 27, 1839–1853, doi:10.1175/2010JTECHA1448.1, 2010.
- Keppel-Aleks, G., Toon, G. C., Wennberg, P. O., and Deutscher, N. M.: Reducing the impact of source brightness fluctuations on spectra obtained by Fourier-transform spectrometry, *Appl. Opt.*, 46, 4774–4779, doi:10.1364/AO.46.004774, 2007.
- Keppel-Aleks, G., Wennberg, P. O., and Schneider, T.: Sources of variations in total column carbon dioxide, *Atmospheric Chemistry and Physics*, 11, 3581–3593, doi:10.5194/acp-11-3581-2011, 2011.
- Kiel, M., Hase, F., Blumenstock, T., and Kirner, O.: Comparison of XCO abundances from the Total Carbon Column Observing Network and the Network for the Detection of Atmospheric Composition Change measured in Karlsruhe, *Atmospheric Measurement Techniques*, 9, 2223–2239, doi:10.5194/amt-9-2223-2016, 2016a.
- Kiel, M., Wunch, D., Wennberg, P. O., Toon, G. C., Hase, F., and Blumenstock, T.: Improved retrieval of gas abundances from near-infrared solar FTIR spectra measured at the Karlsruhe TCCON station, *Atmospheric Measurement Techniques*, 9, 669–682, doi:10.5194/amt-9-669-2016, 2016b.
- Kirner, O., Ruhnke, R., Buchholz-Dietsch, J., Jöckel, P., Brühl, C., and Steil, B.: Simulation of polar stratospheric clouds in the chemistry-climate-model EMAC via the submodel PSC, *Geosci. Model Dev.*, 4, 169–182, doi:10.5194/gmd-4-169-2011, 2011.
- Klappenbach, F., Bertleff, M., Kostinek, J., Hase, F., Blumenstock, T., Agusti-Panareda, A., Razinger, M., and Butz, A.: Accurate mobile remote sensing of XCO<sub>2</sub> and XCH<sub>4</sub> latitudinal transects from aboard a research vessel, *Atmospheric Measurement Techniques*, 8, 5023–5038, doi:10.5194/amt-8-5023-2015, 2015.
- Kopp, G. and Lean, J. L.: A new, lower value of total solar irradiance: Evidence and climate significance, *Geophysical Research Letters*, 38, doi:10.1029/2010GL045777, l01706, 2011.
- Kramer, I.: Time series of tropospheric trace gases derived from ground-based FTIR measurements, Ph.D. thesis, Karlsruhe Institute of Technology, 2007.

- Kurylo, M. J.: Network for the detection of stratospheric change, *Proc. Soc. Photo-Opt. Instrum. Eng.*, 1491, 168–174, doi:10.1117/12.46658, 1991.
- Le Quéré, C., Moriarty, R., Andrew, R. M., Canadell, J. G., Sitch, S., Korsbakken, J. I., Friedlingstein, P., Peters, G. P., Andres, R. J., Boden, T. A., Houghton, R. A., House, J. I., Keeling, R. F., Tans, P., Arneeth, A., Bakker, D. C. E., Barbero, L., Bopp, L., Chang, J., Chevallier, F., Chini, L. P., Ciais, P., Fader, M., Feely, R. A., Gkritzalis, T., Harris, I., Hauck, J., Ilyina, T., Jain, A. K., Kato, E., Kitidis, V., Klein Goldewijk, K., Koven, C., Landschützer, P., Lauvset, S. K., Lefèvre, N., Lenton, A., Lima, I. D., Metzl, N., Millero, F., Munro, D. R., Murata, A., Nabel, J. E. M. S., Nakaoka, S., Nojiri, Y., O’Brien, K., Olsen, A., Ono, T., Pérez, F. F., Pfeil, B., Pierrot, D., Poulter, B., Rehder, G., Rödenbeck, C., Saito, S., Schuster, U., Schwinger, J., Séférian, R., Steinhoff, T., Stocker, B. D., Sutton, A. J., Takahashi, T., Tilbrook, B., van der Laan-Luijkx, I. T., van der Werf, G. R., van Heuven, S., Vandemark, D., Viovy, N., Wiltshire, A., Zaehle, S., and Zeng, N.: Global Carbon Budget 2015, *Earth System Science Data*, 7, 349–396, doi:10.5194/essd-7-349-2015, 2015.
- Liu, Y., Lin, J., Huang, G., Guo, Y., and Duan, C.: Simple empirical analytical approximation to the Voigt profile, *J. Opt. Soc. Am. B.*, 18, 666–672, doi:10.1364/JOSAB.18.000666, 2001.
- Logan, J. A., Prather, M. J., Wofsy, S. C., and McElroy, M. B.: Tropospheric chemistry: A global perspective, *Journal of Geophysical Research: Oceans*, 86, 7210–7254, doi:10.1029/JC086iC08p07210, 1981.
- Luo, M., Cicerone, R. J., and Russell, J. M.: Analysis of Halogen Occultation Experiment HF versus CH<sub>4</sub> correlation plots: Chemistry and transport implications, *Journal of Geophysical Research: Atmospheres*, 100, 13 927–13 937, doi:10.1029/95JD00621, 1995.
- Marsh, D. R., Mills, M. J., Kinnison, D. E., Lamarque, J.-F., Calvo, N., and Polvani, L. M.: Climate Change from 1850 to 2005 Simulated in CESM1(WACCM), *Journal of Climate*, 26, 7372–7391, doi:10.1175/JCLI-D-12-00558.1, 2013.
- Meerkötter, R. and Vázquez-Navarro, M.: Atmospheric Physics: Background – Methods – Trends, Chap. Earth’s Radiation Budget: The Driver for Weather and Climate, 55–67, Springer Berlin Heidelberg, Berlin, Heidelberg, doi:10.1007/978-3-642-30183-4\_4, 2012.
- Meier, A., Toon, G. C., Rinsland, C. P., Goldman, A., and Hase, F.: Spectroscopic Atlas of Atmospheric Microwindows in the Middle Infra-Red, Vol. 048 of *IRF technical report*, Swedish Institute of Space Physics, Kiruna, Sweden, 2004.

- Meinshausen, M., Smith, S. J., Calvin, K., Daniel, J. S., Kainuma, M. L. T., Lamarque, J.-F., Matsumoto, K., Montzka, S. A., Raper, S. C. B., Riahi, K., Thomson, A., Velders, G. J. M., and van Vuuren, D. P.: The RCP greenhouse gas concentrations and their extensions from 1765 to 2300, *Climatic Change*, 109, 213–241, doi:10.1007/s10584-011-0156-z, 2011.
- Messerschmidt, J., Geibel, M. C., Blumenstock, T., Chen, H., Deutscher, N. M., Engel, A., Feist, D. G., Gerbig, C., Gisi, M., Hase, F., Katrynski, K., Kolle, O., Lavrič, J. V., Notholt, J., Palm, M., Ramonet, M., Rettinger, M., Schmidt, M., Sussmann, R., Toon, G. C., Truong, F., Warneke, T., Wennberg, P. O., Wunch, D., and Xueref-Remy, I.: Calibration of TCCON column-averaged CO<sub>2</sub>: the first aircraft campaign over European TCCON sites, *Atmos. Chem. Phys.*, 11, 10 765–10 777, doi:10.5194/acp-11-10765-2011, 2011.
- Meul, S., Dameris, M., Langematz, U., Abalichin, J., Kerschbaumer, A., Kubin, A., and Oberländer-Hayn, S.: Impact of rising greenhouse gas concentrations on future tropical ozone and UV exposure, *Geophysical Research Letters*, 43, 2919–2927, doi: 10.1002/2016GL067997, 2016GL067997, 2016.
- Michelson, A. A. and Morley, E. W.: On the relative motion of the Earth and the luminiferous ether, *American Journal of Science, Series 3 Vol. 34*, 333–345, doi:10.2475/ajs.s3-34.203.333, 1887.
- Morino, I., Uchino, O., Inoue, M., Yoshida, Y., Yokota, T., Wennberg, P. O., Toon, G. C., Wunch, D., Roehl, C. M., Notholt, J., Warneke, T., Messerschmidt, J., Griffith, D. W. T., Deutscher, N. M., Sherlock, V., Connor, B., Robinson, J., Sussmann, R., and Rettinger, M.: Preliminary validation of column-averaged volume mixing ratios of carbon dioxide and methane retrieved from GOSAT short-wavelength infrared spectra, *Atmos. Meas. Tech.*, 4, 1061–1076, doi:10.5194/amt-4-1061-2011, 2011.
- Morse, P. M.: Diatomic Molecules According to the Wave Mechanics. II. Vibrational Levels, *Phys. Rev.*, 34, 57–64, doi:10.1103/PhysRev.34.57, 1929.
- Newman, S. M., Lane, I. C., Orr-Ewing, A. J., Newnham, D. A., and Ballard, J.: Integrated absorption intensity and Einstein coefficients for the O<sub>2</sub> a<sup>1</sup>Δ<sub>g</sub> – X<sup>3</sup>Σ<sub>g</sub><sup>-</sup> (0, 0) transition: A comparison of cavity ringdown and high resolution Fourier transform spectroscopy with a long-path absorption cell, *The Journal of Chemical Physics*, 110, 10 749–10 757, doi:http://dx.doi.org/10.1063/1.479018, 1999.
- NOAA: Committee on Extension to the Standard Atmosphere, U.S. Standard Atmosphere, U.S. Government Printing Office, Washington, D.C., USA, 1976.

- Norton, R. H. and Rinsland, C. P.: ATMOS data processing and science analysis methods, *Appl. Opt.*, 30, 389–400, doi:10.1364/AO.30.000389, 1991.
- Olsen, S. C. and Randerson, J. T.: Differences between surface and column atmospheric CO<sub>2</sub> and implications for carbon cycle research, *Journal of Geophysical Research: Atmospheres*, 109, doi:10.1029/2003JD003968, d02301, 2004.
- Pan, L. L., Bowman, K. P., Atlas, E. L., Wofsy, S. C., Zhang, F., Bresch, J. F., Ridley, B. A., Pittman, J. V., Homeyer, C. R., Romashkin, P., and Cooper, W. A.: The Stratosphere–Troposphere Analyses of Regional Transport 2008 Experiment, *Bulletin of the American Meteorological Society*, 91, 327–342, doi:10.1175/2009BAMS2865.1, 2010.
- Phillips, D. L.: A Technique for the Numerical Solution of Certain Integral Equations of the First Kind, *J. ACM*, 9, 84–97, doi:10.1145/321105.321114, 1962.
- Plieninger, J., Laeng, A., Lossow, S., von Clarmann, T., Stiller, G. P., Kellmann, S., Linden, A., Kiefer, M., Walker, K. A., Noel, S., Hervig, M. E., McHugh, M., Lambert, A., Urban, J., Elkins, J. W., and Murtagh, D.: Validation of revised methane and nitrous oxide profiles from MIPAS-ENVISAT, *Atmospheric Measurement Techniques*, 9, 765–779, doi:10.5194/amt-9-765-2016, 2016.
- Ponater, M., Dietmüller, S., and Sausen, R.: Atmospheric Physics: Background – Methods – Trends, Chap. Greenhouse Effect, Radiative Forcing and Climate Sensitivity, 85–100, Springer Berlin Heidelberg, Berlin, Heidelberg, doi:10.1007/978-3-642-30183-4\_6, 2012.
- Prather, M. J., Holmes, C. D., and Hsu, J.: Reactive greenhouse gas scenarios: Systematic exploration of uncertainties and the role of atmospheric chemistry, *Geophysical Research Letters*, 39, doi:10.1029/2012GL051440, l09803, 2012.
- Reuter, M., Buchwitz, M., Hilker, M., Heymann, J., Schneising, O., Pillai, D., Bovensmann, H., Burrows, J. P., Bösch, H., Parker, R., Butz, A., Hasekamp, O., O’Dell, C. W., Yoshida, Y., Gerbig, C., Nehr Korn, T., Deutscher, N. M., Warneke, T., Notholt, J., Hase, F., Kivi, R., Sussmann, R., Machida, T., Matsueda, H., and Sawa, Y.: Satellite-inferred European carbon sink larger than expected, *Atmos. Chem. Phys.*, 14, 13 739–13 753, doi:10.5194/acp-14-13739-2014, 2014.
- Rienecker, M. M., Suarez, M. J., Gelaro, R., Todling, R., Bacmeister, J., Liu, E., Bosilovich, M. G., Schubert, S. D., Takacs, L., Kim, G.-K., Bloom, S., Chen, J., Collins, D., Conaty, A., da Silva, A., Gu, W., Joiner, J., Koster, R. D., Lucchesi, R., Molod, A., Owens, T., Pawson, S., Pegion, P., Redder, C. R., Reichle, R., Robertson, F. R., Ruddick, A. G., Sienkiewicz, M., and Woollen, J.: MERRA: NASA’s Modern-Era Retrospective Analysis

- for Research and Applications, *Journal of Climate*, 24, 3624–3648, doi:10.1175/JCLI-D-11-00015.1, 2011.
- Rigby, M., Prinn, R. G., Fraser, P. J., Simmonds, P. G., Langenfelds, R. L., Huang, J., Cunnold, D. M., Steele, L. P., Krummel, P. B., Weiss, R. F., O’Doherty, S., Salameh, P. K., Wang, H. J., Harth, C. M., Mühle, J., and Porter, L. W.: Renewed growth of atmospheric methane, *Geophysical Research Letters*, 35, doi:10.1029/2008GL036037, 122805, 2008.
- Rinsland, C. P., Jones, N. B., Connor, B. J., Logan, J. A., Pougatchev, N. S., Goldman, A., Murcray, F. J., Stephen, T. M., Pine, A. S., Zander, R., Mahieu, E., and Demoulin, P.: Northern and southern hemisphere ground-based infrared spectroscopic measurements of tropospheric carbon monoxide and ethane, *Journal of Geophysical Research: Atmospheres*, 103, 28 197–28 217, doi:10.1029/98JD02515, 1998.
- Rodgers, C.: *Inverse Methods for Atmospheric Sounding: Theory and Practice*, Series on Atmospheric, Oceanic and Planetary Physics, World Scientific, Singapur, 2000.
- Rodgers, C. D. and Connor, B. J.: Intercomparison of remote sounding instruments, *Journal of Geophysical Research: Atmospheres*, 108, doi:10.1029/2002JD002299, 4116, 2003.
- Rodriguez, O.: Des lois geometriques qui regissent les desplacements d’un systeme solide dans l’espace et de la variation des coordonnees provenant de desplacements consideres independamment des causes qui peuvent les produire, *J. Math. Pure Appl.*, 5, 380–440, 1840.
- Roeckner, E., Brokopf, R., Esch, M., Giorgetta, M., Hagemann, S., Kornblueh, L., Manzini, E., Schlese, U., and Schulzweida, U.: Sensitivity of Simulated Climate to Horizontal and Vertical Resolution in the ECHAM5 Atmosphere Model, *Journal of Climate*, 19, 3771–3791, doi:10.1175/JCLI3824.1, 2006.
- Rosenkranz, P.: Shape of the 5 mm oxygen band in the atmosphere, *IEEE Transactions on Antennas and Propagation*, 23, 498–506, doi:10.1109/TAP.1975.1141119, 1975.
- Rothman, L., Gordon, I., Barbe, A., Benner, D., Bernath, P., Birk, M., Boudon, V., Brown, L., Campargue, A., Champion, J.-P., Chance, K., Coudert, L., Dana, V., Devi, V., Fally, S., Flaud, J.-M., Gamache, R., Goldman, A., Jacquemart, D., Kleiner, I., Lacombe, N., Lafferty, W., Mandin, J.-Y., Massie, S., Mikhailenko, S., Miller, C., Moazzen-Ahmadi, N., Naumenko, O., Nikitin, A., Orphal, J., Perevalov, V., Perrin, A., Predoi-Cross, A., Rinsland, C., Rotger, M., Šimečková, M., Smith, M., Sung, K., Tashkun, S., Tennyson, J., Toth, R., Vandaele, A., and Auwera, J. V.: The HITRAN 2008 molecular spectroscopic

- database, *Journal of Quantitative Spectroscopy and Radiative Transfer*, 110, 533 – 572, doi:10.1016/j.jqsrt.2009.02.013, 2009.
- Rothman, L., Gordon, I., Babikov, Y., Barbe, A., Benner, D. C., Bernath, P., Birk, M., Bizzocchi, L., Boudon, V., Brown, L., Campargue, A., Chance, K., Cohen, E., Coudert, L., Devi, V., Drouin, B., Fayt, A., Flaud, J.-M., Gamache, R., Harrison, J., Hartmann, J.-M., Hill, C., Hodges, J., Jacquemart, D., Jolly, A., Lamouroux, J., Roy, R. L., Li, G., Long, D., Lyulin, O., Mackie, C., Massie, S., Mikhailenko, S., Müller, H., Naumenko, O., Nikitin, A., Orphal, J., Perevalov, V., Perrin, A., Polovtseva, E., Richard, C., Smith, M., Starikova, E., Sung, K., Tashkun, S., Tennyson, J., Toon, G., Tyuterev, V., and Wagner, G.: The HITRAN2012 molecular spectroscopic database, *Journal of Quantitative Spectroscopy and Radiative Transfer*, 130, 4 – 50, doi:10.1016/j.jqsrt.2013.07.002, 2013.
- Sander, R., Kerkweg, A., Jöckel, P., and Lelieveld, J.: Technical note: The new comprehensive atmospheric chemistry module MECCA, *Atmos. Chem. Phys.*, 5, 445–450, doi:10.5194/acp-5-445-2005, 2005.
- Sander, S., Friedl, R., Barker, J., Golden, D., rylo, M., Wine, P., Abbatt, J., Burkholder, J., Kolb, C.E. d Moortgat, G., Huie, R., and Orkin, V.: Chemical kinetics and photochemical data for use in atmospheric studies: Evaluation No. 17, JPL Publication 10–6, Jet Propulsion Laboratory, Pasadena, USA, 2011.
- Schlager, H., Grewe, V., and Roiger, A.: Atmospheric Physics: Background – Methods – Trends, Chap. Chemical Composition of the Atmosphere, 17–35, Springer Berlin Heidelberg, Berlin, Heidelberg, doi:10.1007/978-3-642-30183-4\_2, 2012.
- Schneider, M., Hase, F., and Blumenstock, T.: Water vapour profiles by ground-based FTIR spectroscopy: study for an optimised retrieval and its validation, *Atmos. Chem. Phys.*, 6, 811–830, doi:10.5194/acp-6-811-2006, 2006.
- Schneider, M., Barthlott, S., Hase, F., González, Y., Yoshimura, K., García, O. E., Sepúlveda, E., Gomez-Pelaez, A., Gisi, M., Kohlhepp, R., Dohe, S., Blumenstock, T., Wiegeler, A., Christner, E., Strong, K., Weaver, D., Palm, M., Deutscher, N. M., Warneke, T., Notholt, J., Lejeune, B., Demoulin, P., Jones, N., Griffith, D. W. T., Smale, D., and Robinson, J.: Ground-based remote sensing of tropospheric water vapour isotopologues within the project MUSICA, *Atmos. Meas. Tech.*, 5, 3007–3027, doi:10.5194/amt-5-3007-2012, 2012.
- Seiler, W. and Fishman, J.: The distribution of carbon monoxide and ozone in the free troposphere, *Journal of Geophysical Research: Oceans*, 86, 7255–7265, doi:10.1029/JC086iC08p07255, 1981.

- Seinfeld, J. and Pandis, S.: Atmospheric Chemistry and Physics: From Air Pollution to Climate Change, A Wiley-Interscience publication, Wiley, Hoboken, New Jersey, 2006.
- Singh, H. B., Brune, W. H., Crawford, J. H., Jacob, D. J., and Russell, P. B.: Overview of the summer 2004 Intercontinental Chemical Transport Experiment–North America (INTEX-A), *Journal of Geophysical Research: Atmospheres*, 111, doi:10.1029/2006JD007905, d24S01, 2006.
- Smith, K. M. and Newnham, D. A.: Near-infrared absorption cross sections and integrated absorption intensities of molecular oxygen ( $O_2$ ,  $O_2-O_2$ , and  $O_2-N_2$ ), *Journal of Geophysical Research: Atmospheres*, 105, 7383–7396, doi:10.1029/1999JD901171, 2000.
- Spiering, F. R. and van der Zande, W. J.: Collision induced absorption in the  $a_1\Delta(v = 2) \leftarrow X^3\Sigma_g^-(v = 0)$  band of molecular oxygen, *Phys. Chem.*, 14, 9923–9928, doi:10.1039/C2CP40961E, 2012.
- Spivakovsky, C., Logan, J., Montzka, S., Balkanski, Y., Foreman-Fowler, M., Jones, D., Horowitz, L., Fusco, A., Brenninkmeijer, C., Prather, M., et al.: Three-dimensional climatological distribution of tropospheric OH: Update and evaluation, *Journal of Geophysical Research*, 105, 8931–8980, doi:10.1029/1999JD901006, 2000.
- Sussmann, R., Stremme, W., Buchwitz, M., and de Beek, R.: Validation of ENVISAT/SCIAMACHY columnar methane by solar FTIR spectrometry at the Ground-Truthing Station Zugspitze, *Atmos. Chem. Phys.*, 5, 2419–2429, doi:10.5194/acp-5-2419-2005, 2005.
- Sussmann, R., Forster, F., Rettinger, M., and Jones, N.: Strategy for high-accuracy-and-precision retrieval of atmospheric methane from the mid-infrared FTIR network, *Atmospheric Measurement Techniques*, 4, 1943–1964, doi:10.5194/amt-4-1943-2011, 2011.
- Tans, P.: An Accounting of the Observed Increase in Oceanic and Atmospheric  $CO_2$  and an Outlook for the Future, *Oceanography*, 22, 2009.
- Thompson, A. M.: The Oxidizing Capacity of the Earth’s Atmosphere: Probable Past and Future Changes, *Science*, 256, 1157–1165, doi:10.1126/science.256.5060.1157, 1992.
- Tonkov, M., Filippov, N., Timofeyev, Y., and Polyakov, A.: A simple model of the line mixing effect for atmospheric applications: Theoretical background and comparison with experimental profiles, *Journal of Quantitative Spectroscopy and Radiative Transfer*, 56, 783 – 795, doi:http://dx.doi.org/10.1016/S0022-4073(96)00113-6, 1996.
- Toon, G. C.: The JPL MkIV interferometer, *Opt. Photon. News*, 2, 19–21, doi:10.1364/OPN.2.10.000019, 1991.

- Wang, Z., Chappellaz, J., Martinerie, P., Park, K., Petrenko, V., Witrant, E., Emmons, L. K., Blunier, T., Brenninkmeijer, C. A. M., and Mak, J. E.: The isotopic record of Northern Hemisphere atmospheric carbon monoxide since 1950: implications for the CO budget, *Atmos. Chem. Phys.*, 12, 4365–4377, doi:10.5194/acp-12-4365-2012, 2012.
- Washenfelder, R. A., Wennberg, P. O., and Toon, G. C.: Tropospheric methane retrieved from ground-based near-IR solar absorption spectra, *Geophysical Research Letters*, 30, doi:10.1029/2003GL017969, 2226, 2003.
- Washenfelder, R. A., Toon, G. C., Blavier, J.-F., Yang, Z., Allen, N. T., Wennberg, P. O., Vay, S. A., Matross, D. M., and Daube, B. C.: Carbon dioxide column abundances at the Wisconsin Tall Tower site, *Journal of Geophysical Research: Atmospheres*, 111, doi:10.1029/2006JD007154, d22305, 2006.
- Wiegele, A., Schneider, M., Hase, F., Barthlott, S., García, O. E., Sepúlveda, E., González, Y., Blumenstock, T., Raffalski, U., Gisi, M., and Kohlhepp, R.: The MUSICA MetOp/IASI H<sub>2</sub>O and  $\delta$ D products: characterisation and long-term comparison to NDACC/FTIR data, *Atmospheric Measurement Techniques*, 7, 2719–2732, doi:10.5194/amt-7-2719-2014, 2014.
- Wofsy, S. C.: HIAPER Pole-to-Pole Observations (HIPPO): fine-grained, global-scale measurements of climatically important atmospheric gases and aerosols, *Philosophical Transactions of the Royal Society of London A: Mathematical, Physical and Engineering Sciences*, 369, 2073–2086, doi:10.1098/rsta.2010.0313, 2011.
- Woiwode, W., Höpfner, M., Bi, L., Pitts, M. C., Poole, L. R., Oelhaf, H., Molleker, S., Borrmann, S., Klingebiel, M., Belyaev, G., Ebersoldt, A., Griessbach, S., Groß, J.-U., Gulde, T., Krämer, M., Maucher, G., Piesch, C., Rolf, C., Sartorius, C., Spang, R., and Orphal, J.: Spectroscopic evidence for large aspherical  $\beta$ -NAT particles involved in denitrification in the December 2011 Arctic stratosphere, *Atmospheric Chemistry and Physics Discussions*, 2016, 1–44, doi:10.5194/acp-2016-146, 2016.
- Wunch, D., Toon, G. C., Wennberg, P. O., Wofsy, S. C., Stephens, B. B., Fischer, M. L., Uchino, O., Abshire, J. B., Bernath, P., Biraud, S. C., Blavier, J.-F. L., Boone, C., Bowman, K. P., Browell, E. V., Campos, T., Connor, B. J., Daube, B. C., Deutscher, N. M., Diao, M., Elkins, J. W., Gerbig, C., Gottlieb, E., Griffith, D. W. T., Hurst, D. F., Jiménez, R., Keppel-Aleks, G., Kort, E. A., Macatangay, R., Machida, T., Matsueda, H., Moore, F., Morino, I., Park, S., Robinson, J., Roehl, C. M., Sawa, Y., Sherlock, V., Sweeney, C., Tanaka, T., and Zondlo, M. A.: Calibration of the Total Carbon Column Observing Network using aircraft profile data, *Atmos. Meas. Tech.*, 3, 1351–1362, doi:10.5194/amt-3-1351-2010, 2010.

- Wunch, D., Toon, G. C., Blavier, J.-F. L., Washenfelder, R. A., Notholt, J., Connor, B. J., Griffith, D. W. T., Sherlock, V., and Wennberg, P. O.: The Total Carbon Column Observing Network, *Philosophical Transactions of the Royal Society of London A: Mathematical, Physical and Engineering Sciences*, 369, 2087–2112, doi:10.1098/rsta.2010.0240, 2011.
- Wunch, D., Toon, G. C., Sherlock, V., Deutscher, N. M., Liu, C., Feist, D. G., and Wennberg, P. O.: The Total Carbon Column Observing Network’s GGG2014 Data Version, Tech. rep., Carbon Dioxide Information Analysis Center, Oak Ridge National Laboratory, Oak Ridge, Tennessee, U.S.A., doi:10.14291/tccon.ggg2014.documentation.R0/1221662, 2015.
- Yang, Z., Wennberg, P., Cageao, R., Pongetti, T., Toon, G., and Sander, S.: Ground-based photon path measurements from solar absorption spectra of the O<sub>2</sub> A-band, *Journal of Quantitative Spectroscopy and Radiative Transfer*, 90, 309 – 321, doi: <http://dx.doi.org/10.1016/j.jqsrt.2004.03.020>, 2005.
- Yokota, T., Yoshida, Y., Eguchi, N., Ota, Y., Tanaka, T., Watanabe, H., and Maksyutov, S.: Global Concentrations of CO<sub>2</sub> and CH<sub>4</sub> Retrieved from GOSAT: First Preliminary Results, *SOLA*, 5, 160–163, doi:10.2151/sola.2009-041, 2009.
- Yoshida, Y., Kikuchi, N., Morino, I., Uchino, O., Oshchepkov, S., Bril, A., Saeki, T., Schutgens, N., Toon, G. C., Wunch, D., Roehl, C. M., Wennberg, P. O., Griffith, D. W. T., Deutscher, N. M., Warneke, T., Notholt, J., Robinson, J., Sherlock, V., Connor, B., Rettinger, M., Sussmann, R., Ahonen, P., Heikkinen, P., Kyrö, E., Mendonca, J., Strong, K., Hase, F., Dohe, S., and Yokota, T.: Improvement of the retrieval algorithm for GOSAT SWIR XCO<sub>2</sub> and XCH<sub>4</sub> and their validation using TCCON data, *Atmospheric Measurement Techniques*, 6, 1533–1547, doi:10.5194/amt-6-1533-2013, 2013.
- Zbinden, R. M., Thouret, V., Ricaud, P., Carminati, F., Cammas, J.-P., and Nédélec, P.: Climatology of pure tropospheric profiles and column contents of ozone and carbon monoxide using MOZAIC in the mid-northern latitudes (24° N to 50° N) from 1994 to 2009, *Atmospheric Chemistry and Physics*, 13, 12 363–12 388, doi:10.5194/acp-13-12363-2013, 2013.
- Zhou, M., Dils, B., Wang, P., Detmers, R., Yoshida, Y., O’Dell, C. W., Feist, D. G., Velazco, V. A., Schneider, M., and De Mazière, M.: Validation of TANSO-FTS/GOSAT XCO<sub>2</sub> and XCH<sub>4</sub> glint mode retrievals using TCCON data from near-ocean sites, *Atmospheric Measurement Techniques*, 9, 1415–1430, doi:10.5194/amt-9-1415-2016, 2016.

# List of Figures

2.1	The Earth's vertical structure . . . . .	7
2.2	Simplified model of the Earth's radiation budget . . . . .	9
2.3	Transition processes . . . . .	15
2.4	Model of a vibrating diatomic molecule . . . . .	16
2.5	Potentials for harmonic and anharmonic oscillators . . . . .	18
2.6	Rotating diatomic molecule . . . . .	19
2.7	Non-rigid rotor . . . . .	20
2.8	Energy levels for a rigid and non-rigid rotor . . . . .	22
2.9	Simulated transmission spectrum and energy levels for vibrating rotor . . . . .	24
2.10	CO transmission spectra for different temperatures . . . . .	25
2.11	Line profile shapes . . . . .	27
2.12	Illustration of a Michelson interferometer . . . . .	29
2.13	Locations of operating FTIR spectrometers . . . . .	34
2.14	Radiative transfer geometry . . . . .	36
3.1	Karlsruhe FTS site . . . . .	42
3.2	FTS spectrometer . . . . .	44
3.3	Detectors and dichroic beamsplitter . . . . .	44
3.4	Karlsruhe InSb and InGaAs spectrum . . . . .	46
3.5	NDACC filters . . . . .	47
3.6	Difference between Karlsruhe and Park Falls spectra . . . . .	63
3.7	Difference between Karlsruhe and Izaña spectra . . . . .	63
3.8	Spectral fits indicating continuum variations . . . . .	66
3.9	Black body cavity low resolution spectrum . . . . .	67
3.10	Spectral fits for black body cavity spectra . . . . .	68
3.11	NDACC H <sub>2</sub> O spectral fit . . . . .	69
4.1	Legendre polynomials . . . . .	73
4.2	Improvement of $\sigma_{\text{rms}}$ . . . . .	73
4.3	Spectral fits using modified analysis strategy . . . . .	75
4.4	Different spectral filters . . . . .	76
4.5	Airmass dependence . . . . .	79

4.6	TCCON XCO <sub>2</sub> calibration curve . . . . .	83
4.7	TCCON XCO <sub>2</sub> calibration curve for European sites . . . . .	83
4.8	TCCON XCH <sub>4</sub> calibration curve . . . . .	84
4.9	TCCON XCH <sub>4</sub> calibration curve for European sites . . . . .	85
4.10	XCO <sub>2</sub> and XCH <sub>4</sub> differences for other TCCON sites . . . . .	86
4.11	Guiding points and O <sub>2</sub> CIA . . . . .	87
5.1	CO a priori VMR profiles . . . . .	96
5.2	NDACC CO spectral fits . . . . .	96
5.3	TCCON CO spectral fits . . . . .	97
5.4	TCCON CO interfering gases . . . . .	98
5.5	MIR profile error estimation . . . . .	100
5.6	NIR profile error estimation . . . . .	100
5.7	O <sub>2</sub> spectral fits . . . . .	103
5.8	Difference between spectroscopically derived C <sub>dryair</sub> . . . . .	103
5.9	Difference between calculated C <sub>dryair</sub> . . . . .	104
5.10	Impact of a priori change on NDACC retrieval . . . . .	105
5.11	Impact of a priori change on TCCON retrieval . . . . .	106
5.12	Impact of line parameter change . . . . .	108
5.13	TCCON and NDACC XCO comparison . . . . .	109
5.14	XCO bias contributions . . . . .	110
5.15	SZA correction impact . . . . .	112
5.16	Relative impact of SZA correction . . . . .	113
5.17	EMAC CO VMR profiles . . . . .	118
5.18	NDACC and TCCON column averaged kernels . . . . .	119
5.19	Estimation of smoothing error . . . . .	119

# List of Tables

3.1	NDACC filters . . . . .	47
3.2	TCCON target gases . . . . .	51
3.3	TCCON airmass independent correction factors . . . . .	52
3.4	NDACC target gases . . . . .	55
4.1	Karlsruhe modified TCCON retrieval strategy . . . . .	76
4.2	Change in DMFs due to modified TCCON retrieval strategy . . . . .	80
5.1	NDACC and TCCON CO retrieval strategies . . . . .	95
5.2	Estimated uncertainties for the error estimation . . . . .	99
5.3	Total column error estimation for CO . . . . .	101



## List of Acronyms

<b>AD</b>	airmass dependent correction factor
<b>AI</b>	Airmass independent calibration factor
<b>AP</b>	common a priori VMR profile
<b>AVK</b>	averaging kernel
<b>CFC</b>	chlorofluorocarbon
<b>CIA</b>	collision induced absorption
<b>cw</b>	center wavenumber given in $\text{cm}^{-1}$
<b>DMF</b>	column averaged dry-air mole fraction
<b>ECMWF</b>	European Centre for Medium-range Weather Forecasts
<b>EMAC</b>	ECHAM/MESSy Atmospheric Chemistry
<b>FTIR</b>	Fourier Transform Infrared
<b>FTS</b>	Fourier Transform Infrared spectrometer
<b>FWHM</b>	full width at half maximum
<b>GFIT</b>	non-linear least-squares fitting algorithm used within the TCCON
<b>GHG</b>	greenhouse gas
<b>GOSAT</b>	Greenhouse Gases Observing Satellite
<b>HCFC</b>	hydrochlorofluorocarbon
<b>HFC</b>	hydrofluorocarbon
<b>HITRAN</b>	High Resolution Transmission parameter compilation
<b>IASI</b>	Infrared Atmospheric Sounding Interferometer
<b>ILS</b>	instrumental line shape
<b>IMECC</b>	Infrastructure for Measurement of the European Carbon Cycle project
<b>IMK</b>	Institute of Meteorology and Climate Research

<b>InGaAs</b>	indium gallium arsenide
<b>InSb</b>	indium antimonide
<b>IPCC</b>	International Panel on Climate Change
<b>IR</b>	infrared
<b>IRWG</b>	Infrared Working Group
<b>ISO</b>	modified treatment of isotopic identities
<b>KIT</b>	Karlsruhe Institute of Technology
<b>LTE</b>	local thermodynamic equilibrium
<b>LOS</b>	line of sight
<b>MCT</b>	mercury cadmium telluride
<b>MERRA</b>	Modern-era retrospective analysis
<b>MIR</b>	mid infrared
<b>MUSICA</b>	Multi-platform remote Sensing of Isotopologues for investigating the Cycle of Atmospheric water project
<b>NCEP/NCAR</b>	National Centers for Environmental Prediction/National Center for Atmospheric Research
<b>NDACC</b>	Network for the Detection of Atmospheric Composition Change
<b>NIR</b>	near infrared
<b>NMHC</b>	non methane hydrocarbons
<b>NMVOC</b>	non methane volatile organic compound
<b>OCO-2</b>	Orbiting Carbon Observatory 2
<b>PROFFIT</b>	non-linear least-squares fitting algorithm used within the NDACC
<b>RF</b>	radiative forcing
<b>RTE</b>	radiative transfer equation
<b>SBF</b>	solar brightness fluctuation

<b>SCIAMACHY</b>	SCanning Imaging Absorption SpectroMeter for Atmospheric CHartographY
<b>SFIT</b>	non-linear least-squares fitting algorithm used within the NDACC
<b>SNR</b>	signal-to-noise ratio
<b>SZA</b>	solar zenith angle
<b>TCCON</b>	Total Carbon Column Observing Network
<b>TOA</b>	top of the atmosphere
<b>TSI</b>	total solar irradiance
<b>UV</b>	ultraviolet
<b>VMR</b>	volume mixing ratio
<b>WACCM</b>	Whole Atmospheric Chemistry Climate Model
<b>WMO</b>	World Meteorological Organization



## Acknowledgements

Hiermit möchte ich mich sehr herzlich bei Herrn Prof. Dr. Johannes Orphal für die interessante Themenstellung und die Übernahme des Referats bedanken. Mein Dank gilt auch Herrn Priv. Doz. Dr. Michael Höpfner für die Übernahme des Korreferats und der Durchsicht der vorliegenden Arbeit.

Mein besonderer Dank gilt Dr. Thomas Blumenstock und Dr. Frank Hase. Vielen Dank für die Unterstützung und Bereitschaft für unzählige Diskussionen interessanter wissenschaftlicher Fragestellungen in den letzten drei Jahren. Ich danke Dr. Thomas Blumenstock für die Möglichkeit, meine wissenschaftlichen Ergebnisse auf zahlreichen internationalen Konferenzen an den verschiedensten Orten dieser Welt vorgestellt haben zu dürfen. Ich danke Dr. Frank Hase für seine Bereitschaft zu jeder Zeit Fragen zu beantworten und seine Expertise weiterzugeben. Ich danke der gesamten Boden-Arbeitsgruppe für ihre Unterstützung und die gemeinsame tolle Zeit miteinander. Die gemeinsamen Abende im Grossman's bleiben unvergessen.

Ich danke der Karlsruhe Graduate School for Climate and Environment (GRACE) für die Unterstützung meines Auslandsaufenthaltes am California Institute of Technology.

I gratefully thank Prof. Dr. Paul O. Wennberg for hosting me at the California Institute of Technology. Thank you for the warm welcome and excellent hospitality. I would like to thank Dr. Geoffrey C. Toon for many helpful discussions and for the tour at the Jet Propulsion Laboratory. My special thanks go to Dr. Debra Wunch. Thank you for supervising me and making my stay at Caltech as comfortable as possible. Thank you for your time, helpful discussions on GFIT, and your endless patience. I thank the entire Carbon Cycle group for a great time in Pasadena.

Ich möchte mich herzlichst bei meiner Familie und Freunden bedanken, ohne deren Unterstützung diese Arbeit nicht möglich gewesen wäre.

Mein größter Dank gilt meiner Freundin Jenny. Vielen Dank für deine nie endende Rücksicht, Geduld und Motivation während der letzten Jahre. Ohne dich und deiner endlosen Unterstützung wäre diese Arbeit nicht möglich gewesen. Vielen Dank, dass du immer für mich da bist.